Universidad
Carlos III de Madrid

Dynamic radial deformations of nonlinear elastic structures

On the influence of constitutive modeling

Author: Damián Aranda-Iglesias

Supervisor: José A. Rodríguez-Martínez

Co-Supervisor: Guadalupe Vadillo

Department of Continuum Mechanics and Structural Analysis
University Carlos III of Madrid

Leganés, June 9, 2017

Dynamic radial deformations of nonlinear elastic structures

On the influence of constitutive modeling

This dissertation is submitted for the degree of *Doctor of Philosophy*

Author: Damián Aranda-Iglesias
Supervisor: José A. Rodríguez-Martínez
Co-Supervisor: Guadalupe Vadillo Martín

Members of the Evaluation Committee:

Prof. Ignacio Romero	Technical University of Madrid, Spain
Prof. Massimo Ruzzene	Georgia Institute of Technology, USA
Prof. Antonino Morassi	University of Udine, Italy

University Carlos III of Madrid
Department of Continuum Mechanics
and Structural Analysis
Leganés, June 9, 2017.

A Sara, mi compañera en esta y en todas mis aventuras.
A Paco, Mariló y Concha, nunca estaré suficientemente agradecido.

Acknowledgements

I owe my deepest gratitude to my mentor and friend **José A. Rodríguez Martínez**. Thank you for your enthusiasm, your energy, all the opportunities, and your unconditional encouragement and support. I feel really lucky to have shared this trip with you!

I also want to express my warmest gratitude to my other supervisor **Guadalupe Vadillo Martín**, your affable, thoughtful and receptive personality has enlightened some of the tougher moments. Thanks!

A very special gratitude goes out to **Óscar López-Pamies**, professor of the Department of Civil and Environmental Engineering of the University of Illinois at Urbana-Champaign, and my supervisor during my research stay. It has been my pleasure to work with you, thanks for sharing so much wisdom with me and for your support and advice.

Furthermore, I would like to acknowledge the collaboration in this research of **Prof. Volokh** and **Prof. Rubin** from Technion – Israel Institute of Technology. I have learned a lot working together and your contribution has certainly improved the quality of this research.

Many thanks to my colleagues at UC3M: **Dani, Vila, Mahy, Javi, Vaz, Sara, Luis, Ángel, Mata, Pablo, Lorena** and **Óscar**. Thanks you for your help, your friendship and for all the fun we have had in the last years. In a very special way I would like to mention here **Daniel García Gonzalez, Alejandro Mahy Soler** and **Javier Vila Morán**. I will miss our stimulating and endless discussions guys!

I will always be indebted to my *alter ego* **David Rodríguez Martinez**. Thank you for your help, not only reviewing this document but supporting me at every step.

Last but not least, I would like to thank my family: **Paco, Mariló, Concha** and **Sara**. None of this would have been possible without your daily back up. I will never be grateful enough

Abstract

The objective of this dissertation is to develop a comprehensive theoretical approach to the role of the constitutive model on the dynamic radial deformations of nonlinear elastic structures. Using 1D and 2D models, cylindrical and spherical thick-walled shells are considered. These geometries are representative of man-made and natural structures that can be found in a wide variety of engineering applications and biological systems. Lead-rubber bearings, vibration isolators, peristaltic pumps, rubber bushings, saccular aneurysms or arteries are examples of nonlinear elastic structures with spherical and cylindrical geometries that are constantly subjected to all kinds of vibrational and dynamic loads. The research, which starts by considering isotropic, incompressible and rate independent constitutive models, is based on the systematic incorporation of compressibility, viscosity and anisotropy in the description of the mechanical response of the material. We investigate free and forced vibrations using different initial and boundary conditions: (1) *ab initio* elastic stored and kinetic energies, (2) constant radial pressures, (3) linearly time dependent radial pressures and (4) harmonic time dependent radial pressures. While the isotropic and incompressible 1D elastic structures subjected to constant pressure admit an analytical closed-form solution, all the other cases need to be solved numerically. To this end, we have developed in this work a number of specific numerical schemes. The overall outcome of this dissertation is to make it plain that the constitutive model used to describe the mechanical behavior of thick-walled shells plays a fundamental role in the nonlinear dynamics of such structures. In particular, we have demonstrated the influence of the constitutive model on: (1) the loss of oscillatory behavior of the structure, (2) the transition from periodic motions to quasi-periodic and chaotic motions, (3) the nonlinear resonances of the shells, (4) the propagation of shock waves within the structure and (5) the onset and development of cavitation instabilities.

Table of contents

Part I

Introduction and fundamental concepts of nonlinear solid mechanics

1 Introduction

This doctoral research aims to provide a comprehensive analysis of the dynamic behavior of nonlinear elastic cylindrical and spherical structures subjected to dynamic loading. In particular, this dissertation develops a rigorous theoretical approach on the influence of the constitutive model in the large amplitude vibrations of these kind of structures when subjected to a wide variety of loading conditions.

1.1 Research background and motivation

From natural rubber to synthetic elastomers, highly deformable elastic polymers have become widely used in modern industry. All kinds of components such as: tires, shock mounts, seals, couplings, bridge and building bearings, footwear, hoses, conveyor belts, gloves, medical devices, adhesives, thread, tire curing bladders, caulking and sealants, cable insulation, vibration isolators, pond liners, roofing membranes or lip seals of ball-bearings, among others, are common applications of these materials. Most of the aforementioned components and parts are subjected to vibrational or dynamic deformations during their service life.

For instance, extreme dynamic loads are found in classical civil engineering applications: the so-called **lead-rubber bearings (LRBs)** are used for seismic isolation of building bases (Datta, 2010). These devices, as the one presented in Fig. 1.1a, consist of thin cylindrical layers of synthetic or natural rubber inserted between reinforced steel plates with a metallic central lead core. During an earthquake the base of the LRB, which is in contact with the ground, shakes laterally. The rubber layers combined with the steel plates provide lateral flexibility to the bearing, helping to isolate the building foundations from the ground movement. In addition, the lead plug dissipates the earthquake energy by deforming plastically. Despite its lateral flexibility, provided by the rubber, these

devices remain very rigid in the vertical direction being able to support the weight of the building or the bridge with very small axial deformations. Nowadays LBRs are one of the most popular solutions to isolate structures from earthquake forces. Several buildings located in areas with an increased risk of seismic activity such as the National Museum and the Parliament of New Zealand, or the Civil Protection Center in Foligno, Italy (see Fig. 1.1b), have been protected with this technology. The analysis of the dynamic behavior of these devices is a complex task due to the nonlinearity of the problem arising from both the mechanical response of the rubber (and from the lead core) and the large deformations potentially reached during an earthquake. While great efforts have been made in this direction (Hwang and Chiou, 1996; Hwang and Sheng, 1994; Mohan and Krishnankutty, 2017; Robinson, 1982), modeling LBRs still remains as an open topic of great interest in the field of Solids Mechanics.

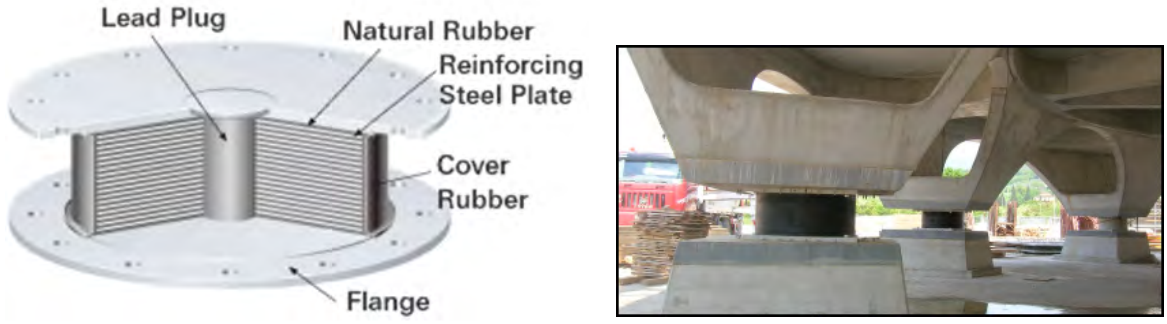

(a) *(b)*

Fig. 1.1 (a) Schematic of a Lead-Rubber Bearing. Source: http://www.bridgestone.com (b) Centro Operativo Emergenza e Formazione of the Civil Protection Center in Foligno (Italy). The building is protected by 10 high-damping rubber bearings with a 1 *m diameter. Source: http://old.enea.it*

Rubber bushings usually employed in vehicle suspension systems are also commonly subjected to dynamic and vibrational loads (see Fig. 1.2). These devices, often made of synthetic rubber or polyurethane, separates the faces of two metal parts while allowing a certain amount of movement. Their main purpose is to add an extra damping effect in the joint helping to isolate the chassis of the vehicle from the vibrations. Several researchers have studied the nonlinear dynamics of these bushings in order to improve their design (Coja and Kari, 2007; Kari, 2003; Karlsson and Persson, 2003; Sjöberg, 2002).

Another problem directly related to the dynamic response of elastomers is the **cavitation** process that occurs in rubber under high triaxiality loading conditions. This phenomenon is the main concern for tire manufacturers that see in cavitation a potential

(a) *(b)*

Fig. 1.2 (a) Rubber bushings of a Porsche 993. Image source: http://www.elephantracing.com. (b) Schematic representation of the position of rubber bushings in a car. Image source: http://dsportmag.com

problem for the reliability of their products. Large hydrostatic stress states may lead to the growth of inherent defects, which are present in most types of rubbers. In broad terms, when rubber is subjected to critically large mechanical forces, these underlying defects may suddenly grow elastically up to the point at which the surrounding polymeric chains reach their maximum elongation. Beyond this point, defects may continue to grow inelastically through a fracture process, i.e., by the irreversible creation of new surfaces. Such defects can be of various natures (e.g., weak regions of the polymer network, actual holes, dust particles) and of various geometries ranging from submicron to supramicron in length scale (Gent, 1990). In their experiments, Yamabe et al. (2011) pressurized cylindrical specimens of ethylene-propylene-diene-methylene (EPDM) transparent rubber with hydrogen gas up to 10 MPa during 24 hours. During this time the gas diffused inside the rubber defects. When they decompressed the specimens to 0.1 MPa, the defects in the rubber were enlarged, becoming visible to an optical microscope (see Fig. 1.3). The phenomenon of cavitation has drawn the attention of several researches mainly due to its role as the initiator of internal damage in the material. The work of Gent and Lindley (1959) provided the first explanation of the phenomenon of cavitation. The authors carried out tensile tests on *poker chip* specimens of 20 *mm* diameter and thicknesses ranging from 0.6 to 9.8 *mm*, made up of natural rubber, carbon-black filled natural rubber, and a polybutadiene synthetic rubber. At smaller thicknesses, a clear kink in the nominal macroscopic stress versus extension plot was observed On a post-mortem examination of the rubber, they found that below the critical value of the stress, there was no visible internal damage, while above this value, cracks were found. These experiments have been repeated more recently by Bayraktar et al. (2008) who registered the damage

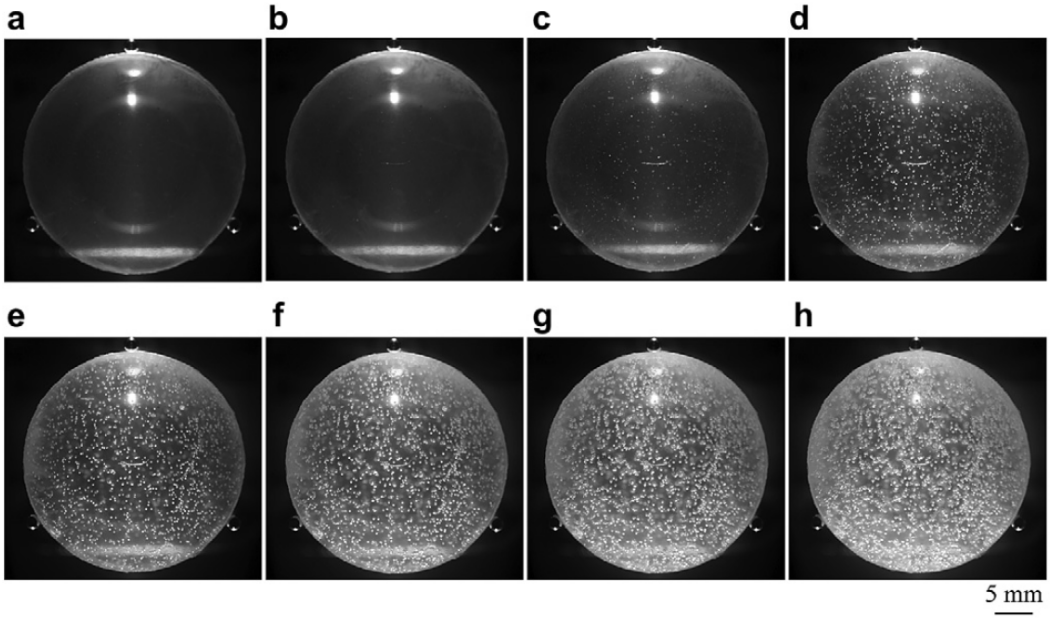

.

Fig. 1.3 Optical microscope images of internal cracks of a specimen exposed to hydrogen gas at 10 MPa: (a) during pressurization, (b) during decompression, (c)0 min after decompression, (d) 1 min (e) 2 min (f) 3 min, (g) 4 min, (h) 5 min. Image source: Yamabe et al. (2011)

evolution in NR (natural rubber) vulcanized and reinforced with carbon black and in SBR (styrene-butadiene-rubber) specimens by using X-ray computed tomography (CT) (see Figures 1.4 and 1.5). In an attempt to explain their experimental findings, Gent and Lindley (1959) proposed to consider the cavitation as an elastic instability. In particular, based on the analysis of Green and Zerna (1954) for thick spherical shells, Gent and Lindley (1959) considered the elastostatic problem of the radially symmetric deformation of a single vacuous spherical cavity of infinitesimal size embedded in the center of a Neo-Hookean rubber ball and subjected to uniform hydrostatic pressure in its outer face. They found that, as the applied pressure approaches the critical value, $P = \frac{5}{2}\mu$ where μ denotes the initial shear modulus of the rubber at zero strain, the size of the cavity suddenly becomes finite. Given that this theoretical result agrees reasonably well with some of their experimental observations, the pioneering work of Gent and Lindley (1959) prompted a plethora of further experimental, theoretical, and computational investigations (see, e.g., Ball (1982); Cho et al. (1987); Cristiano et al. (2010); Gent and Park (1984); Hang-Sheng and Abeyaratne (1992); Kabaria et al. (2015); Kumar et al. (2016); Lefevre et al. (2014); Lian and Li (2012); Lopez-Pamies (2008); Lopez-Pamies et al. (2011a,b); Nakamura and Lopez-Pamies (2012); Oberth and Bruenner (1965);

Poulain et al. (2017); Stringfellow and Abeyaratne (1989); Xu and Henao (2011) clearly following their view of cavitation as an elastic phenomenon.

Furthermore, through direct comparisons with experiments, Lefevre et al. (2014) have recently confirmed the prevailing belief that the nonlinear elastic properties of rubber play a significant role in the phenomenon of cavitation. These comparisons have also suggested that cavitation in rubber may possibly depend, in addition to the nonlinear elastic properties of the rubber, on inertial effects and/or on the viscous dissipation innate to rubber. The reason behind this claim is that the growth of defects into large cavities takes place locally in time through an extremely fast process. Note that in Chapter 7 we provide new insights into the relevance of inertial and viscous dissipation effects on the onset of cavitation in rubber.

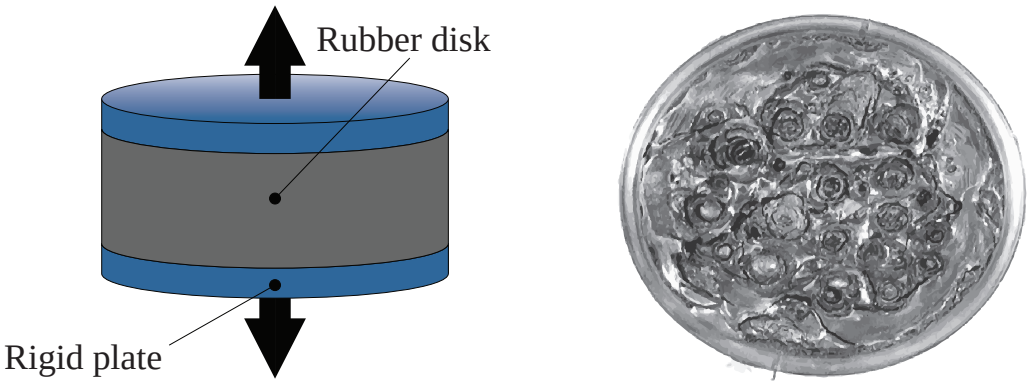

Fig. 1.4 (a)Loading conditions in the Gent and Lindley (1959) poker chip experiments (b) Post-mortem specimen of Natural Rubber. Image source: Bayraktar et al. (2008)

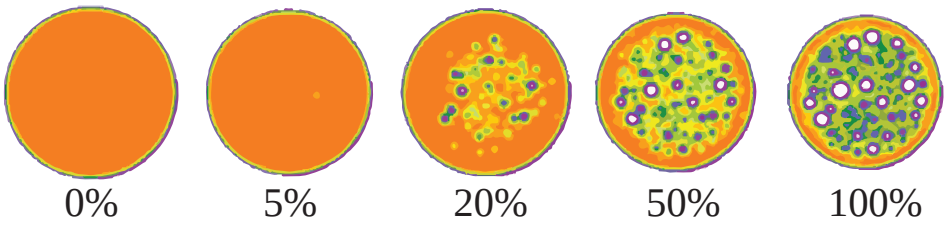

Fig. 1.5 CT evolution of cavitation in Natural Rubber as a function of deformation. Image source: Bayraktar et al. (2008)

Another promising technology attracting nowadays the attention of the scientific community are the so-called **electro-active polymers (EAPs)**. These materials present

some activity (usually large changes in shape or size) when they are stimulated with an electric field. The principal application of EAPs are as actuators, such as artificial muscles (Bar-Cohen, 2000), tactile and haptic interfaces (Keplinger et al., 2010), energy generation and harvesting (Chiba et al., 2009) or several types of sensors (Wang et al., 2016). Numerous investigations have focused on quasi-static applications of EAPs. However, one of the strengths of this technology is that the electric input provides a precise control on the dynamic deformation of the structure, which makes it possible to couple the movement of the EAP to any other sensor. Some applications involving dynamic (oscillatory) behavior of these materials have arisen due to the latter. For instance, an interesting idea is to use these devices to perform **active vibration control (AVC)** of structures (Preumont, 2011). AVC is the active application of force in an equal and opposite fashion to the forces imposed by external vibrations with the aim of maintaining the structure virtually free of vibrations due to the cancellation of forces. Many precision industrial processes cannot take place if the machinery is being affected by vibrations. For example, the high level of accuracy required in the production of semiconductor wafers, frequently used in the fabrication of integrated circuits and solar cells, necessitate of a vibration-free environment (Wang et al., 2015). Since AVC applications have only recently been considered for EAPs actuators, few studies have been published in this regard (Kaal and Herold, 2011; Papaspiridis and Antoniadis, 2008; Sarban et al., 2011; Sarban and Jones, 2010; Sarban et al., 2010; Zhao et al., 2016). These seminal works are focused on the analysis of the non-linear dynamic response of these devices. The inherent nonlinear effects in EAPs, coming from the nonlinear geometric and constitutive responses of the polymer, demand a detailed study of the dynamical behavior of these devices and the development of new concepts in control theory.

Moreover, a large amount of dynamic applications for nonlinear elastic materials have arisen in the biomedical engineering field. Mechatronic systems with peristaltic-like actuation capabilities, i.e., successive contractions that propagate in a wave down a tube forcing the contents onward, are being developed for a variety of applications: spanning from infusion pumps, microfluidic devices, and other biomedical systems (Dario et al., 2000; Hu et al., 2002; Jaffrin and Shapiro, 1971). It should be highlighted the application of these materials in **external left-ventricular assist systems (LVAS)**. Classical left-ventricular assist devices consist of a pump with one end attached to the left ventricle of the heart and the other end to the aorta. Blood flows from the ventricle into the LVAS and then it is pumped out into the aorta, where it then flows to the rest of the body. This system helps a weak heart to prevent the congestive heart failure, which is one of the deadliest diseases all over the world. Several patented designs such as the

Thoratec's HeartMate®, the Baxter'sNovacor®, the Arrow International® or the Inc.'s LionHeart® are already available in the market. However, implanting an LVAS is a dangerous operation that involves open heart surgery. Furthermore, there may exist some problems related to the direct contact of blood with the machinery of the pump (known as hemolysis). In order to solve these problems, and based on the pioneering work of Shahinpoor (Carpi and Smela, 2009, Chapter 7), the idea of helping a weak heart by compressing it from the outside with a soft and intelligent polymer has gained acceptance in the medical community. Several geometries such as cylindrical peristaltic pumps (see Fig. 1.6a) or a four-fingered device (see Fig. 1.6b) have been proposed by different research groups. To increase the range of deformations that EAPs can withstand under an electric field, conductive particles are added to these polymers; see e.g., Intanoo et al. (2012). The constitutive modeling of these composite materials is a challenge for the scientific community and many theories are currently being developed for the homogenization and electro-mechanical coupling of these new polymers; see e.g., Lefèvre and Lopez-Pamies (2017); Lefèvre and Lopez-Pamies (2017).

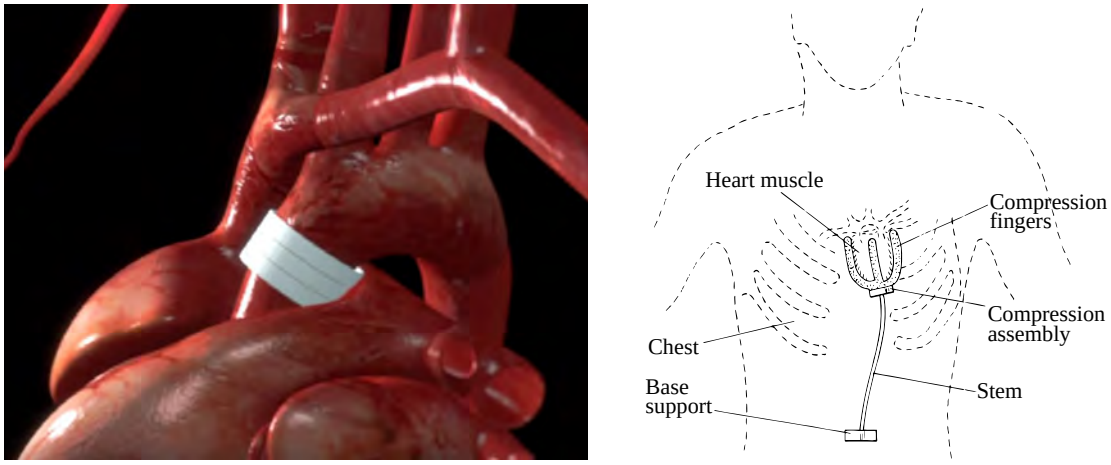

(a) *(b)*

Fig. 1.6 (a)Three-ring peristaltic pump prototipe developed at the Integrated Actuators Laboratory of the École Polytechnique Fédérale de Lausanne. Image source: https://actu.epfl.ch. (b) Schematic of the four-fingered LVAS developed by Shahinpoor (2002). Image source: Shahinpoor (2002)

To find the origins of the constitutive modeling of nonlinear elastic materials one must go back in time several decades. The fundamental elasticity concepts were established in the celebrated work of Green and Zerna (1954), which was extended in the decade of the 1980s to the field of biomechanics; see e.g., the pioneering work of Fung (1993). Since then, the mechanical modeling of living (soft) tissues has been a subject of great interest

to the scientific community and remains one of the most active research topics in our days (Holzapfel and Ogden, 2003; Li and Qian, 2013; Mollica et al., 2007; Payan, 2012). As an example, let us comment here the nonlinear visco-elastic and anisotropic constitutive model developed by Gasser et al. (2006) for the mechanical response of a human artery. This constitutive model is based in the histology of a healthy elastic artery, such as the one schematically illustrated in Fig. 1.7. With this model, Gasser et al. (2006) were able to take into account, among other features, the statistic dispersion of the collagen fibers orientations in the artery wall. This model has been proved to reproduce reasonably well the mechanics of the human arteries under a variety of realistic loading conditions. Note that arteries are subjected to dynamic (cyclic) loading conditions, governed by

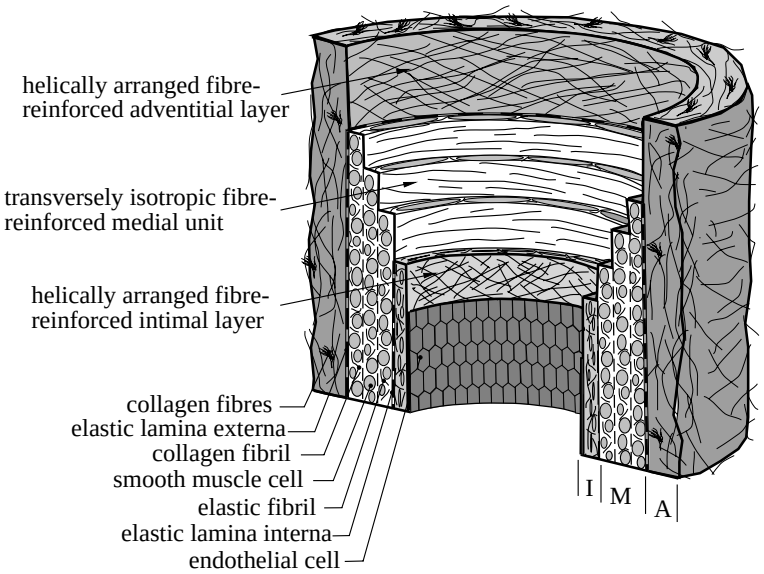

.

Fig. 1.7 Diagrammatic model of the major components of a healthy elastic artery composed of three layers: intima (I), media (M), adventitia (A). Source: Gasser et al. (2006)

the heart rate, throughout our life. Thus, the analysis of their vibrational response has aroused the attention of the scientific community. For instance, several publications have discussed whether the dynamic loading induced by the pulsatile blood flow may influence the enlargement and development of **aneurysmal lesions**. Aneurysms are abnormal dilatations of vessels in the vascular system. They exist in two major forms attending to their shapes: fusiform and saccular (see Fig. 1.8a). Fusiform aneurysms are found mainly in the human abdominal aorta and saccular aneurysms are found mostly in cerebral blood vessels. The Circle of Willis (see Fig. 1.8b) is the junction of the four main arteries, two carotid arteries and two vertebral arteries, that supply the brain

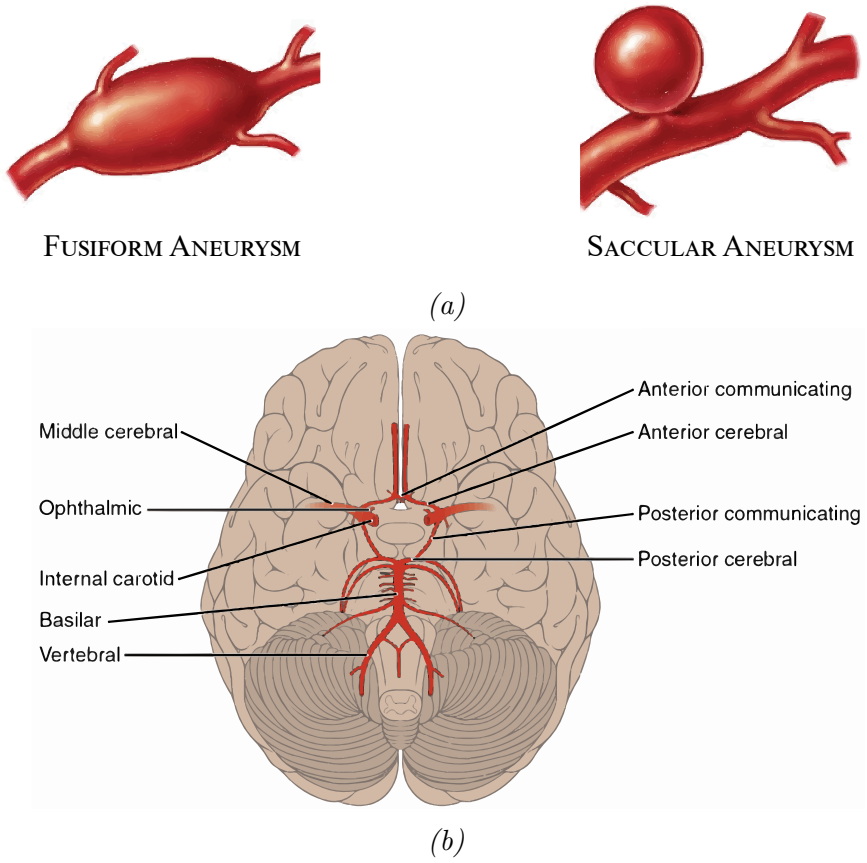

Fig. 1.8 (a) Types of aneurysms attending to their shape, adapted from http://www.mountsinai.org. (b) Schematic representation of the Circle of Willis. Source: http://www.joeniekrofoundation.com

with nutrition (especially oxygen and glucose). This loop of arteries is located at the base of the brain and sends out smaller branch arteries to all the different parts of the brain. The junctions where these arteries come together may develop weak spots. These weak spots can balloon out and be filled with blood, creating the outpouchings of blood vessels known as aneurysms. These sac-like areas may leak or rupture, spilling blood into surrounding brain tissue. The Brain Aneurysm Foundation reports that 2 in 100 people in the US have an unruptured brain aneurysm and the annual rate of rupture is about 8-10 per $100,000$ people. There is a brain aneurysm rupture every 18 minutes. Ruptured brain aneurysms are fatal in about 40% of cases. Of those who survive, about 66% suffer some permanent neurological deficit. Angiography or arteriography is a medical imaging technique used to visualize the inside, or lumen, of blood vessels and organs of the body, with particular interest in the arteries, veins, and the heart chambers. This

is traditionally done by injecting a radio-opaque contrast agent into the blood vessel and imaging using X-ray based techniques such as fluoroscopy. Fig. 1.9 presents an angiography of $\sim 14mm$ saccular aneurysm located in the trunk of the basilar artery reported by Buckle and Rabadi (2006).

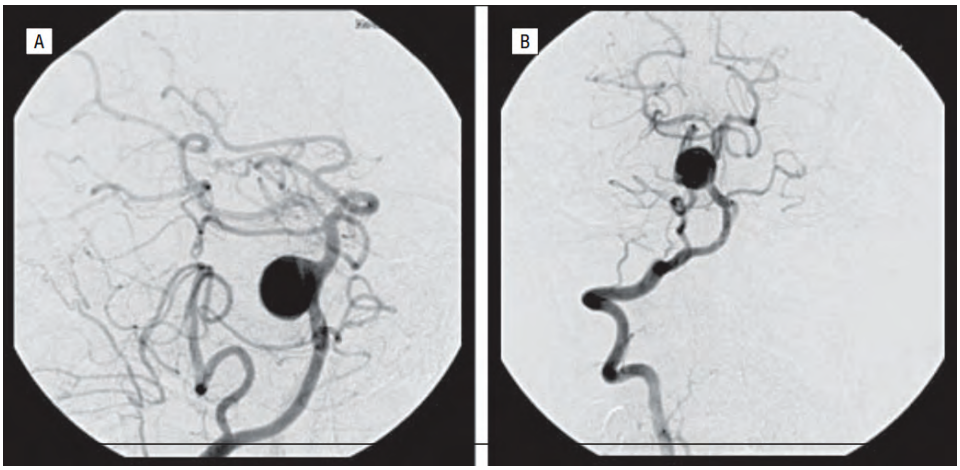

Fig. 1.9 Angiography of $\sim 14mm$ *saccular aneurysm located in the trunk of the basilar artery. Source: Buckle and Rabadi (2006).*

The question of whether mechanical instabilities, both static and dynamic, may cause the enlargement and rupture of saccular aneurysms has been debated by the scientific community during the last 40 years. Several researchers, such as Akkas (1990) and Austin et al. (1989), pointed out that the existence of limit point instabilities (i.e. mathematical bifurcations in the quasi-static response of the aneurysm) could be a reason for the growth and rupture of this type of lesions. Alternatively, other authors like Jain (1963), Sekhar and Heros (1981) and Sekhar et al. (1988) suggested that the pulsatile blood flow could excite the natural frequency of the aneurysm making it dynamically unstable. This hypothesis was supported by the results of Simkins and Stehbens (1973) and nan Hung and Botwin (1975), who studied the elastodynamics of berry aneurysms and showed that the natural frequency of this type of lesions may lie within the range of bruit frequencies registered during surgery. Note that in Chapter 4 we analyze the occurrence of dynamic instabilities in idealized intracranial saccular aneurysms subjected to pulsatile blood flow and surrounded by cerebral spinal fluid. Moreover, other organs (e.g. brain, liver, kidneys, etc) can also be subjected to dynamic loads under special circumstances such as falls or traffic accidents. A great interest has recently arisen in the scientific community to study and analyze the dynamic behavior of different biological structures (Chen and Ostoja-Starzewski, 2010; David and Humphrey, 2003; Garcia-Gonzalez et al., 2017; Haslach and Humphrey, 2004; Humphrey and Canham, 2000; Humphrey and Haslach,

2003; Sahoo et al., 2016; Wright et al., 2013). A better understanding of the mechanical behavior of living tissue can be helpful in several applications such as the design of bulletproof vests, helmets, prosthesis, or even the diagnosis and prevention of certain diseases.

This introduction has brought to light the extensive use of elastomers in the production of parts, components and devices, with application in many different industrial fields, which have to face dynamic and vibrational loads during their daily operation. In addition, we have described some examples in which (soft) biological tissues and organs are also subjected to this type of loading conditions. So far, the dynamic behavior of structures made of rubber-like and soft biological materials has not been studied in sufficiently depth. As we have previously mentioned in this introduction, the analysis of the dynamic behavior of these structures is especially complicated due to the geometrical and material nonlinearities involved. Therefore, the objective of this dissertation, as it is described in the next section, is to analyze the dynamics of nonlinear elastic structures paying particular attention to the role played by the constitutive model used to describe the mechanical response of the material.

1.2 General objective and structure of the dissertation

The objective of this research is to present a systematic analysis of the nonlinear dynamics of canonical structures, such as cylindrical and spherical thick-walled shells[1], modeled with different nonlinear elastic constitutive equations. Starting from a simple incompressible and hyperelastic material, different sensitivities such as compressibility, viscosity, or anisotropy are sequentially introduced in the constitutive behavior of the material. In each case, the effect of the constitutive model on the dynamic response of the problem at hand is analyzed. The cylindrical and spherical geometries, although simple, are the canonical representation of most of the structures previously presented (see Figures 1.1, 1.2, 1.6a, 1.7 and 1.8a). The research conducted through this doctoral thesis is organized as follows:

Part II of this document, which is constituted by chapters 3, 4 and 5, is focused on **incompressible and compressible isotropic hyperelastic constitutive models**.

[1]Note that, although these structures are referred to as thick-walled shells, no two-dimensional simplification of the balance equations has been used. The problem is formulated in a three-dimensional way in all cases analyzed.

In **Chapter 3**, the nonlinear vibrations of thick-walled cylindrical shells subjected to radially symmetric dynamic inflation are analyzed. The shell material is taken to be isotropic and incompressible within the framework of finite nonlinear elasticity. In particular, Mooney-Rivlin and Yeoh constitutive models have been chosen to describe the mechanical behavior of the cylinder. We have carried out a systematic comparison of the results for both models when the cylinder is subjected to: (1) a constant pressure and (2) a harmonic time-dependent pressure. In **Chapter 4**, the non-linear dynamics of thick-walled spherical shells is analyzed. Specifically, the formulation is adapted to analyze the occurrence of dynamic instabilities in idealized intracranial saccular aneurysms subjected to pulsatile blood flow and surrounded by cerebral spinal fluid. Finally, in **Chapter 5** we investigate the role played by the material compressibility in the oscillatory behavior of hyperelastic spherical shells subjected to dynamic inflation. For this purpose, we carried out a comprehensive nondimensional numerical analysis using: (1) a finite differences MacCormack's scheme implemented in MATLAB and (2) a finite elements model developed in ABAQUS/Explicit (ABAQUS/Explicit, 2014).

Part III of this dissertation is focused on **incompressible, isotropic and viscous hyperelastic constitutive models**. In **Chapter 6** the nonlinear vibrations of thick-walled cylindrical shells subjected to radially symmetric dynamic inflation are analyzed. Some specific dynamical features directly related to the viscosity of the constitutive formulation, such as nonlinear resonance frequencies or the existence of scape bands in the frequency diagrams of the structure are addressed. In **Chapter 7** we provide insights into the relevance of inertial and viscous effects on the onset of cavitation in rubber. To this end, we consider the basic problem of the radially symmetric dynamic deformation of spherical defects embedded in the center of spheres made up of an isotropic incompressible nonlinear viscoelastic solid that is subjected to external hydrostatic loading. Based on this simplified calculation, the limits of the loading rate from which the viscous and inertial effects begin to play an important role in the problem of cavitation are determined.

Part IV of this document, composed only by **Chapter 8**, is devoted to the analysis of the nonlinear bi-dimensional vibrations of a cylindrical shell structure subjected to *ab initio* elastic stored and kinetic energies. Following Rubin and Jabareen (2007, 2010), we use an **anisotropic incompressible hyperelastic constitutive model** to describe the material behavior. We have shown that, depending on the geometry of the shell and the material parameters, the response of the structure can be periodic, quasi-periodic or chaotic.

Finally, the fundamental concepts of Nonlinear solid Mechanics, required to conduct the research described in the chapters above, are thoroughly defined in **Chapter 2** (also included in **Part I**). Moreover, **Chapter 9** (included in **Part V**), presents the main conclusions of this work, along with some research proposals for future works. The references used to build this research are also given in **Part V** of this document.

1.3 Originality and quality of the research

The originality of this doctoral research derive from the thorough analysis, with unprecedented magnitude in literature, performed on the influence of the constitutive model in the dynamic behavior of cylindrical and spherical (canonical) nonlinear elastic structures subjected to a wide variety of loading conditions. Several constitutive formulations have been investigated and the specific roles of compressibility, viscosity and anisotropy have been identified. In particular, we have demonstrated the influence of the constitutive model on: (1) the loss of oscillatory behavior of the structure, (2) the transition from periodic motion to quasi-periodic and chaotic, (3) the nonlinear resonances diagrams of the shells, (4) the propagation of shock waves within the structure and (5) the onset and development of cavitation instabilities. The quality of this doctoral thesis is demonstrated by the seven publications that shall come out from this research:

- Aranda-Iglesias D., Vadillo G., Rodríguez-Martínez J. A. Constitutive sensitivity of the oscillatory behavior of hyperelastic cylindrical shells. Journal of Sound and Vibration. 2015; 358: 199–216.

- Kumar A., Aranda-Iglesias D., López-Pamies O. Some remarks on the effects of inertia and viscous dissipation in the onset of cavitation in rubber. Journal of Elasticity. 2017; 126: 201–213.

- Aranda-Iglesias D., Vadillo G., Rodríguez-Martínez J. A., Volokh K. Y. Modeling deformation and failure of elastomers at high strain rates. Mechanics of Materials. 2017; 104: 85–92.

- Aranda-Iglesias D., Vadillo G., Rodríguez-Martínez J. A. Oscillatory behavior of compressible hyperelastic shells subjected to dynamic inflation: a numerical study. Acta Mechanica. 2017; In press.

- Aranda-Iglesias D., Ramón-Lozano C., Rodríguez-Martínez J. A. Nonlinear resonances of an idealized saccular aneurysm. Submitted for publication.

- Aranda-Iglesias D., Rubin M. B., Rodríguez-Martínez J. A. Nonlinear axisymmetric vibrations of a circular hyperelastic orthotropic plate. Submitted for publication.
- Aranda-Iglesias D., Rodríguez-Martínez J. A. Periodic, quasi-periodic and chaotic motion of hyperelastic spherical shells subjected to time dependent inflation. In preparation.

Note also that three of these papers are joint works with renowned scientists within the field of Solid Mechanics who belong to prestigious research Universities: M. B. Rubin and K. Y. Volokh from the TECHNION (Israel) and O. López-Pamies from the University of Illinois at Urbana-Champaign (USA).

2 Nonlinear solid mechanics

This chapter is devoted to introduce the fundamental principles of nonlinear solid mechanics necessary for the further development of this dissertation. For the sake of clarity, most of the demonstrations have been omitted and only the equations that will be needed in further chapters are presented. For a more elaborative and inclusive discussion, the reader is referred to Bergstrom (2015), Holzapfel (2000) and Ogden (1997), from where this chapter has been adapted. The structure of the chapter is as follows: in Section 2.1 we discuss the kinematic aspects of motion and deformation of a continuum body both in Lagrangian and Eulerian descriptions. In Section 2.2 we introduce the fundamental concept of stress. In Section 2.3 we provide the classical balance principles and finally in Section 2.4 we introduce the general features of hyperelastic constitutive models.

2.1 Kinematics

Let a deformable continuum body $\mathcal{B}$ consists of infinitely many material points $\mathrm{P} \in \mathcal{B}$ in the Euclidean space $\mathbb{R}^3$ at time t. During its motion the body changes its position from the reference configuration Ω_0 to the current configuration Ω, both named as space regions occupied by the body $\mathcal{B}$ at different times. We agree subsequently that the **reference** or **undeformed** configuration Ω_0 coincides with the initial configuration at time $t = 0$. As time evolves, a material point that occupies a position given by the vector $\mathbf{X}$ in the reference configuration Ω_0 moves to a new position given by the vector $\mathbf{x}$ in the current configuration Ω. These two locations are related by the bijective and twice continuously differentiable mapping χ such that

$$\mathbf{x} = \chi(\mathbf{X}, \mathbf{t}). \tag{2.1}$$

Material and spatial descriptions The **material** or **Lagrangian description** is the representation of the main variables of the deformation process with respect to the material coordinates (X_1, X_2, X_3) and time t, which is given by Eq. (2.1). In this description, we focus on the behavior of a particle while moving. On the other hand, the **spatial** or **Eulerian description** is the characterization of the motion (or any other quantity) in terms of the spatial coordinates (x_1, x_2, x_3) and time t, which is given by $\mathbf{X} = \chi^{-1}(\mathbf{x}, \mathbf{t})$. In the Eulerian description, attention is focused on a fixed point in space, analyzing its evolution as time evolves.

Following the definition of motion stated above, material velocity and material acceleration of a body are introduced as follows

$$\mathbf{V}(\mathbf{X}, t) = \frac{\partial \boldsymbol{\chi}(\mathbf{X}, t)}{\partial t}, \qquad \mathbf{A}(\mathbf{X}, t) = \frac{\partial \mathbf{V}(\mathbf{X}, t)}{\partial t} = \frac{\partial^2 \boldsymbol{\chi}(\mathbf{X}, t)}{\partial t^2}, \tag{2.2}$$

while spatial velocity and spatial acceleration are given by

$$\mathbf{v}(\mathbf{x}, t) = \mathbf{V}\left[\boldsymbol{\chi}^{-1}(\mathbf{x}, t), t\right]; \qquad \mathbf{a}(\mathbf{x}, t) = \mathbf{A}\left[\boldsymbol{\chi}^{-1}(\mathbf{x}, t), t\right]. \tag{2.3}$$

Remark. *Throughout the different problems studied in this dissertation we found more convenient to work with the material description rather than the spatial description.*

2.1.1 Deformation gradient

Let us focus on the variations of size and shape of a body under a deformation from the reference configuration Ω_0 to the current configuration Ω. The relation between the current infinitesimal line element $\mathrm{d}\mathbf{x}$ to the initial infinitesimal line element $\mathrm{d}\mathbf{X}$ is given by

$$\mathrm{d}\mathbf{x} = \mathbf{F}(\mathbf{X}, \mathbf{t})\, \mathrm{d}\mathbf{X}, \tag{2.4}$$

where the quantity $\mathbf{F}$, referred to as the **deformation gradient**, is defined as follows

$$\mathbf{F}(\mathbf{X}, t) = \frac{\partial \mathbf{x}}{\partial \mathbf{X}} = \frac{\partial \boldsymbol{\chi}(\mathbf{X}, t)}{\partial \mathbf{X}} = \mathrm{Grad}\, \mathbf{x}(\mathbf{X}, t). \tag{2.5}$$

The deformation gradient is the primary measure of deformation, and it establishes a linear transformation that generates a vector $\mathrm{d}\mathbf{x}$ in the spatial description by the action of the tensor $\mathbf{F}$ on the vector $\mathrm{d}\mathbf{X}$. Similarly, the current and the reference infinitesimal volume elements $\mathrm{d}v$ and $\mathrm{d}V$ respectively, formed by the infinitesimal line elements $\mathrm{d}\mathbf{x}$ and $\mathrm{d}\mathbf{X}$ are related by

$$\mathrm{d}v = J(\mathbf{X}, t)\, \mathrm{d}V, \tag{2.6}$$

where J is the determinant of the deformation gradient $\mathbf{F}$, known as the **volume ratio**.

$$J(\mathbf{X}, t) = \det\mathbf{F}(\mathbf{X}, t) > 0. \tag{2.7}$$

2.1.2 Strain tensors

The deformation gradient introduced in the previous section is the fundamental kinematic (second-order) tensor that describes the evolution of material elements during motion in finite deformation kinematics. However, unlike displacements which are measurable quantities, strain is an non-measurable concept introduced to simplify the analysis. Therefore, different definitions and names of strain tensors have been proposed in the literature over time. Throughout this section we briefly present the most commonly used, namely: the right Cauchy-Green strain tensor $\mathbf{C}$, the Green-Lagrange strain tensor $\mathbf{E}$ and the left Cauchy-Green strain tensor $\mathbf{b}$.

The length of the material line element $\mathrm{d}\mathbf{X}$ at point $\mathbf{X}$ and time $t = 0$ changes from $\mathrm{d}\varepsilon$ to $\lambda\mathrm{d}\varepsilon$ at time t (see Fig.2.1). The quantity λ is called the **stretch ratio** or **stretch**, and it can be defined as the length $\lambda = \| \boldsymbol{\lambda}_{\mathbf{a}_0} \|$ of the stretch vector $\boldsymbol{\lambda}_{\mathbf{a}_0}$ in the direction of the unit vector $\mathbf{a}_0$

$$\boldsymbol{\lambda}_{\mathbf{a}_0}(\mathbf{X}, t) = \mathbf{F}(\mathbf{X}, t)\,\mathbf{a}_0. \tag{2.8}$$

The stretch λ is a quantitative measure of the magnitude of vector $\boldsymbol{\lambda}_{\mathbf{a}_0}$ and its value provides information about the nature of the stretching, considering that it has been extended, unstretched or compressed if $\lambda > 1$, $\lambda = 1$ or $\lambda < 1$, respectively. Taking the square of λ and using definition (2.8) we have that

$$\lambda^2 = \boldsymbol{\lambda}_{\mathbf{a}_0} \cdot \boldsymbol{\lambda}_{\mathbf{a}_0} = \mathbf{F}\mathbf{a}_0 \cdot \mathbf{F}\mathbf{a}_0 = \mathbf{a}_0 \cdot \mathbf{F}^T\mathbf{F}\mathbf{a}_0 = \mathbf{a}_0 \cdot \mathbf{C}\mathbf{a}_0, \tag{2.9}$$

where

$$\mathbf{C} = \mathbf{F}^T\mathbf{F}. \tag{2.10}$$

Tensor $\mathbf{C}$ is the **right Cauchy-Green** tensor, which is a strain measure in material coordinates. This will be the strain measure mainly employed in the development of this dissertation.

The change in vectors' squared lengths is an alternative strain measure known as tensor $\mathbf{E}$ or **Green-Lagrange strain tensor**

$$\frac{1}{2}\left[(\lambda\mathrm{d}\varepsilon)^2 - \mathrm{d}\varepsilon^2\right] = \mathrm{d}\mathbf{X} \cdot \mathbf{E}\mathrm{d}\mathbf{X}, \tag{2.11}$$

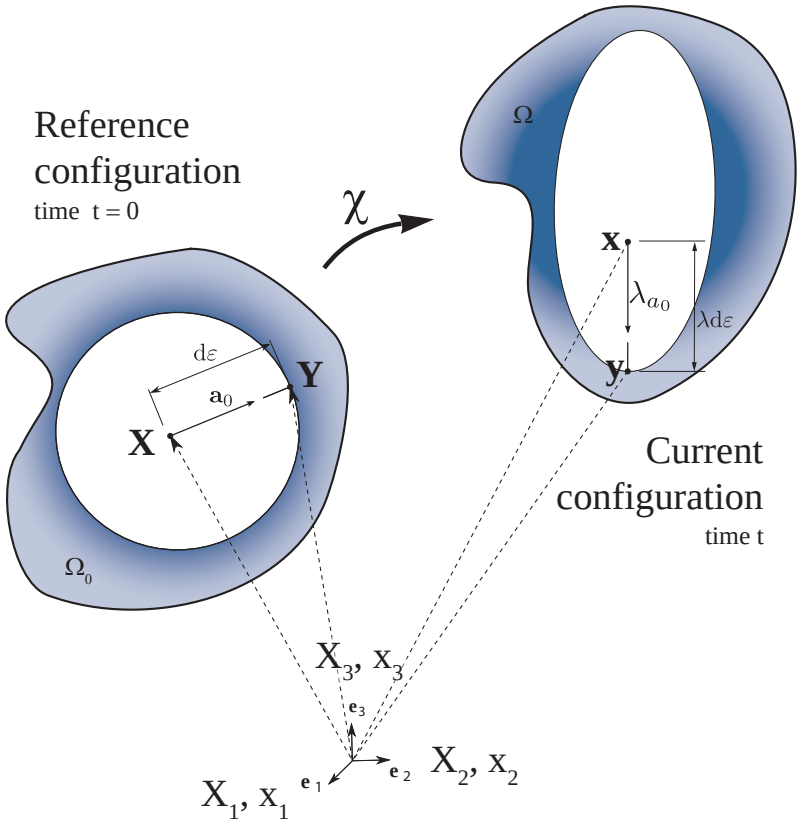

Fig. 2.1 Deformation of a material line element in material description, adapted from Holzapfel (2000).

where

$$\mathbf{E} = \frac{1}{2}\left(\mathbf{F}^T\mathbf{F} - \mathbf{I}\right) = \frac{1}{2}\left(\mathbf{C} - \mathbf{I}\right). \tag{2.12}$$

Alternatively, all these strain tensors can be defined in the spatial description if all quantities are referred to the current configuration. In that case, the stretch vector $\boldsymbol{\lambda}_a$ in the direction of the unit vector $\mathbf{a}$ is

$$\boldsymbol{\lambda}_{\mathbf{a}}^{-1}\left(\mathbf{x}, t\right) = \mathbf{F}^{-1}\left(\mathbf{x}, t\right)\mathbf{a}, \tag{2.13}$$

where the length of the inverse stretch vector $\boldsymbol{\lambda}_{\mathbf{a}}^{-1}$ is the inverse stretch ratio λ^{-1}. Following the same procedure as in the material description, the square of the inverse stretch ratio is

$$\lambda^{-2} = \boldsymbol{\lambda}_{\mathbf{a}}^{-1} \cdot \boldsymbol{\lambda}_{\mathbf{a}}^{-1} = \mathbf{F}^{-1}\mathbf{a} \cdot \mathbf{F}^{-1}\mathbf{a} = \mathbf{a} \cdot \mathbf{F}^{-T}\mathbf{F}^{-1}\mathbf{a} = \mathbf{a} \cdot \mathbf{b}^{-1}\mathbf{a}, \tag{2.14}$$

where $\mathbf{b}^{-1} = \mathbf{F}^{-T}\mathbf{F}^{-1}$ is the inverse of the **left Cauchy-Green tensor b** defined by

$$\mathbf{b} = \mathbf{F}\mathbf{F}^{T}. \tag{2.15}$$

2.1.3 The rate of deformation tensors

In this section we briefly introduce the spatial and material velocity gradients and their decompositions. To that end, let us take the gradient of the spatial velocity field $\mathbf{v}(\mathbf{x}, t)$ in the spatial description

$$\mathbf{l}(\mathbf{x}, t) = \frac{\partial \mathbf{v}(\mathbf{x}, t)}{\partial \mathbf{x}} = \mathrm{grad}\mathbf{v}(\mathbf{x}, t), \tag{2.16}$$

where the second-order and non-symmetric tensor $\mathbf{l}$ is called **spatial velocity gradient**. Now the operation can be repeated in the material description to obtain the **material velocity gradient**. If we take the material time derivative of the deformation gradient $\mathbf{F}$, we have that

$$\begin{aligned}\dot{\mathbf{F}}(\mathbf{X}, t) = \frac{\partial}{\partial t}\left(\frac{\partial \boldsymbol{\chi}(\mathbf{X}, t)}{\partial \mathbf{X}}\right) = \frac{\partial}{\partial \mathbf{X}}\left(\frac{\partial \boldsymbol{\chi}(\mathbf{X}, t)}{\partial t}\right) = \\ = \frac{\partial \mathbf{V}(\mathbf{X}, t)}{\partial \mathbf{X}} = \mathrm{Grad}\mathbf{V}(\mathbf{X}, t).\end{aligned} \tag{2.17}$$

Using equations (2.2), (2.3) and (2.16), the spatial velocity gradient $\mathbf{l}$ can be rewritten in the following useful form

$$\mathbf{l} = \frac{\partial \mathbf{v}}{\partial \mathbf{x}} = \frac{\partial \dot{\boldsymbol{\chi}}(\mathbf{X}, t)}{\partial \mathbf{X}}\frac{\partial \mathbf{X}}{\partial \mathbf{x}} = \dot{\mathbf{F}}\mathbf{F}^{-1}. \tag{2.18}$$

Furthermore, the spatial velocity gradient can be decomposed into a symmetric and skew symmetric part as

$$\mathbf{l}(\mathbf{x}, t) = \mathbf{d}(\mathbf{x}, t) + \mathbf{w}(\mathbf{x}, t), \tag{2.19}$$

where

$$\mathbf{d} = \frac{1}{2}\left(\mathbf{l} + \mathbf{l}^{T}\right) = \frac{1}{2}\left(\mathrm{grad}\mathbf{v} + \mathrm{grad}^{T}\mathbf{v}\right) = \mathbf{d}^{T}, \tag{2.20}$$

$$\mathbf{w} = \frac{1}{2}\left(\mathbf{l} - \mathbf{l}^{T}\right) = \frac{1}{2}\left(\mathrm{grad}\mathbf{v} - \mathrm{grad}^{T}\mathbf{v}\right) = -\mathbf{w}^{T}. \tag{2.21}$$

The symmetric part of the spatial velocity gradient $\mathbf{l}$ is the covariant second-order **rate of deformation tensor d** and the skew symmetric part of $\mathbf{l}$ is the covariant second-order **spin tensor w**.

2.2 The concept of stress

Consider a deformable continuum body $\mathcal{B}$ occupying a space region Ω with boundary surface $\partial\Omega$ at time t, as the one presented in Fig. 2.2. Let us assume some arbitrary forces (external forces) acting on the boundary surface $\partial\Omega$ and a plane π dividing the body $\mathcal{B}$ in two parts. Associated at each point $\mathbf{x}$ belonging to the (internal) separation surface, we define a unitary outward normal vector $\mathbf{n}$ and an infinitesimal surface element $\mathrm{d}a$. As a result of the interaction of both portions, forces are transmitted through the (internal) plane surface generating a traction vector $\mathbf{t}$ at $\mathbf{x}$. Here, $\mathbf{t}$ represents the Cauchy (or true) traction vector (i.e., a force measured per unit of surface area defined in the current configuration) exerted on $\mathrm{d}a$ with outward normal $\mathbf{n}$.

This configuration has its counterpart in the initial (undeformed) configuration where the body $\mathcal{B}$ occupies a space region Ω_0 with boundary $\partial\Omega_0$. In the undeformed configuration, the position vector, normal vector and surface element are denoted by $\mathbf{X}$, $\mathbf{N}$ and $\mathrm{d}A$, respectively. The traction vector $\mathbf{T}$ in the reference configuration represents the first Piola-Kirchhoff (or nominal) traction vector (i.e., a force measured per unit surface area defined in the reference configuration). Assumed the **Cauchy's fundamental postulate**, the stress vectors $\mathbf{t}$ and $\mathbf{T}$ depend on the surfaces π and π_0 only though the (unit) normals $\mathbf{n}$ and $\mathbf{N}$ to the considered surfaces, as indicated in Fig. 2.2

We now state **Cauchy's theorem**: provided it is continuous in $\mathbf{x}$, the stress vector $\mathbf{t}(\mathbf{x}, \mathbf{n})$ depends linearly on $\mathbf{n}$; i.e., there exist a second order tensor field $\boldsymbol{\sigma}$ independent of $\mathbf{n}$ such that

$$\mathbf{t}(\mathbf{x}, t, \mathbf{n}) = \boldsymbol{\sigma}(\mathbf{x}, t)\mathbf{n}, \tag{2.22}$$

where $\boldsymbol{\sigma}$ denotes a symmetric spatial tensor field called the **Cauchy (or true) stress tensor** (the symmetry proof can be found in Holzapfel (2000)). Equivalently, in the reference configuration

$$\mathbf{T}(\mathbf{X}, t, \mathbf{N}) = \mathbf{S}(\mathbf{X}, t)\mathbf{N}, \tag{2.23}$$

where $\mathbf{S}$ characterizes the non-symmetric **first Piola-Kirchhoff (or nominal) stress tensor**. The relation between these stress tensors is given by (the proof is omitted).

$$\boldsymbol{\sigma} = J^{-1}\mathbf{S}\mathbf{F}^{\mathbf{T}}. \tag{2.24}$$

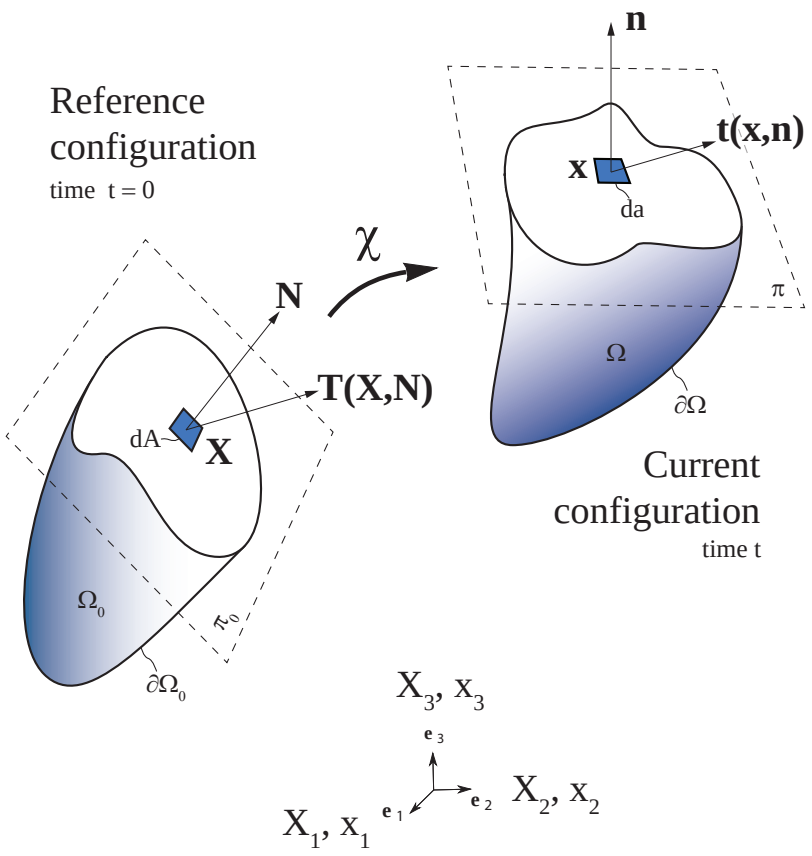

Fig. 2.2 Traction vectors acting on infinitesimal surface elements with outward unit normals, adapted from Holzapfel (2000).

2.3 Balance principles

In this section we introduce the mass, linear momentum and angular momentum principles that will be used in the problems analyzed in following chapters. Furthermore, we briefly introduce the first law of thermodynamics in its simplified version where only mechanical energy is considered.

2.3.1 Conservation of mass

From a non-relativistic point of view, mass cannot be produced or destroyed. So, if there are neither mass sources nor mass sinks, the mass m of a body is a conserved quantity. Considering a closed system, the previous statement can be mathematically expressed as

$$m = \int_{\Omega_0} \rho_0(\mathbf{X}) dV = \int_{\Omega} \rho(\mathbf{x}, t) dv = \text{const} > 0, \tag{2.25}$$

where $\rho_0 = \rho_0(\mathbf{X}) > 0$ and $\rho = \rho(\mathbf{x}, t) > 0$ are the reference and the spatial mass density respectively. The previous expression can be stated in local form as

$$\rho_0(\mathbf{X})dV = \rho(\mathbf{x}, t)dv > 0. \tag{2.26}$$

Continuity mass equation . Using the definition of the volume ratio $\mathrm{d}v = J(\mathbf{X}, t)\mathrm{d}V$ and changing the independent space variable from $\mathbf{x} = \chi(\mathbf{X}, \mathbf{t})$ to $\mathbf{X}$, the mass balance Eq. (2.25) can be rewritten as

$$\int_{\Omega_0} \left[\rho_0(\mathbf{X}) - \rho(\boldsymbol{\chi}(\mathbf{X}, t), t)J(\mathbf{X}, t)\right] \mathrm{d}V = 0. \tag{2.27}$$

Taking into account that V is a generic volume of the solid, the previous equation must be met at all material points, leading to the so-called continuity mass equation in the material or Lagrangian description

$$\rho_0(\mathbf{X}) = \rho(\boldsymbol{\chi}(\mathbf{X}, t), t)J(\mathbf{X}, t). \tag{2.28}$$

2.3.2 Balance of linear momentum

Consider a body $\mathcal{B}$ occupying a region Ω with boundary surface $\partial\Omega$ at time t. With the motion defined by $\mathbf{x} = \boldsymbol{\chi}(\mathbf{X}, t)$, the mass density by $\rho = \rho(\mathbf{x}, t)$ and the spatial velocity by $\mathbf{v} = \mathbf{v}(\mathbf{x}, t)$, the total linear momentum L is defined as follows

$$\mathbf{L}(t) = \int_{\Omega} \rho(\mathbf{x}, t)\mathbf{v}(\mathbf{x}, t)\mathrm{d}v = \int_{\Omega_0} \rho_0(\mathbf{X})\, \mathbf{V}(\mathbf{X}, t)\, \mathrm{d}V, \tag{2.29}$$

in which the vector-valued function has been also expressed in the reference configuration ρ_0, $\mathbf{V}$ and $\mathrm{d}V$.

Let us assume a structure of forces acting on the continuum body $\mathcal{B}$ consisting of: (1) a Cauchy vector field $\mathbf{t}(\mathbf{x}, t, \mathbf{n})$ acting on $\partial\Omega$, as introduced in Section 2.2, and (2) a spatial vector field $\mathbf{b} = \mathbf{b}(\mathbf{x}, t)$ called the body force[1] acting on Ω. Then, the balance of linear momentum for deformable bodies can be stated as: *the sum of the surface and volumetric forces acting on a body are equal to the time derivative of the linear momentum of the body.* So the global form of the balance of linear momentum in the spatial description is

$$\frac{D}{Dt}\int_{\Omega} \rho\mathbf{v}\mathrm{d}v = \int_{\partial\Omega} \mathbf{t}\mathrm{d}s + \int_{\Omega} \mathbf{b}\mathrm{d}v. \tag{2.30}$$

[1]Note that the symbol $\mathbf{b}$ should not be confused with the left Cauchy-Green strain tensor introduced in Eq. (2.15)

In the Lagrangian description the equivalent process leads to the following equation

$$\frac{\mathrm{D}}{\mathrm{D}t}\int_{\Omega_0}\rho_0\mathbf{V}\mathrm{d}V=\int_{\partial\Omega_0}\mathbf{T}\mathrm{d}S+\int_{\Omega_0}\mathbf{B}\mathrm{d}V, \tag{2.31}$$

where $\mathbf{B}=\mathbf{B}\left(\mathbf{X},t\right)$ is the reference body force and $\mathbf{T}=\mathbf{T}\left(\mathbf{X},t,\mathbf{N}\right)$ is the Piola-Kirchhoff traction vector introduced in Section 2.2.

Cauchy's first equation of motion . Applying the integral form of the Cauchy's stress theorem, stated in equations (2.22) and (2.23), and the divergence theorem, which converts the surface integral into a volume integral, we find that

$$\int_{\partial\Omega}\mathbf{t}(\mathbf{x},t,\mathbf{n})\mathrm{d}s=\int_{\partial\Omega}\boldsymbol{\sigma}(\mathbf{x},t)\mathbf{n}\mathrm{d}s=\int_{\Omega}\mathrm{div}\boldsymbol{\sigma}(\mathbf{x},t)\mathrm{d}v, \tag{2.32}$$

where $\boldsymbol{\sigma}$ is the Cauchy stress tensor as introduced in Section 2.2. Substituting this result into the balance of linear momentum equation (2.30), we find the so-called Cauchy's first equation of motion in global form

$$\int_{\Omega}\left(\mathrm{div}\boldsymbol{\sigma}+\mathbf{b}-\rho\dot{\mathbf{v}}\right)\mathrm{d}v=0. \tag{2.33}$$

Since this relation holds for any volume, it can be rewritten in local form as

$$\mathrm{div}\boldsymbol{\sigma}+\mathbf{b}=\rho\dot{\mathbf{v}}. \tag{2.34}$$

Moreover, the previous expression has its counterpart in the material description

$$\mathrm{Div}\mathbf{S}+\mathbf{B}=\rho_0\dot{\mathbf{V}}, \tag{2.35}$$

where $\mathbf{S}$ is the first Piola-Kirchhoff stress tensor in material coordinates as introduced in Section 2.2.

2.3.3 Balance of angular momentum

Consider a body $\mathcal{B}$ occupying a region Ω with boundary surface $\partial\Omega$ at time t. The total angular momentum $\mathbf{J}$ relative to a fixed point $\mathbf{x}_0$ is defined as

$$\mathbf{J}(t)=\int_{\Omega}\left[\mathbf{r}\times\rho(\mathbf{x},t)\mathbf{v}(\mathbf{x},t)\right]\mathrm{d}v=\int_{\Omega_0}\left[\mathbf{r}\times\rho_0\left(\mathbf{X}\right)\mathbf{V}\left(\mathbf{X},t\right)\right]\mathrm{d}V, \tag{2.36}$$

where the position vector $\mathbf{r}$ is given by $\mathbf{r}(\mathbf{x}) = \mathbf{x} - \mathbf{x}_0 = \boldsymbol{\chi}(\mathbf{X}, t) - \mathbf{x}_0$ and the vector-valued function has been also expressed in the reference configuration ρ_0, $\mathbf{V}$ and $\mathrm{d}V$. Furthermore, the resultant moment $\mathbf{M}(t)$ in the spatial description corresponding to the Cauchy vector field $\mathbf{t}(\mathbf{x}, t, \mathbf{n})$ and the body forces $\mathbf{b} = \mathbf{b}(\mathbf{x}, t)$ introduced in the previous section can be computed as

$$\mathbf{M}(t) = \int_{\partial\Omega} (\mathbf{r} \times \mathbf{t}) \, \mathrm{d}s + \int_{\Omega} (\mathbf{r} \times \mathbf{b}) \, \mathrm{d}v. \tag{2.37}$$

Based on these definitions, the balance of angular momentum for deformable bodies can be stated as: *the sum of moments from surface and volumetric forces acting on a body is equal to the time derivative of the angular momentum of the body.* Therefore, in its global form and spatial description, the balance of angular momentum is given by

$$\frac{\mathrm{D}}{\mathrm{D}t} \int_{\Omega} (\mathbf{r} \times \rho\mathbf{v}) \, \mathrm{d}v = \int_{\partial\Omega} (\mathbf{r} \times \mathbf{t}) \, \mathrm{d}s + \int_{\Omega} (\mathbf{r} \times \mathbf{b}) \, \mathrm{d}v. \tag{2.38}$$

The equivalent form of the previous expression in the material description is given by

$$\frac{\mathrm{D}}{\mathrm{D}t} \int_{\Omega_0} (\mathbf{r} \times \rho_0\mathbf{V}) \, \mathrm{d}\mathbf{V} = \int_{\partial\Omega_0} (\mathbf{r} \times \mathbf{T}) \, \mathrm{d}S + \int_{\Omega_0} (\mathbf{r} \times \mathbf{B}) \, \mathrm{d}V. \tag{2.39}$$

2.3.4 First law of thermodynamics

Consider a body $\mathcal{B}$ occupying a region Ω with boundary surface $\partial\Omega$ at time t. Let us assume that the body has an internal heat generation per unit of current volume r, and a heat flux $\mathbf{q}$ streaming through the body's boundary to the surroundings. Furthermore, the body is also subjected to the surface tractions $\mathbf{t}$ and body forces $\mathbf{b}$ introduced in previous sections.

We now state the first law of thermodynamics (Bergstrom, 2015; IV and V, 2008): *the rate at which the energy increases in a system is equal to the sum of the rate of heat supplied to the system and the rate of work done by the external forces.* Previous statement can be written as the following balance law in the current configuration

$$\frac{\mathrm{D}}{\mathrm{D}t} \int_{\Omega} \left(\frac{1}{2}\rho\mathbf{v}^2 + e \right) \mathrm{d}v = \int_{\partial\Omega} (\mathbf{t} \cdot \mathbf{v} - \mathbf{q} \cdot \mathbf{n}) \, \mathrm{d}s + \int_{\Omega} (\mathbf{b} \cdot \mathbf{v} + r) \, \mathrm{d}v, \tag{2.40}$$

or in material description as

$$\frac{\mathrm{D}}{\mathrm{D}t} \int_{\Omega_0} \left(\frac{1}{2}\rho_0\mathbf{V}^2 + e_0 \right) \mathrm{d}V = \int_{\partial\Omega_0} (\mathbf{T} \cdot \mathbf{V} - \mathbf{Q} \cdot \mathbf{N}) \, \mathrm{d}S + \int_{\Omega_0} (\mathbf{B} \cdot \mathbf{V} + R) \, \mathrm{d}V, \tag{2.41}$$

where e and e_0 are the internal energy per unit of current and reference volume, respectively. Furthermore, the surface heat flux and volumetric heat generation in the reference configuration have been denoted as $\mathbf{Q}$ and R, respectively.

By using Eq. (2.6) and provided that $\mathrm{D}/\mathrm{D}t(\rho\, J) = 0$ (see Eq. (2.28)) we can transform the left hand side of Eq. (2.40) as

$$\begin{aligned}\frac{\mathrm{D}}{\mathrm{D}t}\int_{\Omega}\left(\frac{1}{2}\rho\mathbf{v}^2+e\right)\mathrm{d}v = \frac{\mathrm{D}}{\mathrm{D}t}\int_{\Omega_0}\left(\frac{1}{2}\rho\mathbf{v}^2 J+eJ\right)\mathrm{d}V = \\ \int_{\Omega_0}\left(\dot{e}J+e\dot{J}+\frac{1}{2}\frac{\mathrm{D}}{\mathrm{D}t}(\rho+J)\mathbf{v}^2+\dot{\mathbf{v}}\cdot\mathbf{v}J\rho\right)\mathrm{d}V = \\ \int_{\Omega}\left(\dot{e}+e\,\mathrm{div}\,\mathbf{v}+\rho\,\dot{\mathbf{v}}\cdot\mathbf{v}\right)\mathrm{d}v.\end{aligned} \tag{2.42}$$

Applying the divergence theorem, the rate of heat supply to the system and the rate of work produced by the external surface forces can be rewritten as

$$\int_{\partial\Omega}-\mathbf{q}\cdot\mathbf{n}\mathrm{d}s+\int_{\Omega}r\,\mathrm{d}v=\int_{\Omega}\left(-\mathrm{div}\,\mathbf{q}+r\right)\,\mathrm{d}v, \tag{2.43}$$

$$\int_{\partial\Omega}\mathbf{t}\cdot\mathbf{v}\mathrm{d}s+\int_{\Omega}\mathbf{b}\cdot\mathbf{v}\,\mathrm{d}v=\int_{\Omega}\left(\mathrm{div}\,\boldsymbol{\sigma}\cdot\mathbf{v}+\boldsymbol{\sigma}:\mathbf{d}\right)\,\mathrm{d}v. \tag{2.44}$$

Introducing equations (2.42), (2.43) and (2.44) into Eq. (2.40) we obtain the following expression

$$\int_{\Omega}\left(\boldsymbol{\sigma}:\mathbf{d}-\mathrm{div}\,\mathbf{q}+r-\left[\mathrm{div}\,\boldsymbol{\sigma}+\mathbf{b}-\rho\dot{\mathbf{v}}\right]\cdot\mathbf{v}-\dot{e}-e\,\mathrm{div}\,\mathbf{v}\right)\,\mathrm{d}v=0, \tag{2.45}$$

where, from the Cauchy's first equation of motion (2.34), the quantity in brackets is equal to zero. As the previous relation holds for any volume, it can be rewritten in the local form

$$\boldsymbol{\sigma}:\mathbf{d}-\mathrm{div}\,\mathbf{q}+r=\dot{e}+e\,\mathrm{div}\,\mathbf{v}. \tag{2.46}$$

The previous expression can be deduced similarly in the reference configuration as

$$\mathbf{S}:\dot{\mathbf{F}}-\mathrm{Div}\,\mathbf{Q}+R=\dot{e}_0. \tag{2.47}$$

Balance of Mechanical Energy . Throughout the problems presented in this dissertation we will consider only mechanical energy; i.e, other forms of energy, such as thermal energy, will be neglected. Under these conditions, the balance of energy is not an additional statement to be satisfied, it is conversely a consequence of the Cauchy's first equation of motion stated in Eq. (2.34) and Eq. (2.35). However, due to its scalar

character we have used the balance of mechanical energy in several occasions during this dissertation, obtaining interesting results and conclusions, and therefore it is introduced here.

Let us start defining the **rate of external mechanical work** $\mathcal{P}_{\text{ext}}$ as the power produced in the system by the surface tractions $\mathbf{t}$ and the body forces $\mathbf{b}$

$$\mathcal{P}_{\text{ext}}(t) = \int_{\partial\Omega} (\mathbf{t}\cdot\mathbf{v})\,\mathrm{d}s + \int_{\Omega} (\mathbf{b}\cdot\mathbf{v})\,\mathrm{d}v. \tag{2.48}$$

By using the Cauchy's stress theorem (Eq. 2.22) and the divergence theorem, the previous equation can be rewritten as

$$\begin{aligned}\mathcal{P}_{\text{ext}}(t) &= \int_{\Omega} (\operatorname{div}(\boldsymbol{\sigma}\mathbf{v}) + \mathbf{b}\cdot\mathbf{v})\,\mathrm{d}v = \int_{\Omega} (\boldsymbol{\sigma} : \mathbf{l} + (\operatorname{div}\boldsymbol{\sigma})\cdot\mathbf{v} + \mathbf{b}\cdot\mathbf{v})\,\mathrm{d}v \\ &= \int_{\Omega} \boldsymbol{\sigma} : \mathbf{d}\,\mathrm{d}v + \int_{\Omega} \rho\dot{\mathbf{v}}\cdot\mathbf{v}\,\mathrm{d}v = \int_{\Omega} \boldsymbol{\sigma} : \mathbf{d}\,\mathrm{d}v + \frac{\mathrm{D}}{\mathrm{D}t}\int_{\Omega} \frac{1}{2}\rho\mathbf{v}^2\,\mathrm{d}v \\ &= \mathcal{P}_{\text{int}}(t) + \frac{\mathrm{D}}{\mathrm{D}t}\mathcal{K}(t),\end{aligned} \tag{2.49}$$

where $\mathcal{P}_{\text{int}}$ is the **stress power** or the **rate of internal mechanical work** and $\mathcal{K}$ is the **kinetic energy** of the body

$$\mathcal{K}(t) = \int_{\Omega} \left(\frac{1}{2}\rho\mathbf{v}\cdot\mathbf{v}\right)\mathrm{d}v. \tag{2.50}$$

Each term in the previous equation can be described in a reference or material configuration. Therefore, the rate of internal mechanical work (stress-power) can be rewritten as

$$\mathcal{P}_{\text{int}}(t) = \int_{\Omega_0} \left(\mathbf{S} : \dot{\mathbf{F}}\right)\mathrm{d}V = \int_{\Omega_0} \operatorname{tr}\left(\mathbf{S}^T\dot{\mathbf{F}}\right)\mathrm{d}V \tag{2.51}$$

the external mechanical power as

$$\mathcal{P}_{\text{ext}}(t) = \int_{\partial\Omega_0} (\mathbf{T}\cdot\mathbf{V})\,\mathrm{d}S + \int_{\Omega_0} (\mathbf{B}\cdot\mathbf{V})\,\mathrm{d}V \tag{2.52}$$

and the kinetic energy as

$$\mathcal{K}(t) = \int_{\Omega_0} \left(\frac{1}{2}\rho_0\mathbf{V}\cdot\mathbf{V}\right)\mathrm{d}V \tag{2.53}$$

where the stress power has been formulated using the conjugated pair: first Piola-Kirhchoff stress tensor $\mathbf{S}$ and the rate of deformation gradient $\dot{\mathbf{F}}$.

Conservative systems . Let us consider a simplified case of the balance of mechanical energy that will be of great interest in some of the problems analyzed

throughout this dissertation. Let us define two scalar-valued functions called the **total strain energy (or internal potential energy)** $\mathcal{U}_{\text{int}}$ and the **potential energy of the external loading (or external potential energy)** $\mathcal{U}_{\text{ext}}$. A mechanical system is called conservative if these functions satisfy

$$\mathcal{P}_{\text{int}}(t) = \frac{\mathrm{D}\,\mathcal{U}_{\text{int}}(t)}{\mathrm{D}t}, \qquad \mathcal{P}_{\text{ext}}(t) = -\frac{\mathrm{D}\,\mathcal{U}_{\text{ext}}(t)}{\mathrm{D}t} \tag{2.54}$$

Under these conditions the balance of mechanical energy (2.49) implies that the sum of the total potential energy $\mathcal{U}_{\text{int}} + \mathcal{U}_{\text{ext}}$ and the kinetic energy $\mathcal{K}$ remain constant during the dynamical deformation process ($\boldsymbol{\chi}$)

$$\mathcal{U}_{\text{int}} + \mathcal{U}_{\text{ext}} + \mathcal{K} = \text{const.} \tag{2.55}$$

2.3.5 Second law of thermodynamics

Following Bergstrom (2015) and IV and V (2008), we can state the second law of thermodynamics[2] as: *the total production of entropy per unit of time of a thermally isolated macroscopic system never decreases.* Where, the total production of entropy per unit of time $\Gamma(t)$ can be computed as the rate of entropy accumulation in the system minus the rate of entropy input through heat transfer minus the rate of entropy input through volumetric heat generation, as indicated below.

$$\Gamma(t) = \frac{\mathrm{D}}{\mathrm{D}t}\int_{\Omega}\eta(\mathbf{x},t)\mathrm{d}v + \int_{\partial\Omega}\frac{\mathbf{q}}{T}\cdot\mathbf{n}\mathrm{d}s - \int_{\Omega}\frac{r}{T}\mathrm{d}v \geq 0, \tag{2.56}$$

$$\Gamma(t) = \frac{\mathrm{D}}{\mathrm{D}t}\int_{\Omega_0}\eta_0(\mathbf{X},t)\mathrm{d}V + \int_{\partial\Omega_0}\frac{\mathbf{Q}}{T_0}\cdot\mathbf{N}\mathrm{d}S - \int_{\Omega}\frac{R}{T_0}\mathrm{d}V \geq 0, \tag{2.57}$$

where η and η_0 are the entropy of the system per unit current and reference volume, respectively, and T, T_0 are the temperature of the system in current and reference configurations, respectively. The previous two equations are often referred to as the **Clausius-Duhem equation**.

By using the divergence theorem, the local forms of the Clausius-Duhem equations are given by

$$\dot{\eta} + \eta\,\mathrm{div}\,\mathbf{v} \geq -\mathrm{div}\left(\frac{\mathbf{q}}{T}\right) + \frac{r}{T}, \tag{2.58}$$

$$\dot{\eta}_0 \geq -\mathrm{Div}\left(\frac{\mathbf{Q}}{T_0}\right) + \frac{R}{T_0}. \tag{2.59}$$

[2]While the second law of thermodynamics is *not* a balance principle, we introduce it into this section for the sake of brevity

Clausius-Planck inequality and heat conduction . Let us rewrite Eq. (2.59) eliminating the heat source R by means of Eq. (2.47) and expanding the divergence operator[3] as

$$\mathbf{S} : \dot{\mathbf{F}} - \dot{e}_0 + T_0\, \dot{\eta}_0 - \frac{1}{T_0}\mathbf{Q} \cdot \operatorname{Grad} T_0 \geq 0 \tag{2.60}$$

Assuming that heat always flows from warmer to colder regions, the entropy production by heat conduction must be non-negative; i.e., $-(1/T_0)\mathbf{Q} \cdot \operatorname{Grad} T_0 \geq 0$. Based on the previous restriction, the Clausius-Duhem inequality (Eq. 2.60) leads to an alternative stronger form of the second law of thermodynamics, often referred to as **Clausius-Planck inequality**, which we present here only in material description.

$$\mathcal{D}_{\text{int}} = \mathbf{S} : \dot{\mathbf{F}} - \dot{e}_0 + T_0\, \dot{\eta}_0 \geq 0, \tag{2.61}$$

where $\mathcal{D}_{\text{int}} \geq 0$ is the internal dissipation or local production of entropy.

2.4 Hyperelastic constitutive models

The so-called hyperelastic models are a type of non-linear elastic constitutive models that are suitable for finite deformations and are commonly used to model a wide range of materials including polymers, rubber-like materials and soft tissues. A hyperelastic material (often referred to as Green-elastic material) postulates the existence of a **Helmholtz free-energy function** ψ defined per unit of reference volume, such that

$$\psi = e_0 - T_0\, \eta_0. \tag{2.62}$$

This thermodynamic potential measures the useful work that can be obtained from a closed thermodynamic system at a constant temperature.

In this section we will focus on a purely mechanical theory, that is, thermal effects are ignored and T_0 and η_0 are omitted from Eq. (2.62). Furthermore, let us consider the case of homogeneous materials in which ψ is solely a function of the deformation gradient $\psi = \psi(\mathbf{F})$ or any other strain tensor, under these conditions ψ is referred to as the **strain-energy function** or **stored-energy function**. The constitutive equation of a hyperelastic material can be derived directly from the Clausius-Planck form of the second law of thermodynamics (Eq. 2.61), which degenerates to an equality in the case

[3] Note that $-\operatorname{Div}\left(\frac{\mathbf{Q}}{T_0}\right) = -\frac{\operatorname{Div}\mathbf{Q}}{T_0} + \frac{\mathbf{Q}\operatorname{Grad} T_0}{T_0^2}$

of perfectly elastic materials.

$$\mathcal{D}_{\text{int}} = \mathbf{S} : \dot{\mathbf{F}} - \dot{\psi} = \left(\mathbf{S} - \frac{\partial \psi(\mathbf{F})}{\partial \mathbf{F}} \right) : \dot{\mathbf{F}} = 0. \tag{2.63}$$

Since $\mathbf{F}$ and $\dot{\mathbf{F}}$ can be arbitrarily chosen, the expression in brackets must be zero, giving the constitutive equation for a hyperelastic material

$$\mathbf{S} = \frac{\partial \psi(\mathbf{F})}{\partial \mathbf{F}}. \tag{2.64}$$

The previous procedure is often referred to as the **Coleman-Noll procedure** (Coleman and Gurtin, 1967; Coleman and Noll, 1963). By using the relation (2.24) we can write the constitutive equation for the Cauchy stress tensor as

$$\boldsymbol{\sigma} = J^{-1} \frac{\partial \psi(\mathbf{F})}{\partial \mathbf{F}} \mathbf{F}^T = J^{-1} \mathbf{F} \left(\frac{\partial \psi(\mathbf{F})}{\partial \mathbf{F}} \right)^T. \tag{2.65}$$

The constitutive equations (2.64) and (2.65) become more complex as we introduce additional material characteristics such as strain rate dependence or anisotropy. To ease reading this text, these enhanced hyperelastic constitutive models will be introduced in further chapters as needed.

Assuming material isotropy, the strain-energy function can be expressed alternatively in terms of the principal invariants of its argument

$$\psi = \psi(I_1, I_2, I_3), \tag{2.66}$$

where $I_1 = \text{tr}(\boldsymbol{C}) = \text{tr}(\boldsymbol{b})$, $I_2 = \frac{1}{2}\left[(\text{tr}\boldsymbol{C})^2 - \text{tr}\boldsymbol{C}^2\right] = \frac{1}{2}\left[(\text{tr}\boldsymbol{b})^2 - \text{tr}\boldsymbol{b}^2\right]$ and $I_3 = J^2$.

Remark. *Equation (2.66) will be the preferred form of the strain-energy function throughout this document.*

Incompressible hyperelastic materials . In several of the problems formulated in this dissertation it will be assumed that the material is incompressible during the deformation process, i.e., J=1. Under this assumption, it is necessary to complement the constitutive equations (2.64) and (2.65) with a Lagrange multiplier p so they remain bijective. Let us define the incompressible strain energy as

$$\psi = \psi(\mathbf{F}) - p(J - 1). \tag{2.67}$$

Then, following the Coleman-Noll procedure, the first Piola-Kichhoff and Cauchy stress tensors can be deduced to be

$$\mathbf{S} = \frac{\partial \psi(\mathbf{F})}{\partial \mathbf{F}} - p\mathbf{F}^{-T}, \qquad \boldsymbol{\sigma} = \frac{\partial \psi(\mathbf{F})}{\partial \mathbf{F}}\mathbf{F}^{T} - p\mathbf{I} = \mathbf{F}\left(\frac{\partial \psi(\mathbf{F})}{\partial \mathbf{F}}\right)^{T} - p\mathbf{I}. \tag{2.68}$$

Compressible hyperelastic materials . Chapter 5 of this dissertation is devoted to the analysis of the effect of compressibility in the oscillatory behavior of thick-walled hyperelastic spherical shells. The compressible constitutive equations presented in Chapter 5 will follow the *volumetric-isochoric* multiplicative decomposition of the deformation gradient (Flory, 1961)

$$\mathbf{F} = \left(J^{1/3}\mathbf{I}\right)\overline{\mathbf{F}}, \qquad \mathbf{C} = \left(J^{2/3}\mathbf{I}\right)\overline{\mathbf{C}}, \qquad \mathbf{b} = \left(J^{2/3}\mathbf{I}\right)\overline{\mathbf{b}}, \tag{2.69}$$

where $\left(J^{1/3}\mathbf{I}\right)$ and $\left(J^{2/3}\mathbf{I}\right)$ are associated with the volume-changing deformations, while $\overline{\mathbf{F}}$, $\overline{\mathbf{C}} = \overline{\mathbf{F}}^{T}\overline{\mathbf{F}}$ and $\overline{\mathbf{b}} = \overline{\mathbf{F}}\overline{\mathbf{F}}^{T}$ are associated with the volume-preserving deformations.

Let us assume, based on the previous kinematic decomposition, a strain energy function of the form

$$\psi(\mathbf{F}) = \psi_{\text{vol}}(J) + \psi_{\text{iso}}(\overline{\mathbf{F}}), \tag{2.70}$$

where $\psi_{\text{vol}}(J)$ and $\psi_{\text{iso}}(\overline{\mathbf{F}})$ describe the **volumetric** and **isochoric** elastic response of the material, respectively. Provided Eq. (2.70), the constitutive equations for the compressible hyperelastic material are given by (2.64) and (2.65).

Assuming material isotropy, the strain energy function (2.70) admits the following representation in terms of strain invariants

$$\psi = \psi_{\text{vol}}(J) + \psi_{\text{iso}}(\overline{I}_1, \overline{I}_2), \tag{2.71}$$

where $\overline{I}_1 = J^{-2/3}I_1$, $\overline{I}_2 = J^{-4/3}I_2$ and $\overline{I}_3 = 1$ are the principal invariants of the isochoric strain tensors $\overline{\mathbf{C}}$ and $\overline{\mathbf{b}}$.

Part II

1D finite vibrations of isotropic hyperelastic structures

3 Incompressible isotropic hyperelastic cylindrical structures

Periodic, quasi-periodic and chaotic motion

This chapter is devoted to the analysis of the nonlinear vibrations of thick-walled cylindrical shells subjected to a radially symmetric dynamic inflation. The material is taken to be isotropic and incompressible within the framework of finite nonlinear elasticity. In particular, Mooney-Rivlin and Yeoh constitutive models have been chosen to describe the mechanical behavior of the cylinder. We have carried out a systematic comparison of the results for both models when the cylinder is subjected to (1) a constant pressure in the radial direction and (2) a harmonic time-dependent pressure. Our analysis reveals the complexity of the oscillatory behavior of this structure despite its geometrical simplicity and the substantial differences between the constitutive models; even though both Helmholtz free-energy functions have been calibrated using the same experimental data.

3.1 Introduction

The analysis of the dynamic behavior of incompressible hyperelastic shells aroused the interest of the scientific community thanks to the pioneering works of Knowles (1960, 1962). In these papers Knowles investigated for the first time the large-amplitude radial oscillations of a very long thick-walled cylindrical tube. Namely, the problem of free oscillations with arbitrary amplitude was considered in Knowles (1960) and the problem of forced oscillations with Heaviside step pressure boundary condition was explored in Knowles (1962). Shortly after, Zhong-Heng and Solecki (1963) inspected the large amplitude vibrations of thick-walled spherical hyperelastic incompressible bodies. The work of Zhong-Heng and Solecki (1963) was later revisited, and adapted to the thin-walled spherical shell by Wang (1965).

In any of these seminal works, due to the incompressibility of the material, the problem at hand was reduced to that of an autonomous motion of a system with a single degree of freedom. Thus, the emphasis of Knowles (1960, 1962); Wang (1965); Zhong-Heng and Solecki (1963) was on obtaining exact expressions for the period of oscillations while, due to the severe (geometrical and material) nonlinearity of these problems (Shahinpoor and Balakrishnan, 1978), the actual states of strain and stress were not determined. Significant efforts were made over the following years to get rid of this incompleteness and provide a full description of the stress, strain and displacement fields of the problems at hand. In this regard, it is worth mentioning the work of Nowinski and Wang (1966) and the series of papers by Shahinpoor and co-workers (Balakrishnan and Shahinpoor, 1977, 1978; Shahinpoor, 1972b; Shahinpoor and Balakrishnan, 1978; Shahinpoor and Nowinski, 1971) that were focused on obtaining complete solutions for the full set of field variables involved in these problems. The great interest raised during the 60's and 70's by the nonlinear oscillations of hyperelastic shells has continued to the present, as detailed in the recent review of Alijani and Amabili (2014). Furthermore, in recent years, we have to emphasize the contributions of Beatty (2011a,b), Verron et al. (1999, 2001) and Humphrey and co-workers (David and Humphrey, 2003; Haslach and Humphrey, 2004; Shah and Humphrey, 1999) who investigated the stability of thick and thin-walled cylindrical and spherical shells subjected to dynamic inflation. The loss of stability (loss of oscillatory behavior) was identified as a key factor that limits the capacity of hyperelastic shells to withstand large deformations under dynamic loading.

All the authors cited in previous paragraphs have raised (at least up to some extent) the key role played by the constitutive model in the dynamic response of hyperelastic shells, and specifically in the critical conditions which lead to the loss of stability of the structure. In this regard, we have to mention the latest works of Gonçalves et al. (2009) and Soares and Gonçalves (2012, 2014), who made a thorough investigation of the nonlinear vibrations of circular, annular and rectangular hyperelastic membranes. The authors showed the constitutive sensitivity of these problems using different strain energy functions calibrated with the same experimental results. In the words of Soares and Gonçalves (2014) *the choice of an appropriate constitutive law is a key step in the mathematical modeling of hyperelastic materials.* This statement is further supported by Selvadurai (2006), who studied the role played by the constitutive model on the deflection of hyperelastic membranes. Selvadurai (2006) concluded that the selection of an appropriate (accurate) strain energy function becomes especially relevant when the objective is to model the large strain behavior of hyperelastic solids. Moreover, this conclusion is in line with the main outcome derived from the work of Lacarbonara

et al. (2014), who showed the key role played by the material nonlinearity in the flexural vibrations of elastic rings. In addition, Antman and Lacarbonara (2009) and Lacarbonara and Antman (2012) have shown the critical influence that material compressibility and viscosity have on the radial motions of cylindrical and spherical shells.

As it can be deduced from all the references stated in previous paragraphs, the problem of a cylindrical shell subjected to a radial Heaviside pressure in its boundary has received great attention since the seminal works of Knowles (1960) and Knowles (1962). However, of all the works previously cited, that of Antman and Lacarbonara (2009) is the only one to consider periodic forcing on a cylindrical shell. As it will be analyze in this chapter, if periodic forcing is considered, the governing system of equations becomes non-autonomous, complicating the analysis of the dynamic response of the structure. Under these conditions the system presents not only periodic but quasi-periodic and chaotic solutions.

Hence, moved by these works which pointed out the constitutive sensitivity of the oscillatory behavior of hyperelastic shells, in this chapter we revisit the original problem of Knowles (1960, 1962) under two different loading conditions (1) a constant pressure in the radial direction and (2) a harmonic time-dependent pressure. Two constitutive models, Mooney-Rivlin and Yeoh, calibrated with the same set of experimental data (see Bucchi and Hearn (2013a,b)), are taken into consideration. A methodical confrontation of the results obtained from both constitutive models raises their influence on the dynamic response of the cylindrical shell. Thus, we have obtained the initial, loading and geometrical conditions which, depending on the constitutive model, impede the oscillatory response of the shell. In addition, for the specific cases in which the shell shows periodic motion we have explored the influence of the constitutive model in the period of the oscillations. Furthermore, we have analyzed the Poincaré sections in the case of periodic forcing for different boundary conditions, giving a complete description of the orbit topologies and analyzing their stability.

3.2 Problem formulation

In this section we formulate the problem of a thick-walled cylindrical shell subjected to radially symmetric dynamic inflation. The material is taken to be isotropic and incompressible, within the framework of finite nonlinear elasticity. The main features of the mathematical derivation are presented, while further details can be found in the pioneering works of Knowles (1960, 1962).

Recall from Chapter 2 that the current position vector $\mathbf{x}$ in the deformed configuration $\Omega \subset \mathbb{R}^3$ at time t of the material point that occupies the location $\mathbf{X} \in \Omega_0$ is given by $\mathbf{x} = \boldsymbol{\chi}(\mathbf{X}, t)$, where $\boldsymbol{\chi}$ is a bijective and twice continuously differentiable mapping. The associated deformation gradient, right Cauchy-Green strain tensor and volume ratio at $\mathbf{X} \in \Omega_0$ are denoted by

$$\begin{gathered} \mathbf{F}(\mathbf{X}, t) = \operatorname{Grad} \boldsymbol{\chi}(\mathbf{X}, t), \ \mathbf{C}(\mathbf{X}, t) = \mathbf{F}^{\mathrm{T}}(\mathbf{X}, t)\mathbf{F}(\mathbf{X}, t), \\ J(\mathbf{X}, t) = \det \mathbf{F}(\mathbf{X}, t). \end{gathered} \tag{3.1}$$

Moreover, the balance of linear momentum in the material description requires that

$$\operatorname{Div} \mathbf{S}(\mathbf{X}, t) = \rho_0 \ddot{\boldsymbol{\chi}}(\mathbf{X}, t) \quad \text{in} \quad \Omega_0, \tag{3.2}$$

where the dots denote differentiation with respect to time, $\mathbf{S}$ stands for the first Piola-Kirchhoff stress tensor, and ρ_0 is the constant[1] mass density of the shell material in its undeformed configuration Ω_0.

3.2.1 Constitutive model

Two isotropic incompressible nonlinear elastic models are considered for the shell material. They both respond to the following polynomial strain-energy function[2]

$$\psi(I_1, I_2) = \sum_{i,j=0}^{N} C_{ij}(I_1 - 3)^i (I_2 - 3)^j, \tag{3.3}$$

where C_{ij} are empirically determined material parameters and $I_1 = \operatorname{tr}(\mathbf{C})$, $I_2 = \frac{1}{2}\left[(\operatorname{tr}\mathbf{C})^2 - \operatorname{tr}\mathbf{C}^2\right]$ are the first and second invariants of the right Cauchy-Green strain tensor. Namely, we use the so-called Mooney-Rivlin and Yeoh models.

$$\psi_{\mathrm{M}}(I_1, I_2) = C_{\mathrm{M}10}(I_1 - 3) + C_{\mathrm{M}01}(I_2 - 3), \tag{3.4}$$

$$\psi_{\mathrm{Y}}(I_1, I_2) = C_{\mathrm{Y}10}(I_1 - 3) + C_{\mathrm{Y}20}(I_1 - 3)^2 + C_{\mathrm{Y}30}(I_1 - 3)^3. \tag{3.5}$$

Moreover, from Bucchi and Hearn (2013b) we take $C_{\mathrm{M}10} = 210587.307$ MPa, $C_{\mathrm{M}01} = 1504.76719$ MPa for the Mooney-Rivlin and $C_{\mathrm{Y}10} = 190592.559$ MPa, $C_{\mathrm{Y}20} = -1634.89996$ MPa, $C_{\mathrm{Y}30} = 41.3399927$ MPa for the Yeoh model. These material constants correspond to vulcanized rubber and were originally reported by Treloar (1944). These two constitutive

[1] The focus of this work is on homogeneous solids thus the choice of constant mass density ρ_0.
[2] Throughout this work we consider isothermal conditions.

models are selected because they have different functional dependence on $\mathbf{F}$, which allows to explore the influence of the constitutive model in the oscillatory behavior of the cylindrical shell.

3.2.2 Radially symmetric dynamic deformation

Let us define the reference configuration Ω_0 of the thick-walled cylindrical shell by the polar coordinates $\{R, \Theta, Z\}$ such that

$$A \leq R \leq B, \qquad 0 \leq \Theta \leq 2\pi, \qquad 0 \leq Z \leq L. \tag{3.6}$$

If we restrict our attention to radially symmetric motions with **plane strain in the Z direction**, the current geometry is given by

$$a(t) \leqslant r(R,t) \leqslant b(t), \qquad \theta = \Theta, \qquad z = Z, \tag{3.7}$$

where $\{r, \theta, z\}$ are cylindrical polar coordinates in the current configuration Ω (see Fig. 3.1). Under these conditions the deformation gradient can be expressed in a right-handed vector basis $\{\mathbf{e}_r, \mathbf{e}_\theta, \mathbf{e}_z\}$ of a cylindrical polar coordinate system (see Appendix A) as follows

$$\mathbf{F} = \left(\frac{1}{\lambda(R,t)}\right) \mathbf{e}_r \otimes \mathbf{e}_r + \lambda(R,t)\, \mathbf{e}_\theta \otimes \mathbf{e}_\theta + \mathbf{e}_z \otimes \mathbf{e}_z, \tag{3.8}$$

where the principal stretches corresponding to the directions $\{r, \theta, z\}$ are given by

$$\lambda_r = \frac{\partial r(R,t)}{\partial R}, \quad \lambda_\theta = \frac{r(R,t)}{R} = \lambda, \quad \lambda_z = \frac{z}{Z} = 1, \tag{3.9}$$

and we have used the incompressibility restriction $J = \lambda_r(R,t)\lambda(R,t) = 1$. Similarly, the first Piola-Kirchhoff stress tensor corresponding to the deformation gradient (3.8) can be proved to be also of the spectral form

$$\mathbf{S} = S_r(R,t)\, \mathbf{e}_r \otimes \mathbf{e}_r + S_\theta(R,t)\, \mathbf{e}_\theta \otimes \mathbf{e}_\theta + S_z(R,t)\mathbf{e}_z \otimes \mathbf{e}_z. \tag{3.10}$$

The principal stresses $S_r(R,t)$ and $S_\theta(R,t)$ are such that (see e.g. Ogden (1997))

$$S_\theta(R,t) - \frac{S_r(R,t)}{\lambda^2(R,t)} = W'\left(\lambda(R,t)\right), \tag{3.11}$$

where $W' = \frac{\mathrm{d}W(\lambda)}{\mathrm{d}\lambda}$ and $W(\lambda) = \psi(I_1, I_2)$.

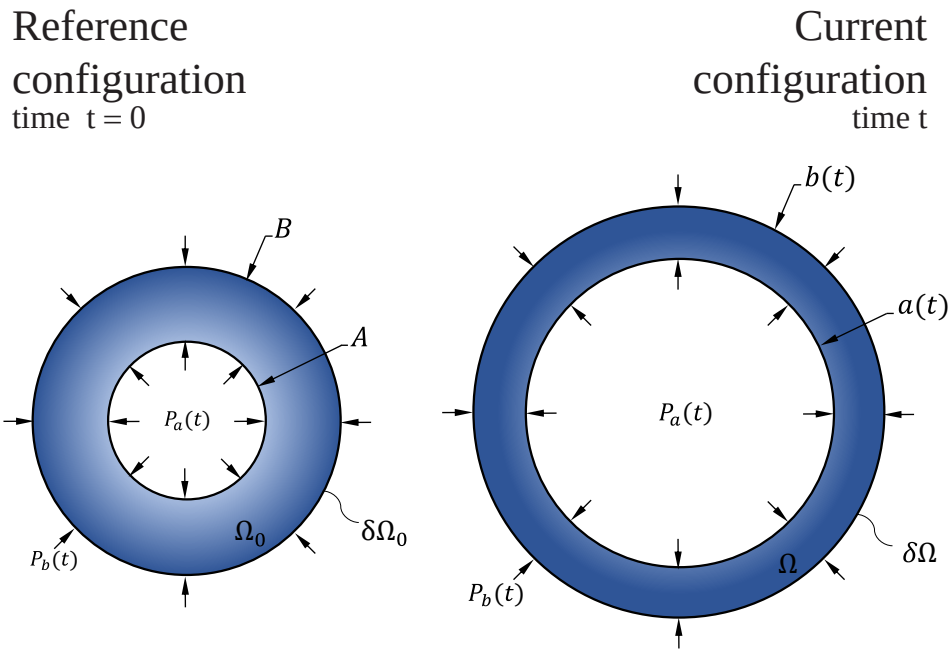

Fig. 3.1 Schematic representation of the radially symmetric deformation process of a thick-walled cylindrical shell

Under these conditions the balance of linear momentum (3.2) reduces to

$$\frac{\partial S_r(R,t)}{\partial R} + \frac{S_r(R,t) - S_\theta(R,t)}{R} = \rho_0 \, \ddot{r}(R,t). \tag{3.12}$$

Moreover, it follows from the incompressibility condition $J = \lambda_r(R,t)\lambda(R,t) = 1$ that

$$\lambda(R,t) = \left(\frac{B^2}{R^2}(\lambda_b^2(t) - 1) + 1\right)^{1/2}, \tag{3.13}$$

where $\lambda_b(t) = b(t)/B$ stands for the circumferential stretch in the outer face of the cylinder. The expression (3.13) can be alternatively written as $\lambda(R,t) = (A^2/R^2(\lambda_a^2(t) - 1) + 1)^{1/2}$ in terms of the stretch in the inner face of the cylinder $\lambda_a(t) = a(t)/A$. For our purposes here, we find dealing with the form (3.13) in terms of the outer stretch $\lambda_b(t)$ more convenient. Taking the derivatives of Eq.(3.13) with respect to R and t we obtain the following relations

$$\frac{\partial \lambda}{\partial R} = -\frac{\lambda^2 - 1}{R\lambda}, \tag{3.14}$$

$$\ddot{\lambda} = \frac{\lambda^2 - 1}{\lambda_b^2 - 1}\left[\frac{\dot{\lambda_b}^2 + \lambda_b \ddot{\lambda_b}}{\lambda} - \frac{\lambda_b^2 \dot{\lambda_b}^2}{\lambda_b^2 - 1}\frac{\lambda^2 - 1}{\lambda^3}\right], \tag{3.15}$$

where **function arguments are omitted** here and in some of the subsequent development to ease notation. At this stage, it proves convenient to rewrite the equation of motion (3.12) with $\lambda(R,t)$ as the independent space variable instead of R. With help of the expressions (3.14) and (3.15), the result reads as

$$\frac{\partial}{\partial\lambda}\left[\frac{S_r}{\lambda}\right] = -\frac{S_\theta - \frac{S_r}{\lambda^2}}{\lambda^2-1} + \rho_0 B^2\left[\frac{\lambda_b^2\dot{\lambda}_b^2}{(\lambda_b^2-1)\lambda^3} - \frac{\dot{\lambda}_b^2+\lambda_b\ddot{\lambda}_b}{\lambda(\lambda^2-1)}\right]. \tag{3.16}$$

Assuming now that the inner boundary ($R=A$) is subjected to a pressure $P_a(t)$, defined per unit of current area. While, the outer face ($R=B$) is subjected to a pressure $P_b(t)$ (see Fig. 3.1), the boundary conditions are given by

$$S_r(A,t) = -P_a(t)\lambda_a \quad \text{and} \quad S_r(B,t) = -P_b(t)\lambda_b, \tag{3.17}$$

where $P_a(t)$ and $P_b(t)$ are any functions of choice (suitably well behaved). Hence, integration of Eq.(3.16) with help of Eq.(3.17) and Eq.(3.11) yields

$$\Delta P = \int_{\lambda_b}^{\left(\frac{\lambda_b^2-1}{f_0}+1\right)^{1/2}} \frac{W'(\lambda)}{\lambda^2-1}\mathrm{d}\lambda + \frac{\rho_0 B^2}{2}\left[\ln\left(\frac{\lambda_b^2}{\lambda_b^2+f_0-1}\right)\lambda_b\ddot{\lambda}_b + \left(\ln\left(\frac{\lambda_b^2}{\lambda_b^2+f_0-1}\right) + \frac{f_0-1}{\lambda_b^2+f_0-1}\right)\dot{\lambda}_b^2\right], \tag{3.18}$$

where we have introduced the non-dimensional parameters $f_0 = \frac{A^2}{B^2}$ and $\Delta P = P_a(t) - P_b(t)$.

Remark. *To be noticed that $f_0 \in (0,1)$ takes into account the thickness of the shell. In the limit of $f_0 \to 1$ the classical expressions for a cylindrical membrane are recovered, while the case of $f_0 \to 0$ corresponds to a solid cylindrical region.*

At this point, it is interesting to introduce the following length, mass and time scales in order to pose the problem in non-dimensional form

$$[L] = B, \qquad [M] = \rho B^3, \qquad [T] = \sqrt{\frac{\rho B^2}{C_{\mathrm{M10}}}}, \tag{3.19}$$

As a result, Eq.(3.18) can be rewritten as follows

$$\Delta\overline{P} = \int_{\lambda_b}^{\left(\frac{\lambda_b^2-1}{f_0}+1\right)^{1/2}} \frac{\overline{W}'(\lambda)}{\lambda^2-1}\mathrm{d}\lambda + \frac{1}{2}\ln\left(\frac{\lambda_b^2}{\lambda_b^2+f_0-1}\right)\lambda_b\ddot{\lambda}_b + \frac{1}{2}\left(\ln\left(\frac{\lambda_b^2}{\lambda_b^2+f_0-1}\right) + \frac{f_0-1}{\lambda_b^2+f_0-1}\right)\dot{\lambda}_b^2, \tag{3.20}$$

where $\Delta\overline{P} = \Delta P/C_{\mathrm{M10}}$, $\overline{W} = W/C_{\mathrm{M10}}$, and now a superposed dot denotes differentiation with respect to the dimensionless time τ.

3.3 Sample results: autonomous system

In this section we consider the cylindrical shell subjected to a constant pressure

$$\Delta\overline{P} = \overline{P}\, H(t), \tag{3.21}$$

where $H(t)$ is the Heaviside function. Under these conditions, and upon multiplication by $2\lambda_b$, the equation of motion (3.20) can be rewritten as

$$2\lambda_b\, \overline{P} = 2\lambda_b \int_{\lambda_b}^{\left(\frac{\lambda_b^2-1}{f_0}+1\right)^{1/2}} \frac{\overline{W}'(\lambda)}{\lambda^2-1}\mathrm{d}\lambda + \frac{\mathrm{d}}{\mathrm{d}\lambda_b}\left[\frac{1}{2}\ln\left(\frac{\lambda_b^2}{\lambda_b^2+f_0-1}\right)\lambda_b^2\dot{\lambda}_b^2\right]. \tag{3.22}$$

The previous expression can be integrated in time[3] to obtain the **energy equation**

$$\mathcal{U}_{\mathrm{ext}} + \mathcal{U}_{\mathrm{int}} + \mathcal{K} = C, \tag{3.23}$$

where

$$\begin{aligned} \mathcal{U}_{\mathrm{int}} &= \int_1^{\lambda_b} 2\xi \int_{\xi}^{\left(\frac{\xi^2-1}{f_0}+1\right)^{1/2}} \frac{\overline{W}'(\lambda)}{\lambda^2-1}\mathrm{d}\lambda\, \mathrm{d}\xi, \\ \mathcal{U}_{\mathrm{ext}} &= \overline{P}(1-\lambda_b^2), \qquad \mathcal{K} = \frac{1}{2}\ln\left(\frac{\lambda_b^2}{\lambda_b^2+f_0-1}\right)\lambda_b^2\dot{\lambda}_b^2, \end{aligned} \tag{3.24}$$

are the total strain energy, the potential energy of the external loading and the kinetic energy of the cylinder, respectively [4] . The constant C can be computed from the initial conditions as the energy at $\tau = 0$. To simplify the analysis, **the shell is assumed to be initially in equilibrium and unstretched**, $\lambda_b(0) = 1$ and $\dot{\lambda}_b(0) = 0$, which leads to $C = 0$.

From Eq. 3.23 an expression for the phase portrait $(\lambda_b - \dot{\lambda}_b)$ of the particle can be explicitly obtained

$$\dot{\lambda}_b(\lambda_b) = \left(\frac{\mathcal{U}_{\mathrm{ext}} + \mathcal{U}_{\mathrm{int}}}{\frac{1}{2}\ln\left(\frac{\lambda_b^2+f_0-1}{\lambda_b^2}\right)\lambda_b^2}\right)^{1/2}. \tag{3.25}$$

[3] It should be noted that, under these conditions, $\mathrm{d}\lambda_b = \dot{\lambda}_b \mathrm{d}\tau$

[4] Specifically, expressions (3.24) correspond to the non-dimensional energies except for a factor of $\pi\frac{H}{B}$

To be noted that the motion is periodic if (and only if) the expression $\mathcal{U}_{\text{ext}} + \mathcal{U}_{\text{int}}$ has at least two real roots. In that case, the non-dimensional period $\overline{T}$ can be calculated as

$$\overline{T} = \int_{\lambda_b^{\min}}^{\lambda_b^{\max}} \dot{\lambda}_b^{-1}(\lambda_b) \mathrm{d}\lambda_b, \tag{3.26}$$

with $\lambda_b^{\min}$ and $\lambda_b^{\max}$ being the minimum and maximum values of λ_b during the oscillation. These points can be calculated imposing the total potential energy to be zero ($\mathcal{U}_{\text{ext}} + \mathcal{U}_{\text{int}} = 0$).

Mooney-Rivlin constitutive model: assuming the Mooney-Rivlin model for the cylinder material, the total strain energy is given by

$$\mathcal{U}_{\text{int}} = (1 + \frac{C_{\text{M01}}}{C_{\text{M10}}})(\lambda_b^2 - 1) \ln\left(\frac{\lambda_b^2 + f_0 - 1}{f_0 \lambda_b^2}\right). \tag{3.27}$$

Then, the minimum and maximum values of λ_b during the oscillation (i.e. the points in which $\dot{\lambda}_b = 0$) can be calculated imposing the total potential energy to be zero

$$\lambda_b^{\min} = 1, \qquad \lambda_b^{\max} = \left(\frac{f_0 - 1}{f_0 \exp\left(\frac{\overline{P}}{1 + C_{\text{M01}}/C_{\text{M10}}}\right) - 1}\right)^{1/2}. \tag{3.28}$$

For positive applied pressures ($\overline{P} > 0$), the minimum value of λ_b corresponds to the initial conditions and the maximum value of λ_b gives the maximum circumferential stretch that can be reached during the periodic motion. The expression that defines the critical pressure for which the shell shows oscillatory behavior is

$$\overline{P}_{c+} = \lim_{\lambda_b \to \infty} (1 + \frac{C_{\text{M01}}}{C_{\text{M10}}}) \ln\left(\frac{\lambda_b^2 + f_0 - 1}{f_0 \lambda_b^2}\right) = (1 + \frac{C_{\text{M01}}}{C_{\text{M10}}}) \ln\left(\frac{1}{f_0}\right). \tag{3.29}$$

For negative applied pressures ($\overline{P} < 0$), the maximum value of λ_b is given by the initial conditions. However, from Eq.(3.28) it can be proved that there is no bound for the oscillatory behavior if the pressure is negative.

$$\overline{P}_{c-} = \lim_{\lambda_b \to 0} (1 + \frac{C_{\text{M01}}}{C_{\text{M10}}}) \ln\left(\frac{\lambda_b^2 + f_0 - 1}{f_0 \lambda_b^2}\right) = -\infty. \tag{3.30}$$

Remark. *To be noticed that, if the shell is* ***not*** *assumed to be initially in equilibrium and unstretched i.e.* $(C \neq 0)$*, the calculation of* $\overline{P}_{c+}$ *leads to the same value, so the oscillatory motion is lost for* $\overline{P} > \overline{P}_{c+}$ *irrespective of the initial conditions.*

Yeoh constitutive model: assuming the Yeoh model for the cylinder material, the total strain energy is given by

$$\begin{aligned}\mathcal{U}_{\text{int}} = \frac{\left(\lambda_b^2-1\right)^2}{2C_{\text{M10}}}\Bigg[2(C_{\text{Y2}}-3C_{\text{Y3}})\left(\frac{1}{f_0+\lambda_b^2-1}+\frac{1}{f_0}-\frac{1}{\lambda_b^2}\right)- \\ 2C_{\text{Y2}}+C_{\text{Y3}}\left(\lambda_b^2-1\right)\left(\frac{1}{f_0^2}-\frac{1}{\left(f_0+\lambda_b^2-1\right)^2}+\frac{1}{\lambda_b^4}\right)+C_{\text{Y3}}\left(7-\lambda_b^2\right)+ \\ \frac{2(C_{\text{Y1}}-2C_{\text{Y2}}+6C_{\text{Y3}})}{\lambda_b^2-1}\ln\left(\frac{f_0+\lambda_b^2-1}{f_0\lambda_b^2}\right)\Bigg].\end{aligned} \tag{3.31}$$

Following the same procedure as for the Mooney-Rivlin, it is easy to check that there are no bounds in the oscillatory behavior of the cylinder for the Yeoh constitutive model neither for positive nor negative applied pressures.

Figures (3.2a) and (3.2b) present the evolution of the potential energy $(\mathcal{U}_{\text{ext}}+\mathcal{U}_{\text{int}})$ with the circumferential stretch in the outer face of the shell (λ_b) for Mooney-Rivlin and Yeoh constitutive models, respectively. Moreover, figures (3.2c) and (3.2d) present the corresponding phase portraits, $\dot{\lambda}_b$ versus λ_b. The bifurcation behavior predicted in Eq.(3.29) can be observed in the case of the Mooney-Rivlin material model: the $\mathcal{U}_{\text{ext}}+\mathcal{U}_{\text{int}}$ versus λ_b curves for applied pressures equal or greater than the critical one $\overline{P}_{c+}$ only intersects once the λ_b axis which implies that the shell does not oscillate.

Fig. (3.3a) depicts the relation between the applied pressure $(\overline{P})$ and the maximum stretch of the oscillation (λ_b^{max}) for both constitutive models investigated. For the Yeoh material the curve first increases with λ_b^{max} showing a concave-downwards shape, reaches an inflection point for $\overline{P}=0.54$ and then increases again showing a concave-upwards shape. This behavior is significantly different from the $\overline{P}-\lambda_b^{max}$ corresponding to the Mooney-Rivlin model that shows an concave-downwards shape no matter the value of λ_b^{max} and an horizontal asymptote at $\overline{P}=\overline{P}_{c+}$.

Fig.(3.3b) presents the period of the oscillation $(\overline{T})$ versus the applied pressure $(\overline{P})$ for both constitutive models. For the Mooney-Rivlin model the period of the oscillation increases monotonically with the applied pressure showing a concave-upwards shape and vertical asymptote for $\overline{P}=\overline{P}_{c+}$. For the Yeoh material the period increases with the applied pressure up to $\overline{P}=0.54$. This value defines the maximum period of the oscillation. To be noticed that $\overline{P}=0.54$ determines the inflection point in Fig.(3.3a). For applied pressures greater than 0.54 the period decreases monotonically with $\overline{P}$.

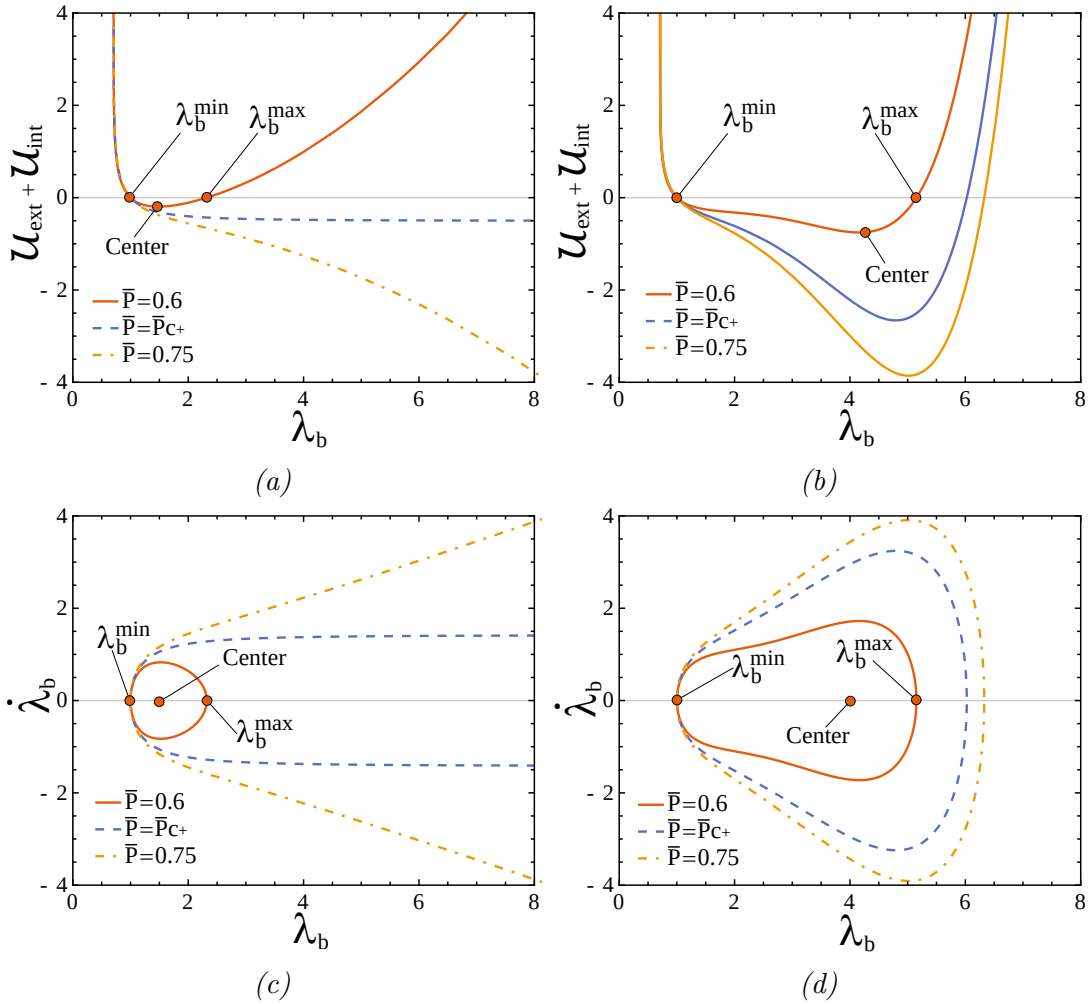

Fig. 3.2 Bifurcation behavior for constant applied pressure for Mooney-Rivlin (Figs a and c) and Yeoh (Figs b and d) constitutive models. Initial volume fraction $f_0 = 0.5$.

3.4 Sample results: non-autonomous system

In the previous section we have restricted our attention to autonomous systems (constant applied pressure). However, in many practical applications time dependent external forces, including periodic inputs, are of great interest. In this section, a periodically forced non-autonomous system of differential equations is analyzed. Poincaré sections and Lyapunov exponents are used to determine (qualitatively and quantitatively, respectively) whether the response of the structure is periodic, quasi-periodic or chaotic. In autonomous systems, as the one analyzed in previous section, trajectories plotted in the phase space $(\lambda_b, \dot{\lambda}_b)$ cannot cross, and the Poincaré-Bendixon theorem implies that there is no possibility

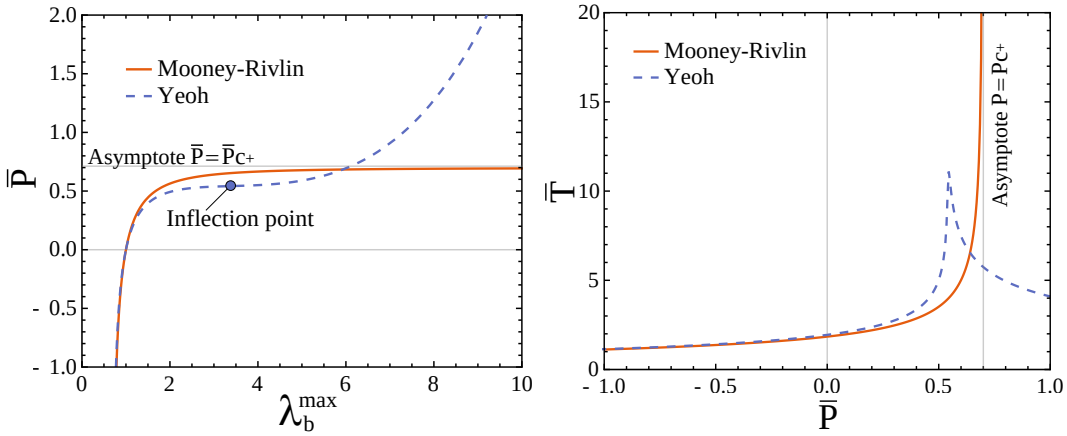

Fig. 3.3 (a) Relation between the applied pressure $\overline{P}$ and the maximum stretch in the outer face of the shell λ_b^{max}. (b) Evolution of the period $\overline{T}$ with the applied pressure $\overline{P}$.

of chaotic behavior in two dimensions. On the other hand, if a time dependent force is considered, the phase space increases in one dimension and **periodic, quasi-periodic and chaotic motions are possible**.

The time dependent periodic applied pressure considered in this section is

$$\Delta\overline{P} = \overline{P}(1+\cos(\overline{\omega}\,\tau)), \tag{3.32}$$

where the non-dimensional frequency $\overline{\omega}$ and the non-dimensional pressure $\overline{P}$ are given by $\overline{\omega} = \omega\sqrt{\rho B^2/C_{\mathrm{M10}}}$ and $\overline{P} = P/C_{\mathrm{M10}}$.

The trajectories of a non-autonomous system subjected to a periodic loading can be represented in terms of an autonomous flow in a torus. Calling $x = \lambda_b$, $y = \dot{\lambda}_b$, $\theta = \overline{\omega}\,\tau$, the non-dimensional equation of motion (3.20) can be rewritten as the following system of three first order ordinary differential equations.

$$\begin{aligned}
\dot{x} &= y,\\
\dot{y} &= \frac{2\Delta\overline{P}(\theta) - 2\int_{x}^{\left(\frac{x^2-1}{f_0}+1\right)^{1/2}} \frac{\overline{W}'(\lambda)}{\lambda^2-1}\mathrm{d}\lambda - \left(\ln\left(\frac{x^2}{x^2+f_0-1}\right) + \frac{f_0-1}{x^2+f_0-1}\right) y^2}{\ln\left(\frac{x^2}{x^2+f_0-1}\right) x},\\
\dot{\theta} &= \overline{\omega}.
\end{aligned} \tag{3.33}$$

This transformation highlights the fact that a non-autonomous system of order n can be treated as an autonomous system of order n+1. Representing the phase space $\{x, y, \theta\}$

in cylindrical polar coordinates where x, y and θ are the radial, vertical and angular coordinates, respectively, it can be proved that the trajectories are always confined in a torus. As an example, Fig. 3.4a depicts the torus corresponding to $f_0 = 0.5$, $\overline{P} = 0.3$ and $\overline{\omega} = 1$ with initial conditions $(\lambda_b, \dot{\lambda}_b) = (1.7, 0)$ for the Mooney-Rivlin material model [5]. The red line corresponds to a quasi-periodic trajectory flowing around the torus with non-dimensional period $\overline{T} = 2\pi/\overline{\omega}$. Periodic and quasi-periodic trajectories will lie on the surface of the torus, while chaotic trajectories penetrate inside the volume. This structure of the solution naturally leads to the concept of the Poincaré section. The Poincaré map (Fig. 3.4b) can be understood as the intersection of the torus with any of the planes with $\theta = \text{const}$. In other words, it is an stroboscopic view of the trajectory in the $(\lambda_b, \dot{\lambda}_b)$ plane at the points that satisfy $\tau = k\overline{T}$, being k a natural number. This technique reduces the phase space trajectory of dimension n to a discrete mapping of dimension $n - 1$ that contains all the dynamical information of the system. Below we

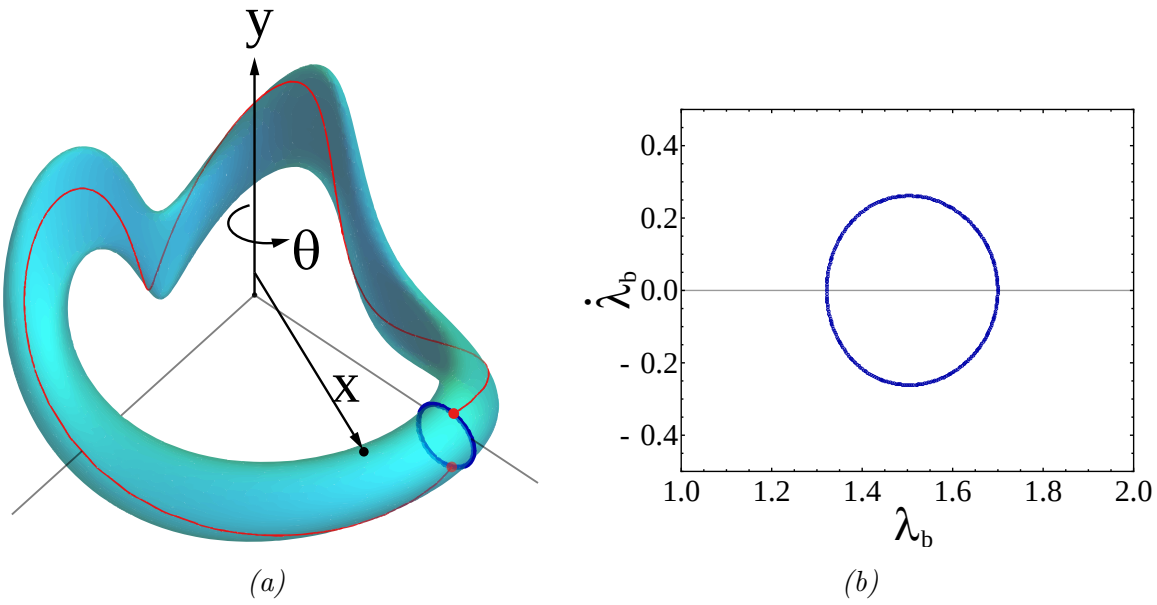

(a) *(b)*

Fig. 3.4 (a) Three-dimensional torus in the (x, y, θ) phase space corresponding to a quasi-periodic trajectory. (b) Poincaré section corresponding to the plane $\theta = 0$.

present a list with the main ideas that come out from the Poincaré map representation:

- The Poincaré section might contain a single point, indicating a periodic orbit with period $\overline{T}$.

[5] These values have been selected for the sole purpose of presenting to the reader the structure of the solution.

- If the Poincaré section contains k isolated points, the corresponding trajectory is periodic with period $k\overline{T}$.
- A quasi-periodic trajectory will lead to close curves in the Poincaré maps (as the one presented in Fig. 3.4b).
- A chaotic motion will show up filling a two-dimensional region of the Poincaré section.

Following with the same configuration ($f_0 = 0.5$ and $\overline{\omega} = 1$), for the Mooney-Rivlin material, we analyze now the stability of the different trajectories formed as the applied pressure $\overline{P}$ changes. Fig. (3.5) depicts the Poincaré maps for the Mooney-Rivlin material in the case of $\overline{P} = 0.3$ and $\overline{P} = 0.352$. We have scanned a wide variety of initial conditions in order to show in the Poincaré maps all the different orbit topologies that are possible for the specific level of pressure considered. Considering additional initial conditions will only provide topologically identical orbits to those already plotted, but with different amplitude (like the two blue orbits in Fig. 3.5a). In other words, to complete the white

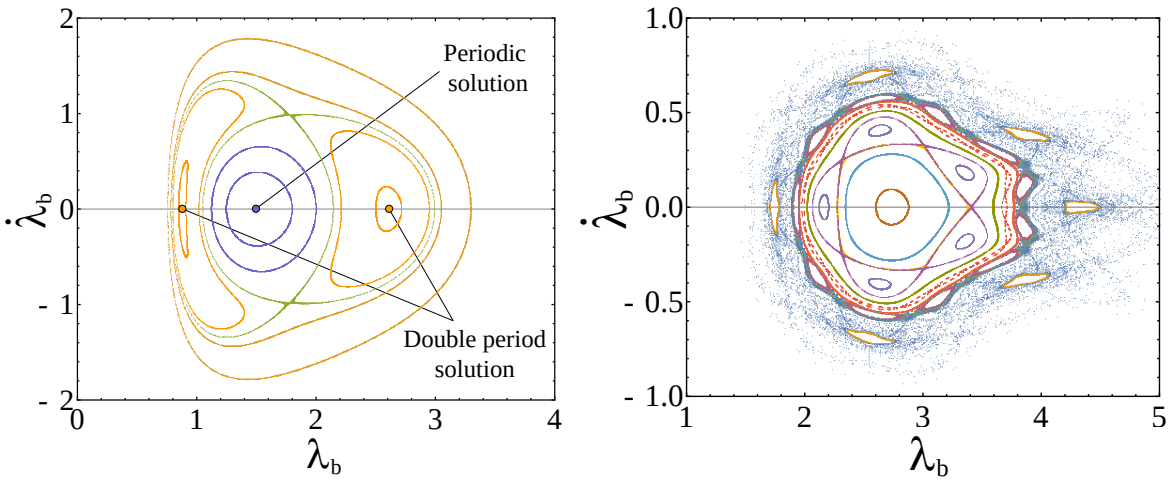

Fig. 3.5 Poincaré maps for the Mooney-Rivlin model with different values of the applied pressure $\overline{P}$. (a) $\overline{P} = 0.3$ and (b) $\overline{P} = 0.352$. $f_0 = 0.5$ and $\overline{\omega} = 1$.

space in Fig. 3.5 will not provide additional relevant information but it will reduce the clarity of the plots. For $\overline{P} = 0.3$, the system is close to the linear regime (stretches are relatively small) and only periodic and quasi-periodic trajectories are possible. As the value of $\overline{P}$ is increased up to 0.352, chaotic regions appear in the explored phase portrait (see Section 3.4.1 for details). Figures (3.6a) and (3.6b) present the time evolution and the phase portraits of the two periodic trajectories indicated in Fig. (3.5a). It can be

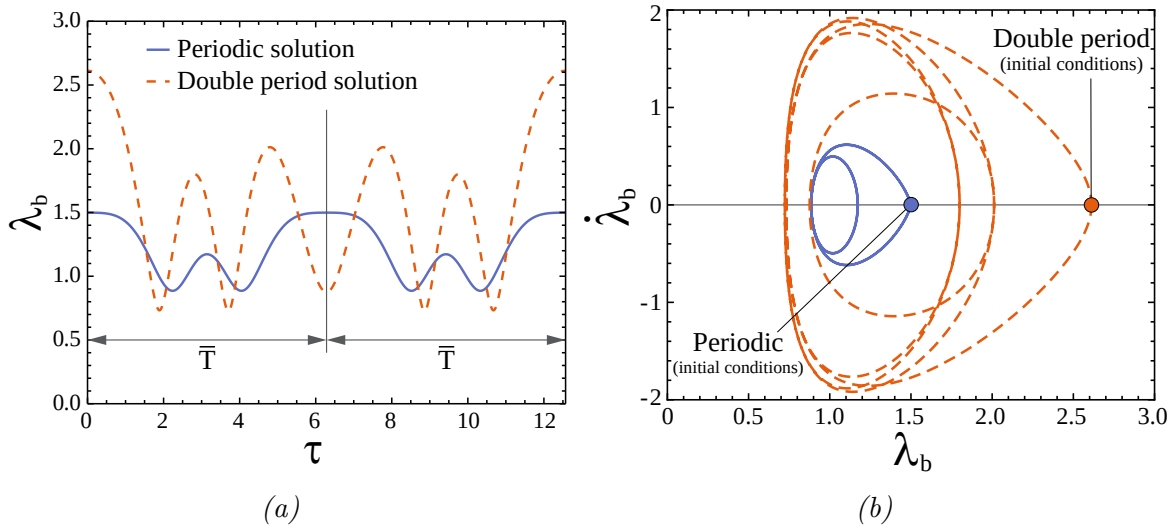

(a) *(b)*

Fig. 3.6 Time evolution and phase portraits for the periodic orbits presented in Fig. (3.5a).

seen that for the single-period solution $\tau = \overline{T} = 2\pi$, while for the double-period solution $\tau = 2\overline{T} = 4\pi$, where it has to be recalled that $\overline{T}$ is the period of the external force.

On the other hand, Fig. (3.7) represents the evolution of the Poincaré map for the Yeoh material model as the value of $\overline{P}$ changes. As in the analysis of the results obtained from the Mooney-Rivlin model, we have taken $f_0 = 0.5$ and $\overline{\omega} = 1$. For $\overline{P} = 0.22$ (Fig.3.7a), only periodic and quasi-periodic orbits are present. A pair of periodic orbits with periods $\overline{T}$ and $2\overline{T}$ are identified in the figure with brown and blue points, respectively. For $\overline{P} = 0.26$ (Fig.3.7b), as predicted by the Kolmogorov-Arnold-Moser (or KAM) theory (see e.g. Arnol'd (2013)), due to the increase of external work supplied to the system, some of the tori are destroyed (those with rational winding number [6], often referred to as resonant tori). These tori break up into chains of alternating elliptic and hyperbolic fixed points as predicted by the Poincaré–Birkhoff fixed point theorem (Birkhoff, 1913). These chains can be easily identified in Fig.(3.7b). Furthermore, the onset of chaotic behavior is appreciated in the vicinity of some of the hyperbolic points. For $\overline{P} = 0.268$ (Fig.3.7c), the ordered and stochastic regions have comparable size; the periodic islands have been highlighted in the plot indicating with the same color which ones are generated by the same trajectory [7]. Finally, for $\overline{P} = 0.29$ almost all the explored phase space

[6] When the trajectories lying on the surface of a torus are described in the angle-action variables, the winding number is defined as the ratio between the two orbiting frequencies. A system with a rational winding number is mode-locked, whereas a system with an irrational winding number is quasi-periodic. See, e.g., Arnol'd (2013) for further details.

[7] For interpretation of the references to color in the text, the reader is referred to the web version of this dissertation

present chaotic behavior. The orbits designated as IC_1 and IC_2 in Fig. (3.7a) and (3.7d), respectively, will be further analyzed with more detail in the next section.

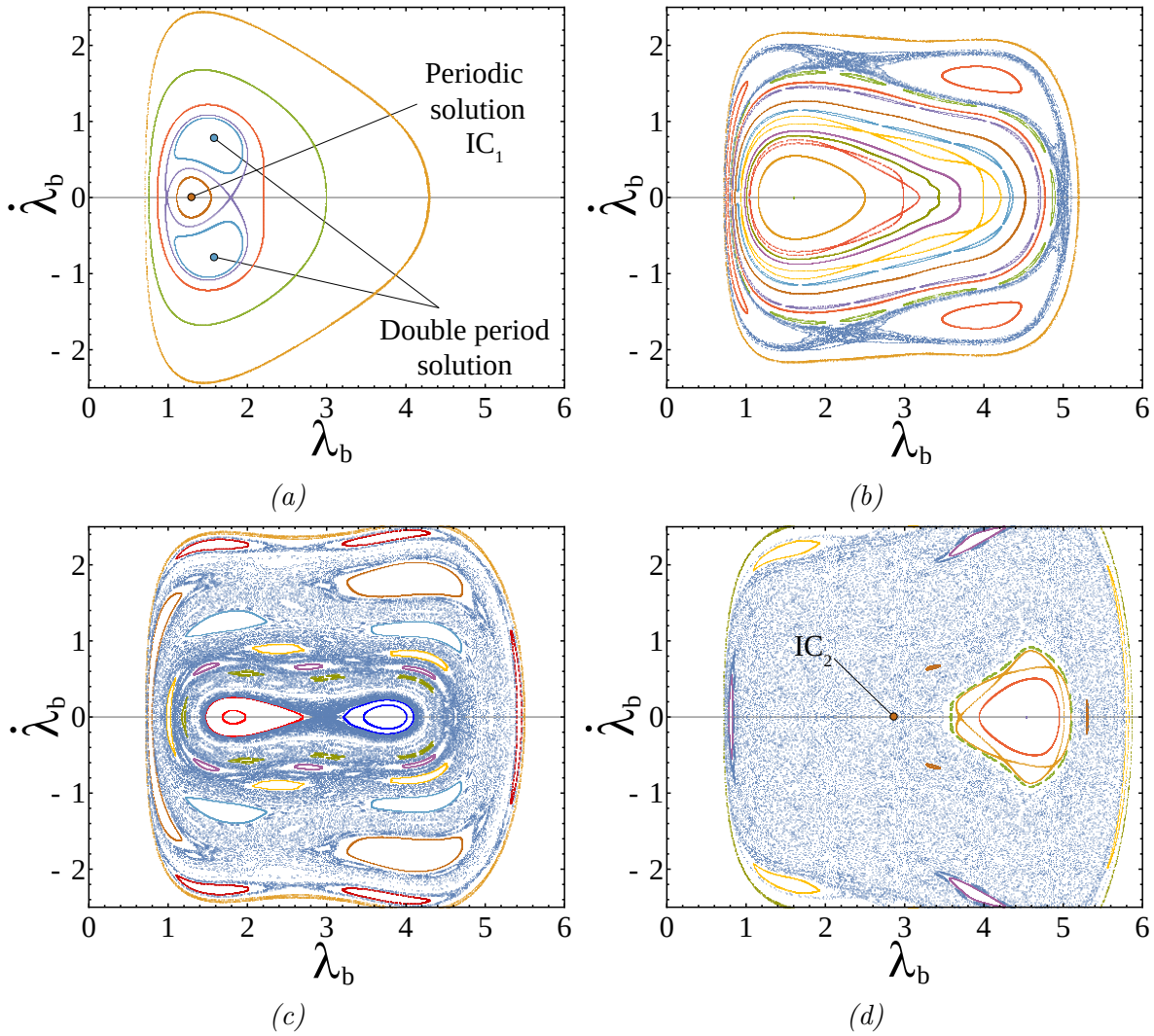

Fig. 3.7 Poincaré maps for the Yeoh model with different values of the applied pressure $\overline{P}$. *(a)* $\overline{P} = 0.22$, *(b)* $\overline{P} = 0.26$, *(c)* $\overline{P} = 0.268$, *(d)* $\overline{P} = 0.29$. $f_0 = 0.5$ *and* $\overline{\omega} = 1$.

3.4.1 Lyapunov exponents

One of the main indicators of chaotic behavior is the sensitive dependence on initial conditions. The **Lyapunov exponent (LE)** provide a quantitative measurement to characterize the separation in time of two orbits, starting from arbitrary close initial points. A positive Lyapunov exponent is usually interpreted as an indicator of chaotic behavior (provided some other conditions are met; *e.g.*, phase space compactness). While

a rigorous derivation of the Lyapunov exponent can be found elsewhere (Lynch, 2007; Strogatz, 2014; Thompson and Stewart, 1986), the basic formulation is introduced in this section for completeness.

Consider a *fiducial* orbit "$\mathbf{x}_f$", and a second *test* orbit labeled "$\mathbf{x}_t$" that starts very close to the first one. Both orbits solve the equations of motion (3.33)

$$\frac{\mathrm{d}\mathbf{x}_f}{\mathrm{d}\tau} = \mathbf{G}(\mathbf{x}_f), \qquad \frac{\mathrm{d}\mathbf{x}_t}{\mathrm{d}\tau} = \mathbf{G}(\mathbf{x}_t), \tag{3.34}$$

where $\mathbf{x}(\tau) = (x(\tau), y(\tau), \theta(\tau))$. The distance between these two orbits at any time τ is $d(\tau) = \mathbf{x}_f(\tau) - \mathbf{x}_t(\tau)$ evolves in time according to

$$\dot{\mathbf{d}}(\tau) = \dot{\mathbf{x}}_f(\tau) - \dot{\mathbf{x}}_t(\tau) = \mathbf{G}(\mathbf{x}_f) - \mathbf{G}(\mathbf{x}_t). \tag{3.35}$$

Since both orbits are considered very close to each other, the following linear expansion can be performed

$$\mathbf{G}(\mathbf{x}_t) \approx \mathbf{G}(\mathbf{x}_f) + \left.\frac{\partial \mathbf{G}}{\partial \mathbf{x}}\right|_{\mathbf{x}_f} \mathbf{d}(\tau). \tag{3.36}$$

Substituting in Eq.(3.35)

$$\dot{\mathbf{d}}(\tau) = \left.\frac{\partial \mathbf{G}}{\partial \mathbf{x}}\right|_{\mathbf{x}_f} \mathbf{d}(\tau). \tag{3.37}$$

This ordinary differential equation has the following solution

$$\mathbf{d}(\tau) = d_0 \mathrm{e}^{\boldsymbol{\lambda}\tau}, \tag{3.38}$$

where $d_0 = |\mathbf{d}(0)|$ is the initial distance between the orbits and $\boldsymbol{\lambda} = \left.\frac{\partial \mathbf{G}}{\partial \mathbf{x}}\right|_{\mathbf{x}_f}$ is the so called locally exponential divergence rate, which can be written also as

$$\boldsymbol{\lambda} = \frac{1}{\tau} \ln\left(\frac{\mathbf{d}(\tau)}{d_0}\right). \tag{3.39}$$

Even regular orbits may present a transient behavior for small times that appears to be chaotic (but it is not). Furthermore, the initial distance between the *fiducial* and *test* orbits should be infinitesimal to ensure the validity of the linear approximation at any time. To account for these details, a formal definition of the **Lyapunov exponent** is completed taking the following limits

$$\boldsymbol{\lambda}_L = \lim_{\substack{d_0 \to 0 \\ \tau \to \infty}} \left[\frac{1}{\tau} \ln\left(\frac{\mathbf{d}(\tau)}{d_0}\right)\right]. \tag{3.40}$$

In a n-dimensional phase space there is a **spectrum of Lyapunov exponents**, one LE per dimension, indicating whether there is exponential separation in each dimension and the maximum of this set is the so-called maximal Lyapunov exponent or the **Lyapunov characteristic exponent (LCE)**. If even one of the LE is positive, the system is usually considered as chaotic. The conservation of the phase space volume in conservative systems (see Liouville theorem at, e.g., Lynch (2007); Strogatz (2014); Thompson and Stewart (1986)) implies that the sum of the Lyapunov exponents must be zero. Therefore, in regular motions (i.e., periodic and quasi-periodic orbits) all must be zero.

To numerically compute the LCE, we follow the *renormalization* scheme introduced by Benettin and collaborators (see the series of papers of Benettin et al. (1980a,b, 1976); Benettin and Strelcyn (1978)). While this method allows to compute the hole Lyapunov spectrum, in this section we implement a simplified version to compute only the LCE. The main steps of the procedure are described below.

Consider an initial condition $\mathbf{r}_0 = (x_0, y_0)$ for the system (3.33) that defines the *fiducial* orbit and a second *test* orbit $\mathbf{r}_{t0} = \mathbf{r}_0 + \mathbf{d}_0$, being the length of the distance vector $d_0 = \|\mathbf{d}_0\|$. After some time τ_r, the positions of both orbits are given by $\mathbf{r}_1 = (x(\tau_r), y(\tau_r))$ and $\mathbf{r}_{t1} = \mathbf{r}_1 + \mathbf{d}_1(\tau_r)$. At this point, the position of the *test* orbit is *renormalized* along the vector $\mathbf{d}_1(\tau_r)$ until the distance between both orbits is again d_0. The process is systematically repeated at integers multiples of τ_r. Fig.(3.8) presents a diagram of the method.

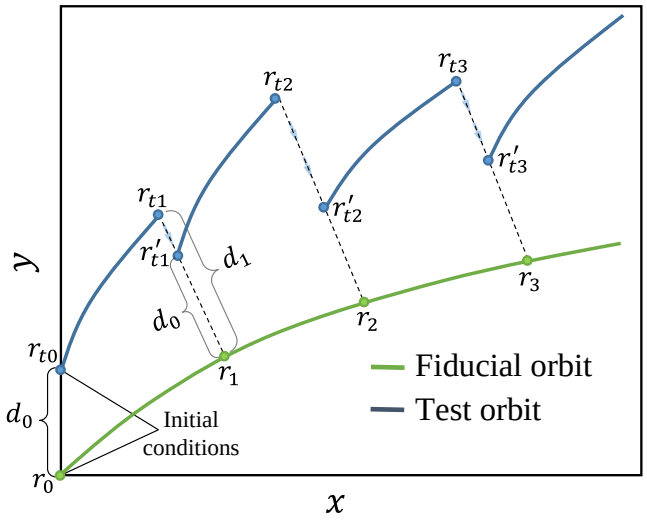

Fig. 3.8 Schematic representation of the Benettin and co-workers (Benettin et al., 1980a,b, 1976; Benettin and Strelcyn, 1978) renormalization scheme.

For each time $\tau = k\tau_r$ with $k = 1, 2, 3...$ the normalized position vector of the test orbit is computed as

$$\mathbf{r}'_{tk} = \mathbf{r}_k + \frac{d_0}{|\mathbf{d}_k(t)|}\mathbf{d}_k(t), \tag{3.41}$$

and the value of the Lyapunov exponent is given by

$$\lambda_k = \frac{1}{k\tau_r}\sum_{j=1}^{k} \ln\left(\frac{d_j}{d_0}\right). \tag{3.42}$$

The Lyapunov characteristic exponent (λ_{LCE}) is then computed as the limit of λ_k when $k \to \infty$.

Fig. (3.9) shows the Lyapunov exponents for (a) **periodic** orbit identified with initial conditions market as IC_1 in Fig. 3.7a and (b) **chaotic** orbit identified with initial conditions market as IC_2 in Fig. 3.7d. As anticipated before, the Lyapunov characteristic exponent of the periodic orbit IC_1 approaches zero as $k \to \infty$, while in the case of the chaotic orbit IC_2 we find an asymptote at $\lambda_{LCE} = 0.041 \pm 0.0003$, where the error has been computed as the typical deviation of the last 200 points. This makes clear that the motions we have identified as periodic, quasi-periodic and chaotic in the analysis of the Poincaré maps is correct.

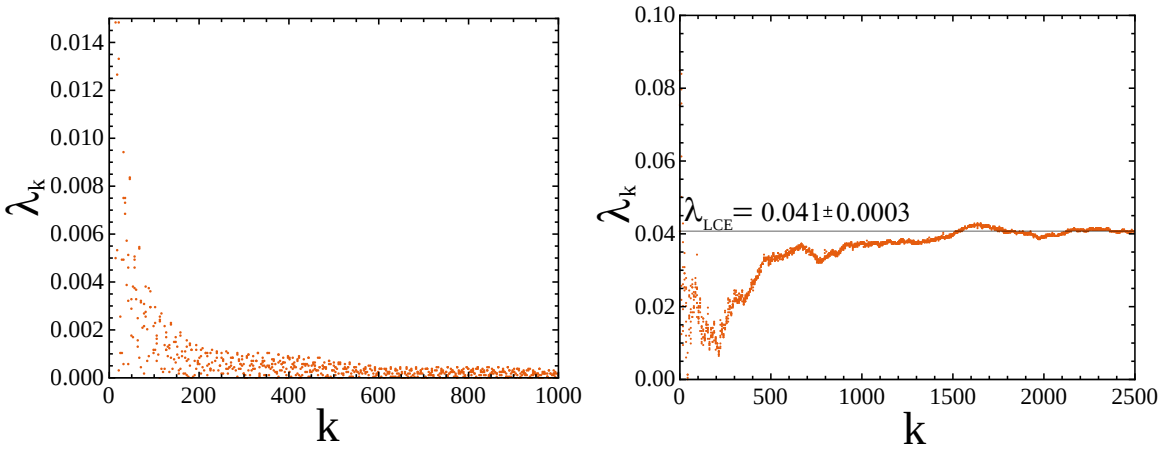

Fig. 3.9 Lyapunov exponents for (a) a periodic orbit identified with initial conditions market as IC_1 in Fig. 3.7a and (b) a chaotic orbit identified with initial conditions market as IC_2 in Fig. 3.7d.

3.5 Summary and conclusions

In this chapter we have analyzed the influence of the constitutive model on the dynamic response of isotropic incompressible hyperelastic cylindrical shells subjected to internal pressure. Two constitutive models calibrated with the same experimental data are used: Mooney-Rivlin and Yeoh. We considered autonomous and non-autonomous systems. In the autonomous case the pressure is defined by a Heaviside function and in the non-autonomous case by a harmonic function. The analysis has revealed the great sensitivity of the problem to the model used to describe the material behavior, namely:

- Autonomous system: the structure either shows periodic oscillatory motion or expands unbounded. The problem has a closed-form solution which allows to obtain the elastic strain energy, the potential energy and the kinetic energy of the system at any time. This, in turn, allows to determine analytically the limits in pressure for which the response of the structure is oscillatory. In the cases for which the cylinder oscillates, we have also obtained analytically the phase portraits and the period of the oscillations. The comparison between Mooney-Rivlin and Yeoh materials shows that the dynamic response of the structure (limits of the oscillatory motion, amplitude and period of the oscillations...) is strongly dependent on the constitutive model. For instance, while the Yeoh material predicts the oscillatory response of the structure no matter the value of the applied pressure, the Mooney-Rivlin material shows a bifurcation pressure above which the cylinder expands unbounded.

- Non-autonomous system: the structure either shows periodic, quasi-periodic or chaotic oscillatory motion, or expands unbounded. The temporal dependence of the applied pressure impedes to obtain a closed-form solution of the problem, which has to be solved numerically transforming the original non-autonomous problem of order 2 into an autonomous problem of order 3. The representation of this system in cylindrical polar coordinates highlight the toroidal structure of the solution. The intersection of the torus with planes for which the angular coordinate of the cylindrical system is constant allows to obtain the Poincaré maps, which illustrate the nature of the motion of the system as a function of the initial conditions of the problem. We have observed that, as the applied pressure increases, the motion of the cylinder goes from being periodic and quasi-periodic to being chaotic for most of the initial conditions explored. We have also shown that the transition

between the periodic, quasi-periodic and chaotic responses is strongly dependent on the constitutive model.

4 Incompressible isotropic hyperelastic spherical structures

Nonlinear resonances in idealized aneurysmal lesions

This chapter investigates the non-linear dynamics of thick-walled spherical structures. Specifically, the formulation is adapted to analyze the occurrence of dynamic instabilities in idealized intracranial saccular aneurysms subjected to pulsatile blood flow and surrounded by cerebral spinal fluid. The problem has been approached extending the original 2D model of Shah and Humphrey (1999) to a 3D framework. The justification for using a 3D formulation arises from the works of Suzuki and Ohara (1978), MacDonald et al. (2000) and Costalat et al. (2011), who showed experimental evidences of intracranial aneurysms with a ratio between wall thickness and inner radius larger that 0.1. Two different material models have been used to describe the mechanical behavior of the aneurysm wall: Neo-Hookean and Mooney-Rivlin. For the first time in literature the dynamic response of the aneurysm has been analyzed using complete nonlinear resonance diagrams that have been obtained from a numerical procedure specifically designed for that purpose. Our numerical results show that, for a wide range of wall thicknesses and both constitutive models considered, the saccular aneurysms are dynamically stable within the range of frequencies associated to the normal heart rates, which confirms previous results of Shah and Humphrey (1999). On the other hand, our results also show that the geometric and material nonlinearities of the problem could bring closer than expected the resonance frequencies of the aneurysm to the frequencies of the pulsatile blood flow.

4.1 Introduction

The question of whether mechanical instabilities, both static and dynamic, may cause the enlargement and rupture of saccular aneurysms has been debated by the scientific community during the last 40 years. Several researchers, such as Akkas (1990) and

Austin et al. (1989), pointed out that the existence of limit point instabilities (i.e., mathematical bifurcations in the quasi-static response of the aneurysm) could be a reason for the growth and rupture of this type of lesions. Alternatively, other authors like Jain (1963), Sekhar and Heros (1981) and Sekhar et al. (1988) suggested that the pulsatile blood flow could excite the natural frequency of the aneurysm making it dynamically unstable. This hypothesis was supported by the results of Simkins and Stehbens (1973) and nan Hung and Botwin (1975), who studied the elastodynamics of berry aneurysms and showed that the natural frequency of these type of lesions may lie within the range of bruit frequencies that commonly accompany aneurysms. However, despite the nonlinear stress-strain response exhibited by the aneurysm wall over finite strains, these authors used the classical shell membrane theory in their analysis, which assumes infinitesimal strains and linear material behavior. Furthermore, they ignored the contribution of the Cerebral Spinal Fluid (CSF) surrounding the lesion. Thus, the idea that resonances may cause the rupture of intracranial aneurysms has been gradually losing support within the scientific community.

Shah and Humphrey (1999) and David and Humphrey (2003) studied the nonlinear elastodynamics of a sub-class of spherical aneurysms subjected to pulsatile blood pressure and surrounded by CSF. The aneurysm wall was modeled using a Fung-type pseudostrain-energy function (Fung, 1993), which included strain rate dependence. These works brought to light that both surrounding fluid and material viscosity help to increase the dynamic stability of the aneurysm. Shortly after, Haslach and Humphrey (2004) provided further insights into the effect of the mechanical behavior of the aneurysm wall on the dynamic response of the lesion. Through the comparison of various strain energy functions, the authors pointed out the great sensitivity of the dynamic behavior of the aneurysm to the constitutive model used to describe the aneurysm wall. In particular, they stressed the fact that it is essential for the (correct) analysis of the dynamic stability of aneurysms to use constitutive models specifically formulated and calibrated for the aneurysm wall. It was shown that the opposite may give rise to misleading results which predict dynamic instabilities that are not present in actual tissue.

In this research we revisit the works of Humphrey and co-workers (David and Humphrey, 2003; Haslach and Humphrey, 2004; Shah and Humphrey, 1999) and extend their 2D elastodynamics model to a 3D framework [1] in order to study the dynamic response of idealized saccular aneurysms. Many aneurysms show small wall thicknesses, hence, they can be modeled relying on membrane hypothesis. However, in several works such as Suzuki and Ohara (1978), MacDonald et al. (2000) and Costalat et al. (2011) the

[1] For which we have followed the pioneering work of Knowles (1962)

authors obtained experimental evidences of intracranial aneurysms with a ratio between wall thickness and inner radius larger that 0.1. This leads to non-negligible radial stresses through the aneurysm wall and therefore a 3D formulation is needed. Another original feature of our research is that we have obtained, for the first time in literature, the complete nonlinear resonance diagrams that characterize the dynamic response of an aneurysm as a function of the pulsatile blood flow. A Mooney-Rivlin type constitutive model, calibrated by Costalat et al. (2011) using experimental data obtained from 16 different intracranial aneurysms tested under physiological conditions, has been used to describe the mechanical behavior of the aneurysm wall. The results are systematically compared with those obtained from a simple Neo-Hookean model widely applied to characterize the behavior of rubber-like materials. This research reveals that, for any of the constitutive models used and irrespective of the thickness of the aneurysm wall, the resonance frequencies of the aneurysm do not lie within the range of frequencies associated to the normal heart rates, which in turn seems to confirm the earlier findings of Shah and Humphrey (1999).

4.2 Problem formulation

In this section we formulate the problem of an idealized intracranial saccular (spherical) aneurysm surrounded by CSF and subjected to pulsating, and radially symmetric, blood pressure (see Fig. 4.1). The original contribution is to extend the 2D formulation developed by Humphrey and co-workers (David and Humphrey, 2003; Shah and Humphrey, 1999) to a 3D framework. The formulation is similar to that presented in Chapter 3, adapted in this case to a spherical geometry and incorporating an external fluid.

Recall from Chapter 2 that the current position vector $\mathbf{x}$ in the deformed configuration $\Omega \subset \mathbb{R}^3$ at time t of the material point that occupies the location $\mathbf{X} \in \Omega_0$ is given by $\mathbf{x} = \boldsymbol{\chi}(\mathbf{X}, t)$, where $\boldsymbol{\chi}$ is a bijective and twice continuously differentiable mapping. The associated deformation gradient, right Cauchy-Green strain tensor and volume ratio at $\mathbf{X} \in \Omega_0$ are denoted by

$$\begin{gathered} \mathbf{F}(\mathbf{X}, t) = \operatorname{Grad} \boldsymbol{\chi}(\mathbf{X}, t), \ \mathbf{C}(\mathbf{X}, t) = \mathbf{F}^{\mathrm{T}}(\mathbf{X}, t)\mathbf{F}(\mathbf{X}, t), \\ J(\mathbf{X}, t) = \det \mathbf{F}(\mathbf{X}, t). \end{gathered} \tag{4.1}$$

Moreover, the balance of linear momentum in the material description requires that

$$\operatorname{Div} \mathbf{S}(\mathbf{X}, t) = \rho_0 \ddot{\boldsymbol{\chi}}(\mathbf{X}, t) \quad \text{in} \quad \Omega_0, \tag{4.2}$$

where the dots denote differentiation with respect to time, **S** stands for the first Piola-Kirchhoff stress tensor, and ρ_0 is the constant mass density of the shell material in its undeformed configuration Ω_0.

4.2.1 The aneurysm wall

Following Shah and Humphrey (1999), the aneurysm wall is taken to be incompressible and isotropic within the framework of finite nonlinear elasticity. While the hypothesis of homogeneous and isotropic properties is likely a gross approximation (Ryan and Humphrey, 1999), it allows us to follow Humphrey and Haslach (2003) and therefore study the elastodynamics of the aneurysmal lesion. The aneurysm occupies a volume Ω_0 defined by the spherical polar coordinates (R, Θ, Φ) in some reference configuration such that $A \leq R \leq B$. In this case, we have taken $A = 4.3\ mm$ and $B = 4.67\ mm$ which, based on the work of Costalat et al. (2011), represent average values for the inner and outer radii of intracranial aneurysmal lesions.

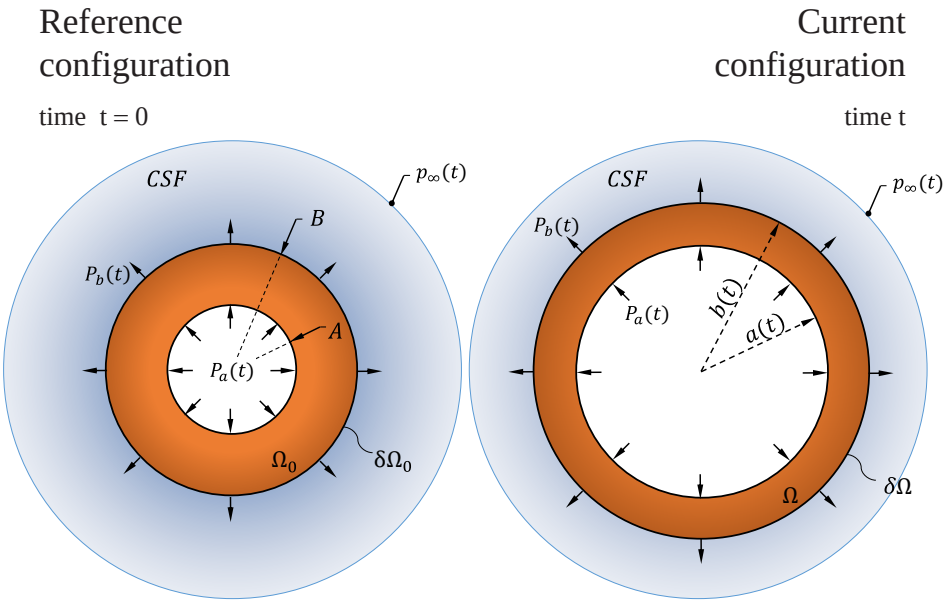

Fig. 4.1 Schematic representation of an idealized saccular (spherical) aneurysm surrounded by cerebral spinal fluid and subjected to radially symmetric pulsating blood pressure. (a) reference and (b) deformed configurations.

Since the material is deformed so that the spherical symmetry is maintained, the motion is given by

$$r = r(R, t), \qquad \theta = \Theta, \qquad \phi = \Phi, \tag{4.3}$$

where (r, θ, ϕ) are spherical polar coordinates in the current configuration Ω such that $a(t) \leq r(R,t) \leq b(t)$. Under this conditions the deformation gradient assumes the following form

$$\mathbf{F} = \frac{1}{\lambda^2(R,t)}\, \mathbf{e}_r \otimes \mathbf{e}_r + \lambda(R,t)\, \mathbf{e}_\theta \otimes \mathbf{e}_\theta + \lambda(R,t)\, \mathbf{e}_\phi \otimes \mathbf{e}_\phi, \tag{4.4}$$

where the principal stretches corresponding to the directions r, θ, ϕ are given by

$$\lambda_r(R,t) = \frac{\partial r(R,t)}{\partial R}, \qquad \lambda(R,t) = \frac{r(R,t)}{R} = \lambda_\theta(R,t) = \lambda_\phi(R,t), \tag{4.5}$$

and the incompressibility restriction $J = \lambda_r(R,t)\lambda^2(R,t) = 1$ has been used. Similarly, the first Piola-Kirchhoff stress tensor can be proved to be of the spectral form

$$\mathbf{S} = S_r(R,t)\, \mathbf{e}_r \otimes \mathbf{e}_r + S_\theta(R,t)\, \mathbf{e}_\theta \otimes \mathbf{e}_\theta + S_\theta(R,t)\mathbf{e}_\phi \otimes \mathbf{e}_\phi. \tag{4.6}$$

Hence, the balance of linear momentum presented in Eq. 4.2 reduces to

$$\frac{\partial S_r(R,t)}{\partial R} + 2\frac{S_r(R,t) - S_\theta(R,t)}{R} = \rho_0 \ddot{r}(R,t), \tag{4.7}$$

where a superposed dot denotes differentiation with respect to time and $\rho_0 = 1050\ \mathrm{kg/m^3}$ is the reference density of the aneurysm wall (Shah and Humphrey, 1999). Moreover, it follows from the incompressibility condition that

$$\lambda(R,t) = \left(\frac{B^3}{R^3}(\lambda_b^3(t) - 1) + 1\right)^{1/3}, \tag{4.8}$$

where $\lambda_b(t) = \frac{b(t)}{B}$ stands for the circumferential stretch in the outer surface of the aneurysm wall[2]. We take the derivatives of Eq. (4.8) with respect to R and t to obtain respectively

$$\frac{\partial \lambda}{\partial R} = -\frac{\lambda^3 - 1}{R\lambda^2}, \tag{4.9}$$

$$\ddot{\lambda} = \frac{\lambda^3 - 1}{\lambda_b^3 - 1}\left(\frac{2\lambda_b \dot{\lambda_b}^2 + \lambda_b^2 \ddot{\lambda_b}}{\lambda^2} - \frac{2\,\lambda_b^4 \dot{\lambda_b}^2}{\lambda_b^3 - 1}\frac{\lambda^3 - 1}{\lambda^5}\right), \tag{4.10}$$

[2]The function (4.8) can be alternatively written as $\lambda(R,t) = \left(\frac{A^3}{R^3}(\lambda_a^3(t) - 1) + 1\right)^{1/3}$ in terms of the stretch in the inner face $\lambda_a(t) = a(t)/A$. For our purposes here, we find dealing with the form (4.8) in terms of the outer stretch $\lambda_b(t)$ more convenient.

where **function arguments are omitted** here and in most of the subsequent development to ease notation. At this stage, it proves convenient to rewrite the equation of motion (4.7) with $\lambda(R,t)$ as the independent space variable instead of R. The result reads as

$$-\frac{\partial}{\partial\lambda}\left[\frac{S_r}{\lambda^2}\right]=\frac{2\left(S_\theta-\dfrac{S_r}{\lambda^3}\right)}{\lambda^3-1}+\frac{\rho_0 B^2}{(\lambda_b^3-1)^{1/3}(\lambda^3-1)^{2/3}}\left[\frac{2\lambda_b^4-2\lambda_b\lambda^3}{\lambda^5(\lambda_b^3-1)}\dot{\lambda}_b^2+\frac{\lambda_b^2}{\lambda^2}\ddot{\lambda}_b\right]. \quad (4.11)$$

Assuming now that the inner boundary ($R=A$) is subjected to a pressure $P_a(t)$ per unit of current area due to the blood flow. While the outer face ($R=B$) is subjected to a pressure $P_b(t)$ due to the CSF (see Fig. 3.1), the boundary conditions are given by

$$S_r(A,t)=P_a(t)\lambda_a^2(t) \quad \text{and} \quad S_r(B,t)=P_b(t)\lambda_b^2(t). \quad (4.12)$$

Furthermore, for an incompressible spherical shell it can be proved that (see, e.g., Ogden (1997), p. 284)

$$S_\theta(R,t)-\frac{S_r(R,t)}{\lambda^3(R,t)}=\frac{1}{2}W'\left(\lambda(R,t)\right). \quad (4.13)$$

Here the function $W(\lambda)$ is defined as

$$W(\lambda)=\psi(I_1,I_2), \quad (4.14)$$

where ψ is the strain energy function that determines the mechanical behavior of the material. The specific form of ψ will be defined in Section 4.2.5.

With help of (4.13), Eq. (4.7) can be integrated over the thickness of the aneurysm to obtain

$$\begin{aligned}P_a-P_b=\int_{\lambda_b}^{\left(\frac{\lambda_b^3+f_0-1}{f_0}\right)^{1/3}}\frac{W'}{\lambda^3-1}\,d\lambda-\rho B^2\left(1-\frac{\lambda_b}{(\lambda_b^3+f_0-1)^{1/3}}\right)\lambda_b\ddot{\lambda}_b-\\ \rho B^2\left(\frac{3}{2}+\frac{\lambda_b^4}{2(\lambda_b^3+f_0-1)^{4/3}}-\frac{2\lambda_b}{(\lambda_b^3+f_0-1)^{1/3}}\right)\dot{\lambda}_b^{\,2},\end{aligned} \quad (4.15)$$

where the superscript prime denotes differentiation with respect to the circumferential stretch and $f_0=\frac{A^3}{B^3}=0.78$ is a dimensionless parameter that characterizes the thickness of the aneurysm wall, as in Chapter 3. The specific forms of $P_a(t)$ and $P_b(t)$ are provided in sections 4.2.2 and 4.2.3.

4.2.2 Blood pressure

Based on the data measured by Ferguson (1972) for human saccular aneurysms, and assuming a uniform pressure inside the lesion, the blood pressure is represented by the following Fourier series

$$P_a(t) = P_m + \sum_{n=1}^{N} \left(A_n \cos(n\omega t) + B_n \sin(n\omega t) \right), \tag{4.16}$$

where $P_m = 67.5$ mmHg is the mean pressure (Shah and Humphrey, 1999), A_n and B_n are the Fourier coefficients for N harmonics, and ω is the fundamental circular frequency. Following Shah and Humphrey (1999) we have considered 5 harmonics: $A_1 = -7.13$, $B_1 = 4.64$, $A_2 = -3.08$, $B_2 = -1.18$, $A_3 = -0.130$, $B_3 = -0.564$, $A_4 = -0.205$, $B_4 = -0.346$, $A_5 = 0.0662$ and $B_5 = -0.120$; all quantities are given in mmHg.

4.2.3 Cerebral spinal fluid

The CSF is assumed incompressible and Newtonian. The continuity equation takes the form

$$\frac{1}{r^2}\frac{\partial}{\partial r}(r^2\, v_r) = 0. \tag{4.17}$$

The previous expression implies that the radial velocity is of the form $v_r(r,t) = \frac{c(t)}{r^2}$, where the function $c(t)$ is found by matching the fluid and aneurysm wall velocities at $r = b$. Therefore, we obtain the following expression that relates the radial velocity of the CSF and the stretch (and stretch rate) in the outer surface of the aneurysm

$$v_r(r,t) = \frac{B^3 \lambda_b^2 \dot{\lambda}_b}{r^2}. \tag{4.18}$$

Moreover, the balance of linear momentum along the radial direction takes the form

$$\rho_f \left(\frac{\partial v_r}{\partial t} + v_r \frac{\partial v_r}{\partial r} \right) = -\frac{\partial p}{\partial r} + \mu \left(\frac{1}{r^2}\frac{\partial}{\partial r}\left(r^2 \frac{\partial v_r}{\partial r} \right) - 2\frac{v_r}{r^2} \right), \tag{4.19}$$

where p denotes pressure. Moreover, $\rho_f = 1000$ kg/m^3 and $\mu = 1.26 \cdot 10^{-4}$ Ns/m^2 are the density and the viscosity of the CSF, respectively (Shah and Humphrey, 1999). Next, we insert Eq. (4.18) into Eq. (4.19) to obtain

$$\frac{\partial p}{\partial r} = -\rho_f \left(\frac{B^3}{r^2} \left(\lambda_b^2 \ddot{\lambda}_b + 2\lambda_b \dot{\lambda}_b^2 \right) - \frac{2B^6 \lambda_b^4}{r^5} \dot{\lambda}_b^2 \right). \tag{4.20}$$

Integrating the previous equation over the range $r \in (b, \infty)$, we obtain an expression for the **static** pressure exerted by the CSF on the outer surface of the aneurysm (p_b^s)

$$p_b^s(t) = p_\infty + \rho_f B^2 \left(\lambda_b \ddot{\lambda}_b + \frac{3}{2}\dot{\lambda}_b^2\right), \tag{4.21}$$

where $p_\infty = 3$ mmHg is the remote pressure assumed constant (Shah and Humphrey, 1999). Moreover, relying on the constitutive equations of incompressible Newtonian fluids, we compute the **dynamic** pressure (radial stress) caused by the deformation of the CSF on the aneurysm wall (p_b^d)

$$p_b^d(t) = 4\mu \frac{\dot{\lambda}_b}{\lambda_b}. \tag{4.22}$$

Therefore, the total pressure exerted by the cerebral spinal fluid on the outer surface of the aneurysm is

$$P_b(t) = -p_b^s(t) - p_b^d(t). \tag{4.23}$$

4.2.4 Dimensionless governing equation

As in Chapter 3, the following length, mass and time scales are introduced in order to pose the problem in non-dimensional form

$$[L] = B, \qquad [M] = \rho B^3, \qquad [T] = \sqrt{\frac{\rho B^2}{C_{\text{M10}}}}, \tag{4.24}$$

where C_{M10} is a material constant as will be further discussed in Section 4.2.5. Previous non-dimensional groups, together with equations (4.16) and (4.23), are inserted into Eq. (4.15) to obtain the following dimensionless governing equation, where $\lambda_b(\tau)$ is the only unknown of the problem

$$\begin{aligned}\Delta\overline{P} = \int_{\lambda_b}^{\left(\frac{\lambda_b^3+f_0-1}{f_0}\right)^{1/3}} \frac{\overline{W}'}{\lambda^3-1}\, d\lambda + 4\kappa\frac{\dot{\lambda}_b}{\lambda_b} + \overline{\rho}\left(\lambda_b\ddot{\lambda}_b + \frac{3}{2}\dot{\lambda}_b^2\right) \\ - \left(\left(1 - \frac{\lambda_b}{(\lambda_b^3+f_0-1)^{1/3}}\right)\lambda_b\ddot{\lambda}_b + \left(\frac{3}{2} + \frac{\lambda_b^4}{2(\lambda_b^3+f_0-1)^{4/3}} - \frac{2\lambda_b}{(\lambda_b^3+f_0-1)^{1/3}}\right)\dot{\lambda_b}^2\right),\end{aligned} \tag{4.25}$$

where

$$\Delta\overline{P} = \overline{P}_m + \sum_{n=1}^{N}\left(\overline{A}_n\cos(n\tau\overline{\omega}) + \overline{B}_n\sin(n\tau\overline{\omega})\right) - \overline{p}_\infty. \tag{4.26}$$

In this case a superposed dot denotes differentiation with respect to the dimensionless time τ. Note that when $f_0 \to 1$ we recover Eq. (12) of Shah and Humphrey (1999). The adimensionalization procedure brings to light 8 additional non-dimensional groups (additional to f_0 introduced in Eq. (4.15)) that govern the problem at hand

$$\begin{aligned}
&\overline{W} = \frac{W}{C_{\mathrm{M10}}}, && \overline{P}_m = \frac{P_m}{C_{\mathrm{M10}}}, && \overline{p}_\infty = \frac{p_\infty}{C_{\mathrm{M10}}},\\
&\overline{A}_i = \frac{A_i}{C_{\mathrm{M10}}}, && \overline{B}_i = \frac{B_i}{C_{\mathrm{M10}}}, && \text{for} \quad i = 1,2,3,4,5.\\
&\overline{\omega} = \omega\sqrt{\frac{\rho B^2}{C_{\mathrm{M10}}}}, && \kappa = \frac{\mu}{B\sqrt{\rho\, C_{\mathrm{M10}}}}, && \overline{\rho} = \frac{\rho_f}{\rho},
\end{aligned}$$

where $\overline{W}$ is the non-dimensional strain energy function, $\overline{P}_m$ is the dimensionless mean pressure applied in the inner surface of the aneurysm, $\overline{p}_\infty$ is the dimensionless remote pressure, and $\overline{A}_i$ and $\overline{B}_i$ are the dimensionless harmonics coefficients. Moreover, $\overline{\omega}$ is the dimensionless fundamental frequency, which was already used in Chapter 3, κ defines the ratio between the characteristic time scales of CSF and aneurysm wall and $\overline{\rho}$ is the ratio between CSF and aneurysm wall densities. Note that in Section 4.4 we will systematically vary $\overline{\omega}$ in order to obtain the resonance diagrams of the aneurysm.

4.2.5 Constitutive model

Two different strain energy functions are used to describe the mechanical behavior of the aneurysm wall. They both respond to the following polynomial form

$$\psi = \sum_{i,j=0}^{N} C_{ij}(I_1 - 3)^i (I_2 - 3)^j, \tag{4.27}$$

where C_{ij} are empirically determined material parameters and I_1, I_2 are the first and second invariants of the right Cauchy-Green strain tensor, respectively. Namely, we use the so-called Neo-Hookean and 3-parameters Mooney-Rivlin models.

- Neo-Hookean model

$$\psi = C_{\mathrm{N10}}(I_1 - 3). \tag{4.28}$$

- 3-parameters Mooney-Rivlin model

$$\psi = C_{\mathrm{M10}}(I_1 - 3) + C_{\mathrm{M01}}(I_2 - 3) + C_{\mathrm{M11}}(I_1 - 3)(I_2 - 3). \tag{4.29}$$

Recall that the strain energy function $W(\lambda)$ used in previous sections is defined as $W(\lambda) = \psi(I_1, I_2)$. The 3-parameter Mooney-Rivlin model was calibrated by Costalat et al. (2011) using experimental results obtained from 16 intracranial saccular aneurysms tested in uniaxial tension under physiological conditions. The resulting parameters values are: $C_{\mathrm{M10}} = 0.19$ MPa, $C_{\mathrm{M01}} = 0.024$ MPa and $C_{\mathrm{M11}} = 7.87$ MPa. For the Neo-Hookean model we have taken $C_{\mathrm{N10}} = 0.214$ MPa, which ensures that Neo-Hookean and Mooney-Rivlin models provide the same shear modulus in the linear limit. While both constitutive models were originally formulated for rubber-like materials, they have been widely used in the literature to model the mechanical behavior of aneurysms (Costalat et al., 2011; Gundiah et al., 2007; Tóth et al., 2005). The comparison between Neo-Hookean and Mooney-Rivlin models that will be developed in Section 4.4 will bring to light the key role played by the mechanical behavior of the aneurysm wall in the dynamic response of the aneurysm.

4.3 Numerical solution

In this section we describe the numerical procedure designed to analyze the dynamic response of the aneurysm. The numerical scheme relies on two main techniques: the *shooting method* and the *sequential continuation method*. The combination of these two techniques allows to obtain the resonance diagrams of the aneurysmal lesion that will be presented in Section 4.4.

Following the same procedure presented in Chapter 3, let us reduce Eq. (4.25) to the following system of two first-order differential equations where $z_1 = \lambda_b$ and $z_2 = \dot{\lambda}_b$.

$$\dot{z_1} = z_2, \tag{4.30}$$

$$\dot{z_2} = \frac{\Delta\overline{P} - \int_{z_1}^{\left(\frac{z_1^3+f_0-1}{f_0}\right)^{1/3}} \frac{\overline{W}'(\lambda)}{\lambda^3-1}\, d\lambda - 4\kappa\frac{z_2}{z_1} + \left(\frac{3}{2} + \frac{z_1^4}{2(z_1^3+f_0-1)^{4/3}} - \frac{2z_1}{(z_1^3+f_0-1)^{1/3}} - \frac{3}{2}\overline{\rho}\right) z_2^2}{\left(\overline{\rho} + \frac{z_1}{(z_1^3+f_o-1)^{1/3}} - 1\right) z_1}. \tag{4.31}$$

The harmonically forced system described by equations (4.30)-(4.31) is transformed into an autonomous system adding the following two differential equations whose stable solutions are the non-autonomous terms

$$\dot{z_3} = z_3(1 - z_3^2 - z_4^2) - \overline{w} z_4, \tag{4.32}$$

$$\dot{z_4} = z_4(1 - z_3^2 - z_4^2) + \overline{w} z_3. \tag{4.33}$$

Taking as initial conditions $z_3(0) = 1$ and $z_4(0) = 0$, the solutions of these equations are $z_3(\tau) = \sin(\overline{w}\tau)$ and $z_4(\tau) = \cos(\overline{w}\tau)$, respectively. Expanding[3] Eq. (4.16) in terms of $\sin(\overline{w}\tau)$ and $\cos(\overline{w}\tau)$, the problem can be handled as an autonomous system of dimension $n = 4$ that has the following vectorial form

$$\frac{\mathrm{d}\mathbf{z}}{\mathrm{d}\tau} = \mathbf{G}(\mathbf{z}), \tag{4.34}$$

where $\mathbf{z} = (z_1, z_2, z_3, z_4)^{\mathrm{T}}$. Since our attention is restricted to the periodic response of the aneurysm (resonances), the solutions of interest satisfy the condition $\mathbf{z}(\tau) = \mathbf{z}(\tau + T)$ where T is the period of the oscillation. This allows to formulate the following two-point boundary value problem

$$\frac{\mathrm{d}\mathbf{z}}{\mathrm{d}\tau} = \mathbf{G}(\mathbf{z}), \qquad \mathbf{z}(0) = \mathbf{z}_0, \quad \mathbf{z}(T) = \mathbf{z}_0, \tag{4.35}$$

where $\mathbf{z}_0$ is a vector containing the initial conditions. Note that $\mathbf{z}_0$ and T are, *a priori*, unknown.

4.3.1 Shooting method

The problem defined by (4.35) is solved using the *shooting method* (Allgower and Georg, 2011; Peeters et al., 2009; Seydel, 2009). For that purpose, we define the periodicity condition

$$\mathbf{H}(\mathbf{z}_0, T) \equiv \mathbf{z}(\mathbf{z}_0, T) - \mathbf{z}_0 = 0, \tag{4.36}$$

where $\mathbf{H}(\mathbf{z}_0, T)$ is the so-called *shooting function*. Note that the solution at time T is now expressed as $\mathbf{z}(\mathbf{z}_0, T)$ in order to highlight the dependence of the problem solution with the initial conditions $\mathbf{z}_0$.

The shooting technique starts with a trial value for $(\mathbf{z}_0, T)$. The solution of the system is then obtained by numerical integration of the system of equations (4.30)-(4.33). In general, the trial value will not satisfy the periodicity condition given by Eq. (4.36). Therefore, a Newton-Raphson iteration scheme is used to correct the initial trial and converge to the actual solution. The corrections $(\Delta\mathbf{z}_0, \Delta T)$ are obtained from the

[3] The trigonometric expansion is given by $\sin(n\alpha) = \sum_{k=0}^{n} \binom{n}{k} \cos^k \alpha \, \sin^{n-k} \alpha \, \sin(1/2(n-k)\pi)$ and $\cos(n\alpha) = \sum_{k=0}^{n} \binom{n}{k} \cos^k \alpha \, \sin^{n-k} \alpha \, \cos(1/2(n-k)\pi)$

following linear expansion of the periodicity condition

$$\mathbf{H}(\mathbf{z}_0+\Delta\mathbf{z}_0, T+\Delta T) \approx \mathbf{H}(\mathbf{z}_0, T) + \left.\frac{\partial \mathbf{H}}{\partial \mathbf{z}_0}\right|_{(\mathbf{z}_0,T)} \Delta\mathbf{z}_0 + \left.\frac{\partial \mathbf{H}}{\partial T}\right|_{(\mathbf{z}_0,T)} \Delta T + \text{H.O.T} = 0, \quad (4.37)$$

where the coefficients of previous linear system ($\partial\mathbf{H}/\partial T$, $\partial\mathbf{H}/\partial\mathbf{z}_0$) have to be calculated. From Eq. (4.36) it follows that the $n \times 1$ coefficient vector $\partial\mathbf{H}/\partial T$ is given by

$$\frac{\partial \mathbf{H}}{\partial T}(\mathbf{z}_0, T) = \left.\frac{\partial \mathbf{z}(\tau, \mathbf{z}_0)}{\partial \tau}\right|_T = \mathbf{G}(\mathbf{z}_0). \quad (4.38)$$

Also from Eq. (4.36) it follows that the $n \times n$ Jacobian matrix $\partial\mathbf{H}/\partial\mathbf{z}_0$ is

$$\frac{\partial \mathbf{H}}{\partial \mathbf{z}_0}(\mathbf{z}_0, T) = \left.\frac{\partial \mathbf{z}(\tau, \mathbf{z}_0)}{\partial \mathbf{z}_0}\right|_T - \mathbf{I}, \quad (4.39)$$

where $\mathbf{I}$ is the $n \times n$ identity matrix. The matrix $\partial\mathbf{z}(\tau, \mathbf{z}_0)/\partial\mathbf{z}_0$ is calculated as described by Peeters et al. (2009). For that, we differentiate the system of equations (4.30)-(4.33) with respect to the initial conditions

$$\frac{\partial}{\partial \mathbf{z}_0}\left(\frac{\mathrm{d}\mathbf{z}(\tau, \mathbf{z}_0)}{\mathrm{d}\tau}\right) = \frac{\partial \mathbf{G}(\mathbf{z}(\tau, \mathbf{z}_0))}{\partial \mathbf{z}_0}. \quad (4.40)$$

Changing the order of the derivatives in the left hand side of the previous equation and applying the chain rule in the right hand side it yields

$$\frac{\mathrm{d}}{\mathrm{d}\tau}\left(\frac{\partial \mathbf{z}(\tau, \mathbf{z}_0)}{\partial \mathbf{z}_0}\right) = \frac{\partial \mathbf{G}(\mathbf{z})}{\partial \mathbf{z}} \frac{\partial \mathbf{z}(\tau, \mathbf{z}_0)}{\partial \mathbf{z}_0}, \quad (4.41)$$

with initial conditions $\partial\mathbf{z}(0, \mathbf{z}_0)/\partial\mathbf{z}_0 = \mathbf{I}$. The matrix $\partial\mathbf{z}(\tau, \mathbf{z}_0)/\partial\mathbf{z}_0$ for $\tau = T$ can be then computed integrating numerically previous expression.

In order to determine the $n+1$ corrections $(\Delta\mathbf{z}_0, \Delta T)$ we need an additional equation to be added to the system of n equations defined by (4.37). The additional equation is obtained following Seydel (2009). For an autonomous system the periodic solutions are invariant to linear shifts of the time origin, which implies that the phase of the solution is arbitrary. Hence, a restriction (often referred to as the *phase condition*) must be imposed to remove this arbitrariness. For this task, we set one component of the initial values vector $\mathbf{z}_0$ equal to zero. In the problem at hand, it is especially suited to take $z_2 = 0$ since this amounts to consider that the stretch rate of the outer surface of the aneurysm is initially zero (system initially at rest).

We carry out this iteration process to obtain $\mathbf{z}(\mathbf{z}_0, T)$ until the following convergence condition, taken from Peeters et al. (2009) and Sracic and Allen (2011), is reached

$$\frac{||\mathbf{H}(\mathbf{z}_0, T)||}{||\mathbf{z}_0||} < \varepsilon, \tag{4.42}$$

where $\varepsilon = 10^{-6}$ is the tolerance.

4.3.2 Sequential continuation

Once a solution $\mathbf{z}^{\mathrm{j}}(\mathbf{z}_0^{\mathrm{j}}, T^{\mathrm{j}})$ is found for the normalized frequency $\overline{\omega}^{\mathrm{j}}$, this input parameter is incremented by $\Delta\overline{\omega}^{\mathrm{j}}$

$$\overline{\omega}^{\mathrm{j}+1} = \overline{\omega}^{\mathrm{j}} + \Delta\overline{\omega}^{\mathrm{j}}. \tag{4.43}$$

The shooting method then restarts to calculate the corresponding solution $\mathbf{z}^{\mathrm{j}+1}(\mathbf{z}_0^{\mathrm{j}+1}, T^{\mathrm{j}+1})$ using the current solution $(\mathbf{z}_0^{\mathrm{j}}, T^{\mathrm{j}})$ as the initial trial. The sequential continuation method stands out due to its robustness and relatively small computational cost. Nevertheless, we acknowledge that it fails at the bifurcation points of the resonance diagrams, as further discussed in Section 4.4.

4.3.3 Stability of the periodic solution

The stability of the solution, corresponding to each value of $\overline{\omega}$ considered, is evaluated using Floquet stability theory. For that purpose we monitor the eigenvalues of the so-called *Monodromy matrix* $\frac{\partial \mathbf{z}(T, \mathbf{z}_0)}{\partial \mathbf{z}_0}$, which appeared in Eq. (4.41). If the modulus of any of the eigenvalues of this matrix is greater than 1, the periodic solution is considered to be unstable. The classical unit circle representation (see Fig. 4.2) presents that the loss of stability can take place in three different ways:

i. A real eigenvalue exits the unit circle at $(1, 0)$. This represents a transcritical cyclic-fold or symmetry-breaking bifurcation.

ii. A real eigenvalue exits the unit circle at $(-1, 0)$. This represents a period doubling bifurcation.

iii. A complex conjugate pair of eigenvalues exit the unit circle anywhere else. This represents a secondary Hopf or Niemark bifurcation.

The stability of the solution is further discussed in Section 4.4 when the numerical results are presented.

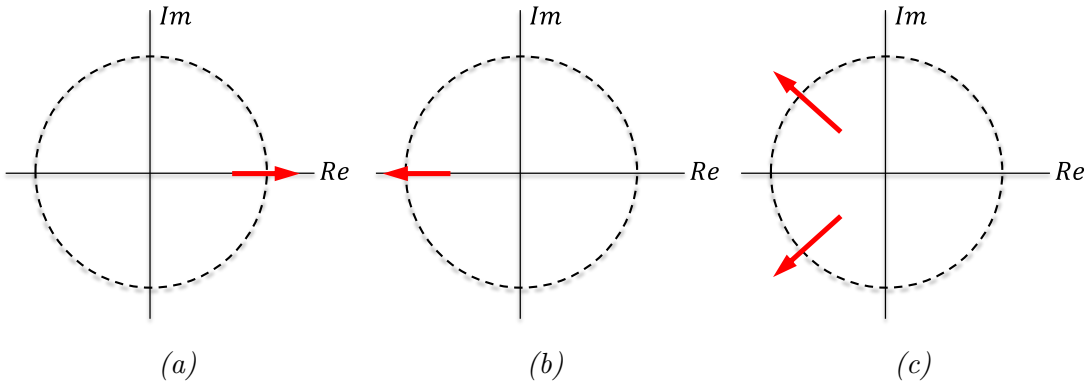

Fig. 4.2 Unit circle representation: imaginary versus real part of the eigenvalues of the Monodromy matrix. Three different scenarios which lead to the loss of stability of the solution: (a) cyclic-fold bifurcation, (b) period doubling bifurcation and (c) Hopf bifurcation.

4.4 Sample results

The goal of this section is to provide sample numerical results which bring to light the relation between the applied frequency $\overline{\omega}$ and the amplitude of the periodic motion of the aneurysm. In order to carry out this analysis, we first need to characterize (for each frequency) the transient response of the system: the end of the transient regime determines the onset of the periodic motion.

Fig. 4.3 depicts: (a) the pressure applied on the aneurysm $\Delta\overline{P}$ versus the loading time τ, (b) the circumferential stretch in the outer surface of the aneurysm λ_b versus the loading time τ and (c) the circumferential stretch rate $\dot{\lambda}_b$ versus the circumferential stretch λ_b in the outer surface of the aneurysm (phase diagram). While Fig. 4.3a is obtained directly from Eq. (4.16), figures 4.3b and 4.3c have been obtained after solving equations (4.30) and (4.31) using a fourth order Runge-Kutta method. We have taken $\overline{\omega} = 1$ and assumed that the aneurysm is initially unstretched and at rest. The Mooney-Rivlin constitutive model is considered. The geometric, loading and material parameters used in the calculation are those reported in sections 4.2 and 4.2.5, with a single exception: the viscosity of the fluid has been increased to obtain $\kappa = 0.1$. The purpose is to provide a clear illustration of the dissipation of energy by the CSF.

Fig. 4.3a presents the evolution of the applied pressure with time, where T is the period given by $\overline{\omega}$ and determined by the time elapsed between two consecutive peaks.

Fig. 4.3b enables to identify the transient and steady-state regimes in the oscillatory response of the system. The transient regime lasts until $\tau \approx 30$ and it is characterized by the gradual decrease in the amplitude of the oscillations of the aneurysm (dashed line). This behavior is caused by the energy dissipated by the CSF. The steady-state regime,

which develops for $\tau \gtrsim 30$, is characterized by the periodic response of the aneurysm (solid line). One can identify a repetitive pattern in the $\lambda_b - \tau$ curve which is determined by the period T previously noted in Fig. 4.3a.

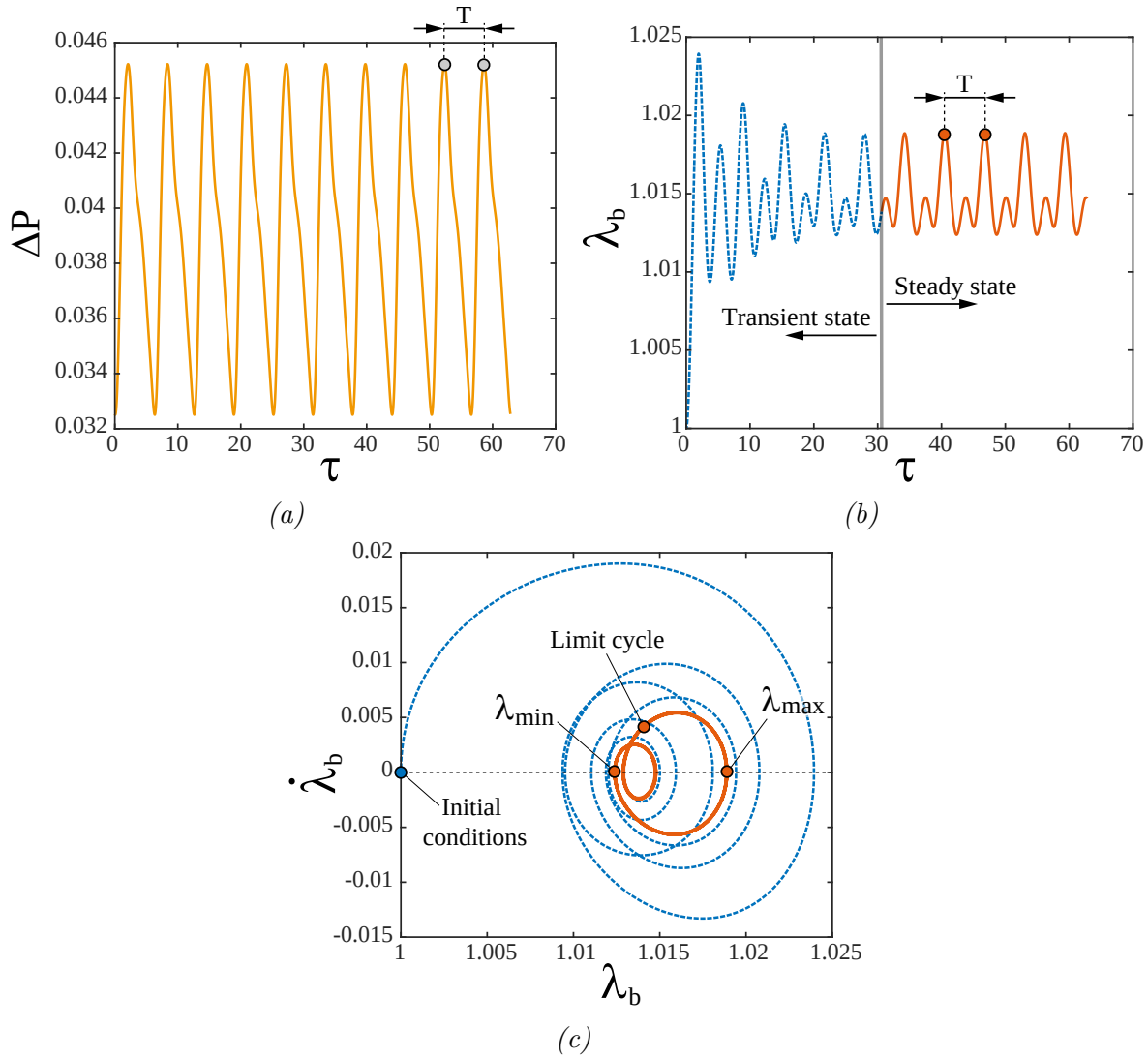

Fig. 4.3 (a) Pressure applied in the inner surface of the aneurysm $\Delta\overline{P}$ versus loading time τ, (b) circumferential stretch in the outer surface of the aneurysm λ_b versus loading time τ and (c) circumferential stretch rate $\dot{\lambda}_b$ versus circumferential stretch λ_b in the outer surface of the aneurysm (phase diagram). The Mooney-Rivlin constitutive model is considered. The normalized frequency is $\overline{\omega} = 1$. The aneurysm is initially unstretched and at rest.

Finally, Fig. 4.3c depicts the phase diagram corresponding to the outer surface of the aneurysm. We observe that the transient response (dashed line) is also characterized by a gradual decrease in the velocity of the oscillations of the aneurysm. The oscillations become slower and shorter in amplitude until the motion becomes periodic, as illustrated

by the limit cycle identified by a solid line. Note that the limit cycle is non-symmetric, which implies the existence of symmetry breaking bifurcations. This limit cycle (characterized by the period T), which results from the balance between the work of the applied pressure and the energy dissipated by the CSF, is the focus of our attention in the forthcoming analysis. Namely, our aim is to identify the dependences of the amplitude of the limit cycle with the applied frequency, the thickness of the aneurysm and the specific constitutive model used to describe the aneurysm wall.

Figures 4.4a and 4.4b represent the resonance diagrams, $\lambda_{max} - \lambda_{min}$ versus $\overline{\omega}$, for Neo-Hookean and Mooney-Rivlin constitutive models, respectively. Note that λ_{max} and λ_{min} are the maximum and minimum stretches of the limit cycle, as indicated in Fig. 4.3c. The geometric, loading and material parameters reported in sections 4.2 and 4.2.5 are used in the calculations, including the fluid viscosity (unlike in the previous example). The normalized frequencies investigated range from 0.01 to 100.

The excursions in $\lambda_{max} - \lambda_{min}$ correspond to resonances of the aneurysm: dramatic increase of the amplitude of the oscillations for some specific frequencies. Note that these excursions are tilted, which illustrates the interplay between the natural frequency and the amplitude of the oscillations. This interplay is caused by the nonlinear nature of the problem at hand, which includes geometric and material nonlinearities. The excursion that leads to the maximum amplitude of the oscillations is the so-called fundamental (or primary) resonance of the aneurysm. The other excursions are the so-called super-harmonic resonances. We have calculated the stable and unstable branches of the excursions, which are plotted using solid and dashed lines in figures 4.4a and 4.4b, respectively. While the sequential continuation method fails at the bifurcation points of the diagram, it is enough to start the numerical procedure with a stable (unstable) limit cycle to calculate the whole stable (unstable) branch. Note also that, following the procedure reported in Section 4.3.3, we have identified the cyclic fold bifurcations that define some of the intersections between stable and unstable branches.

Neo-Hookean constitutive model: the $\lambda_{max} - \lambda_{min}$ excursions are tilted to the left. This behavior is called softening and implies that in order to rise the amplitude of the oscillations, a decrease in the applied frequency is required. Thereby, tilting of the resonance diagram implies that the nonlinear resonance frequency (maximum amplitude of the oscillation) occurs for $\overline{\omega} = 0.4$; i.e., away from the natural frequency of the aneurysm (onset of the main excursion), which is located at $\overline{\omega} \approx 1$. The amplitude of the nonlinear resonance frequency is ≈ 5.5. Besides the main resonance, we have identified six super-harmonics. The stable and unstable branches of each excursion are located on the right and left sides of the peak, respectively. Note that the maximum

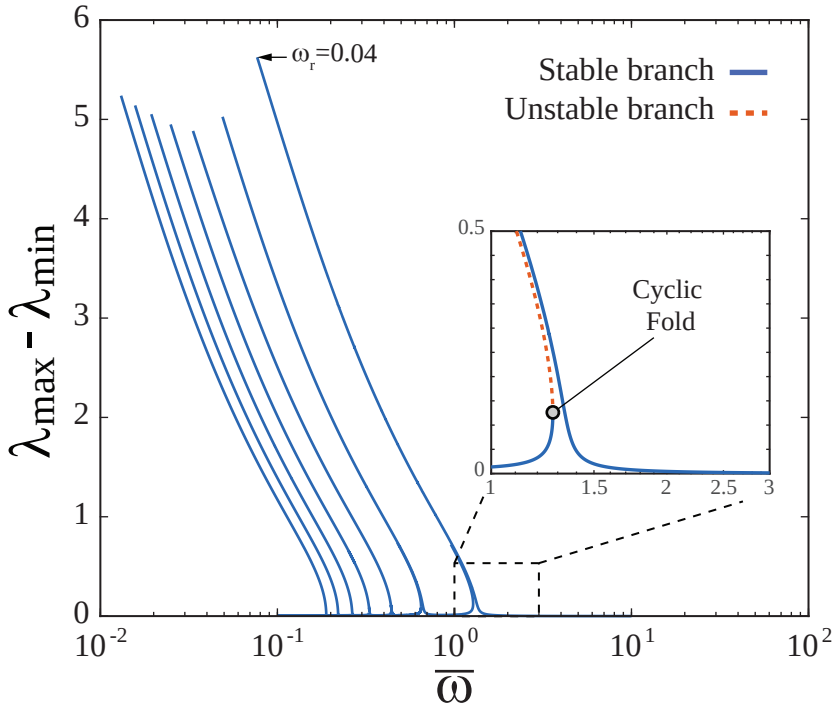

(a)

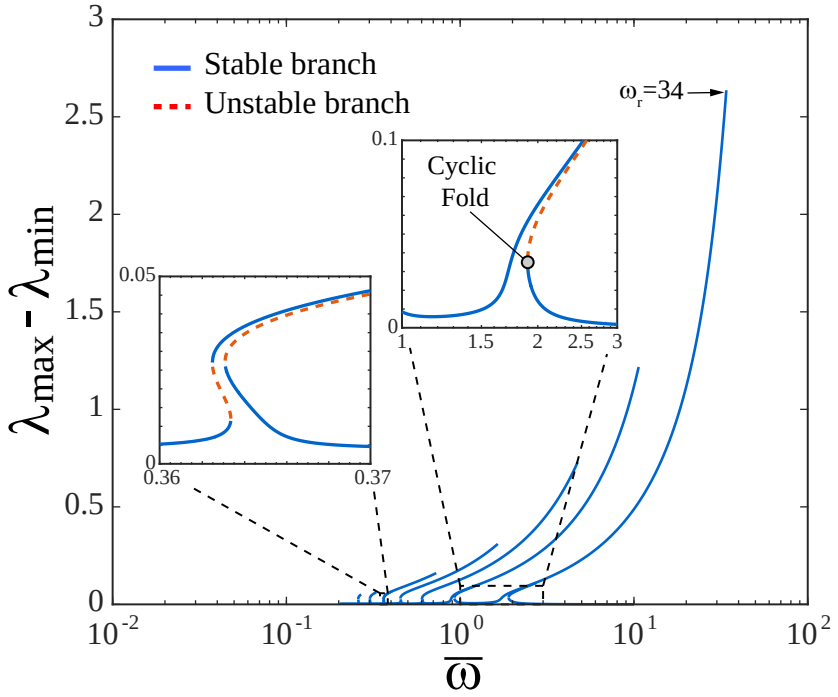

(b)

Fig. 4.4 Resonance diagrams, $\lambda_{max} - \lambda_{min}$ versus $\overline{\omega}$, for (a) Neo-Hookean and (b) Mooney-Rivlin constitutive models. The reference geometric, loading and material parameters reported in sections 4.2 and 4.2.5 are used. The aneurysm is initially unstretched and at rest.

amplitude of the super-harmonics does not decrease monotonically as one moves away from the fundamental (primary) resonance of the aneurysm. The shorter excursion is the second super-harmonic starting from the fundamental resonance. This *unexpected* behavior is most likely related to the fact that the peak of the excursions denotes the loss of the oscillatory behavior of the shell. The aneurysm cannot sustain larger values of stretch within an oscillatory motion and expands unbounded (Aranda-Iglesias et al., 2015; Rodríguez-Martínez et al., 2015).

Mooney-Rivlin constitutive model: the $\lambda_{max} - \lambda_{min}$ excursions are tilted to the right. This behavior, called hardening, is different to the response provided by the Neo-Hookean model. Only the *foot* of the shortest super-harmonics is transiently tilted to the left, showing the so-called snap-through behavior. In general terms, the Mooney-Rivlin material requires an increase in the applied frequency to rise the amplitude of the oscillations. The nonlinear resonance frequency occurs for $\overline{\omega} = 34$, a value significantly greater than the natural frequency of the aneurysm. The amplitude of the nonlinear resonance frequency (≈ 2.6) is significantly smaller than in the case of the Neo-Hookean model. Moreover, we have identified six super-harmonic resonances. In contrast to the case of the Neo-Hookean model, the maximum amplitude of the super-harmonics decreases monotonically as one moves away from the fundamental resonance of the aneurysm. This is due to the fact that now the maximum amplitude of the oscillations is not limited by loss of the oscillatory response of the aneurysm but by the external work applied to the system. The aneurysm could sustain larger values of stretch provided that a larger amount of external work is applied to the system (Aranda-Iglesias et al., 2015; Rodríguez-Martínez et al., 2015).

It becomes apparent the key role played by the constitutive model in the resonance diagram of the aneurysm. The strain energy function determines the amplitude of the oscillations and the nature (softening or hardening) of the interplay between the amplitude of the oscillations and the applied frequency.

On the other hand, it is critical to note that, taking into account the material and geometric parameters given in Section 4.2, the values of $\overline{\omega}$ corresponding to the typical physiologic conditions of an aneurysm range between $2 \cdot 10^{-3}$ and $6.5 \cdot 10^{-3}$. This range is calculated assuming that the minimum and maximum heart rates are 60 and 190 beats per minute, respectively. According to Fig. 4.4, the aneurysm do not show resonances within these values of $\overline{\omega}$; i.e., our results suggest that the pulsatile blood flow cannot lead to the resonance of the aneurysm. This result agrees with the conclusions of Shah and Humphrey (1999) and David and Humphrey (2003), who already stated that the

hypothesis of Simkins and Stehbens (1973) and nan Hung and Botwin (1975) suggesting that saccular aneurysms may be excited at their natural frequency by the pulsatile blood flow, may not be correct. Even in the case of the Neo-Hookean model for which the softening response brings the super-harmonics closer to the maximum frequency of the heart, there is a meaningful gap between the resonance frequency of the lowest super-harmonic ($1.5 \cdot 10^{-2}$) and the frequency of the highest heart rate ($6.5 \cdot 10^{-3}$). Next, we further investigate the possibility of resonances in the aneurysm due to the pulsatile blood flow and, thanks to the 3D formulation derived in Section 4.2, assess the effect of the wall thickness in the oscillatory response of the aneurysm.

Figures 4.5a and 4.5b represent the resonance diagrams, $\lambda_{max} - \lambda_{min}$ versus $\overline{\omega}$, for Neo-Hookean and Mooney-Rivlin constitutive models, respectively. Three different values of the thickness parameter f_0 are investigated: 0.9, 0.78 (reference) and 0.5 for the Neo-Hookean model and 0.98, 0.78 (reference) and 0.5 for the Mooney-Rivlin model. The loading and material parameters reported in sections 4.2 and 4.2.5 are used. The following key observations arise from these graphs:

• The influence of f_0 in the amplitude of the oscillations of the aneurysm depends on the constitutive model. In the case of the Neo-Hookean model, an increase of f_0 (smaller thickness) decreases the maximum amplitude of the resonances. As the thickness of the aneurysm decreases, the oscillatory response of the shell is lost (the unbounded expansion of the shell starts) for smaller values of the ratio $\lambda_{max} - \lambda_{min}$. In fact, for $f_0 = 0.98$ (value investigated in the Mooney-Rivlin case) the aneurysm does not oscillate under these loading conditions. On the contrary, in the case of the Mooney-Rivlin model, an increase of f_0 increases the maximum amplitude of the resonances. In this case the response of the aneurysm is oscillatory regardless of the wall thickness and thus, as expected, the oscillations exhibit larger amplitudes as the thickness decreases.

• Irrespective of the constitutive model considered, the increase of f_0 (which implies smaller thicknesses) shifts to smaller values of the fundamental and the super-harmonic resonances of the aneurysm. The thinner the wall of the aneurysm, the closer the resonance frequencies are to the heart rate. Nevertheless, even in the case of the Neo-Hookean model, the lowest super-harmonic corresponding to the smallest thickness considered is yet far from the highest frequency of the pulsatile blood pressure. Thus, our results broaden the conclusions of Shah and Humphrey (1999) and David and Humphrey (2003) for a wide range of wall thicknesses and reveal that it is unlikely that resonances could lead to the enlargement and rupture of saccular aneurysms.

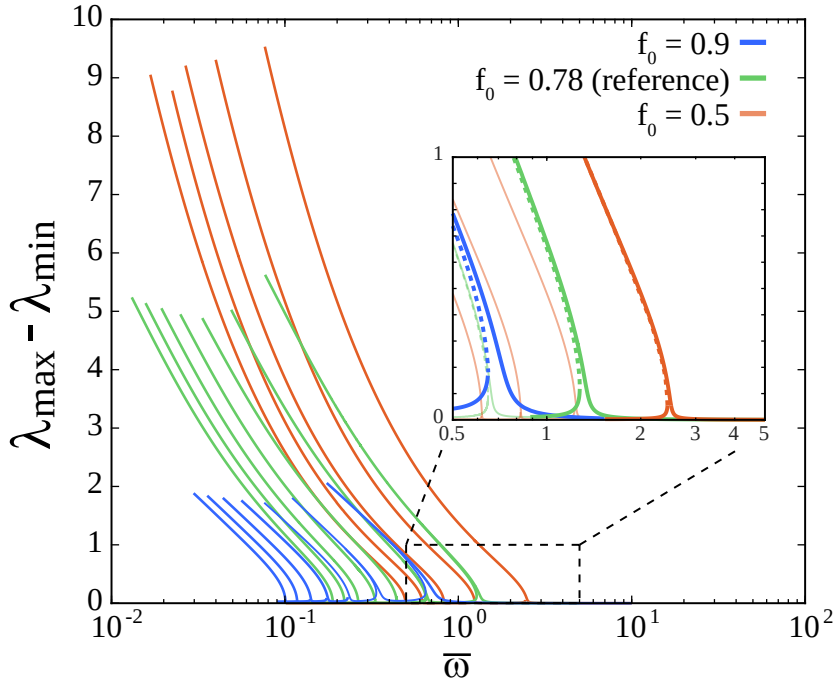

(a)

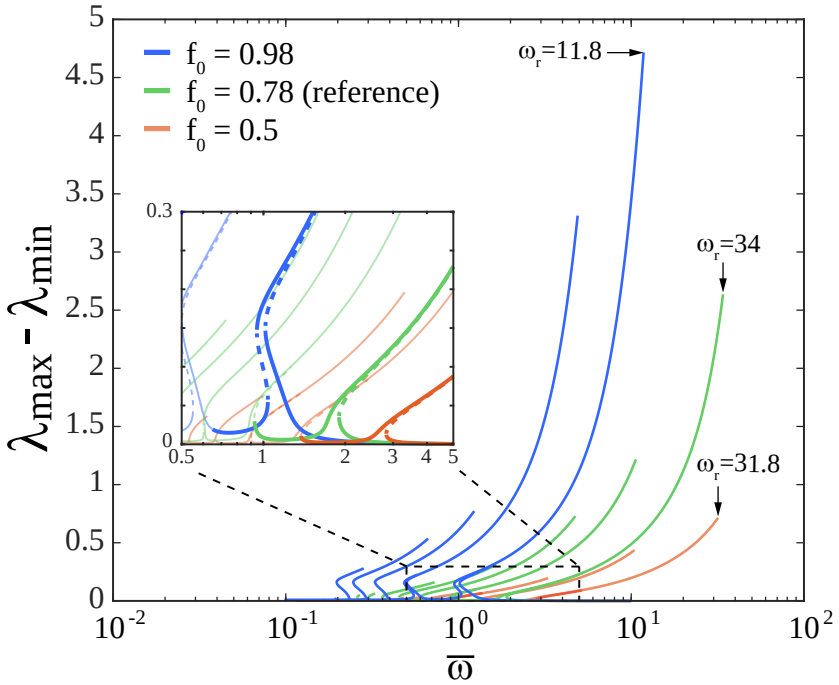

(b)

Fig. 4.5 Resonance diagrams, $\lambda_{max} - \lambda_{min}$ versus $\overline{\omega}$, for (a) Neo-Hookean and (b) Mooney-Rivlin constitutive models. Three different values of the thickness parameter f_0 are investigated: 0.9, 0.78 *(reference) and* 0.5 *for the Neo-Hookean model and* 0.98, 0.78 *(reference) and* 0.5 *for the Mooney-Rivlin. The loading and material parameters reported in sections 4.2 and 4.2.5 are used. The aneurysm is initially unstretched and at rest.*

4.5 Summary and conclusions

In this chapter we have presented the extension to a 3D framework of the formulation developed by Shah and Humphrey (1999) to model the dynamic behavior of idealized intracranial saccular aneurysms subjected to pulsatile blood flow and surrounded by cerebral spinal fluid. The need for a 3D formulation arises from the experimental measurements of Suzuki and Ohara (1978), MacDonald et al. (2000) and Costalat et al. (2011) who provided evidences of saccular aneurysms with ratios of wall thickness to inner radius larger that 0.1.

For the first time in literature, the dynamic response of the aneurysm has been analyzed using nonlinear resonance diagrams obtained from a numerical procedure specifically designed for that purpose. Two different constitutive models have been used in the analysis: Neo-Hookean and Mooney-Rivlin. For each material model we have identified the fundamental resonance and six super-harmonics. A critical outcome of this research is to show that none of these resonances, for any of the constitutive models used and irrespective of the thickness of the aneurysm, lies within the frequencies associated to the normal heart rates. Thus, in agreement with David and Humphrey (2003), our results seem to discard the hypothesis of saccular aneurysms being led to rupture because they are excited at their natural frequency by the pulsatile blood flow. However, our results also show that the nonlinearities of the problem could bring closer than expected the resonance frequencies of the aneurysm to the usual frequencies of the heart. This finding, that has been rarely discussed in the literature, has been found to be strongly dependent on the constitutive model. It is thus highlighted that the description of the mechanical response of the aneurysm wall has a great influence on the dynamic response of this type of lesions.

5 Compressible isotropic hyperelastic spherical structures

The role of stress waves propagation

In this chapter we investigate the role played by the material compressibility in the oscillatory behavior of hyperelastic spherical shells subjected to dynamic inflation. For that purpose we carried out a comprehensive nondimensional numerical analysis using: (1) a finite differences MacCormack's scheme implemented in MATLAB and (2) a finite element model developed in ABAQUS/Explicit (ABAQUS/Explicit, 2014). We have detected that numerical dispersion and diffusion impose limits to the capacity of the computations to describe the shock wave that emanates from the inner surface of the shell due to the application of the inflation pressure. Nevertheless, both numerical approaches capture the essential features that describe the oscillatory behavior of the shell, including the maximum stretch of the oscillation. Using the key nondimensional groups that control the problem at hand, we have conducted a parametric study to assess the role played by nondimensional applied pressure, material compressibility and nondimensional shell thickness in the oscillatory behavior of the specimen. We have shown the interplay between the maximum amplitude of the oscillation and the applied pressure, and obtained the critical pressure for which the oscillatory behavior is lost, leading to an unbounded expansion of the spherical shell. Moreover, our calculations have revealed that the wave propagation within the specimen plays a key role in the dynamic response of the shell. The phase portraits used to represent the oscillatory behavior of the spherical shell show a characteristic sawtooth form that is accentuated with the increase of material compressibility and shell thickness.

5.1 Introduction

As discussed in the introductory section of Chapter 3, the first studies dealing with the non-linear dynamic behavior of hyperelastic shells are dated in the early 60's. Knowles

(1960, 1962) investigated, for the first time, the large-amplitude radial oscillations of very long thick-walled cylindrical tubes. Shortly after, Zhong-Heng and Solecki (1963) inspected the large-amplitude vibrations of thick-walled spherical shells. In these seminal works, free and forced oscillations with Heaviside step pressure boundary condition were explored. The material was considered incompressible and the problems were reduced to that of an autonomous motion of a system with a single degree of freedom (see 3). The authors provided exact solutions of the trajectory and period of vibrations, and paid special attention to the critical initial and loading conditions that preclude the oscillatory response of the shell.

The interest in large-amplitude radial vibrations of hyperelastic incompressible bodies has continued to the present day. A significant number of papers have been published over the last five decades on this specific topic (e.g. Balakrishnan and Shahinpoor (1978); Beatty (2007); Nowinski and Wang (1966); Rodríguez-Martínez et al. (2015); Shahinpoor (1972b)). For instance, Humphrey and co-workers David and Humphrey (2003); Shah and Humphrey (1999) studied the axisymmetric deformations of spherical hyperelastic shells subjected to inner and outer pressure to assess the mechanical (dynamic) stability of intracranial saccular aneurysms. The axisymmetric dynamic deformations of (dielectric) elastomeric spherical membranes were also investigated by Mockensturm and Goulbourne (2006) to assess how these structures could be used as reciprocating and peristaltic pumps. We should also mention the works of Gonçalves et al. (2009); Soares and Gonçalves (2012, 2014) who studied the free and forced nonlinear vibrations of pre-stretched (circular, annular and rectangular) hyperelastic membranes subjected to transversal harmonic pressure. The authors developed a single degree-of-freedom model that was verified via comparisons with finite element calculations performed with the code ABAQUS. This series of works highlighted the influence of the pre-stretching ratio, the strain energy function used to model the material, and the frequency of the applied pressure on the dynamic response of the membrane.

Alternatively, Amabili and co-workers (Amabili et al., 2016; Breslavsky et al., 2014a,b) proposed a dynamic local model to investigate the nonlinear vibrations of rectangular hyperelastic plates. The model, which allowed to include the *commonly ignored* in-plane displacements to the analysis of bending vibrations of hyperelastic plates (Breslavsky et al., 2014b), was validated with experiments and numerical simulations performed with ABAQUS. The reader is referred to the recent and very detailed review of Alijani and Amabili (2014) to obtain further information about the literature published over the last 50 years on the dynamic behavior of hyperelastic shells.

However, the oscillatory behavior of compressible hyperelastic shells has received much less attention. Most likely, this is due to the fact that material compressibility prevents obtaining a closed-form solutions of the shell motion. The problem has to be solved numerically, even in the case that a constant pressure is applied a boundary condition. To the authors' knowledge, the first contribution to this field was published by Haddow and Mioduchowski (1977). This work explored the radial oscillations of compressible hyperelastic spherical shells subjected to a step function pressure at their inner surface. Haddow and Mioduchowski (1977) showed that the response of compressible and incompressible shells subjected to dynamic inflation is significantly different. For incompressible specimens the effect of the pressure is felt instantaneously throughout the shell. In the case of compressible spherical shells, the applied pressure leads to the formation of a shock wave, which propagates back and forth through the thickness of the specimen. In Janele et al. (1989b), Haddow and co-workers further investigated the radial oscillations of compressible hyperelastic spherical shells. For that, they developed a finite difference model, based on a predictor-corrector scheme, that improved the numerical procedure previously used in Haddow and Mioduchowski (1977). Their attention was focused on the constitutive sensitivity of the oscillatory behavior of compressible shells. They used different strain energy functions to model the material behavior and highlighted the differences between the dynamic response of compressible and incompressible specimens. The phase portraits of compressible shells showed a characteristic sawtooth form (this was not observed for incompressible shells), which revealed the effect of the reflected waves in the oscillatory behavior of the spherical specimen. Similar results were obtained in Janele et al. (1989a, 1991), where Haddow and co-workers investigated the dynamic inflation of compressible cylindrical shells. More recently, we should highlight the work of Antman and Lacarbonara (2009), who developed a general approach to the radial motions of compressible nonlinear elastic cylindrical and spherical shells subjected to time dependent pressure. Using the geometrically exact 2-dimensional Cosserat theory developed in Antman (2006), the authors pointed out the significant differences in the dynamic response of cylindrical and spherical shells. The reader is referred to chapter 17 in Antman (2006) to obtain additional information about various engineering problems that arise within the context of the dynamic behavior of nonlinear elastic shells.

The present chapter, which complements the aforementioned works of Antman and Lacarbonara (2009); Haddow and Mioduchowski (1977); Janele et al. (1989b), revisits the problem of a compressible spherical shell subjected to constant pressure at its inner surface. The goal is to provide further insights into the role played by the applied pressure,

the material compressibility and the shell thickness in the oscillatory behavior of the specimen. To this end, we have addressed the problem using two different numerical approaches: (1) a finite differences scheme implemented in MATLAB and (2) a finite element model developed in ABAQUS. On the one hand, we have detected that numerical diffusion and dispersion impose limits to the capacity of (these) numerical methods to describe the shock wave that emanates from the inner surface of the shell due to the applied pressure. On the other hand, we have shown that both numerical approaches capture main features of the oscillatory response of the spherical shell, including the maximum amplitude of the oscillations. Using the key nondimensional groups that control the problem at hand, we have conducted a comprehensive parametric analysis and showed, for different specimen thicknesses and degrees of material compressibility, the interplay between the maximum amplitude of the oscillations and the applied pressure. In addition, we have investigated the critical loading conditions and material behaviors (degrees of compressibility) for which the oscillatory behavior is lost, leading to an unbounded expansion of the spherical shell.

5.2 Problem formulation

In this section we formulate the problem of a thick-walled spherical shell subjected to radially symmetric dynamic inflation. The material is taken to be isotropic and compressible within the framework of finite nonlinear elasticity. The main features of the mathematical derivation are presented, while further details can be found in the work of Janele et al. (1989b).

Recall from Chapter 2 that the current position vector $\mathbf{x}$ in the deformed configuration $\Omega \subset \mathbb{R}^3$ at time t of the material point that occupies the location $\mathbf{X} \in \Omega_0$ is given by $\mathbf{x} = \boldsymbol{\chi}(\mathbf{X}, t)$, where $\boldsymbol{\chi}$ is a bijective and twice continuously differentiable mapping. The associated deformation gradient, right Cauchy-Green strain tensor and volume ratio at $\mathbf{X} \in \Omega_0$ are denoted by

$$\begin{gathered} \mathbf{F}(\mathbf{X}, t) = \operatorname{Grad} \boldsymbol{\chi}(\mathbf{X}, t), \ \mathbf{C}(\mathbf{X}, t) = \mathbf{F}^{\mathrm{T}}(\mathbf{X}, t)\mathbf{F}(\mathbf{X}, t), \\ J(\mathbf{X}, t) = \det \mathbf{F}(\mathbf{X}, t). \end{gathered} \tag{5.1}$$

Moreover, the balance of linear momentum in the material description requires that

$$\operatorname{Div} \mathbf{S}(\mathbf{X}, t) = \rho_0 \ddot{\boldsymbol{\chi}}(\mathbf{X}, t) \quad \text{in} \quad \Omega_0, \tag{5.2}$$

where the dots denote differentiation with respect to time, $\mathbf{S}$ stands for the first Piola-Kirchhoff stress tensor, and ρ_0 is the constant mass density of the shell material in its undeformed configuration Ω_0.

5.2.1 Radially symmetric dynamic deformation

Let $\{R, \Theta, \Phi\}$ denote the spherical polar coordinates in the reference configuration such that $A \leq R \leq B$. If the material is deformed so that the spherical symmetry is maintained, the motion is given by

$$r = r(R, t), \qquad \theta = \Theta, \qquad \phi = \Phi, \tag{5.3}$$

where $\{r, \theta, \phi\}$ are the spherical polar coordinates in the current configuration such that $a \leq r \leq b$. Under these conditions, the deformation gradient tensor is given by

$$\mathbf{F} = \lambda_r \, \mathbf{e}_r \otimes \mathbf{e}_r + \lambda \, \mathbf{e}_\theta \otimes \mathbf{e}_\theta + \lambda \, \mathbf{e}_\phi \otimes \mathbf{e}_\phi, \tag{5.4}$$

where the principal stretches corresponding to the directions r, θ, ϕ are given by

$$\lambda_r = \frac{\partial r}{\partial R}, \quad \lambda = \lambda_\theta = \lambda_\phi = \frac{r}{R}. \tag{5.5}$$

Moreover, the particle velocity is $v(R, t) = \frac{\partial r(R,t)}{\partial t}$ and the first Piola-Kirchoff stress tensor assumes the following form

$$\mathbf{S} = S_r \, \mathbf{e}_r \otimes \mathbf{e}_r + S_\theta \, \mathbf{e}_\theta \otimes \mathbf{e}_\theta + S_\theta \, \mathbf{e}_\phi \otimes \mathbf{e}_\phi. \tag{5.6}$$

The fundamental equations, formulated in Lagrangian description, which govern the loading process, are given below.

Kinematic relations. Based on the definitions of the radial and circumferential stretches, we deduce the following kinematic relations

$$\frac{\partial \lambda_r}{\partial t} - \frac{\partial v}{\partial R} = 0, \qquad \frac{\partial \lambda}{\partial t} - \frac{v}{R} = 0. \tag{5.7}$$

Hereinafter, we indistinctly denote the circumferential stretch rate as $\frac{\partial \lambda}{\partial t}$ or $\dot{\lambda}$.

Conservation of linear momentum. The balance of linear momentum presented in Eq. (5.2) reduces to

$$\rho_0 \frac{\partial v}{\partial t} - \frac{\partial S_r}{\partial R} - \frac{2\,(S_r - S_\theta)}{R} = 0. \tag{5.8}$$

5.2.2 Constitutive model

In this work our attention is restricted to isothermal loading processes at constant temperatures. Following Ogden (1997), we use the following *isochoric-volumetric* decomposition of the strain energy function, as introduced in Chapter 2.

$$\psi(\overline{I}_1, \overline{I}_2, J) = \psi_{iso}(\overline{I}_1, \overline{I}_2) + \psi_{vol}(J), \tag{5.9}$$

where $\overline{I}_1 = J^{-2/3}(\lambda_r^2 + 2\lambda^2)$ and $\overline{I}_2 = J^{-4/3}(2\lambda_r^2\lambda^2 + \lambda^4)$ are the first and second invariants of the isochoric part of the right Cauchy-Green strain tensor, being $J = \lambda_r\lambda^2$ the determinant of the deformation gradient tensor. We have selected the Mooney-Rivlin material model to characterize the isochoric part

$$\psi_{iso}(\overline{I}_1, \overline{I}_2) = C_{10}\left(\overline{I}_1 - 3\right) + C_{01}\left(\overline{I}_2 - 3\right), \tag{5.10}$$

where C_{10} and C_{01} are material parameters such that $\mu = 2(C_{10} + C_{01})$ is the initial shear modulus. From Bucchi and Hearn (2013b) we have taken $C_{10} = 210587.307$ MPa and $C_{01} = 1504.76719$ MPa. These material constants correspond to vulcanized rubber and were originally reported by Treloar (1944). We have selected the following expression first proposed by Ogden (1972) to characterize the volumetric part

$$\psi_{vol}(J) = \frac{K}{\beta^2}\left(\beta \ln J + J^{-\beta} - 1\right), \tag{5.11}$$

where K is the initial bulk modulus and β is an empirical material parameter. Note that, in the limit of small deformations, $K = \frac{2\mu(1+\nu)}{3(1-2\nu)}$ where ν is the initial Poisson ratio. In forthcoming sections of this chapter, we will carry out systematic variations of ν in order to explore the role played by the material compressibility in the dynamic response of the spherical shell. Moreover, according to Ogden (1972), we have taken $\beta = 9$. Finally, if the strain energy function takes the form $W(\lambda_r, \lambda) = \psi(\overline{I}_1, \overline{I}_2, J)$, the radial and circumferential stresses are given by

$$S_r = \frac{\partial W}{\partial \lambda_r}, \qquad S_\theta = \frac{1}{2}\frac{\partial W}{\partial \lambda}. \tag{5.12}$$

5.2.3 Initial and boundary conditions

The formulation of the problem is completed with the following initial and boundary conditions

$$S_r\left(R, 0\right) = S_\theta\left(R, 0\right) = 0, \qquad v\left(R, 0\right) = 0, \tag{5.13}$$

$$S_r\left(A,t\right)=-\lambda(A,t)^2P, \qquad S_r\left(B,t\right)=0, \tag{5.14}$$

where P is a constant pressure per unit of current area applied in the inner surface of the spherical shell. Note that the relation between the radial Piola-Kirchoff stress and the radial Cauchy stress is $S_r=\lambda^2\sigma_r$. Therefore, the boundary condition in the inner surface of the shell can be alternatively expressed as $\sigma_r\left(A,t\right)=-P$. These relations will be used in Section 5.5 to analyze the stress field in the spherical shell during the loading process.

5.2.4 Dimensionless formulation

It is convenient at this point to introduce the following set of non-dimensional variables

$$\begin{gathered}\overline{R}=\frac{R}{A}, \qquad \overline{r}=\frac{r}{A}, \qquad \overline{S}_r=\frac{S_r}{C_{10}}, \qquad \overline{S}_\theta=\frac{S_\theta}{C_{10}} \\ \overline{t}=\frac{t}{A}\sqrt{\frac{C_{10}}{\rho_0}}, \qquad \overline{v}=v\sqrt{\frac{\rho_0}{C_{10}}}, \qquad \overline{W}=\frac{W}{C_{10}}, \qquad \overline{P}=\frac{P}{C_{10}}, \qquad f_0=\left(\frac{A}{B}\right)^3,\end{gathered} \tag{5.15}$$

where f_0 is a nondimensional thickness parameter that represent the geometry of the spherical shell, as in previous chapters if this dissertation. This set of nondimensional variables highlights the dependence of the problem on the geometric and loading parameters f_0 and $\overline{P}$ that will be systematically varied in Section 5.6. Previous non-dimensional variables allow to rewrite the kinematic relations and the balance of linear momentum, equations (5.7) and (5.8), as follows

$$\frac{\partial\lambda_r}{\partial\overline{t}}-\frac{\partial\overline{v}}{\partial\overline{R}}=0, \tag{5.16}$$

$$\frac{\partial\lambda}{\partial\overline{t}}-\frac{\overline{v}}{\overline{R}}=0, \tag{5.17}$$

$$\frac{\partial\overline{v}}{\partial\overline{t}}-\frac{\partial\overline{S}_r}{\partial\overline{R}}-\frac{2\left(\overline{S}_r-\overline{S}_\theta\right)}{\overline{R}}=0, \tag{5.18}$$

This system of equations can be rearranged in the form

$$\frac{\partial\mathbf{Q}}{\partial\overline{t}}+\frac{\partial\mathbf{H}\left(\mathbf{Q}\right)}{\partial\overline{R}}+\mathbf{b}\left(\mathbf{Q}\right)=0, \tag{5.19}$$

where $\mathbf{Q}=\left(\lambda_r,\lambda,\overline{v}\right)^{\mathrm{T}}$, $\mathbf{H}=-\left(\overline{v},0,\overline{S}_r\right)^{\mathrm{T}}$ and $\mathbf{b}=-\left(0,\frac{\overline{v}}{\overline{R}},\frac{2\left(\overline{S}_r-\overline{S}_\theta\right)}{\overline{R}}\right)^{\mathrm{T}}$. We can further operate with previous equations in order to obtain the system in a non-conservative form

$$\frac{\partial\mathbf{Q}}{\partial\overline{t}}-\mathbf{M}\frac{\partial\mathbf{Q}}{\partial\overline{R}}+\mathbf{b}\left(\mathbf{Q}\right)=0, \tag{5.20}$$

where

$$\mathbf{M} = \begin{pmatrix} 0 & 0 & -1 \\ 0 & 0 & 0 \\ -\frac{\partial \overline{S}_r}{\partial \lambda_r} & -\frac{\partial \overline{S}_r}{\partial \lambda} & 0 \end{pmatrix}. \tag{5.21}$$

The eigenvalues of $\mathbf{M}$, that will be further analyzed in Section 5.3, are 0 and $\pm\gamma$, where $\gamma = \sqrt{\frac{\partial^2 \overline{W}}{\partial \lambda_r^2}}$. These are the slopes of three families of characteristics in the $\left(\overline{R}, \bar{t}\right)$ plane.

The problem of the dynamic inflation of spherical shells formulated in this section is approached numerically using the methods of finite differences and finite elements. The basic features of the numerical models developed for this purpose are described in sections 5.3 and 5.4.

5.3 Finite differences modeling

This section presents the finite differences scheme used to solve the governing equations defined by (5.19). The scheme is taken from Janele et al. (1989b), who implemented a modification of the MacCormack's predictor-corrector formulation (MacCormack, 1969) to obtain solutions to problems of shear waves emanating from a cylindrical cavity in an unbounded hyperelastic medium (Haddow et al., 1987a,b). Only the main features of the model are presented here since further details can be found in Janele et al. (1989b).

In order to construct the numerical solution, we consider a rectangular grid such that $\Pi = \{\overline{R}_j = 1 + j\Delta\overline{R},\ \bar{t}^n = n\Delta\bar{t}\}$, where $j = 0, \ldots, M$ and $n = 0, \ldots, N$. The integration spatial and time steps are $\Delta\overline{R} = \frac{\overline{B}-1}{M}$ and $\Delta\bar{t}$, where $\overline{B} = B/A$. The forward-backward (predictor-corrector) finite differences relations are, respectively

$$\mathbf{Q}_j^* = \mathbf{Q}_j^n - \frac{\Delta\bar{t}}{\Delta\overline{R}}\left(\mathbf{H}_{j+1}^n - \mathbf{H}_j^n\right) - \Delta\bar{t}\mathbf{b}_j^n, \tag{5.22}$$

$$\mathbf{Q}_j^{n+1} = \frac{1}{2}\left(\mathbf{Q}_j^n + \mathbf{Q}_j^* - \frac{\Delta\bar{t}}{\Delta\overline{R}}\left(\mathbf{H}_j^* - \mathbf{H}_{j-1}^*\right) - \Delta\bar{t}\mathbf{b}_j^*\right), \tag{5.23}$$

where the notation $\mathbf{Q}_j^n = \mathbf{Q}\left(\overline{R}_j, \bar{t}^n\right)$ has been used. The superscript $*$ refers to predicted quantities.

Application of the finite differences scheme requires boundary conditions for the kinematic variables $(\lambda_r, \lambda, \overline{v})$. However, only the relations $\overline{S}_r(A,t) = -\lambda(A,t)^2\overline{P}$ and $\overline{S}_r(B,t) = 0$ are prescribed, which give the relation between λ_r and λ at the inner and outer surfaces of the shell. In order to obtain additional boundary conditions, the finite differences scheme is modified as follows:

• **Inner surface** of the shell (forward-forward scheme): in the **predictor step** the velocity is computed following the forward scheme used in the general formulation (Eq. 5.22). The circumferential stretch is obtained using a finite difference form of Eq. (5.17) taken along the characteristic $\overline{R} = 1$ and the radial stretch is obtained from the prescribed boundary condition (Eq. 5.14).

$$\overline{v}_0^* = \overline{v}_0^n + \frac{\Delta\overline{t}}{\Delta\overline{R}}\left[\left(\overline{S}_r\right)_1^n - \left(\overline{S}_r\right)_0^n\right] + 2\Delta\overline{t}\left[\left(\overline{S}_r\right)_0^n - \left(\overline{S}_\theta\right)_0^n\right], \tag{5.24}$$

$$\lambda_0^* = \lambda_0^n + \frac{\Delta\overline{t}}{2}\left(\overline{v}_0^* + \overline{v}_0^n\right), \tag{5.25}$$

$$\left(\overline{S}_r\right)_0^* = -\left(\lambda_0^*\right)^2 \overline{P}. \tag{5.26}$$

In the **corrector step** we use a similar procedure. However, the backward scheme used in the general formulation for the velocity (Eq. 5.23), is replaced by a forward scheme.

$$\overline{v}_0^{n+1} = \frac{1}{2}\left\{\overline{v}_0^n + \overline{v}_0^* + \frac{\Delta\overline{t}}{\Delta\overline{R}}\left[\left(\overline{S}_r\right)_1^* - \left(\overline{S}_r\right)_0^*\right] + 2\Delta\overline{t}\left[\left(\overline{S}_r\right)_0^* - \left(\overline{S}_\theta\right)_0^*\right]\right\}, \tag{5.27}$$

$$\lambda_0^{n+1} = \lambda_0^n + \frac{\Delta\overline{t}}{2}\left(\overline{v}_0^{n+1} + \overline{v}_0^n\right), \tag{5.28}$$

$$\left(\overline{S}_r\right)_0^{n+1} = -\left(\lambda_0^{n+1}\right)^2 \overline{P}, \tag{5.29}$$

• **Outer surface** of the shell (backward-backward scheme): in the **predictor step** the forward scheme used in the general formulation for the velocity (Eq. 5.22), is replaced by a backward scheme. The circumferential stretch is obtained using a finite difference form of Eq. (5.17) taken along the characteristic $\overline{R} = \overline{B}$ and the radial stretch is obtained from the prescribed boundary condition (Eq. 5.14).

$$\overline{v}_M^* = \overline{v}_M^n + \frac{\Delta\overline{t}}{\Delta\overline{R}}\left[\left(\overline{S}_r\right)_M^n - \left(\overline{S}_r\right)_{M-1}^n\right] + \frac{2\Delta\overline{t}}{\overline{B}}\left[\left(\overline{S}_r\right)_M^n - \left(\overline{S}_\theta\right)_M^n\right] \tag{5.30}$$

$$\lambda_M^* = \lambda_M^n + \frac{\Delta\overline{t}}{2\overline{B}}\left(\overline{v}_M^* + \overline{v}_M^n\right) \tag{5.31}$$

$$\left(\overline{S}_r\right)_M^* = 0 \tag{5.32}$$

In the **corrector step** we use a similar procedure. The backward scheme used in the general formulation for the velocity (Eq. 5.23), is used.

$$\overline{v}_M^{n+1} = \frac{1}{2}\left\{\overline{v}_M^n + \overline{v}_M^* + \frac{\Delta\bar{t}}{\Delta\overline{R}}\left[\left(\overline{S}_r\right)_M^* - \left(\overline{S}_r\right)_{M-1}^*\right] + \frac{2\Delta\bar{t}}{\overline{B}}\left[\left(\overline{S}_r\right)_M^* - \left(\overline{S}_\theta\right)_M^*\right]\right\}, \tag{5.33}$$

$$\lambda_M^{n+1} = \lambda_M^n + \frac{\Delta\bar{t}}{2\overline{B}}\left(\overline{v}_M^{n+1} + \overline{v}_M^n\right), \tag{5.34}$$

$$\left(\overline{S}_r\right)_M^{n+1} = 0. \tag{5.35}$$

To the authors' knowledge, there is no analysis available to determine the stability condition for the scheme (5.22)-(5.23). Nevertheless, following Haddow et al. (1987b), we have investigated the stability of the linear system ($\mathbf{b} = 0$) using the Von-Neumann analysis. In this case, it is required that the Courant number $\xi = \gamma\Delta\bar{t}/\Delta\overline{R} \leq 1$, where γ is the numerically greatest eigenvalue of $\mathbf{M}$. We have used this condition in all our calculations and no numerical instability was encountered (see sections 5.5 and 5.6). Note that γ defines the propagation speed of radial waves in the shell. The non-linearity of the material behavior leads to continuous variations of γ during the the loading process and, consequently, $\Delta\bar{t}$ is adjusted at each time step in order to maintain the same value of ξ with constant $\Delta\overline{R}$. We have selected $\xi = 0.99$, which minimizes numerical diffusion and dispersion (Mendez-Nuñez and Carroll, 1993), and $\Delta\overline{R} = 0.001$ for all the simulations presented in sections 5.5 and 5.6.

It is apparent that the finite differences approach provides flexibility and control over the formulation and resolution of the problem. As such, it is suited to explore the physical phenomena that control the dynamic response of the shell (see Section 5.5).

5.4 Finite elements modeling

This section describes the features of the axisymmetric finite element model developed to simulate the dynamic inflation of spherical hyperelastic shells. The numerical analysis are carried out using the finite element software ABAQUS/Explicit (2014). The strain energy function presented in Section 5.2 has been implemented into the finite element code through a *VUMAT* user subroutine. Consistent with Section 5.2, the problem setting is of a spherical shell with inner and outer radii $\overline{A} = 1$ and $\overline{B}$ (we will perform variations of the shell thickness), respectively (see Fig. 5.1). The solid is initially at rest and unstretched, while a constant internal pressure $\overline{P}$ is applied at the cavity wall.

The model has been meshed using four node axisymmetric reduced integration elements; CAX4R in ABAQUS/Explicit notation. The mesh shows radial symmetry in an attempt to retain the symmetry of the problem and reduce the interference of the mesh in the calculations (see Fig. 5.1). The elements size is constant along the circumferential direction, whereas it increases linearly along the radial direction. Thus, we have ensured that the elements aspect ratio is close to $1:1$ within the whole domain. According to Zukas and Scheffler (2000), such an element shape is optimal for describing dynamic events that involve large gradients of stress and strain. We have placed 200 elements along the circumferential direction, i.e., the size of the elements located beside the inner perimeter is 0.005×0.005. A mesh convergence study has been performed, and phase plane diagrams (stretch rate versus stretch) were compared against a measure of mesh density until the results converged satisfactorily. Note that ABAQUS/Explicit introduces artificial damping in the calculations in order to attenuate the numerical solution and ensure stability. The code generates bulk viscosity pressures, which are linear and quadratic, respectively, in the volumetric strain rate. This artificial viscosity, which introduces numerical diffusion, is controlled by two parameters ϖ (linear viscosity) and χ (quadratic viscosity). In the calculations shown in sections 5.5 and 5.6, we have selected the default values of the code 0.06 and 1.2, respectively.

In comparison with the finite differences simulations, ABAQUS/Explicit calculations are computationally less costly (markedly). For this reason, the finite element model is especially suited to develop parametric analyses that involve a large number of calculations (see Section 5.6).

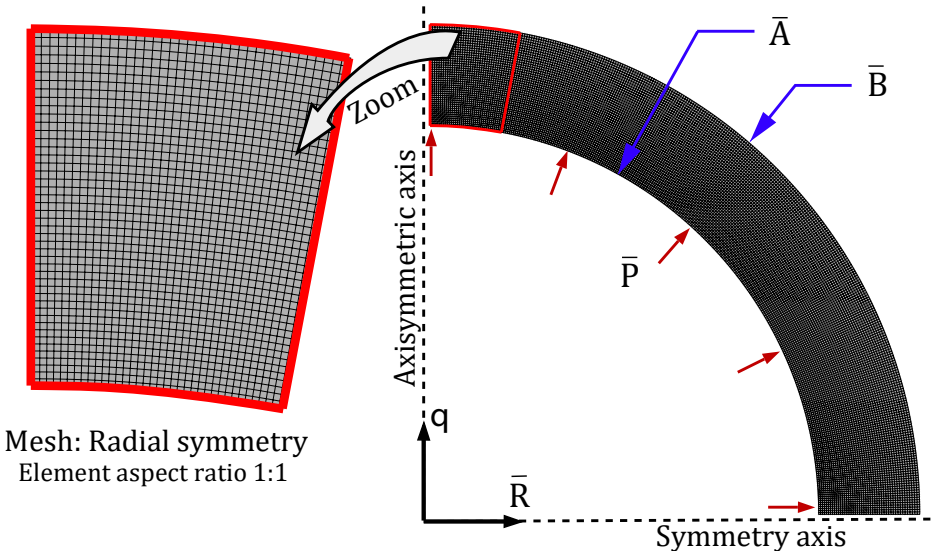

Fig. 5.1 Finite element mesh and mechanical boundary conditions of the spherical shell modeled as an axisymmetric solid.

In the next sections of the chapter we present selected results obtained from the finite differences and finite elements models. Note that very high levels of compressibility are investigated in a range that exceeds the typical values corresponding to rubber-like materials. Nevertheless, exploring highly compressible solids is justified for the sake of better understanding the essential phenomena involved in the dynamic response of compressible hyperelastic shells. The following analysis is composed of two parts. First, we focus on the intervention of stress waves within the specimen, paying specific attention to the role played by the wave propagation phenomena in the dynamic response of the shell. Second, we carry out a systematic variation of (nondimensional) applied pressure, material compressibility and (nondimensional) specimen thickness and analyze the influence of these loading, material and geometric parameters in the oscillatory response of the spherical shell. Throughout the analysis, a comparison between finite differences and finite elements results is conducted. Additional comparisons are carried out with the analytical solution derived in previous chapters for the incompressible sphere.

5.5 Salient features

In this section, we present and discuss some critical outcomes obtained from the numerical models presented in previous sections. Fig. 5.2 shows phase diagrams, $\dot{\lambda}_a$ versus λ_a (stretch and stretch rate in the outer surface), obtained using finite differences and finite

elements simulations. The applied pressure is $\overline{P} = 0.2$, the thickness parameter is $f_0 = 0.5$ and the initial Poisson ratio is $\nu = 0.45$. From this point on, this combination of loading case, geometric condition and material behavior will be referred to as the **reference case**. The phase diagrams present closed orbits, which means that the dynamic response of the spherical shell is oscillatory. Fig. 5.2a depicts the orbit corresponding to the first oscillation and Fig. 5.2b to the third oscillation. Both numerical schemes yield phase plane curves with sawtooth form. This is caused by the reflection of stress waves at the shell boundaries. Note that the sawtooth form of the orbits is attenuated with time. This non-physical behavior is due to numerical diffusion. The attenuation is faster in the case of the finite difference model. Moreover, there is an offset between the finite differences and the finite elements results, which increases with the loading time. This phenomenon is attributed to numerical dispersion. Note that these numerical errors (diffusion and dispersion) barely affect the maximum stretch of the oscillation, which is ~ 1.13 for both numerical approaches used.

Fig. 5.3 depicts the Cauchy radial stress $\overline{\sigma}_R$ and the radial velocity $\overline{v}$ versus the normalized thickness coordinate $\overline{H}$ for the reference loading, geometric and material configurations. The loading time $\overline{t} = 0.0243$ is such that the front wave that emanates from the inner surface of the shell has not yet reached the outer boundary. A comparison between finite differences and finite elements is shown. The agreement between the results obtained from both numerical codes is remarkable. Starting from the inner surface of the shell, we observe that the radial stress $\overline{\sigma}_R$ and the velocity $\overline{v}$ reveal a slight (roughly linear) decrease with the normalized thickness coordinate $\overline{H}$. Approaching $\overline{H} \approx 0.4$ we find a sudden drop in $\overline{\sigma}_R$ and $\overline{v}$, which corresponds to the wave front. The drastic variation in the field variables is caused by the compressibility of the solid. This is evidenced in Fig. 5.4 by the abrupt change in material density observed at the front wave. Nevertheless, the shock is not described as a discontinuity in the calculations because the numerical diffusion smears the wave front across the mesh. Note that the smearing of the shock is more pronounced in the case of the finite differences scheme. Moreover, the finites elements computations present wiggles just behind the shock, which illustrate the numerical dispersion of the finite elements results.

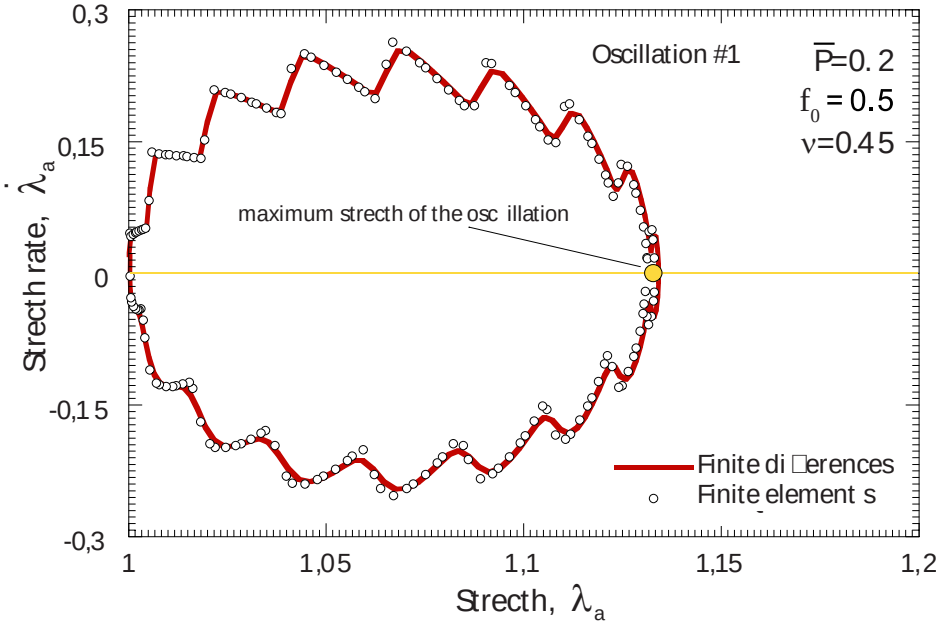

(a)

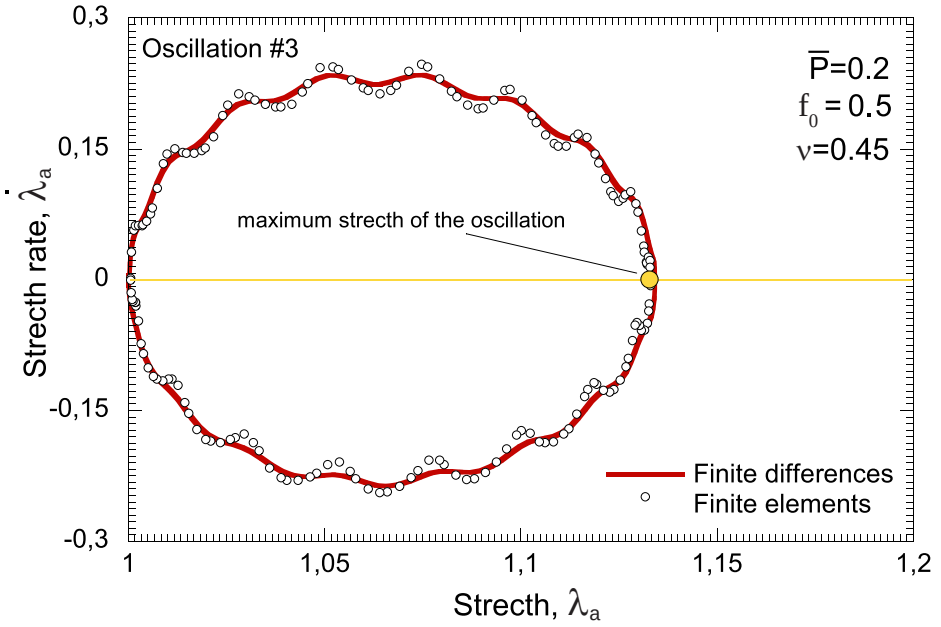

(b)

Fig. 5.2 Comparison between finite differences and finite elements. Phase diagrams, $\dot{\lambda}_a$ versus λ_a. Reference loading case, geometric condition and material behavior: applied pressure $\overline{P} = 0.2$, thickness parameter $f_0 = 0.5$ and initial Poisson ratio $\nu = 0.45$. (a) Oscillation #1 and (b) oscillation #3.

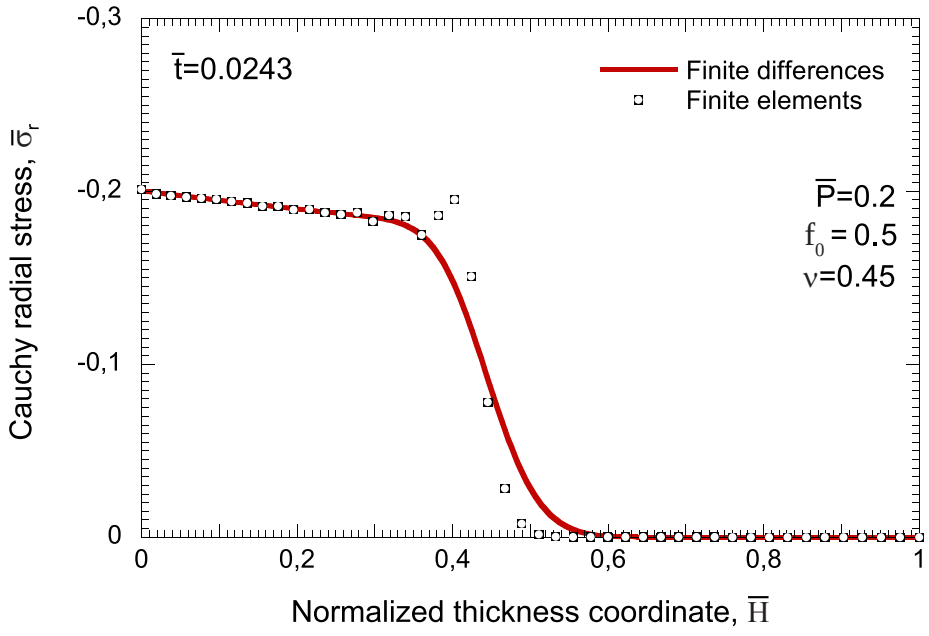

(a)

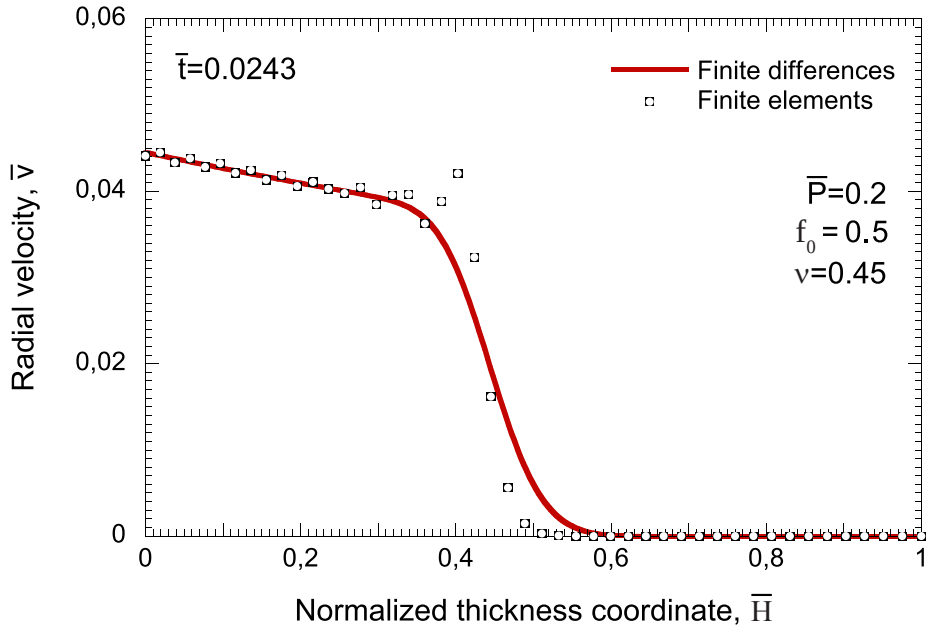

(b)

Fig. 5.3 Comparison between finite differences and finite elements. Reference loading case, geometric condition and material behavior: applied pressure $\overline{P} = 0.2$*, thickness parameter* $f_0 = 0.5$ *and initial Poisson ratio* $\nu = 0.45$*. (a) Cauchy radial stress* $\overline{\sigma}_R$ *and (b) radial velocity* $\overline{v}$ *versus the normalized thickness coordinate* $\overline{H} = \frac{\lambda\overline{R}-\lambda_a}{\lambda_b\overline{B}-\lambda_a}$ *for* $\overline{t} = 0.0243$*.*

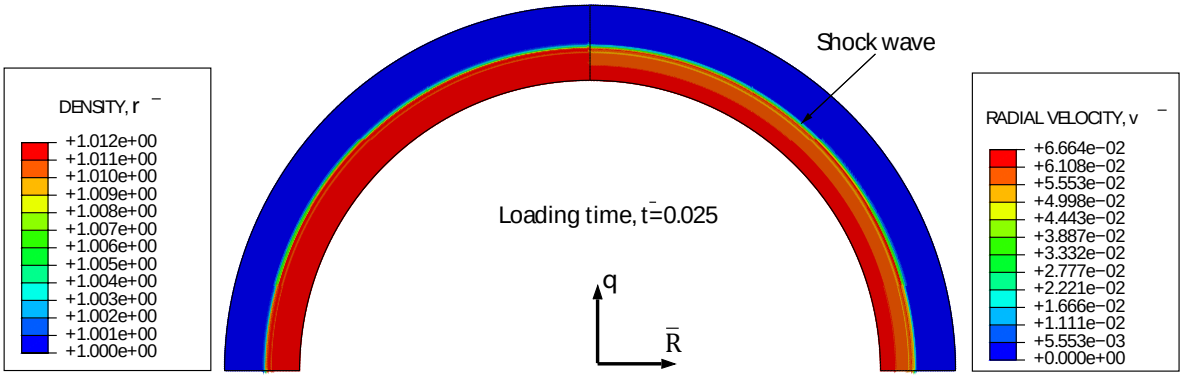

Fig. 5.4 Finite elements. Reference loading case, geometric condition and material behavior: applied pressure $\overline{P} = 0.2$*, thickness parameter* $f_0 = 0.5$ *and initial Poisson ratio* $\nu = 0.45$*. Contours of (a) material density* $\overline{\rho}$ *and (b) radial velocity* $\overline{v}$ *for* $\overline{t} = 0.0243$*.*

It is apparent that dispersive and diffusive effects limit the capacity of both numerical models to describe the shock wave propagation and the sawtooth form of the phase diagrams over extended periods of time. This limitation is especially relevant in the case of the finite differences scheme. Nevertheless, for short loading times, both numerical approaches capture the main physical features that control the oscillatory behavior of the shell, including the maximum stretch of the oscillation. For the first oscillation, the phase diagram predicted by the finite differences and the finite elements is very similar. Thus, relying on the numerical results obtained for the first orbit, in the next section of this chapter we develop a parametric analysis to show the roles played by (nondimensional) applied pressure, material compressibility and (nondimensional) shell thickness in the oscillatory behavior of the spherical shell.

5.6 Parametric analysis

In this section we analyze, throughout numerical simulations, the dependence of the problem on the applied pressure $\overline{P}$, the initial Poisson ratio ν and the thickness of the spherical shell f_0.

5.6.1 The role played by the applied pressure

The goal of this section is twofold: (1) to show the interplay between the maximum amplitude of the oscillation and the applied pressure and (2) to determine the limit imposed by the applied pressure to the oscillatory motion of shell. The reference thickness

parameter $f_0 = 1$ and initial Poisson ratio $\nu = 0.45$ are considered in all the calculations presented below.

Fig. 5.5 represents the phase diagrams obtained using ABAQUS/Explicit for different values of the applied pressure: $\overline{P} = 0.2$, $\overline{P} = 0.3$, $\overline{P} = 0.431$, $\overline{P} = 0.432$ and $\overline{P} = 0.6$. For the applied pressures $\overline{P} = 0.2$, $\overline{P} = 0.3$ and $\overline{P} = 0.431$ the phase portrait is a closed orbit, i.e. the shell shows an oscillatory motion.

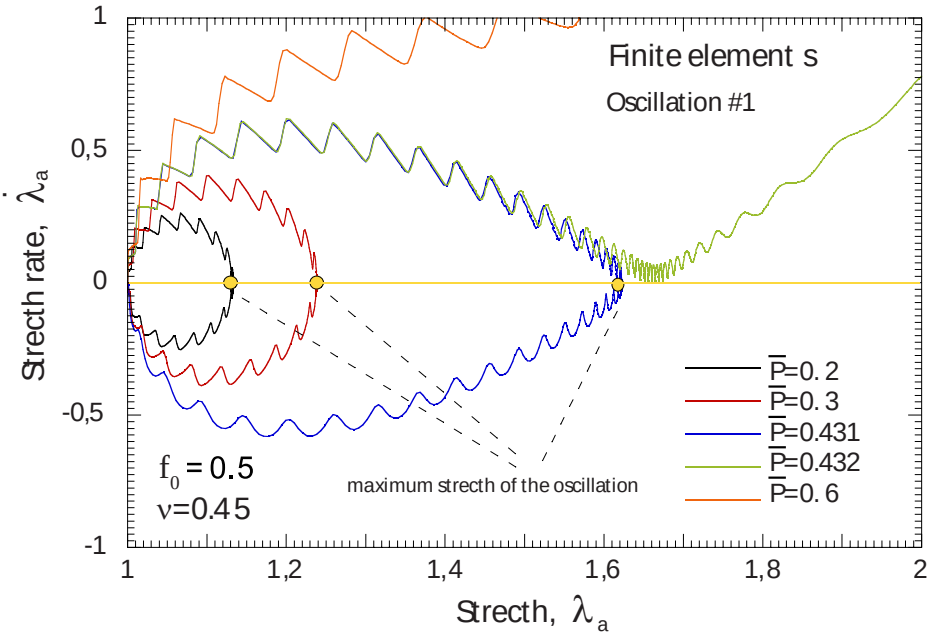

Fig. 5.5 Finite elements. Phase diagrams, $\dot{\lambda}_a$ versus λ_a. Oscillation #1. Reference geometric condition and material behavior: thickness parameter $f_0 = 0.5$ and initial Poisson ratio $\nu = 0.45$. Several loading cases are considered: $\overline{P} = 0.2$, $\overline{P} = 0.3$, $\overline{P} = 0.431$, $\overline{P} = 0.432$ and $\overline{P} = 0.6$.

To be noticed that, as the pressure increases, the shape of the orbit becomes sharpened. For $\overline{P} = 0.432$ and $\overline{P} = 0.6$ the phase diagram is not closed, i.e. the shell undergoes an unbounded expansion. As anticipated, the applied pressure imposes limits to the oscillatory behavior of the shell. Note the differences between the phase portraits corresponding to $\overline{P} = 0.432$ and $\overline{P} = 0.6$. For $\overline{P} = 0.6$ the stretch rate is an increasing function of the stretch. On the contrary, for $\overline{P} = 0.432$ the stretch rate first increases until reaching a relative maximum, then decreases up to a point that $\dot{\lambda}_a$ comes close to zero (if $\dot{\lambda}_a$ reaches 0 an homoclinic orbit is obtained) and finally increases unbounded.

Fig. 5.6 depicts the applied pressure $\overline{P}$ versus the maximum stretch of the oscillation $\lambda_a|_{\dot{\lambda}_a=0}$. A comparison between finite differences and finite elements results is conducted. The agreement between both numerical procedures is remarkable. The amplitude of

the oscillation increases with the applied pressure. The $\overline{P} - \lambda_a|_{\dot{\lambda}_a=0}$ curve presents a power-type concave-down shape that extents up to $\lambda_a|_{\dot{\lambda}_a=0} \approx 1.663$. This value of the maximum stretch is reached for $\overline{P} \approx 0.431$ (pressure corresponding to the homoclinic orbit). Larger values of applied pressure lead to the unbounded expansion of the shell (see the open orbits for $\overline{P} \approx 0.432$ and $\overline{P} \approx 0.6$ in Fig. 5.5).

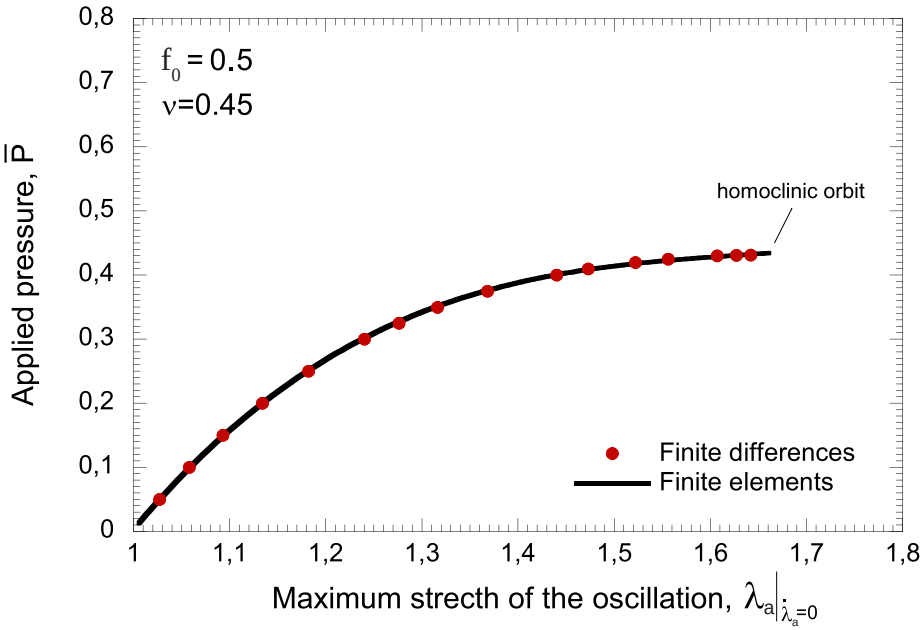

Fig. 5.6 Comparison between finite differences and finite elements. Applied pressure $\overline{P}$ versus maximum stretch of the oscillation $\lambda_a|_{\dot{\lambda}_a=0}$. Reference geometric condition and material behavior: thickness parameter $f_0 = 0.5$ and initial Poisson ratio $\nu = 0.45$.

5.6.2 The role played by the material compressibility

In this section we explore the role played by material compressibility in the dynamic response of the spherical shell. For that purpose, we have carried out ABAQUS/Explicit calculations using initial Poisson ratios within the range $0.05 \leq \nu < 0.5$. For the sake of brevity we do not show finite difference results. Nevertheless, we have checked that finite elements and finite differences show very good agreement. Recall that the results for the incompressible case ($\nu = 0.5$) are obtained from the analytical solution developed in the previous chapter (see Section 4.2, Eq. (4.15)). The reference thickness parameter $f_0 = 0.5$ is considered in all the calculations presented below.

Fig. 5.7 presents phase diagrams obtained using ABAQUS/Explicit for different Poisson ratios and two different applied pressures: $\overline{P} = 0.2$ in Fig. 5.7a and $\overline{P} = 0.3$ in Fig. 5.7b. The sawtooth form of the phase diagram is accentuated with the material

compressibility. The role of stress waves propagation in the dynamic response of the shell increases with the decrease of the initial Poisson ratio. Moreover, at the incompressible limit, the effect of pressure at the inner surface of the shell is felt instantaneously at all radii (no wave propagation), and the phase portrait does not show sawtooth form.

- For $\overline{P} = 0.2$ (see Fig. 5.7a) we have explored 8 different values of the Poisson ratio: 0.29, 0.3, 0.35, 0.4, 0.45, 0.475, 0.495 and 0.5. For $\nu = 0.29$ the shell expands unbounded, as illustrated by the open orbit of the phase diagram. For Poisson ratios $\nu \geq 0.3$ the phase diagram is a closed orbit, as corresponds to an oscillatory response of the shell. For a given applied pressure, the degree of compressibility of the material determines whether or not the shell shows an oscillatory response. Moreover, as ν increases, the maximum stretch of the oscillation decreases. For $\nu = 0.495$ the phase orbit virtually overlaps with the one obtained for the incompressible case and the sawtooth form of the phase diagram is practically negligible.

- For $\overline{P} = 0.3$ (see Fig. 5.7b) we have investigated 7 different values of the Poisson ratio: 0.35, 0.38, 0.4, 0.45, 0.475, 0.495 and 0.5. For $\nu = 0.35$ and $\nu = 0.38$, the open orbits of the phase diagram indicate that the shell expands unbounded. For Poisson ratios $\nu \geq 0.4$, the response of the shell is oscillatory. It becomes apparent that, as $\overline{P}$ increases, the loss of the oscillatory behavior of shell occurs for greater values of ν. Moreover, as in the case of $\overline{P} = 0.2$, for $\nu = 0.495$, the phase diagram can hardly be distinguished from the one corresponding to the incompressible case.

Fig. 5.8 depicts the applied pressure $\overline{P}$ versus the maximum stretch of the oscillation $\lambda_a|_{\dot{\lambda}_a=0}$ for various Poisson ratios $\nu = 0.1$, $\nu = 0.2$ $\nu = 0.3$, $\nu = 0.35$, $\nu = 0.4$, $\nu = 0.45$ and $\nu = 0.5$ (analytical solution). For each value of ν, the end of the curve indicates that an homoclinic orbit has been reached (see Section 5.6.1). Irrespective of the Poisson ratio, the $\overline{P} - \lambda_a|_{\dot{\lambda}_a=0}$ curve shows a power-type concave-down shape. As the value of ν increases, the $\overline{P} - \lambda_a|_{\dot{\lambda}_a=0}$ curve is shifted upwards. The pressure required to reach a given value of $\lambda_a|_{\dot{\lambda}_a=0}$ increases with the Poisson ratio. On the other hand, we observe that the maximum value of $\lambda_a|_{\dot{\lambda}_a=0}$, which corresponds to the homoclinic orbit, strongly decreases with the material compressibility.

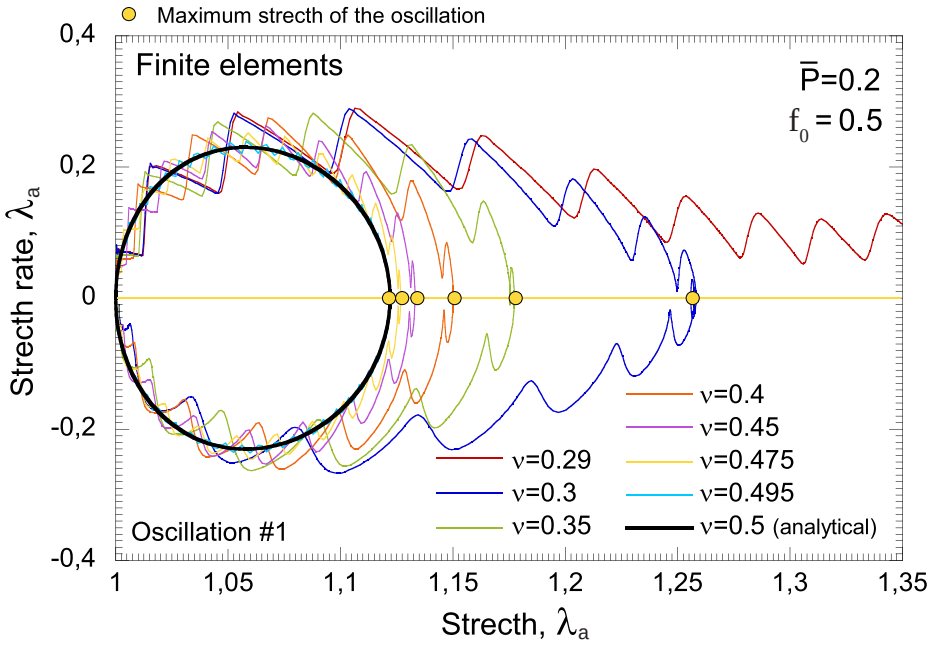

(a)

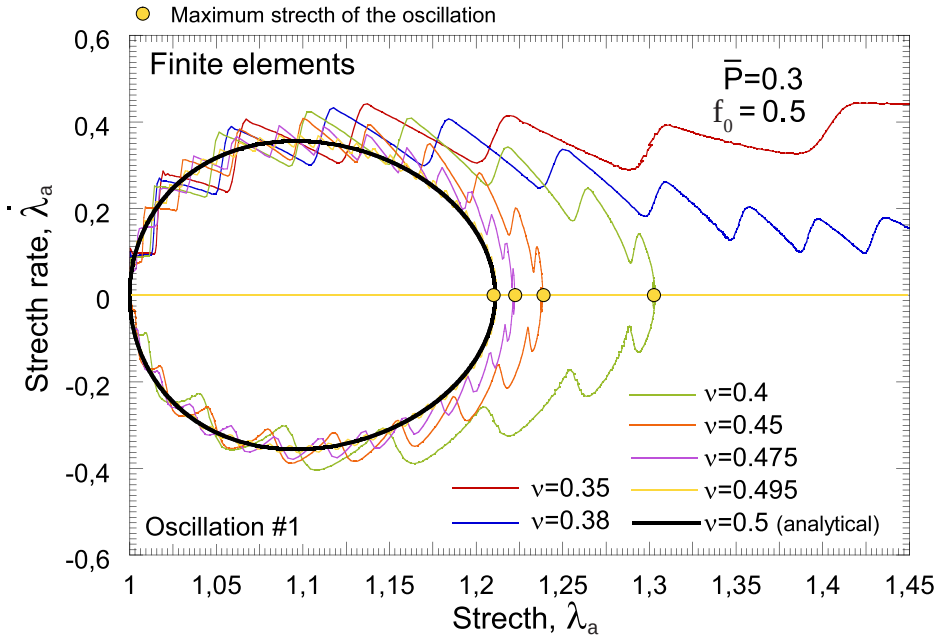

(b)

Fig. 5.7 Finite elements. Phase diagrams, $\dot{\lambda}_a$ versus λ_a. Oscillation #1. Reference geometric condition: thickness parameter $f_0 = 0.5$. Several initial Poisson ratios ranging from $\nu = 0.29$ to $\nu = 0.5$ (analytical solution) are considered. Two applied pressure are investigated: $\overline{P} = 0.2$ in (a) and $\overline{P} = 0.3$ in (b). (For interpretation of the colors coding of this figure, the reader is referred to the online version of this dissertation).

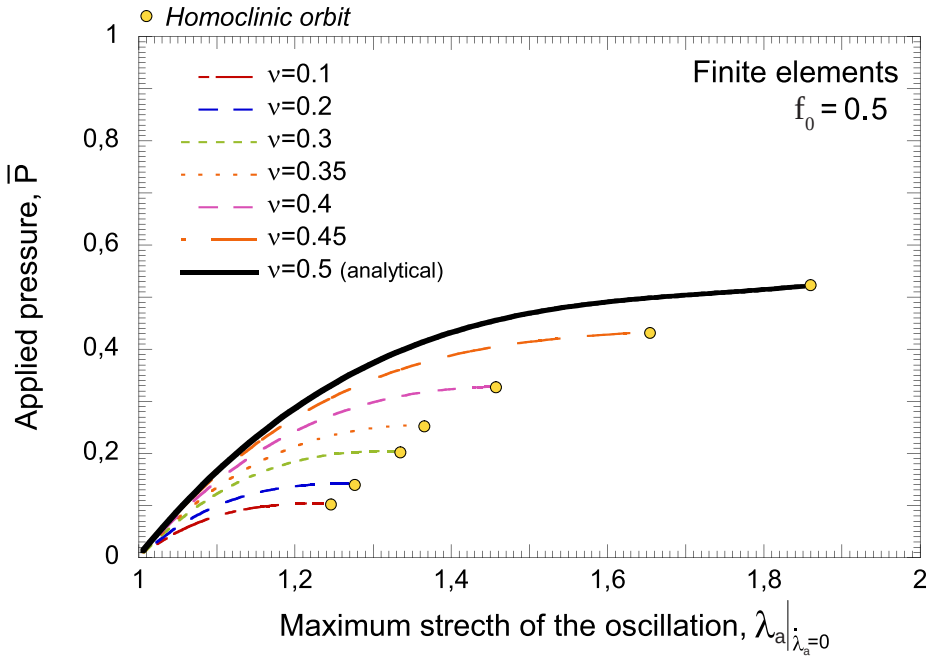

Fig. 5.8 Finite elements. Applied pressure $\overline{P}$ versus maximum stretch of the oscillation $\lambda_a|_{\dot{\lambda}_a=0}$. Reference geometric condition: thickness parameter $f_0 = 0.5$. Several initial Poisson ratios are considered: $\nu = 0.1$, $\nu = 0.2$, $\nu = 0.3$, $\nu = 0.35$, $\nu = 0.4$, $\nu = 0.45$ and $\nu = 0.5$ (analytical solution).

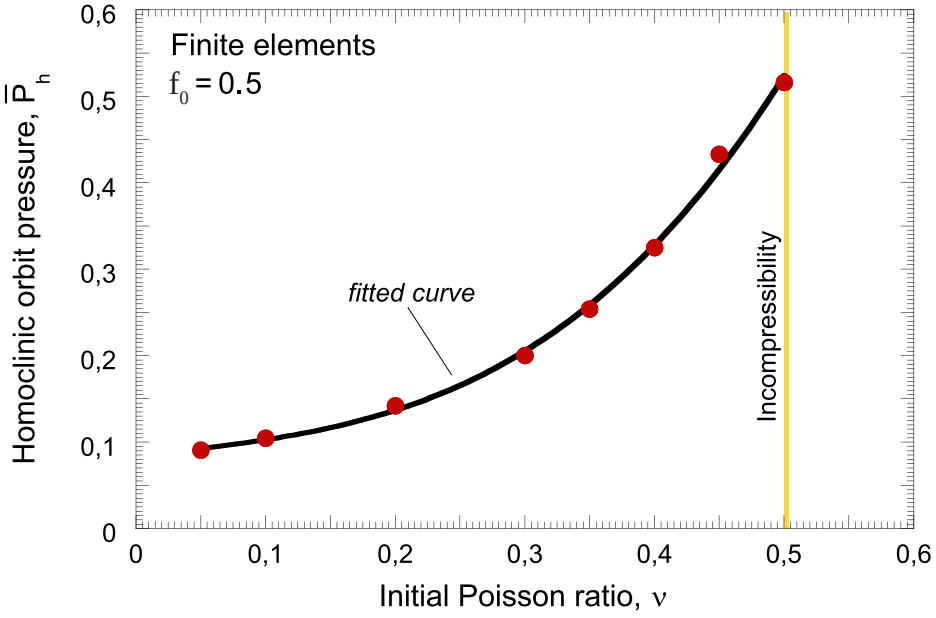

Fig. 5.9 Finite elements. Homoclinic orbit pressure $\overline{P}_h$ versus initial Poisson ratio ν. Reference geometric condition: thickness parameter $f_0 = 0.5$.

This is further illustrated in Fig. 5.9 where the applied pressure corresponding to the homoclinic orbit $\overline{P}_h$ is plotted as a function of the Poisson ratio ν. The $\overline{P}_h - \nu$ curve shows a power-type concave-up shape with a slope that increases as the Poisson ratio approaches incompressibility. While very low values of the Poisson ratio are explored (up to 0.05), for the sake of providing insights into the effect of compressibility on the dynamic response of the shell, we must recall that such values are not representative of rubber-like materials and may not be within the range for which Eq. (5.11) was derived and validated.

5.6.3 The role played by the shell thickness

In this section we assess the role played by the thickness in the dynamic response of the spherical shell. For that purpose, we have carried out finite elements calculations using thickness parameters which range from $f_0 = 1/6$ to $f_0 = 1/26$. The reference applied pressure $\overline{P} = 0.2$ is considered. The finite element simulations obtained using $\nu = 0.45$ are compared with the analytical solution developed for $\nu = 0.5$. While finite differences results are not shown for the sake of brevity, we have checked that they are in agreement with the finite elements calculations.

Fig. 5.10 depicts phase diagrams obtained for $f_0 = 1/6$, $f_0 = 1/11$ and $f_0 = 1/26$. We observe that, as the shell thickness increases, the phase plane orbit becomes gradually reduced: the oscillation is slower and shows smaller amplitude. As the thickness increases, the orbit corresponding to the compressible case looks *less and less* like the ellipse described by the incompressible limit. For $\nu = 0.45$ the number of reflections that occur during the oscillation of the shell decreases as the thickness increases. However, their effect in the shape of the phase portrait is more significant. It is apparent that the role of compressibility in the dynamic response of the spherical shells becomes more important as the thickness increases.

5.7 Summary and conclusions

In this chapter we have explored the role played by the material compressibility in the oscillatory behavior of spherical shells. The specimens have been subjected to a constant inflation pressure step. The compressible Mooney-Rivlin strain energy function has been used to model the material behavior. The investigation has been based on a two-pronged numerical approach: (1) we have implemented a finite differences model in MATLAB and (2) we have developed a finite elements model in ABAQUS/Explicit.

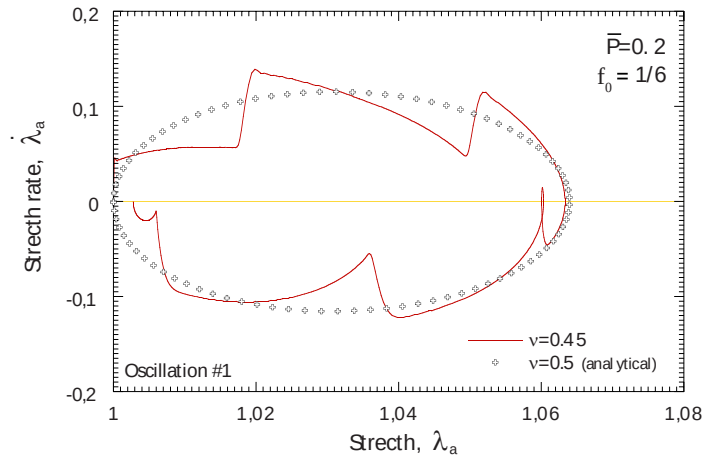

(a)

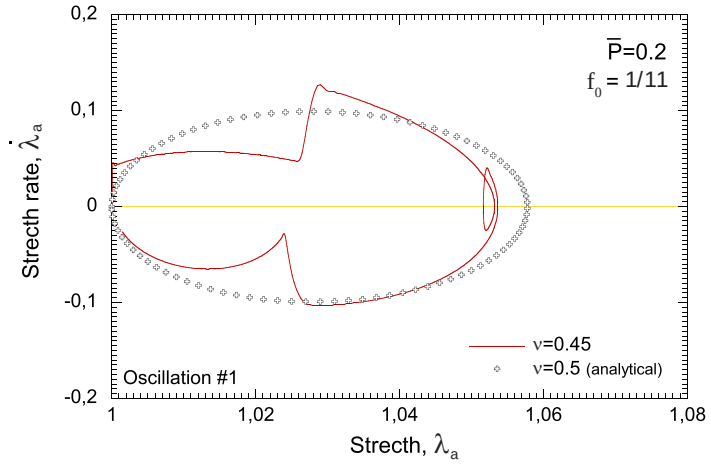

(b)

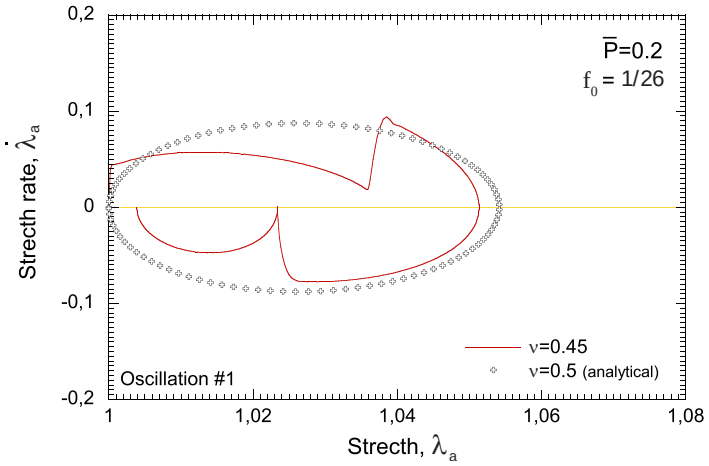

(c)

Fig. 5.10 Phase diagrams, $\dot{\lambda}_a$ versus λ_a. Oscillation #1. Reference loading case: applied pressure $\overline{P} = 0.2$. Three thickness parameters are considered: $f_0 = 1/6$, $f_0 = 1/11$ and $f_0 = 1/26$. Results are shown for two different initial Poisson ratios: $\nu = 0.45$ (finite elements) and $\nu = 0.5$ (analytical solution).

Compressible isotropic hyperelastic spherical structures: the role of stress waves propagation

We have shown that numerical dispersion and diffusion impose limits to the capacity of the finite differences and finite elements models to describe the shock wave that emanates from the inner surface of the shell due to the application of the inflation pressure. Nevertheless, both numerical approaches capture the essential features that describe the oscillatory behavior of the shell, including the maximum stretch of the oscillation. A key point of our methodology is that finite differences and finite elements models show complementary characteristics. The finite differences scheme provides flexibility and control over the formulation and resolution of the problem. As such, it allowed to uncover the physical phenomena that play a critical role in the dynamic response of the specimens. On the other hand, the finite element model presents significantly lower computational cost. As such, it allowed to develop a comprehensive parametric analysis that showed distinctive features of the oscillatory behavior of compressible shells. The systematic comparison and analysis of the finite differences and finite elements results led to the following conclusions:

- The maximum amplitude of the oscillation increases with the applied pressure.
- There is a critical pressure, which defines a critical oscillation amplitude, for which the oscillatory behavior of the shell is lost, leading to an unbounded expansion of the specimen.
- The critical pressure and the critical oscillation amplitude are strongly dependent on the material compressibility.
- The phase portraits used to represent the oscillatory behavior of compressible shells show a sawtooth form caused by the stress waves intervention within the specimen.
- The sawtooth form of the phase portraits is accentuated as the material compressibility and shell thickness increase.
- As the specimen thickness increases, the oscillation of the shell is slower and shows smaller amplitude.

All in all, we have developed an exhaustive numerical analysis that improves the seminal investigations of Haddow and co-workers (Haddow and Mioduchowski, 1977; Janele et al., 1989b) and provides new insights into the oscillatory behavior of compressible hyperelastic spherical shells subjected to dynamic inflation.

Part III

1D finite vibrations of isotropic visco-hyperelastic structures

6 Incompressible isotropic visco-hyperelastic cylindrical structures

Periodic and quasi-periodic motion, and nonlinear resonances

In this chapter we analyze the non-linear oscillations of a thick-walled visco-elastic cylindrical shell subjected to radially symmetric dynamic inflation. The goal is to extend the analysis developed in Chapter 3 to visco-elastic materials. For that purpose, we use the constitutive model originally proposed by Kumar and Lopez-Pamies (2016). This model (that will also be used in Chapter 7) is derived as an specialization of the two potential constitutive framework — also known as the *generalized standard materials* framework — to rubber viscoelasticity. The constitutive formulation accounts for the non-Gaussian elasticity of elastomers, as well as for the deformation enhanced shear thinning of their viscous dissipation governed by reptation dynamics. Two different loading conditions have been considered: (1) a constant pressure and (2) a harmonic time-dependent pressure. Our analysis reveals the strong influence of the visocus dissipation in the dynamic response of the material. For instance, for the case of constant pressure, we have observed that viscosity reduces the load for which the cylinder expands unbounded. In addition, in the case that the response of the shell is oscillatory, we have shown that viscous dissipation gradually reduces the amplitude and velocity of the oscillations until the structure eventually stops. Moreover, for the case of time dependent applied pressure, we have obtained the complete nonlinear resonance diagrams of the structure which reveal the existence of escape bands for which the motion of the cylinder is not periodic.

6.1 Introduction

Kwak et al. (2001) defined *passive damping control as the structure's ability to damp its own oscillations as a result of its structural design or material properties or the incorporation of devices, such as coatings and elastomers, that generate energy dissipation.* As discussed in Chapter 1 of this dissertation, elastomeric isolators are nowadays among

the most widely used type of seismic isolators (Al-Anany and Tait, 2017), and a wide amount of research has been carried out to investigate their effectiveness for the seismic isolation of civil infrastructures (Ghobarah and Ali, 1988; Matsagar and Jangid, 2003; Tsopelas et al., 1996; Wesolowsky and Wilson, 2003). Elastomers are also widely used for vibration isolation in automotive and aerospace industries in order to, for instance, isolate the structure of the car/aircraft from the engine motions (Peng et al., 2015; Vahdati and Saunders, 2002). Within this context, the review of Ibrahim (2008) presents a comprehensive assessment of recent developments of nonlinear isolators in the absence of active control means. Specifically, chapter 7 of this celebrated paper highlights the damping ability of elastomers, which stems from their characteristic viscoelastic behavior Chung (2001), and their extensive in various industrial applications.

The rate dependent response of various types of rubbers (vulcanized rubber, natural rubber, acrylonitrile–butadiene rubber, styrene-butadiene rubber...) has been characterized experimentally, in tension and compression and within a wide range of strain rates, by several authors (Chen et al., 2002; Fatt and Ouyang, 2008; Harwood and Schallamach, 1967; Khan and Farrokh, 2006; Rao et al., 1997; Schallamach et al., 1966) over the last decades. However, the precise micro-structural mechanisms which govern their viscous behavior are not well understood. Nevertheless, in the literature can be found various ways to incorporate viscosity in the constitutive modeling of finite elasticity. For example, a plenty of integral formulations of nonlinear viscoelasticity started from Green and Rivlin (1957, 1960). Further developments are reviewed in Lockett (1972); Carreau et al. (1997); Hoo Fatt and Ouyang (2007) and Wineman (2009). There are also numerous differential formulations of nonlinear viscoelasticity based on the introduction of internal variables and their evolution equations: Lubliner (1985); Lion (1996); Reese and Govindjee (1998a); Bergström and Boyce (1998a); Huber and Tsakmakis (2000); Miehe and Keck (2000); Amin et al. (2006) and Aranda-Iglesias et al. (2017).

In this chapter of the dissertation we use the constitutive model developed by Kumar and Lopez-Pamies (2016), which has been shown to describe reasonably well the response of a broad variety of rubbers over wide ranges, to analyze the nonlinear vibrations of thick-walled cylindrical shells subjected to constant and harmonic time dependent pressure. Despite the large bunch of important applications in which viscoelastic elastomers are used as vibration isolators (as described above), the number of works which focus their attention on the specific influence that material viscosity has on the oscillatory response of hyperelastic structures is very limited (here it is worth mentioning the work of Verron et al. (2001)). For instance, we have shown that material viscosity reduces the critical applied pressure for which the oscillatory response of the structure ceases, leading to the

unbounded expansion of the cylinder. In addition, in the case of time dependent applied pressure, we have obtained the resonances diagrams of the structure and showed that, for certain applied frequency, due to the viscous response of the structure, the motion of the cylinder may turn from periodic to quasi-periodic.

6.2 Problem formulation

In this section we formulate the problem of a infinitely long thick-walled cylinder (plane strain along the axial direction) made of a nonlinear viscoelastic material and subjected to constant and harmonica time dependent pressure. As such, we extend the formulation developed in Chapter 3 to rate dependent materials.

Recall from previous chapters that the current position vector $\mathbf{x}$ in the deformed configuration $\Omega \subset \mathbb{R}^3$ at time t of the material point that occupies the location $\mathbf{X} \in \Omega_0$ is given by $\mathbf{x} = \boldsymbol{\chi}(\mathbf{X}, t)$, where $\boldsymbol{\chi}$ is a bijective and twice continuously differentiable mapping. The associated deformation gradient, right Cauchy-Green strain tensor and volume ratio at $\mathbf{X} \in \Omega_0$ are denoted by

$$\begin{gathered}\mathbf{F}(\mathbf{X}, t) = \operatorname{Grad} \boldsymbol{\chi}(\mathbf{X}, t), \ \mathbf{C}(\mathbf{X}, t) = \mathbf{F}^{\mathrm{T}}(\mathbf{X}, t)\mathbf{F}(\mathbf{X}, t), \\ J(\mathbf{X}, t) = \det \mathbf{F}(\mathbf{X}, t).\end{gathered} \tag{6.1}$$

Moreover, the balance of linear momentum in the material description is

$$\operatorname{Div} \mathbf{S}(\mathbf{X}, t) = \rho_0 \ddot{\boldsymbol{\chi}}(\mathbf{X}, t) \quad \text{in} \quad \Omega_0, \tag{6.2}$$

where the dots denote differentiation with respect to time, $\mathbf{S}$ stands for the first Piola-Kirchhoff stress tensor, and ρ_0 is the constant mass density of the shell material in its undeformed configuration Ω_0.

6.2.1 Constitutive model

Following Kumar and Lopez-Pamies (2016) the shell is assumed to be made up of an isotropic incompressible nonlinear viscoelastic solid whose constitutive response is described by two thermodynamic potentials, a free energy function ψ and a dissipation potential ϕ that are functions of the deformation gradient $\mathbf{F}$ and of an internal variable

$\mathbf{F}^v$ that serves to measure the viscous part of the deformation

$$\psi = \psi(\mathbf{F}, \mathbf{F}^v) \qquad \text{and} \qquad \phi = \phi(\mathbf{F}, \mathbf{F}^v, \dot{\mathbf{F}}^v). \tag{6.3}$$

To proceed further, it is necessary to precisely define the internal variable $\mathbf{F}^v$. Consistently with the rehological model presented in Fig. 6.1, we assume the following multiplicative decomposition of the deformation gradient tensor (Bergstrom, 2015)

$$\mathbf{F} = \mathbf{F}^e\mathbf{F}^v, \tag{6.4}$$

which defines $\mathbf{F}^v$ and where $\mathbf{F}^e$ can be interpreted as the deformation gradient tensor associated with the underlying elastic mapping[1].

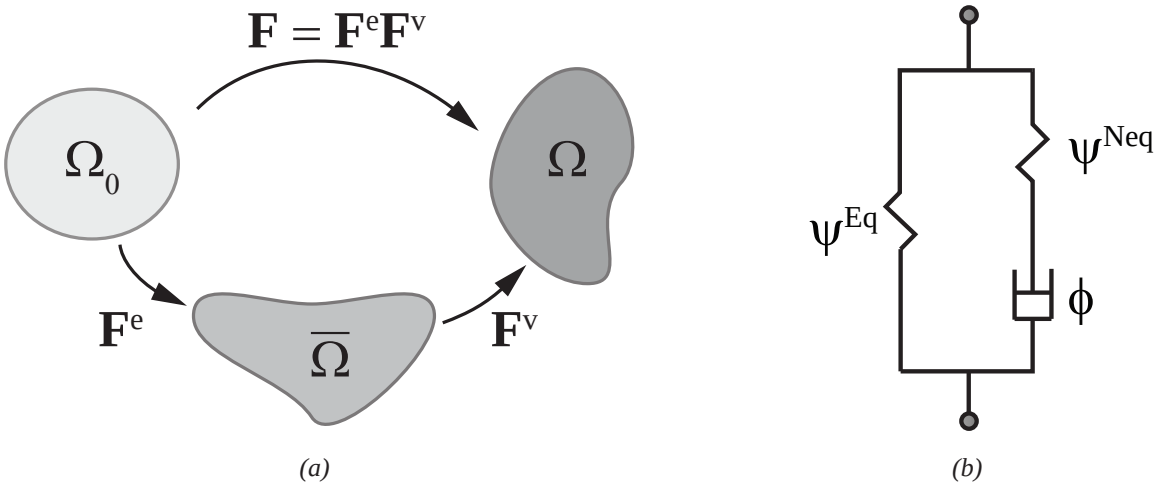

Fig. 6.1 (a) Kinematics of the constitutive model showing the reference or initial configuration Ω_0, the intermediate configuration $\overline{\Omega}$ and the deformed one Ω. (b) Rheological scheme of the constitutive model.

It follows that at each material point $\mathbf{X} \in \Omega_0$ the first Piola-Kirchhoff stress tensor $\mathbf{S}$ is given in terms of $\mathbf{F}$ and $\mathbf{F}^v$ by

$$\mathbf{S} = \frac{\partial \psi}{\partial \mathbf{F}}(\mathbf{F}, \mathbf{F}^v) - p\mathbf{F}^{-T}, \tag{6.5}$$

[1]It should be noted that Eq. (6.4) is a constitutive assumption and other decompositions consistent with the requirements of rubber viscoelasticity, such as $\mathbf{F} = \mathbf{F}^v\mathbf{F}^e$, could be made leading to a different definition of $\mathbf{F}^v$.

where p stands for the arbitrary hydrostatic pressure associated with the incompressibility constraint and $\mathbf{F}^v$ is defined implicitly via the nonlinear ordinary differential equation

$$\frac{\partial \psi}{\partial \mathbf{F}^v}(\mathbf{F}, \mathbf{F}^v) + \frac{\partial \phi}{\partial \dot{\mathbf{F}}^v}(\mathbf{F}, \mathbf{F}^v, \dot{\mathbf{F}}^v) = 0, \tag{6.6}$$

that we assume to be subjected to the initial condition $\mathbf{F}^v = \mathbf{I}$ at $t = 0$. More specifically, the free energy function ψ in the constitutive relation (6.5)–(6.6) is taken to be of the form

$$\psi(\mathbf{F}, \mathbf{F}^v) = \psi^{Eq}(\mathbf{F}) + \psi^{NEq}(\mathbf{F}\mathbf{F}^{v^{-1}}), \tag{6.7}$$

with ψ^{Eq} and ψ^{NEq} denoting any non-negative isotropic functions of choice. Physically, the free energy function ψ^{Eq} serves to characterize the nonlinear elasticity of the rubber at states of thermodynamic equilibrium, while ψ^{NEq} serves to characterize the additional nonlinear elasticity at non-equilibrium states that is to decay in time through viscous dissipation. Moreover, the dissipation potential ϕ in the constitutive relation (6.5)–(6.6) is taken to be of the form (Kumar and Lopez-Pamies, 2016)

$$\phi(\mathbf{F}, \mathbf{F}^v, \dot{\mathbf{F}}^v) = \frac{1}{2}\dot{\mathbf{F}}^v \cdot \mathbf{A}(\mathbf{F}, \mathbf{F}\mathbf{F}^{v^{-1}})\dot{\mathbf{F}}^v, \tag{6.8}$$

with $\mathbf{A}$ denoting any positive-definite fourth-order tensor function of choice such that $A_{ijkl}(\mathbf{QFK}, \mathbf{QFF}^{v^{-1}}) = K_{mj}A_{imkn}(\mathbf{F}, \mathbf{F}\mathbf{F}^{v^{-1}})K_{nl}$ for all $\mathbf{Q}$, $\mathbf{K} \in Orth^+$ and arbitrary $\mathbf{F}$, $\mathbf{F}^v$.

Let us remark that constitutive relations of the form (6.5)–(6.6) with (6.7)–(6.8) have been shown to describe reasonably well the response of a broad variety of rubbers over wide ranges of deformations and deformation rates (see, e.g., Le Tallec et al. (1993), Reese and Govindjee (1998b), Bergström and Boyce (1998b), Kumar and Lopez-Pamies (2016)). For illustration purposes and later reference, we conclude this subsection by spelling out the two-potential rubber viscoelastic model recently introduced by Kumar and Lopez-Pamies (2016). In that model, the free energy functions (6.7) read as follows

$$\psi^{Eq}(\mathbf{F}) = \begin{cases} \dfrac{3^{1-\alpha_1}}{2\alpha_1}\mu_1\left[I_1^{\alpha_1} - 3^{\alpha_1}\right] + \dfrac{3^{1-\alpha_2}}{2\alpha_2}\mu_2\left[I_1^{\alpha_2} - 3^{\alpha_2}\right] & \text{if} \quad \det\mathbf{F} = 1 \\ +\infty & \text{otherwise} \end{cases} \tag{6.9}$$

$$\psi^{NEq}(\mathbf{F}\mathbf{F}^{v^{-1}}) = \begin{cases} \dfrac{3^{1-a_1}}{2a_1}m_1\left[I_1^{e^{a_1}} - 3^{a_1}\right] + \dfrac{3^{1-a_2}}{2a_2}m_2\left[I_1^{e^{a_2}} - 3^{a_2}\right] & \text{if} \quad \det(\mathbf{F}\mathbf{F}^{v^{-1}}) = 1 \\ +\infty & \text{otherwise} \end{cases} \tag{6.10}$$

where $I_1 = \mathrm{tr}(\mathbf{F}^T\mathbf{F})$ and $I_1^e = \mathrm{tr}(\mathbf{C}\mathbf{C}^{v^{-1}})$ with $\mathbf{C} = \mathbf{F}^T\mathbf{F}$ and $\mathbf{C}^v = \mathbf{F}^{vT}\mathbf{F}^v$, while μ_1, α_1, μ_2, α_2, m_1, a_1, m_2, a_2 are real-valued material parameters that may be associated with the non-Gaussian statistical distribution of the underlying polymer chains in the rubber of interest (Lopez-Pamies, 2010). On the other hand, the dissipation potential

(6.8) reads as (Kumar and Lopez-Pamies, 2016)

$$\phi(\mathbf{F},\mathbf{F}^v,\dot{\mathbf{F}}^v)=\begin{cases}\eta_K \dot{F}^v_{ij}F^e_{mi}F^{-1}_{jn}\left[\mathcal{K}_{mnpq}+\mathcal{K}_{mnab}F^e_{ac}F^e_{qc}F^{e\,-1}_{db}F^{e\,-1}_{dp}\right]F^e_{pk}F^{-1}_{lq}\dot{F}^v_{kl} & \text{if} \quad \mathrm{tr}(\dot{\mathbf{F}}^v\mathbf{F}^{v^{-1}})=0\\ +\infty & \text{otherwise}\end{cases} \tag{6.11}$$

where $\mathbf{F}^e=\mathbf{F}\mathbf{F}^{v^{-1}}$, $\mathcal{K}_{ijkl}=1/2\,[\delta_{ik}\delta_{jl}+\delta_{il}\delta_{jk}-2/3\,\delta_{ij}\delta_{kl}]$ with δ_{ij} denoting the Kronecker delta (see Appendix A), and

$$\eta_K(I^e_1,I^e_2,I^v_1)=\eta_\infty+\frac{\eta_0-\eta_\infty+K_1\left[I_1^{v\,\beta_1}-3^{\beta_1}\right]}{1+\left(K_2\,J_2^{NEq}\right)^{\beta_2}} \quad \text{with} \quad J_2^{NEq}=\left(\frac{I_1^{e\,2}}{3}-I^e_2\right)\left(\sum_{r=1}^{2}3^{1-a_r}m_r I_1^{e\,a_r-1}\right)^2. \tag{6.12}$$

Here, $I^e_2=1/2[(\mathrm{tr}(\mathbf{C}\mathbf{C}^{v\,-1}))^2-\mathrm{tr}(\mathbf{C}^{v\,-1}\mathbf{C}\mathbf{C}^{v\,-1}\mathbf{C})]$, $I^v_1=\mathrm{tr}\mathbf{C}^v$, and η_0, η_∞, β_1, β_2, K_1, K_2 are real-valued material parameters that may be associated with the viscous dissipation that stems from the reptational motion of the underlying polymer chains in the rubber of interest (Doi and Edwards, 1988; Kumar and Lopez-Pamies, 2016). The constitutive relation (6.5)–(6.6) implied by the thermodynamic potentials (6.9)–(6.10) and (6.11) can be shown to be given by

$$\mathbf{S}=\left[\sum_{r=1}^{2}3^{1-\alpha_r}\mu_r I_1^{\alpha_r-1}\right]\mathbf{F}+\left[\sum_{r=1}^{2}3^{1-a_r}m_r(\mathbf{C}\cdot\mathbf{C}^{v-1})^{a_r-1}\right]\mathbf{F}\mathbf{C}^{v-1}-p\,\mathbf{F}^{-T}, \tag{6.13}$$

where the symmetric second-order tensor $\mathbf{C}^v=\mathbf{F}^{vT}\mathbf{F}^v$ is solution of the following equation

$$\dot{\mathbf{C}}^v=\frac{\sum_{r=1}^{2}3^{1-a_r}m_r(\mathbf{C}\cdot\mathbf{C}^{v-1})^{a_r-1}}{\eta_K(I^e_1,I^e_2,I^v_1)}\left(\mathbf{C}-\frac{1}{3}(\mathbf{C}\cdot\mathbf{C}^{v-1})\mathbf{C}^v\right). \tag{6.14}$$

6.2.2 Radially symmetric dynamic deformation

The main issues of the formulation of the cylindrical shell subjected to radial pressure have already been presented in Chapter 3 of this dissertation. However, the introduction of a new viscoelastic constitutive model implies that new dissipative terms appear in the balance equation. Therefore, we found it convenient to provide the whole formulation of the problem, again, in this chapter of the thesis, even though some equations are repeated with respect to those presented in Chapter 3.

Let us define the reference configuration Ω_0 of the thick-walled **cylindrical** shell by the polar coordinates $\{R,\Theta,Z\}$ such that

$$A\le R\le B, \qquad 0\le\Theta\le 2\pi, \qquad 0\le Z\le L. \tag{6.15}$$

If we restrict our attention to radially symmetric motions with **plane strain in the Z direction**, the current geometry is given by

$$a(t) \leqslant r(R,t) \leqslant b(t), \qquad \theta = \Theta, \qquad z = Z, \tag{6.16}$$

where $\{r, \theta, z\}$ are cylindrical polar coordinates in the current configuration Ω. Under these conditions the deformation gradient can be expressed as follows

$$\mathbf{F} = \left(\frac{1}{\lambda(R,t)}\right) \mathbf{e}_r \otimes \mathbf{e}_r + \lambda(R,t)\, \mathbf{e}_\theta \otimes \mathbf{e}_\theta + \mathbf{e}_z \otimes \mathbf{e}_z, \tag{6.17}$$

where the principal stretches corresponding to the directions $\{r, \theta, z\}$ are given by

$$\lambda_r = \frac{\partial r(R,t)}{\partial R}, \quad \lambda_\theta = \frac{r(R,t)}{R} = \lambda, \quad \lambda_z = \frac{z}{Z} = 1, \tag{6.18}$$

and we have used the incompressibility restriction $J = \lambda_r(R,t)\lambda(R,t) = 1$. Similarly, the internal variable $\mathbf{F}^v$ defined implicitly by (6.6) admits the spectral representation

$$\mathbf{F}^v = \left(\frac{1}{\lambda^v(R,t)}\right) \mathbf{e}_r \otimes \mathbf{e}_r + \lambda^v(R,t)\, \mathbf{e}_\theta \otimes \mathbf{e}_\theta + \mathbf{e}_z \otimes \mathbf{e}_z, \tag{6.19}$$

where the scalar function $\lambda^v(R,t)$ is solution of a first-order nonlinear ordinary differential equation given by Eq. (6.14).

The first Piola-Kirchhoff stress tensor corresponding to the deformation gradient (6.17) and internal variable (6.19) can now be determined from (6.5)–(6.6) to be of the spectral form

$$\mathbf{S} = S_r(R,t)\, \mathbf{e}_r \otimes \mathbf{e}_r + S_\theta(R,t)\, \mathbf{e}_\theta \otimes \mathbf{e}_\theta + S_z(R,t)\mathbf{e}_z \otimes \mathbf{e}_z. \tag{6.20}$$

Furthermore, the principal stresses S_r and S_θ are such that (see e.g. Ogden (1997))

$$S_\theta(R,t) - \frac{S_r(R,t)}{\lambda^2(R,t)} = W'\left(\lambda(R,t)\right), \tag{6.21}$$

where

$$\begin{gathered} W'(\lambda) = \frac{\mathrm{d}W^{Eq}}{\mathrm{d}\lambda}(\lambda) + \frac{\mathrm{d}W^{NEq}}{\mathrm{d}\lambda}(\lambda/\lambda^v), \\ W^{Eq}(\lambda) = \psi^{Eq}(\mathbf{F}), \quad W^{NEq}(\lambda/\lambda^v) = \psi^{NEq}(\mathbf{F}\mathbf{F}^{v^{-1}}), \end{gathered} \tag{6.22}$$

and it is recalled that λ^v is defined implicitly by (6.14). In view of (6.20), the equation of balance of linear momentum (6.2) reduces to

$$\frac{\partial S_r(R,t)}{\partial R} + \frac{S_r(R,t) - S_\theta(R,t)}{R} = \rho_0 \, \ddot{r}(R,t) \tag{6.23}$$

Assuming now that the inner boundary ($R = A$) is subjected to a pressure $P_a(t)$, **per unit of current area**. While, the outer face ($R = B$) is subjected to a pressure $P_b(t)$, the boundary conditions are given by

$$S_r(A,t) = -P_a(t)\lambda_a \quad \text{and} \quad S_r(B,t) = -P_b(t)\lambda_b \tag{6.24}$$

Moreover, it follows from the incompressibility condition $J = \lambda_r(R,t)\lambda(R,t) = 1$ that

$$\lambda(R,t) = \left(\frac{B^2}{R^2}(\lambda_b^2(t) - 1) + 1\right)^{1/2} \tag{6.25}$$

where $\lambda_b(t) = b(t)/B$ stands for the circumferential stretch in the outer face. The expression (6.25) can be alternatively written as $\lambda(R,t) = (A^2/R^2(\lambda_a^2(t) - 1) + 1)^{1/2}$ in terms of the stretch in the inner face $\lambda_a(t) = a(t)/A$ (following the same notation of previous chapters). For our purposes here, we find dealing with the form (6.25) in terms of the outer stretch $\lambda_b(t)$ more convenient. As in previous chapters, taking the derivatives of Eq. (6.25) with respect to R and t we obtain the following relations

$$\frac{\partial \lambda}{\partial R} = -\frac{\lambda^2 - 1}{R\lambda} \tag{6.26}$$

$$\ddot{\lambda} = \frac{\lambda^2 - 1}{\lambda_b^2 - 1}\left[\frac{\dot{\lambda_b}^2 + \lambda_b \ddot{\lambda_b}}{\lambda} - \frac{\lambda_b^2 \dot{\lambda_b}^2}{\lambda_b^2 - 1}\frac{\lambda^2 - 1}{\lambda^3}\right], \tag{6.27}$$

where, as in previous chapters, **function arguments are omitted** here and in some of the subsequent development to ease notation. At this stage, it proves convenient to rewrite the equation of motion (6.23) with $\lambda(R,t)$ as the independent space variable instead of R. With help of the expressions (6.26) and (6.27) the result reads as

$$\frac{\partial}{\partial \lambda}\left[\frac{S_r}{\lambda}\right] = -\frac{S_\theta - \frac{S_r}{\lambda^2}}{\lambda^2 - 1} + \rho_0 B^2 \left[\frac{\lambda_b^2 \dot{\lambda}_b^2}{(\lambda_b^2 - 1)\lambda^3} - \frac{\dot{\lambda}_b^2 + \lambda_b \ddot{\lambda}_b}{\lambda(\lambda^2 - 1)}\right]. \tag{6.28}$$

After introducing the geometric dimensionless parameter $f_0 = A^2/B^2$, as in previous chapters, and some algebraic manipulation, the integration of the equation of motion

(6.28) with help of (6.21), (6.22), and (6.24), leads to

$$\Delta P = \int_{\lambda_b}^{\left(1+\frac{\lambda_b^2-1}{f_0}\right)^{1/2}} \frac{1}{\lambda^2-1}\frac{\mathrm{d}W^{Eq}(\lambda)}{\mathrm{d}\lambda}\mathrm{d}\lambda + \int_{\lambda_b}^{\left(1+\frac{\lambda_b^2-1}{f_0}\right)^{1/2}} \frac{1}{\lambda^2-1}\frac{\mathrm{d}W^{NEq}(\lambda/\lambda^v)}{\mathrm{d}\lambda}\mathrm{d}\lambda + \frac{\rho_0 B^2}{2}\left[\ln\left(\frac{\lambda_b^2}{\lambda_b^2+f_0-1}\right)\lambda_b\ddot{\lambda}_b + \left(\ln\left(\frac{\lambda_b^2}{\lambda_b^2+f_0-1}\right) + \frac{f_0-1}{\lambda_b^2+f_0-1}\right)\dot{\lambda}_b^2\right], \tag{6.29}$$

where the scalar function $\lambda^v(R,t)$ is solution of Eq. (6.14), which assuming radial symmetry takes the following form

$$\dot{\lambda}^v(R,t) = h\left(\lambda^v(R,t), \lambda(R,t)\right) \tag{6.30}$$

and we consider to be subjected to the initial condition $\lambda^v(R,0) = 1$, as introduced before. The precise form of the function $h(\cdot,\cdot)$ in (6.30) depends, of course, on the choice of free energy functions (6.7) and dissipation potential (6.8). For instance, the precise form of (6.30) for the choice (6.9)–(6.10) and (6.11) is given by

$$\dot{\lambda}^v = \frac{\left(\sum_{r=1}^{2} 3^{1-a_r} m_r \left(\frac{\lambda^{v2}}{\lambda^2} + \frac{\lambda^2}{\lambda^{v2}} + 1\right)^{a_r-1}\right)\left(2\lambda^2 - \frac{\lambda^{v4}}{\lambda^2} - \lambda^{v2}\right)}{6\lambda^v\left[\eta_\infty + \frac{\eta_0 - \eta_\infty + K_1\left[\left(\lambda^{v-2} + \lambda^{v2} + 1\right)^{\beta_1} - 3^{\beta_1}\right]}{1 + \left[\left(\frac{K_2}{3}\left(\frac{\lambda^{v4}}{\lambda^4} + \frac{\lambda^4}{\lambda^{v4}} - \frac{\lambda^{v2}}{\lambda^2} - \frac{\lambda^2}{\lambda^{v2}}\right)\left(\sum_{r=1}^{2} 3^{1-a_r} m_r \left(\frac{\lambda^{v2}}{\lambda^2} + \frac{\lambda^2}{\lambda^{v2}} + 1\right)^{a_r-1}\right)\right)^2\right]^{\beta_2}}\right]} \tag{6.31}$$

For any given applied pressure ΔP, equation (6.29) provides a nonlinear ordinary differential equation for the resulting deformation of the outer boundary, as characterized by λ_b, and hence, by virtue of (6.25), the resulting deformation of every material point in the shell.

Moreover, note that the first term in the right hand side of equation (6.29) corresponds to the pressure due to the elastic part of the response that is in thermodynamic equilibrium. The second term is the pressure stemming from the elastic part of the response that is *not* in thermodynamic equilibrium, namely, the elastic part that decays in time through viscous dissipation. The third and last term corresponds to the pressure due to inertial effects. Thus, the total pressure in the outer boundary can be understood as the sum of these three contributions:

$$P = P^{Eq} + P^{NEq} + P^{Dyn}. \tag{6.32}$$

Note that, unlike in previous chapters, we will not pose the problem in non-dimensional form since, due to the high number of parameters present in the dissipative potential, the dimensionless version of the equations (6.29) and (6.31) does not provide any additional insight into the problem.

6.3 Numerical solution

Following the results presented in Chapter 3, we analyze two different boundary conditions: (1) a constant pressure and (2) a harmonic time-dependent pressure. In order to obtain the stretch field λ_b from Eq. (6.29), we reduce this equation to a system of two first order ordinary differential equations. Calling $z_1 = \lambda_b$ and $z_2 = \dot{\lambda}_b$ we have

$$\dot{z_1} = z_2 \tag{6.33}$$

$$\dot{z_2} = \frac{\Delta P - P^{Eq} - P^{NEq} - \frac{\rho B^2}{2}\left(\ln\left(\frac{z_1^2}{z_1^2+f_0-1}\right) + \frac{f_0-1}{z_1^2+f_0-1}\right) z_2^2}{\frac{\rho B^2}{2}\ln\left(\frac{z_1^2}{z_1^2+f_0-1}\right) z_1} \tag{6.34}$$

Since the evolution equation (6.31) does not admit a closed-form solution for $\lambda^v(R,t)$, we solve it on Gauss quadrature abscissa and make use of the quadrature scheme to compute P^{Eq} and P^{NEq} as described below.

$$\dot{\lambda}_j^v = \frac{\left(\sum_{r=1}^{2} 3^{1-a_r} m_r \left(\frac{\lambda_j^{v2}}{\lambda_j^2} + \frac{\lambda_j^2}{\lambda_j^{v2}} + 1\right)^{a_r-1}\right)\left(2\lambda_j^2 - \frac{\lambda_j^{v4}}{\lambda_j^2} - \lambda_j^{v2}\right)}{6\lambda_j^v\left[\eta_\infty + \frac{\eta_0 - \eta_\infty + K_1\left[\left(\lambda_j^{v-2} + \lambda_j^{v2} + 1\right)^{\beta_1} - 3^{\beta_1}\right]}{1 + \left[\frac{K_2}{3}\left(\frac{\lambda_j^{v4}}{\lambda_j^4} + \frac{\lambda_j^4}{\lambda_j^{v4}} - \frac{\lambda_j^{v2}}{\lambda_j^2} - \frac{\lambda_j^2}{\lambda_j^{v2}}\right)\left(\sum_{r=1}^{2} 3^{1-a_r} m_r \left(\frac{\lambda_j^{v2}}{\lambda_j^2} + \frac{\lambda_j^2}{\lambda_j^{v2}} + 1\right)^{a_r-1}\right)\right]^{\beta_2}}\right]} \tag{6.35}$$

$$P^{Eq}(\lambda_b) = \frac{\lambda_b - \left(1 + \frac{\lambda_b^2-1}{f_0}\right)^{1/2}}{2} \sum_{j=1}^{n} w_j \frac{1}{\lambda_j^2 - 1} \left.\frac{\mathrm{d}W^{Eq}(z)}{\mathrm{d}z}\right|_{z=\lambda_j} \tag{6.36}$$

$$P^{NEq}(\lambda_b, \lambda_1^v, \lambda_2^v, ..., \lambda_n^v) = \frac{\lambda_b - \left(1 + \frac{\lambda_b^2-1}{f_0}\right)^{1/2}}{2} \sum_{j=1}^{n} w_j \left.\frac{\mathrm{d}W^{NEq}(z/\lambda_j^v)}{\mathrm{d}z}\right|_{z=\lambda_j} \tag{6.37}$$

where g_j are the Gauss points, w_j the Gauss weights and λ_j is related with λ_b as

$$\lambda_j = \frac{\lambda_b - \left(1 + \frac{\lambda_b^2-1}{f_0}\right)^{1/2}}{2} g_j + \frac{\lambda_b + \left(1 + \frac{\lambda_b^2-1}{f_0}\right)^{1/2}}{2} \tag{6.38}$$

Therefore, we end up with a system of $n+2$ first order ordinary differential equations for the variables $\{z_1, z_2, \lambda_1^v, \lambda_2^v, ..., \lambda_n^v\}$. Such a system has been solved by using the Matlab® inbuilt ordinary differential equation suite finding the best results with explicit fourth order Runge-Kutta algorithm. To be noticed that this scheme remains fairly general admitting any arbitrary boundary condition $\Delta P(t)$ (suitably well behaved) and can be easily extended to any visco-elastic material model (Bergström and Boyce, 1998b; Le Tallec et al., 1993; Reese and Govindjee, 1998b) as long as it can be defined within the two potential constitutive framework (see Kumar and Lopez-Pamies (2016)).

Furthermore, as in Chapter 4, we are interested in analyzing the frequency response of the structure. For this purpose, the system of $n+2$ ordinary differential equations stated above is complemented with the following two formulas, whose stable solutions are the non-autonomous terms $z_3(t) = \sin(\omega t)$ and $z_4(t) = \cos(\omega, t)$.

$$\dot{z_3} = z_3(1 - z_3^2 - z_4^2) - \omega\ z_4 \tag{6.39}$$

$$\dot{z_4} = z_4(1 - z_3^2 - z_4^2) + \omega\ z_3 \tag{6.40}$$

Hence, the resonance diagrams presented in the next section have been calculated using the shooting method and sequential continuation techniques introduced in Chapter 4 on the previous $n+4$ system of equations for the variables $\{z_1, z_2, z_3, z_4, \lambda_1^v, \lambda_2^v, ..., \lambda_n^v\}$.

6.4 Sample results

In this section, we present some sample results for the above-developed problem that are aimed to exemplify the main aspects of the nonlinear vibrations of the structure. Let us choose $B = 1$ m and $A = 0.707$ m, such that $f_0 = 0.5$ (as in previous chapter). Moreover, we make use of the free energy functions (6.9)-(6.10) and the dissipation potential (6.11) with material parameters $\mu_1 = 1$ MPa, $m_1 = 2$ MPa, $\mu_2 = m_2 = 0$, $\alpha_1 = \alpha_2 = a_1 = a_2 = 1$, $\eta_0 = 2.11$ MPa s, $\eta_\infty = 0.1$ MPa s, $\beta_1 = 3$, $\beta_2 = 1.929$, $K_1 = 442$ MPa s, $K_2 = 1289$ MPa^{-2}. This constitutive choice corresponds to a model that describes reasonably well the response of a Nitrile rubber over wide ranges of deformations and deformation rates (Bergström and Boyce, 1998b; Kumar and Lopez-Pamies, 2016). The mass density of the solid is taken as $\rho_0 = 1000$ kg/m^3.

Provided the material parameter stated above, the free energy functions (6.9)-(6.10) are reduced to Neo-Hookean forms with linear shear moduli μ_1 and m_1 respectively. We can find two different limit scenarios:

- If the thermodynamic equilibrium is satisfied during all the deformation process, i.e. quasi-static stretch rates, the non-equilibrium branch (see Fig. 6.1) will be almost inactive $\psi^{NEq}(\mathbf{F}\mathbf{F}^{v-1}) \approx 0$. Under these conditions the shear modulus of the visco-elastic material will be $\mu \approx \mu_1$
- On the other hand, if the non-equilibrium branch is fully activated during the deformation precess, i.e. high stretch rates, the linear shear modulus of the visco-elastic model will be $\mu = \mu_1 + m_1$.

These two cases, which establish the limits for the stiffness of the visco-elastic material, will be systematically recalled in the next section to analyze the results.

6.4.1 Autonomous system

Following Chapter 3, we start the analysis considering the cylindrical shell subjected to a constant pressure

$$\Delta P = P\ H(t) \tag{6.41}$$

where $H(t)$ is the Heaviside function. Under these loading conditions, the analysis developed in Chapter 3 to compute the bifurcation pressure or critical pressure P_{c+} (pressure that leads to the unbounded expansion of the cylinder) can be applied to the limit cases stated above (see Eq. (3.29)). Hence, the bifurcation pressure for the visco-elastic cylinder will be contained within the following range

$$P_{c+} \in \left(P_{c+}^{\min}, P_{c+}^{\max}\right) \tag{6.42}$$

where $P_{c+}^{\min} = \frac{\mu_1}{2} \ln\left(\frac{1}{f_0}\right)$ and $P_{c+}^{\max} = \frac{\mu_1+m_1}{2} \ln\left(\frac{1}{f_0}\right)$ are the minimum and maximum bifurcation pressures, respectively.

Fig. 6.2a depicts the phase portrait, $\dot{\lambda}_b$ versus λ_b, in the outer face of the cylinder for an applied pressure of $P = 0.45 P_{c+}^{\max}$. The solid orange line corresponds to the visco-elastic solid, while the dashed blue curve corresponds with the limit inviscid case with linear shear moduli $\mu = \mu_1 + m_1$. The amplitude of the first oscillation is comparable for the conservative and the dissipative systems, which implies that the non-equilibrium branch of the visco-elastic model is activated to a large extend. The amplitude of the first oscillation of the viscous material is only slightly greater than the counterpart of the inviscid material. Note also that, while the amplitude and velocity of the oscillations of the conservative system are independet of time (it could not be otherwise), the phase trajectories of the dissipative system evolve with time, as can be seen in Fig. 6.2b, which

presents the time evolution of the stretch in the outer face of the cylinder for the first 3 seconds of loading. The amplitude of the oscillations of the dissipative system first increases with time (for the first 2 oscillations) and then decays, roughly exponentially, due to the viscous dissipation of energy, until the shell stops in an attractor point.

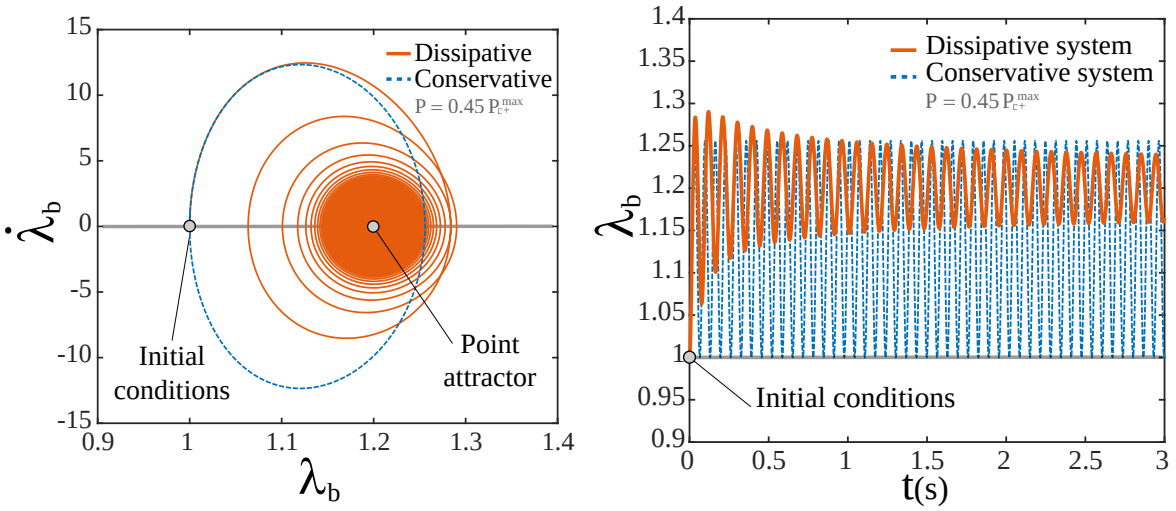

Fig. 6.2 (a) Phase portrait and (b) time evolution for an applied pressure of $P = 0.45P_{c+}^{max}$.

Fig. 6.3a depicts the phase portrait for an applied pressure of $P = 0.52P_{c+}^{\max}$, which corresponds with the bifurcation point for the visco-elastic cylinder. As anticipated, this pressure is contained within the range $P_{c+} \in \left(P_{c+}^{\min}, P_{c+}^{\max}\right)$. Note that the bifurcation of the visco-elastic material occurs in the second oscillation in a saddle point, the latter implying that the limit orbit is homoclinic. Moreover, Fig. 6.3b depicts the phase portrait for an applied pressure of $P = P_{c+}^{\max}$. This pressure corresponds with the bifurcation point for the conservative system. The corresponding phase trajectory for the inviscid material shows a second intersection with the λ_b-axis for $\lambda_b \to \infty$. It is apparent that the bifurcation behaviours for the viscid and inviscid materials are markedly different.

6.4.2 Non-autonomous system

In this section we analyze the periodically forced, non-autonomous, dissipative system. First we present the time evolution of the system to illustrate the dissipative role of the material viscosity that leads to the formation of a limit cycle (as in Chapter 4). Furthermore, we present the frequency-amplitude diagram of the system to illustrate the nonlinear resonance of the structure and the formation of scape bands due to the

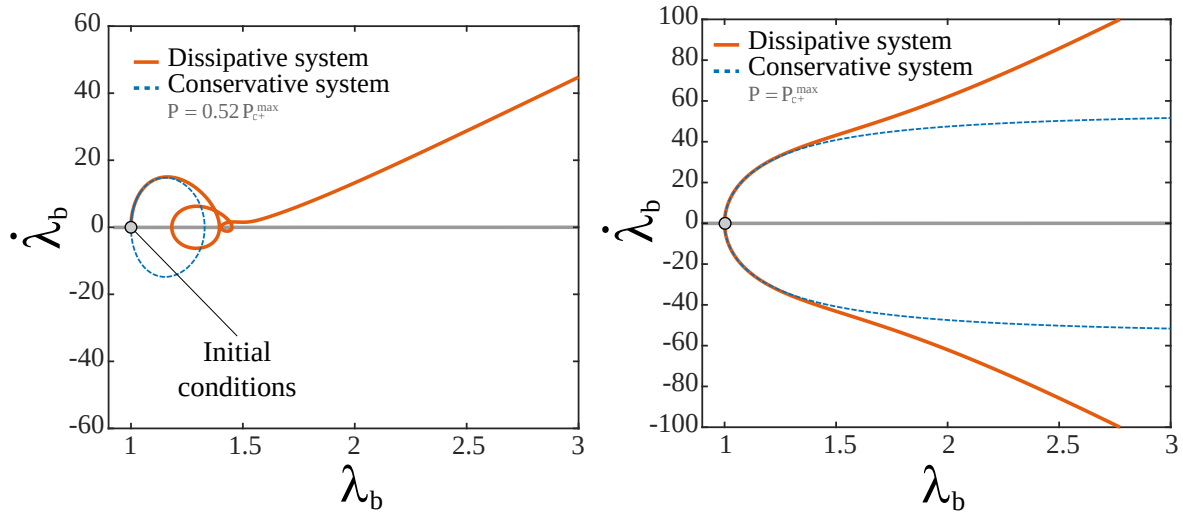

Fig. 6.3 Phase portraits for (a) $P = 0.52P_{c+}^{max}$, which corresponds with the bifurcation pressure of the dissipative system, and (b) $P = P_{c+}^{max}$, which corresponds with the bifurcation pressure of the conservative system.

material viscosity. As in Chapter 3, let us consider the following periodic applied pressure

$$\Delta P = P(1 + \cos(\omega\, t)) \tag{6.43}$$

As already introduced in Chapter 4, a good approximation to the resonance frequency of the system in the linear limit is given by $\omega_R = \sqrt{\frac{\mu}{\rho B^2}}$, where μ is the linear shear modulus of the material. Therefore, based on the limit cases introduced in Section 6.4 we can predict that the resonance frequency will be contained within the following range

$$\omega_R \in \left(\omega_R^{\min}, \omega_R^{\max}\right) \tag{6.44}$$

where $\omega_R^{\min} = \sqrt{\frac{\mu_1}{\rho B^2}} = 31.623$ Hz, and $\omega_R^{\max} = \sqrt{\frac{\mu_1+m_1}{\rho B^2}} = 54.77$ Hz, are the minimum and maximum resonance frequencies, respectively. In Fig. 6.4a we present the time evolution of the stretch $\lambda_b(t)$ during the first 5 seconds for an excitation frequency of $\omega = 54.77$ Hz and an applied pressure of $P = 0.2$ MPa. The transient and the steady states are identified with dashed blue line, and solid orange line, respectively. Identical loading case is depicted in the phase portrait of Fig. 6.4b, where the transient response of the systema and the formation of a limit cycle are very clearly defined.

We have used the shooting method and sequential continuation techniques introduced in Chapter 4 on the $n + 4$ system of equations (6.33)-(6.40) to analyze the frequency response of the structure. Fig. 6.5a depicts the amplitude-frequency response of the

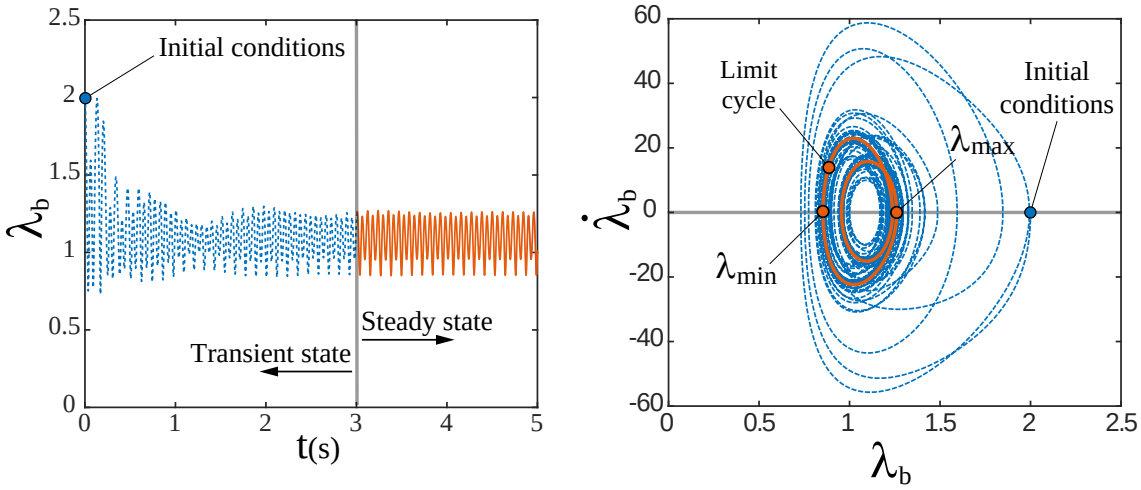

(a) *(b)*

Fig. 6.4 Response of the system for an excitation frequency of $\omega = 55.77$ Hz. Ten Gauss points have been used for the computations. (a) Time evolution of the stretch in the outer face of the cylinder. (b) Phase portrait.

cylinder for an applied pressure of $P = 0.2$ MPa. As for the Mooney-Rivlin material presented in Chapter 4, the $\lambda_{max} - \lambda_{min}$ excursions are tilted to the left. This behavior is called softening and implies that in order to rise the amplitude of the oscillations a decrease in the applied frequency is required. The onset of the main resonance frequency is located at $\omega \approx 54.77$ Hz and evolves until $\omega_r = 30$ due to the tilting of the excursion. The fact that the onset of the main resonance frequency which coincides with the upper limit of the expected range (see Eq. (6.44)) indicates that the non-equilibrium branch is activated almost completely under these loading conditions. Besides the main resonance, we have identified up to three super-harmonics resonances (with much smaller amplitude) at frequencies of 36.22, 27.35 and 21.95 Hz. The stable and unstable branches are indicated in blue solid and orange dashed lines, respectively.

For frequencies above the main resonance, we find a scape band between 88.9 and 131 Hz. In this frequency range, it is not possible to find stable periodic solutions. As an example, figures 6.5b and 6.5c depict the time evolution of the stretch and the Poincaré section for an excitation frequency of $\omega = 100$ Hz. In Fig. 6.5b than the peaks corresponding to the maximum stretch rate of the osccilations do not take the same value, but evolve with time. In 6.5c the closed curve of the Poincaré is a clear indicator of the quasi-periodic character of the solution.

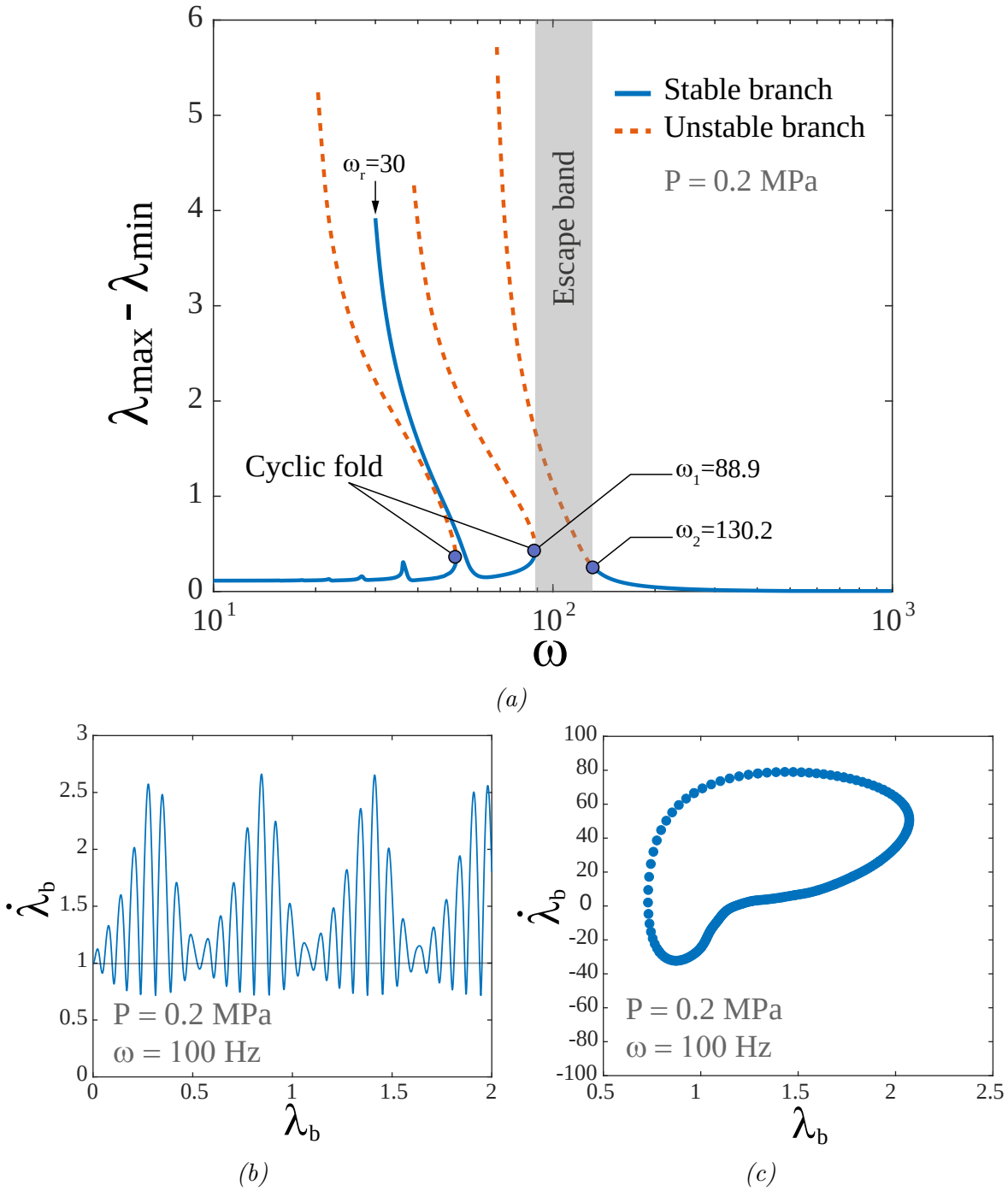

Fig. 6.5 (a) Amplitude-frequency response of the system for an applied pressure of $P = 0.2$ MPa, ten Gauss points have been used in the computations. (b) Time evolution of the stretch in the outer face of the cylinder for a excitation frequency of $\omega = 100$ and $P = 0.2$ MPa. (c) Poincaré section of a solution with excitation frequency of $\omega = 100$ and $P = 0.2$ MPa. The closed curve indicates a quasi-periodic behavior.

6.5 Summary and conclusions

In this chapter we have extended the formulation and analysis developed in Chapter 3 including viscosity in the formulation of the constitutive model used to describe the mechanical response of the cylindrical shell. For that purpose we have used the constitutive description developed by Kumar and Lopez-Pamies (2016) which uses an internal variable to take into account viscous dissipation within the so-called two-potential framework. As in Chapter 3 we have subjected the cylindrical shell to two different boundary conditions: (1) constant pressure and (2) time dependent harmonic pressure. The following key results have been obtained:

- Constant pressure: we have shown that material viscosity reduces the maximum pressure for which the oscillatory response of the structure ceases, leading to the unbounded expansion of the shell. Moreover, for the cases in which the response of the shell is oscillatory, we have shown that viscous dissipation gradually reduces the amplitude and speed of the oscillaotions, leading to the complete stop of the structure provided that sufficiently long times are reached. This behaviour is drastically different to that observed for inviscid materials for which, in absence of any other dissipative source, the structure always oscillate following a given trajectory in the phase plane.

- Time dependent harmonic pressure: following the procedure presented in Chapter 4, we have obtained the complete resonance diagrams of the structure. The key point is the identification of scape bands for which the system cannot reach a limit cycle, i.e. there is no balance between the work of the applied pressure and the energy dissipated by the viscosity of the material. In these cases, we have checked using a Poincaré map representation that the motion of the shell becomes quasi-periodic.

In summary, in this chapter we have presented one of the first studies ever performed on the oscillatory response of visco-hyperelastic shells. We have made clear the relevance of viscous dissipation effects in the response of the structure, which proves the necesity of using accurate constitutive formulations (which include viscosity) in the description of rubber-like materials used in applications of high structural responsibility, like those described in the introductory section of this dissertation.

7 Incompressible isotropic visco-hyperelastic spherical structures

The role of inertia and viscosity in the onset of cavitation

The prevailing belief that the nonlinear elastic properties of rubber play a significant role in the so-called phenomenon of cavitation — that is, the sudden growth of inherent defects in rubber into large enclosed cavities/cracks in response to external stimuli — has recently been supported with experiments by Lefevre et al. (2014). These comparisons have also shown that cavitation in rubber may possibly depend, in addition to the nonlinear elastic properties of the rubber, on inertial effects and/or on the viscous dissipation innate to rubber. This is because the growth of defects into large cavities is locally in time a very fast process.

The purpose of this chapter is to provide further theoretical insights into the relevance of inertial and viscous dissipation effects on the onset of cavitation in rubber. To this end, we consider the basic problem of the radially symmetric dynamic deformation of a spherical defect embedded at the center of a ball made up of an isotropic incompressible nonlinear visco-elastic solid that is subjected to external hydrostatic loading. Specifically, the defect is taken to be vacuous and the visco-elastic behavior of the solid is characterized by the constitutive model originally developed by Kumar and Lopez-Pamies (2016), which was introduced in Chapter 6. It has been found that, at high strain rates, inertia effect play a fundamental role in the onset and development of the cavitation process, on top of viscous dissipation that controls the process at quasi-static loading, when inertia effects are negligible.

7.1 Introduction

With the objective of probing the long-conjectured significance of nonlinear elastic properties in the phenomenon of cavitation in rubber, Lefevre et al. (2014) have recently carried out full-field simulations of the classical experiments of Gent and Lindley (1959)

and Gent and Park (1984) under the premises that the rubber utilized in their specimens was nonlinear elastic (for arbitrarily large deformations) and that the underlying defects at which cavitation could initiate were vacuous and their spatial distribution was random and isotropic. Their results have indicated that accounting just for the nonlinear elasticity of the rubber and the presence of defects suffices, to a great extent, to describe and explain the experiments in the sense of: (*i*) when and where cavitation first occurs (Lopez-Pamies et al., 2011a,b) as well as (*ii*) how cavities continue to grow and interact once they have been *nucleated*. Their results have also suggested that cavitation in rubber may possibly depend, in addition to the nonlinear elastic properties of the materials, on inertial effects and/or on the viscous dissipation innate to rubber. This is because the growth of defects into large cavities is locally in time a very fast process involving stretch rates that exceed 1000 s^{-1}.

The object of this chapter is to provide insight into the relevance of inertial and viscous dissipation effects in the onset of cavitation in rubber. To this end we analyze the basic problem of the radially symmetric dynamic deformation of a single spherical vacuous cavity, or defect, embedded at the center of a ball made up of an isotropic incompressible nonlinear viscoelastic solid that is subjected to external hydrostatic loading. The viscoelastic behavior of the solid is taken to be characterized by the constitutive model originally developed by Kumar and Lopez-Pamies (2016), which was described in Chapter 6 of this dissertation.

To put the problem at hand in perspective, it is fitting to mention that the radially symmetric dynamic deformation of a single spherical cavity embedded in an isotropic *incompressible* nonlinear *elastic* solid appears to have been first examined as early as the 1960s by Zhong-Heng and Solecki (1963) and by Knowles and Jakub (1965). These authors restricted attention to the case when the cavity wall is subjected to a sudden constant pressure while the outer boundary of the solid is traction free and did not concern themselves with exploring the phenomenon of cavitation. About twenty five years later, Chou-Wang and Horgan (1989) made use of the generic solution provided in Knowles and Jakub (1965); Zhong-Heng and Solecki (1963) to study the onset of radially symmetric dynamic cavitation in a Neo-Hookean solid for the specific case when the solid is subjected to a sudden constant pressure on its boundary. Around the same time, the more complex problem of the onset of radially symmetric dynamic cavitation in an isotropic *compressible* nonlinear *elastic* solid was investigated by Pericak-Spector and Spector (1988); see also the more recent works of Pericak-Spector and Spector (1997), Choksi (1997), Giesselmann and Tzavaras (2013) and Miroshnikov and Tzavaras (2015). In particular, motivated by the work of Ball (1982), these authors looked for a special

class of radially symmetric discontinuous solutions — referred to as similarity solutions and physically corresponding to a hole that opens up at the center of the ball — for the equations of elastodynamics in an isotropic compressible ball (without any defect) that is subjected to isotropic affine deformations on its boundary. Much like in elastostatics (Ball, 1982), they found that such solutions exists, and are admissible in the sense of entropy criteria for hyperbolic pdes Lax (1973), so long as the growth conditions of the stored-energy function describing the elasticity of the ball are sufficiently slow.

In contrast to the above-outlined considerable body of work on radially symmetric *elasto*dynamic cavitation, as far as the authors know, the only two results incorporating viscous dissipation in the onset of (either static or dynamic) cavitation in rubber are contained in Cohen and Molinari (2015); Yun and Zhuping (2003). In Yun and Zhuping (2003), the authors presented results for the radially symmetric *static* growth of a vacuous spherical cavity embedded in a certain internal-variable-type nonlinear viscoelastic solid that is subjected on its outer boundary to a hydrostatic pressure that is increased at a constant rate. In Cohen and Molinari (2015), the authors presented results for the radially symmetric *dynamic* growth of a spherical cavity embedded in a certain hereditary-integral-type nonlinear viscoelastic solid that is subjected to two types of displacement boundary conditions on its inner boundary, namely, a sudden constant deformation and a deformation that is increased at a constant rate. In this chapter we complement the aforementioned works providing a thorough analysis on the effects that inertia and viscosity have on the grow rate of a cavity embedded in a rubber viscoelastic medium that is subjected to external hydrostatic loading.

7.2 Problem formulation

In this section we formulate and solve the problem of the radially symmetric dynamic deformation of a spherical vacuous cavity included in the center of a viscoelastic ball and subjected to hydrostatic pressure that increases linearly with time.

Recall from previous chapters that the current position vector $\mathbf{x}$ in the deformed configuration $\Omega \subset \mathbb{R}^3$ at time t of the material point that occupies the location $\mathbf{X} \in \Omega_0$ is given by $\mathbf{x} = \boldsymbol{\chi}(\mathbf{X}, t)$, where $\boldsymbol{\chi}$ is a bijective and twice continuously differentiable mapping. The associated deformation gradient, right Cauchy-Green strain tensor and volume ratio at $\mathbf{X} \in \Omega_0$ are denoted by

$$\begin{gathered}\mathbf{F}(\mathbf{X}, t) = \operatorname{Grad} \boldsymbol{\chi}(\mathbf{X}, t), \ \mathbf{C}(\mathbf{X}, t) = \mathbf{F}^{\mathrm{T}}(\mathbf{X}, t)\mathbf{F}(\mathbf{X}, t), \\ J(\mathbf{X}, t) = \det \mathbf{F}(\mathbf{X}, t).\end{gathered} \tag{7.1}$$

Moreover, the balance of linear momentum in the material description requires that

$$\operatorname{Div}\mathbf{S}(\mathbf{X},t)=\rho_0\ddot{\boldsymbol{\chi}}(\mathbf{X},t)\quad\text{in}\quad\Omega_0, \tag{7.2}$$

where the dots denote differentiation with respect to time, $\mathbf{S}$ stands for the first Piola-Kirchhoff stress tensor, and ρ_0 is the constant mass density of the shell material in its undeformed configuration Ω_0.

7.2.1 Constitutive model

As in the previous chapter, the shell is assumed to be made up of an isotropic incompressible nonlinear viscoelastic solid whose constitutive response is described by the free energy functions (6.9)-(6.10) and the dissipation potential (6.11) firstly derived by Kumar and Lopez-Pamies (2016).

Let us recall that the constitutive relation (6.5)–(6.6) implied by the thermodynamic potentials (6.9)–(6.10) and (6.11) can be shown to be given by

$$\mathbf{S}=\left[\sum_{r=1}^{2}3^{1-\alpha_r}\mu_r I_1^{\alpha_r-1}\right]\mathbf{F}+\left[\sum_{r=1}^{2}3^{1-a_r}m_r(\mathbf{C}\cdot\mathbf{C}^{v-1})^{a_r-1}\right]\mathbf{F}\mathbf{C}^{v-1}-p\,\mathbf{F}^{-T}, \tag{7.3}$$

where the symmetric second-order tensor $\mathbf{C}^v=\mathbf{F}^{vT}\mathbf{F}^v$ is solution of the nonlinear ode

$$\dot{\mathbf{C}}^v=\frac{\sum_{r=1}^{2}3^{1-a_r}m_r(\mathbf{C}\cdot\mathbf{C}^{v-1})^{a_r-1}}{\eta_K(I_1^e,I_2^e,I_1^v)}\left(\mathbf{C}-\frac{1}{3}(\mathbf{C}\cdot\mathbf{C}^{v-1})\mathbf{C}^v\right). \tag{7.4}$$

7.2.2 Radially symmetric dynamic deformations

The basic features of the formulation of the spherically symmetric problem were presented in Chapter 4 of this dissertation. However, considering a different constitutive model leads to several differences in the formulation that, for the sake of clarity, is presented again below.

Consider a **spherical** structure with undeformed geometry Ω_0 defined by the polar coordinates (R,Θ,Φ) such that

$$A\le R\le B;\qquad 0\le\Theta\le 2\pi;\qquad 0\le\Phi\le\pi \tag{7.5}$$

Since the material is deformed so that the spherical symmetry is maintained, the motion is given by

$$r = r(R,t); \qquad \theta = \Theta; \qquad \phi = \Phi \tag{7.6}$$

where (r,θ,ϕ) are spherical polar coordinates in the current configuration Ω such that $a(t) \leq r(R,t) \leq b(t)$. Under these conditions the deformation gradient assumes the following form

$$\mathbf{F} = \left(\frac{1}{\lambda(R,t)}\right)^2 \mathbf{e}_r \otimes \mathbf{e}_r + \lambda(R,t)\, \mathbf{e}_\theta \otimes \mathbf{e}_\theta + \lambda(R,t)\, \mathbf{e}_\phi \otimes \mathbf{e}_\phi \tag{7.7}$$

where the principal stretches corresponding to the directions r,θ,ϕ are given by

$$\lambda_r(R,t) = \frac{\partial r(R,t)}{\partial R}; \quad \lambda(R,t) = \frac{r(R,t)}{R} = \lambda_\theta(R,t) = \lambda_\phi(R,t) \tag{7.8}$$

and the incompressibility restriction $J = \lambda_r(R,t)\, \lambda^2(R,t) = 1$ has been used. Similarly, the internal variable $\mathbf{F}^v$ defined implicitly by the ordinary differential equation (7.4) admits the following spectral representation

$$\mathbf{F}^v = \left(\frac{1}{\lambda^v(R,t)}\right)^2 \mathbf{e}_r \otimes \mathbf{e}_r + \lambda^v(R,t)\, \mathbf{e}_\theta \otimes \mathbf{e}_\theta + \lambda^v(R,t)\mathbf{e}_\phi \otimes \mathbf{e}_\phi \tag{7.9}$$

where the scalar function $\lambda^v(R,t)$ is solution of a first-order nonlinear ode given by Eq. (7.4).

The first Piola-Kirchhoff stress tensor corresponding to the deformation gradient (7.7) and internal variable (7.9) can now be determined from (7.3)–(7.4) to be of the spectral form

$$\mathbf{S} = S_r(R,t)\, \mathbf{e}_r \otimes \mathbf{e}_r + S_\theta(R,t)\, \mathbf{e}_\theta \otimes \mathbf{e}_\theta + S_\theta(R,t)\mathbf{e}_\phi \otimes \mathbf{e}_\phi. \tag{7.10}$$

Moreover, the principal stresses S_r and S_θ are such that

$$S_\theta(R,t) - \frac{S_r(R,t)}{\lambda^3(R,t)} = \frac{1}{2} W'\left(\lambda(R,t)\right). \tag{7.11}$$

where, as in the previous chapter, the strain-energy function $W(\lambda)$ is defined as

$$\begin{gathered} W'(\lambda) = \frac{\mathrm{d}W^{Eq}}{\mathrm{d}\lambda}(\lambda) + \frac{\mathrm{d}W^{NEq}}{\mathrm{d}\lambda}(\lambda/\lambda^v), \\ W^{Eq}(\lambda) = \psi^{Eq}(\mathbf{F}), \quad W^{NEq}(\lambda/\lambda^v) = \psi^{NEq}(\mathbf{F}\mathbf{F}^{v^{-1}}), \end{gathered} \tag{7.12}$$

and it is recalled that λ^v is defined implicitly by the ode (7.4).

In view of (7.10), the equation of balance of linear momentum (7.2) reduces to

$$\frac{\partial S_r(R,t)}{\partial R} + 2\frac{S_r(R,t) - S_\theta(R,t)}{R} = \rho_0 \ddot{r}(R,t). \tag{7.13}$$

Let us now consider, the inner boundary of the spherical shell to be traction free[1]. And the outer boundary to be subjected to the prescribed affine traction per unit of **undeformed** area

$$S_r(A,t) = 0 \quad \text{and} \quad S_r(B,t) = P(t), \tag{7.14}$$

where $P(t)$ is any function of choice (suitably well behaved). Moreover, we consider the following type of initial conditions

$$r(R,0) = R \quad \text{and} \quad \dot{r}(R,0) = 0. \tag{7.15}$$

It follows from the incompressibility condition that

$$\lambda(R,t) = \left(\frac{B^3}{R^3}(\lambda_b^3(t) - 1) + 1\right)^{1/3} \tag{7.16}$$

where $\lambda_b(t) = \frac{b(t)}{B}$ stands for the circumferential stretch in the outer surface of the visco-elastic ball[2]. We take the derivatives of Eq. (7.16) with respect to R and t to obtain respectively

$$\frac{\partial \lambda}{\partial R} = -\frac{\lambda^3 - 1}{R\lambda^2} \tag{7.17}$$

$$\ddot{\lambda} = \frac{\lambda^3 - 1}{\lambda_b^3 - 1}\left(\frac{2\lambda_b \dot{\lambda_b}^2 + \lambda_b^2 \ddot{\lambda_b}}{\lambda^2} - \frac{2\,\lambda_b^4 \dot{\lambda_b}^2}{\lambda_b^3 - 1}\frac{\lambda^3 - 1}{\lambda^5}\right) \tag{7.18}$$

At this stage, it proves convenient to rewrite the equation of motion (7.13) with $\lambda(R,t)$ as the independent space variable instead of R. With help of the expressions (7.17) and (7.18) the result reads as

$$-\frac{\partial}{\partial \lambda}\left[\frac{S_r}{\lambda^2}\right] = \frac{2\left(S_\theta - \dfrac{S_r}{\lambda^3}\right)}{\lambda^3 - 1} + \frac{\rho_0 B^2}{(\lambda_b^3 - 1)^{1/3}(\lambda^3 - 1)^{2/3}}\left[\frac{2\lambda_b^4 - 2\lambda_b\lambda^3}{\lambda^5(\lambda_b^3 - 1)}\dot{\lambda}_b^2 + \frac{\lambda_b^2}{\lambda^2}\ddot{\lambda}_b\right], \tag{7.19}$$

[1] Accounting for a pressurized cavity would not pose any additional difficulty

[2] The function (7.16) can be alternatively written as $\lambda(R,t) = \left(\frac{A^3}{R^3}(\lambda_a^3(t) - 1) + 1\right)^{1/3}$ in terms of the stretch in the inner face $\lambda_a(t) = a(t)/A$. For our purposes here, we find dealing with the form (7.16) in terms of the outer stretch $\lambda_b(t)$ more convenient.

where **function arguments are omitted** here and in most of the subsequent development to ease notation. After introducing the dimensionless geometric parameter $f_0 = A^3/B^3$ (as in previous chapters) to denote the initial volume fraction of the cavity and a little manipulation, the integration of the equation of motion (7.19) with help of (7.11), (7.12), and (7.14) leads to

$$P = \lambda_b^2 \int_{\lambda_b}^{\left(1+\frac{\lambda_b^3-1}{f_0}\right)^{1/3}} \frac{1}{z^3-1}\frac{\mathrm{d}W^{Eq}(z)}{\mathrm{d}z}\mathrm{d}z + \lambda_b^2 \int_{\lambda_b}^{\left(1+\frac{\lambda_b^3-1}{f_0}\right)^{1/3}} \frac{1}{z^3-1}\frac{\mathrm{d}W^{NEq}(z/\lambda^v)}{\mathrm{d}z}\mathrm{d}z + \rho_0 B^2 \lambda_b^2 \left[\left(\frac{2\lambda_b}{(\lambda_b^3+f_0-1)^{1/3}} - \frac{\lambda_b^4}{2(\lambda_b^3+f_0-1)^{4/3}} - \frac{3}{2}\right)\dot{\lambda}_b^2 + \left(\frac{\lambda_b}{(\lambda_b^3+f_0-1)^{1/3}} - 1\right)\lambda_b\ddot{\lambda}_b\right], \tag{7.20}$$

where the scalar function $\lambda^v(R,t)$ is solution of the equation (7.4), which assuming radial symmetry takes the following form

$$\dot{\lambda}^v(R,t) = h\left(\lambda^v(R,t), \lambda(R,t)\right) \tag{7.21}$$

with initial condition $\lambda^v(R,0) = 1$. The precise form of (7.21) for the free energy functions (6.9)–(6.10) and the dissipation potential (6.11) is given by

$$\dot{\lambda}^v = \frac{\left(\sum_{r=1}^{2} 3^{1-a_r} m_r \left(\frac{\lambda^{v2}}{z^2} + 2\frac{z^2}{\lambda^{v2}}\right)^{a_r-1}\right)\left(z^6 - \lambda^{v6}\right)}{6\lambda^v z^4 \left[\eta_\infty + \frac{\eta_0 - \eta_\infty + K_1\left[(2\lambda^{v2} + \lambda^{v-4})^{\beta_1} - 3^{\beta_1}\right]}{1 + \left(\frac{K_2}{3}\left(\frac{z^4}{\lambda^{v4}} + \frac{\lambda^{v8}}{z^8} - 2\frac{\lambda^{v2}}{z^2}\right)\left(\sum_{r=1}^{2} 3^{1-a_r} m_r \left(\frac{\lambda^{v2}}{z^2} + 2\frac{z^2}{\lambda^{v2}}\right)^{a_r-1}\right)^2\right)^{\beta_2}}\right]}. \tag{7.22}$$

For any given applied pressure P on the outer boundary of the shell, equation (7.20) provides a nonlinear ordinary differential equation for the resulting deformation of the outer boundary, as characterized by λ_b, and hence, by virtue of the incompressibility condition, Eq. (7.16), the resulting deformation of every material point in the shell. It is a simple matter to deduce that the initial conditions associated with the ordinary differential equation (7.20) for λ_b are given by $\lambda_b(0) = 1$ and $\dot{\lambda}_b(0) = 0$.

We recall from Chapter 6 that: the first term in the right hand side of equation (7.20) corresponds to the pressure due to the elastic part of the response that is in thermodynamic equilibrium, the second term is the pressure stemming from the elastic part of the response that is *not* in thermodynamic equilibrium and the third term corresponds to the pressure due to inertial effects. Thus, as anticipated in Chapter 6,

the total pressure in the outer boundary can be understood as the sum of these three contributions:

$$P = P^{Eq} + P^{NEq} + P^{Dyn}. \tag{7.23}$$

In the absence of viscous dissipation when $P^{NEq} = 0$, equation (7.20) reduces to the classical result in elastodynamics originally discussed in Knowles and Jakub (1965); Zhong-Heng and Solecki (1963). Moreover, in the additional absence of inertia when $P^{Dyn} = P^{NEq} = 0$, equation (7.20) reduces to the classical result in elastostatics originally discussed in Green and Zerna (1954):

$$P = P^{Eq} = \lambda_b^2 \int_{\lambda_b}^{\left(1+\frac{\lambda_b^3-1}{f_0}\right)^{1/3}} \frac{1}{z^3-1} \frac{\mathrm{d}W^{Eq}(z)}{\mathrm{d}z} \mathrm{d}z. \tag{7.24}$$

Note that,as in previous chapter, we do not pose the problem in non-dimensional form since, due to the high number of parameters present in the constitutive model, the dimensionless version of the governing equations does not provide any additional insight into the problem.

7.3 The limiting case of a vanishingly small cavity: $f_0 \to 0+$

Equation (7.20) is valid for shells with any value of initial volume fraction of cavity in the physical range $f_0 \in (0,1)$. We now focus on the special subclass of shells where the initial volume fraction of cavity is vanishingly small, that is, when $f_0 \to 0+$ and the cavity reduces to a point defect. Upon loading, the size of this defect may suddenly grow from its initially infinitesimal value to a *finite* value at some sufficiently large critical pressure, say P_{cr}. This event corresponds to the onset of cavitation. We denote by t_{cr} the first critical time t of its occurrence. According to (7.20), the critical pressure at which cavitation occurs is then given by

$$\begin{aligned} P_{cr} = \int_1^\infty \frac{1}{z^3-1} \frac{\mathrm{d}W^{Eq}(z)}{\mathrm{d}z} \mathrm{d}z + \int_1^\infty \frac{1}{z^3-1} \frac{\mathrm{d}W^{NEq}(z/\lambda^v)}{\mathrm{d}z} \mathrm{d}z + \\ \rho_0 B^2 \lim_{t\to t_{cr}} \left\{ \left(\frac{2\lambda_b}{(\lambda_b^3-1)^{1/3}} - \frac{\lambda_b^4}{2(\lambda_b^3-1)^{4/3}} - \frac{3}{2} \right) \lambda_b^2 \dot{\lambda}_b^2 + \left(\frac{\lambda_b}{(\lambda_b^3-1)^{1/3}} - 1 \right) \lambda_b^3 \ddot{\lambda}_b \right\}, \end{aligned} \tag{7.25}$$

where, again, λ_v is solution of (7.21) with $\lambda(R,t) = z$. The following remarks are in order:

i) As expected from the preceding discussion of the general form of equation (7.20), the first term in the right hand side of its asymptotic limit (7.25) corresponds to the classical result of Ball for the critical pressure at onset of radially symmetric cavitation in the context of elastostatics Ball (1982).

ii) For realistic models of rubber and irrespectively of the specifics of the applied pressure P, the second term in the right hand side of equation (7.25), that is, the term due to the presence of viscous dissipation, is non-negative and can be of the same order of magnitude as the first term. Physically this entails that *the presence of viscous dissipation can greatly increase the values of the critical pressure P_{cr} at which cavitation ensues in rubber, even when the external loads are applied quasi-statically.* This point is illustrated via some examples in the next section.

iii) The third term in the right hand side of equation (7.25), that is, the term due to inertia, can take on a wide range of positive as well as on negative values depending on the history of the applied pressure P prior to cavitation, namely, the values of P for times $t \in [0, t_{cr})$. This term and hence inertia becomes meaningful when the history of the applied pressure P involves high rates. This point is also illustrated via some examples in the next section.

iv) Much like in the basic context of elastostatic cavitation (see, e.g., Ball (1982)), the unbounded upper limits of integration in the first and second terms of the right hand side of equation (7.25) reveal that the value of the critical pressure P_{cr} depends on the viscoelastic behavior of the rubber at *infinitely large* deformations. While mathematically profound, this, of course, is physically incongruous since rubber behaves as a viscoelastic solid up to a critical set of large but *finite* deformations, beyond which, much like any other solid, it structurally fails. Nevertheless, in view of the recent analysis (Lefevre et al., 2014) of the experiments of Gent and Lindley (1959) and of Gent and Park (1984), equation (7.25) is expected to provide accurate *qualitative* insight into the effects of inertia and viscous dissipation in the onset of cavitation in rubber.

7.4 Sample results

In this section, we present sample numerical results from the above-developed analysis that are aimed at exemplifying the preceding remarks *ii* and *iii*.

For possible comparison with experiments, we choose $B = 1$ cm for the initial outer radius of the shell and consider the realistically small value $A = 10$ μm for the initial inner radius, which corresponds to an initial cavity volume fraction of $f_0 = 10^{-9}$. The hydrostatic pressure on the outer boundary of the shell is taken to be applied at a

constant rate. We write

$$P(t) = \dot{P}_0\, t, \tag{7.26}$$

where $\dot{P}_0$ stands for the prescribed constant pressure rate. Further, we make use of the constitutive model presented in Chapter 6 with material parameters $\mu_1 = 1$ MPa, $m_1 = 2$ MPa, $\mu_2 = m_2 = 0$, $\alpha_1 = \alpha_2 = a_1 = a_2 = 1$, $\eta_0 = 2.11$ MPa s, $\eta_\infty = 0.1$ MPa s, $\beta_1 = 3$, $\beta_2 = 1.929$, $K_1 = 442$ MPa s, $K_2 = 1289$ MPa^{-2}. As in previous chapter, this constitutive choice corresponds to a model that describes reasonably well the response of a Nitrile rubber over wide ranges of deformations and deformation rates Bergström and Boyce (1998b); Kumar and Lopez-Pamies (2016). The mass density of the solid is taken as $\rho_0 = 1000$ kg/m^3.

Granted the above inputs, equation (7.20) specializes to the ordinary differental equation

$$\begin{aligned}\dot{P}_0\, t = {}& \frac{\mu_1}{2}\left[\frac{1}{\lambda_b^2} + 4\lambda_b + \frac{f_0^{1/3}(4 - 5f_0 - 4\lambda_b^3)\lambda_b^2}{(\lambda_b^3 + f_0 - 1)^{4/3}}\right] + 2m_1\lambda_b^2 \int_{\lambda_b}^{\left(1+\frac{\lambda_b^3-1}{f_0}\right)^{1/3}} \frac{z^6 - {\lambda^v}^6}{{\lambda^v}^2 z^5 (z^3-1)}\mathrm{d}z \\ &+ \rho_0 B^2 \lambda_b^2 \left[\left(\frac{2\lambda_b}{(\lambda_b^3 + f_0 - 1)^{1/3}} - \frac{\lambda_b^4}{2(\lambda_b^3 + f_0 - 1)^{4/3}} - \frac{3}{2}\right)\dot{\lambda}_b^2 + \left(\frac{\lambda_b}{(\lambda_b^3 + f_0 - 1)^{1/3}} - 1\right)\lambda_b \ddot{\lambda}_b\right]\end{aligned} \tag{7.27}$$

for the stretch λ_b subject to the initial conditions

$$\lambda_b(0) = 1 \quad \text{and} \quad \dot{\lambda}_b(0) = 0, \tag{7.28}$$

where $\lambda^v = \lambda^v(z,t)$ is defined implicitly by the ode

$$\dot{\lambda}^v = \frac{m_1}{6\lambda^v z^4}\left[\frac{z^6 - {\lambda^v}^6}{\eta_\infty + \dfrac{\eta_0 - \eta_\infty + K_1\left[(2{\lambda^v}^2 + {\lambda^v}^{-4})^{\beta_1} - 3^{\beta_1}\right]}{1 + \left(\dfrac{K_2\, m_1^2}{3}\left[\left(\dfrac{z}{\lambda^v}\right)^4 + \left(\dfrac{z}{\lambda^v}\right)^{-8} - 2\left(\dfrac{z}{\lambda^v}\right)^{-2}\right]\right)^{\beta_2}}}\right]. \tag{7.29}$$

whit $\lambda^v(z,0) = 1$. While the initial-value problem (7.27)–(7.28) with (7.29) does not admit a closed-form solution, it is not difficult to generate numerical solutions for it. We employ here the straightforward approach introduced in Section 6.3, which consist of converting the second-order ordinary differential equation (7.27) into a system of first-order ordinary differential equations and to use Gaussian quadrature to evaluate the integral in (7.27). This approach leads to a system of $2 + n$ first-order ordinary differential equations, where n stands for the number of Gauss points utilized in the

quadrature. The solutions presented below correspond to $n = 100$ and are generated by means of an explicit fifth-order Runge-Kutta scheme (Lawson, 1966).

Figure 7.1 shows the growth of the volume fraction of the cavity in the shell $f = a^3/b^3 = (\lambda_b^3 + f_0 - 1)/\lambda_b^3$, normalized by its initial volume fraction f_0, as a function of the applied pressure (7.26) for three values of constant pressure rate $\dot{P}_0/(\mu_1 + m_1) = 1, 10^3$, and 5×10^5; recall that $\mu_1 = 1$ MPa and $m_1 = 2$ MPa so that these normalized constant pressure rates correspond to $\dot{P}_0 = 3$, 3×10^3, and 15×10^5 MPa/s. To aid the discussion, for all three constant pressure rates $\dot{P}_0/(\mu_1 + m_1) = 1, 10^3$, and 5×10^5, Fig. 7.2 shows as a function of time t the contributions (7.23) from each of the three terms P^{Eq}, P^{NEq}, P^{Dyn} that make up the value of the applied pressure P. Figure 7.2 includes plots as a function of t as well of the resulting stretch rate at the outer boundary of the shell $\dot{\lambda}_b$. For definiteness, all the plots in Figs. 7.1 and 7.2 are shown from $t = 0$ up to the point at which the current volume fraction of the cavity f grows to be four orders of magnitude larger than its initial volume fraction f_0. We consider this instance as the (approximate) time at which cavitation ensues and identify it by t_{cr} in the plots.

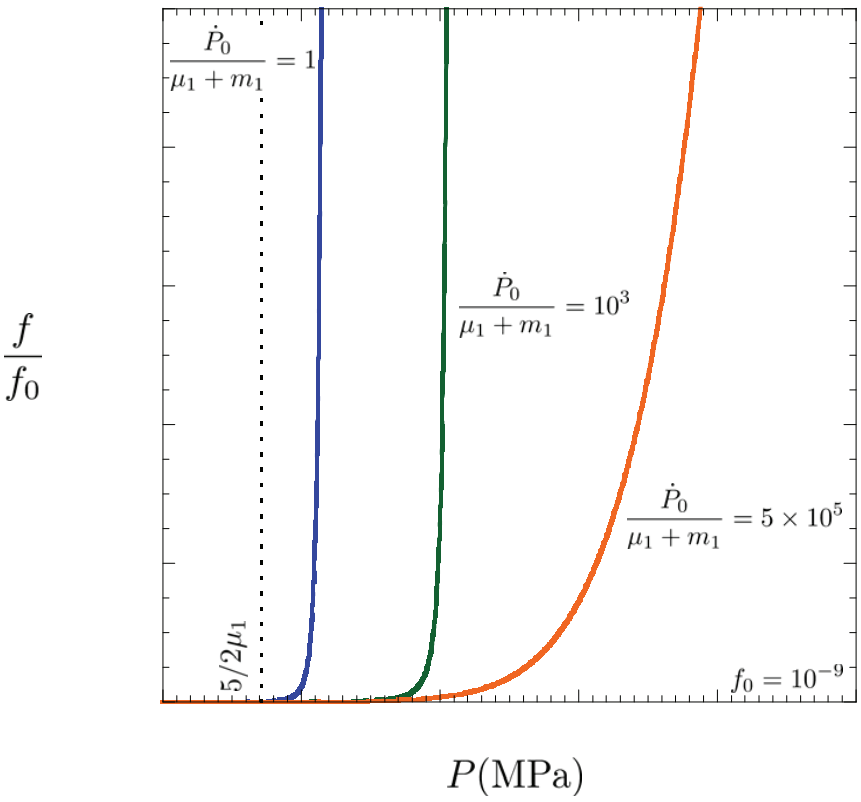

Fig. 7.1 Growth of the volume fraction of the cavity in the shell $f = a^3/b^3 = (\lambda_b^3 + f_0 - 1)/\lambda_b^3$, normalized by its initial volume fraction $f_0 = 10^{-9}$, as a function of the applied pressure (7.26) for the three values of constant pressure rate $\dot{P}_0/(\mu_1 + m_1) = 1, 10^3$, and 5×10^5.

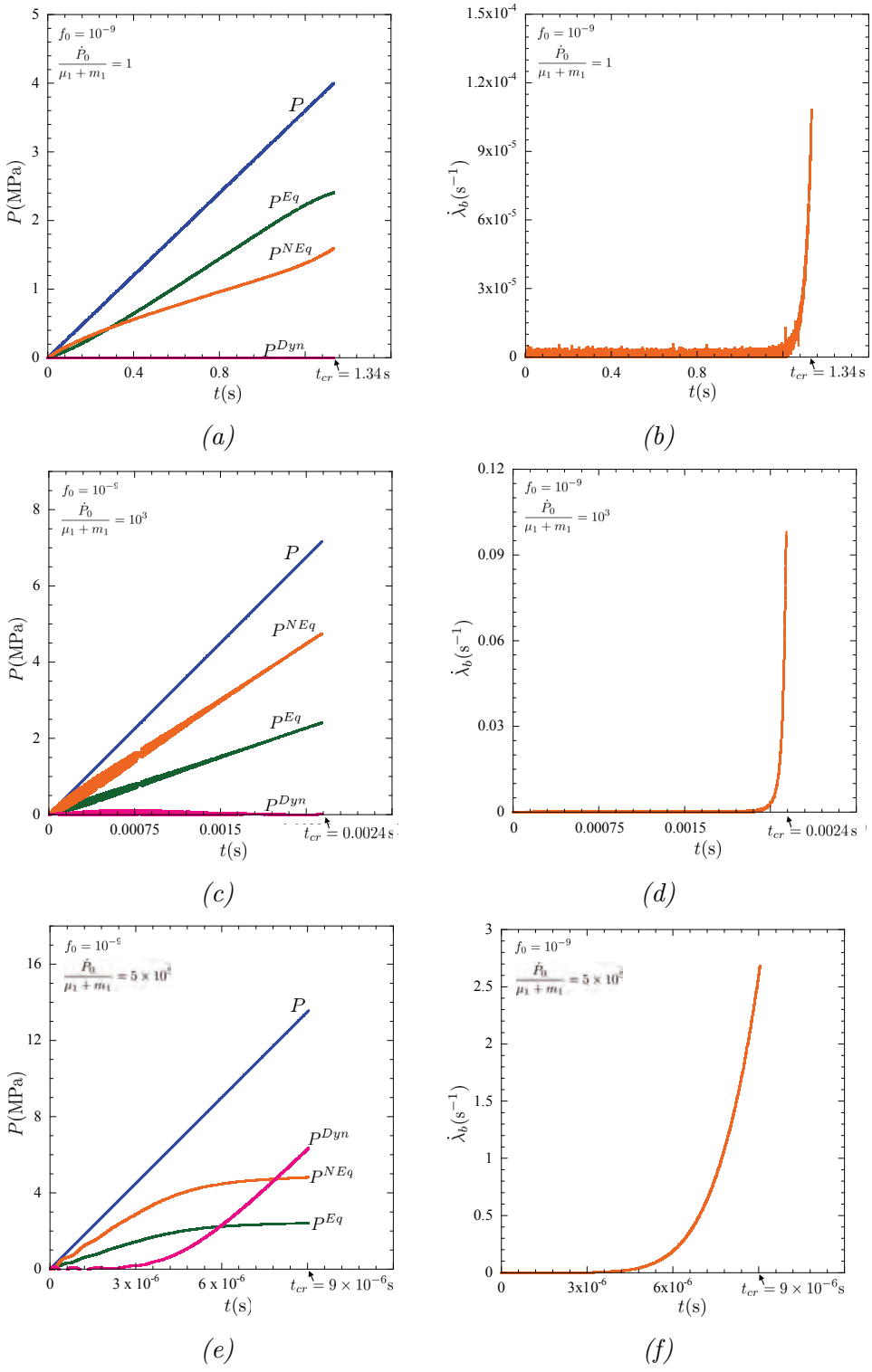

Fig. 7.2 The three contributions making up the value of the applied pressure $P = P^{Eq} + P^{NEq} + P^{Dyn}$ *and the stretch rate at the outer boundary of the shell* $\dot{\lambda}_b$*, all as functions of time* t*. Parts (a)–(b), (c)–(d), (e)–(f) show results, respectively, for the constant pressure rates* $\dot{P}_0/(\mu_1 + m_1) = 1, 10^3,$ *and* 5×10^5*.*

In accord with the general remarks *ii* and *iii* stated above, Fig. 7.1 shows that higher pressure rates lead to higher values of the pressure at which cavitation occurs. Moreover, even for the admittedly low pressure rate of $\dot{P}_0/(\mu_1 + m_1) = 1$, the values of these critical cavitation pressures are higher than the corresponding cavitation pressure in elastostatics, namely, $5/2\mu_1$ (this value is indicated by a dotted line in the figure). This behavior can be understood at once from the results shown in Fig. 7.2. Indeed, Fig. 7.2(e) shows that inertia, as measured by P^{Dyn}, is the leading contributor in the onset of cavitation for the high pressure rate of $\dot{P}_0/(\mu_1 + m_1) = 5 \times 10^5$. Note from Fig. 7.2(f) that this type of loading involves dynamic deformations on the outer boundary of the shell that are also of relatively high rate (i.e., $\dot{\lambda}_b > 1$ s^{-1}). On the other hand, Fig. 7.2(c) shows that inertia is negligible and, instead, viscous dissipation together with elasticity, as measured by P^{NEq} and P^{Eq}, are the leading contributors in the onset of cavitation for the intermediate pressure rate of $\dot{P}_0/(\mu_1 + m_1) = 10^3$. Note from Fig. 7.2(d) that this type of loading involves deformation rates on the outer boundary of the shell that are moderately quasi-static (i.e., $\dot{\lambda}_b \sim 10^{-1}$ s^{-1}). Finally, while inertia remains of course negligible for the even lower pressure rate of $\dot{P}_0/(\mu_1 + m_1) = 1$, Fig. 7.2(a) shows that the onset of cavitation is dominated by elasticity in this case, but also that viscous dissipation continues to play a significant role, even when the associated deformation rate on the outer boundary of the shell (see Fig. 7.2(b)) is admittedly low $\dot{\lambda}_b \sim 10^{-4}$ s^{-1}.

7.5 Summary and conclusions

In this chapter we have explored the role of viscosity and inertia in the growth rate of a spherical cavity embedded in a visco-elastic medium subjected to time dependent hydrostatic loading. Various loading rates, which range from quasi-static to dynamic conditions, are considered. The visco-elastic material has been characterized by the constitutive model developed by Kumar and Lopez-Pamies (2016) which describes the mechanical response of Nitrile rubber over wide ranges of deformations and deformation rates. We have identified the relative contribution of the elastic, viscous and inertial terms to the growth rate of the cavity and obtained the following conclusions:

- Within the whole range of loading rates explored in this chapter, the material viscosity plays a meaningful role in the onset of the cavitation process, which occurs for a greater of pressure value than that obtained from the classical elastostatic solution.

- For the greatest loading rate explored in this work, which involves stretch rates larger than 1 s^{-1}, inertia effects play the leading role in the cavitation process, delaying the onset of cavitation and slowing down the grow rate of the spherical void.

Altogether, the key contribution of this chapter is to make clear the stabilizing role played by viscosity and inertia in the cavitation process of rubber-like materials. It is apparent that cavitation is a dynamic process, strongly influenced by the mechanical response of the material, which requires accurate constitutive descriptions to be modeled.

Part IV

2D finite vibrations of anisotropic hyperelastic structures

8 Incompressible anisotropic hyperelastic cylindrical structures

Periodic, quasi-periodic and chaotic motion in 2D

In this chapter we explore the **two-dimensional** (axial and radial) free vibrations of an incompressible anisotropic hyperelastic cylindrical structure subjected to *ab initio* levels of elastic stored and kinetic energies. Our aim is to complement the one-dimensional case, which only considers radial vibrations, that was investigated in Chapter 3 for the isotropic material. The anisotropic constitutive model used in the present chapter was originally developed by Rubin and Jabareen (2007, 2010). We have carried out a systematic analysis of the parameters which govern the dynamic behavior of the structure, paying special attention to those which describe the anisotropic material response and the geometry/dimensions of the shell. Moreover, using **Poincaré surface of section** and **Lyapunov exponents**, we have shown that the motion of the structure can turn from periodic and quasi-periodic to chaotic as a function of the geometry/dimensions of the shell and the degree of mechanical anisotropy of the material.

8.1 Introduction

As described in the introduction of Chapter 3, the analysis of the nonlinear dynamics of hyperelastic shells started with the pioneering works of Knowles (1960, 1962), and the subsequent developments of Zhong-Heng and Solecki (1963), Wang (1965), Balakrishnan and Shahinpoor (1978) and Shahinpoor and Balakrishnan (1978). These authors focused their attention on incompressible and isotropic hyperelastic materials. The extension of previous studies to compressible hyperelasticity was conducted by Haddow and co-workers Haddow and Mioduchowski (1977); Janele et al. (1989a,b, 1991), as described in the introductory section of Chapter 5.

On the other hand, the influence of material anisotropy on the large-amplitude vibrations of hyperelastic shells has received much less attention. The first paper on

this topic was published by Huilgol (1967), who studied the problem of axisymetric oscillations of an infinitely long cylindrical thick-walled tube, which was curvilinearly transverse-isotropic, i.e., the anisotropy was assumed to exist in the radial direction. The author derived the conditions that strain-energy functions must satisfy for the existence of periodic solutions. Few years later, Shahinpoor (1972a) approached the problem of large-amplitude oscillations of a longitudinally anisotropic thin-walled cylindrical structure subjected to radial pressure and plane strain conditions along its axial direction (plane strain was also considered by Huilgol (1967)). Exact expressions for the dynamic deformations were given upon solving explicitly the non-autonomous time-dependent differential equation that arises when the applied pressure was considered to decay exponentially in time. From this point on, most likely due to the extended use of composite materials such as carbon and glass fiber reinforced polymers in the industry, the works dealing with large-amplitude vibrations of anisotropic elastic materials have mostly used linear elasticity. For example, see the recent works of Toorani (2003), Jansen (2007, 2008), Amabili and Reddy (2010), and other references included in the review of Alijani and Amabili (2014). The number of recent contributions to the field of anisotropic nonlinear elasticity is much more reduced. Within this field, we should highlight the work of Mason and Maluleke (2007), who investigated the radial oscillations of transversely isotropic incompressible thin-walled cylindrical tubes with generalized Mooney-Rivlin strain-energy function and subjected to a time dependent applied pressure. Transversely isotropic cylindrical tubes in the radial, tangential and longitudinal directions were considered. As in the previous works of Huilgol (1967) and Shahinpoor (1972a), the cylinder was subjected to plane strain conditions in the axial direction. The attention of Mason and Maluleke (2007) was focused on calculating the conditions on the strain-energy function and the applied pressure such that the differential equation of motion has a Lie point symmetry generator. Under these conditions, the problem can be reduced to an autonomous system for which analytical solutions exist.

In the present chapter we extend the works of Huilgol (1967), Shahinpoor (1972a) and Mason and Maluleke (2007) to a 2D framework. We study the axisymmetric free vibrations of a nonlinear orthotropic hyperelastic thick-walled cylindrical structure. Unlike in Huilgol (1967), Shahinpoor (1972a) and Mason and Maluleke (2007) no plane strain hypothesis is assumed, i.e., the cylinder deforms in the longitudinal direction. The orthotropic mechanical response of the material is modeled following the constitutive theory developed by Rubin and Jabareen (2007, 2010). We have carried out a systematic analysis to evaluate, for a wide range of initial conditions, the influence of the following factors on the oscillatory response of the structure: (1) the initial elastic and kinetic

energies supplied to the specimen, (2) the dimensions of the shell and (3) the anisotropy of the material. Our results reveal that, depending on the energy of the system, the material constants and the geometrical parameters, the response of the structure can be periodic, quasi-periodic or chaotic.

8.2 Problem formulation

In this section we formulate the problem of an incompressible anisotropic hyperelastic cylindrical structure subjected to radially symmetric deformations. Unlike in previous chapters of this dissertation, the problem is posed within a 2D framework which considers the balance of linear momentum along the radial and axial directions of the cylinder. The material is modeled using the anisotropic constitutive model developed by Rubin and Jabareen (2007, 2010).

Recall from Chapter 2 that the current position vector $\mathbf{x}$ in the deformed configuration $\Omega \subset \mathbb{R}^3$ at time t of the material point that occupies the location $\mathbf{X} \in \Omega_0$ is given by $\mathbf{x} = \boldsymbol{\chi}(\mathbf{X}, t)$, where χ is a bijective and twice continuously differentiable mapping. The associated deformation gradient, right Cauchy-Green strain tensor and volume ratio at $\mathbf{X} \in \Omega_0$ are denoted by

$$\mathbf{F} = \mathrm{Grad}\,\boldsymbol{\chi}, \quad \mathbf{C} = \mathbf{F}^{\mathrm{T}}\mathbf{F}, \quad J = \det\mathbf{F}. \tag{8.1}$$

Furthermore, the balance of linear momentum requires that

$$\mathrm{Div}\,\mathbf{S} = \rho_0 \ddot{\boldsymbol{\chi}} \quad \text{in} \quad \Omega_0, \tag{8.2}$$

where the dots denote differentiation with respect to time, $\mathbf{S}$ stands for the first Piola-Kirchhoff stress tensor, and ρ_0 is the constant mass density of the shell material in its undeformed configuration Ω_0.

8.2.1 Constitutive model

The cylindrical structure is modeled as a nonlinear orthoropic hyperelastic material using the physically-based invariants developed in Rubin and Jabareen (2007, 2010). Using the work of Flory (1961), the unimodular part $\overline{\mathbf{C}}$ of the right Cauchy-Green strain tensor $\mathbf{C}$,

which is a pure measure of distortional deformation, is given by (see Section 2.4)

$$\overline{\mathbf{C}} = J^{-2/3}\mathbf{C}, \quad \det \overline{\mathbf{C}} = 1, \tag{8.3}$$

Moreover, the First Piola-Kirchhoff stress tensor $\mathbf{S}$ can be expressed in the form

$$\mathbf{S} = \overline{\mathbf{S}} - p\mathbf{I}, \quad \text{such that } \overline{\mathbf{S}} \cdot \mathbf{I} = 0, \tag{8.4}$$

where p is the Lagrange multiplier already introduced in Section 2.4 , $\overline{\mathbf{S}}$ is the deviatoric part of $\mathbf{S}$ and $\mathbf{I}$ is the unit second order tensor[1]. General hyperelastic materials experience no distortion when subjected to pure hydrostatic pressure

$$\overline{\mathbf{C}} = \mathbf{I} \text{ for } \overline{\mathbf{S}} = 0 \text{ and } J \neq 1. \tag{8.5}$$

It is further assumed that the hyperelastic material is a solid that has non-zero stiffness to all distortional modes of deformation. In contrast, when an orthotropic hyperelastic material is subjected to hydrostatic pressure it experiences distortion

$$\overline{\mathbf{C}} \neq \mathbf{I} \text{ for } \overline{\mathbf{S}} = 0 \text{ and } J \neq 1. \tag{8.6}$$

The main idea in Rubin and Jabareen (2007, 2010), is to develop invariants of deformation, which are based on the additional distortions required to cause deviatoric stress in an orthotropic solid. Let $\mathbf{a}_i$ $(i = 1, 2, 3)$ be an orthonormal triad of vectors that characterize the principal directions of orthotropy of the material in its reference configuration and let $\mathbf{N}_i$ be the associated structural tensors defined by

$$\mathbf{N}_i = \mathbf{a}_i \otimes \mathbf{a}_i \text{ (no sum on } i = 1, 2, 3). \tag{8.7}$$

Specifically, an orthotropic solid will be in a hydrostatic state of stress *if an only if* $\overline{\mathbf{C}}$ has the form

$$\overline{\mathbf{C}} = \eta_1^2\mathbf{N}_1 + \eta_2^2\mathbf{N}_2 + \eta_3^2\mathbf{N}_3, \tag{8.8}$$

where η_i are positive functions of the dilatation J satisfying the restrictions

$$\eta_i = \eta_i(J), \quad \eta_1\eta_2\eta_3 = 1, \quad \eta_i(1) = 1. \tag{8.9}$$

[1] $\mathbf{A} \cdot \mathbf{B} = \text{tr}(\mathbf{A}\mathbf{B}^{\text{T}})$ denotes the inner product of two second order tensors $\{\mathbf{A}, \mathbf{B}\}$, see appendix A

It was shown in Rubin and Jabareen (2010) that the strain energy ψ^* per unit mass[2] of a general orthotropic material can be expressed as a function of seven invariants

$$\psi^* = \psi^*(J, \beta_i), \tag{8.10}$$

where the invariants $\beta_i\,(i = 1, 2, ..., 6)$ are defined by

$$\beta_i = \left(\frac{1}{\eta_i^2}\overline{\mathbf{C}} + \eta_i^2\overline{\mathbf{C}}^{-1}\right)\cdot\mathbf{N}_i, \quad \beta_i \geqslant 2 \quad \text{(no sum on } i = 1, 2, 3), \tag{8.11}$$

$$\beta_4 = \frac{(\mathbf{N}_1\mathbf{C}\mathbf{N}_2 + \mathbf{N}_2\mathbf{C}\mathbf{N}_1)\cdot\mathbf{C}}{2(\mathbf{C}\cdot\mathbf{N}_1)(\mathbf{C}\cdot\mathbf{N}_2)}, \quad \beta_5 = \frac{(\mathbf{N}_1\mathbf{C}\mathbf{N}_3 + \mathbf{N}_3\mathbf{C}\mathbf{N}_1)\cdot\mathbf{C}}{2(\mathbf{C}\cdot\mathbf{N}_1)(\mathbf{C}\cdot\mathbf{N}_3)}, \tag{8.12}$$

$$\beta_6 = \frac{(\mathbf{N}_2\mathbf{C}\mathbf{N}_3 + \mathbf{N}_3\mathbf{C}\mathbf{N}_2)\cdot\mathbf{C}}{2(\mathbf{C}\cdot\mathbf{N}_2)(\mathbf{C}\cdot\mathbf{N}_3)}. \tag{8.13}$$

Moreover, introducing the definition of the auxiliary functions $n_i(J)$ it follows that

$$n_i = \frac{3J}{\eta_i}\frac{\mathrm{d}\eta_i}{\mathrm{d}J}, \quad n_1 + n_2 + n_3 = 0, \tag{8.14}$$

$$\frac{\partial\eta_i}{\partial\mathbf{C}} = \frac{1}{6}n_i\eta_i\, J^{-2/3}\overline{\mathbf{C}}^{-1} \quad \text{(no sum on } i = 1, 2, 3), \tag{8.15}$$

where we have used that $\frac{\partial J}{\partial\mathbf{C}} = \frac{1}{2}J\mathbf{C}^{-1}$; see e.g., Holzapfel (2000). The derivatives of β_i are given by

$$\frac{\partial\beta_i}{\partial\mathbf{C}} = \mathbf{B}_i \quad (i = 1, 2, ..., 6) \tag{8.16}$$

where

$$\mathbf{B}_i = J^{-2/3}\left[\left(\frac{1}{\eta_i^2}\mathbf{N}_i - \eta_i^2\overline{\mathbf{C}}^{-1}\mathbf{N}_i\overline{\mathbf{C}}^{-1}\right) - \frac{1}{3}(1 + n_i)\left(\frac{1}{\eta_i^2}(\overline{\mathbf{C}}\cdot\mathbf{N}_i) - \eta_i^2(\overline{\mathbf{C}}^{-1}\cdot\mathbf{N}_i)\right)\overline{\mathbf{C}}^{-1}\right], \quad \text{no sum on } i = 1, 2, 3 \tag{8.17}$$

$$\mathbf{B}_4 = \frac{(\mathbf{N}_1\mathbf{C}\mathbf{N}_2 + \mathbf{N}_2\mathbf{C}\mathbf{N}_1) - \beta_4(\mathbf{C}\cdot\mathbf{N}_2)\mathbf{N}_1 - \beta_4(\mathbf{C}\cdot\mathbf{N}_1)\mathbf{N}_2}{(\mathbf{C}\cdot\mathbf{N}_1)(\mathbf{C}\cdot\mathbf{N}_2)}, \tag{8.18}$$

$$\mathbf{B}_5 = \frac{(\mathbf{N}_1\mathbf{C}\mathbf{N}_3 + \mathbf{N}_3\mathbf{C}\mathbf{N}_1) - \beta_5(\mathbf{C}\cdot\mathbf{N}_3)\mathbf{N}_1 - \beta_5(\mathbf{C}\cdot\mathbf{N}_1)\mathbf{N}_3}{(\mathbf{C}\cdot\mathbf{N}_1)(\mathbf{C}\cdot\mathbf{N}_3)}, \tag{8.19}$$

$$\mathbf{B}_6 = \frac{(\mathbf{N}_2\mathbf{C}\mathbf{N}_3 + \mathbf{N}_3\mathbf{C}\mathbf{N}_2) - \beta_6(\mathbf{C}\cdot\mathbf{N}_3)\mathbf{N}_2 - \beta_6(\mathbf{C}\cdot\mathbf{N}_1)\mathbf{N}_3}{(\mathbf{C}\cdot\mathbf{N}_2)(\mathbf{C}\cdot\mathbf{N}_3)}. \tag{8.20}$$

[2]Please notice that the strain energy function ψ^* is defined per unit of mass instead the more common definition per unit of reference volume ψ used in previous chapters

Furthermore, to be noted that the invariants β_i are constants and $\mathbf{B}_i$ vanish when $\overline{\mathbf{C}}$ takes the form (8.8)

$$\beta_i = 2, \quad \beta_{i+3} = 0 \quad \text{for } i = 1, 2, 3, \quad \mathbf{B}_i = 0 \quad \text{for } i = 1, 2, ..., 6. \tag{8.21}$$

Specific constitutive equations. As a special case, let us take ψ^* in the form

$$2\rho_0\psi^* = \sum_{i=1}^{3} K_i(\beta_i - 2) + \sum_{i=4}^{6} K_i\beta_i + K_7(J-1)^2, \quad K_i \geqslant 0, \quad (i = 1, 2, ..., 7)\ , \tag{8.22}$$

where K_i are non-negative material constants. It then follows that $\mathbf{S}$ is given by

$$\mathbf{S} = \sum_{i=1}^{6} K_i \mathbf{F}\mathbf{B}_i + J\, K_7(J-1)\mathbf{F}^{-\mathrm{T}}. \tag{8.23}$$

In addition, consider the special case when n_i are constants so that integration of (8.14) yields

$$\eta_i = J^{n_i/3}, \quad n_1 + n_2 + n_3 = 0. \tag{8.24}$$

This model has nine material constants

$$K_i \ \ (\text{for } i = 1, 2, ..., 7)\ , n_1, n_2, \tag{8.25}$$

which can be related to the components of the small deformation stiffness

$$\rho_0\psi^* = \frac{1}{2}K_{ijkl}E_{ij}E_{kl}, \quad E_{ij} = \mathbf{E}\cdot\mathbf{a}_i \otimes \mathbf{a}_j, \tag{8.26}$$

where E_{ij} are the components of the strain tensor $\mathbf{E}$ relative to $\mathbf{a}_i$ (see, Rubin and Jabareen (2007, 2010)). Hereinafter, we will consider previous constitutive model restricted to the incompressible case; i.e., $J = 1$.

8.2.2 Radially symmetric dynamic deformation

Let us define a reference configuration Ω_0 of the thick-walled **cylindrical** shell by the polar coordinates $\{R, \Theta, Z\}$ such that

$$A \leq R \leq B, \qquad 0 \leq \Theta \leq 2\pi, \qquad -\frac{H}{2} \leq Z \leq \frac{H}{2}. \tag{8.27}$$

Let us consider a radially symmetric deformation process such that the position vectors $\mathbf{X}$ and $\mathbf{x}(\mathbf{X},t)$ in the reference and deformed configurations, respectively, are given by

$$\mathbf{X} = R\mathbf{e}_r + Z\mathbf{e}_z, \quad \mathbf{x} = r(R,t)\mathbf{e}_r + z(Z,t)\mathbf{e}_z, \tag{8.28}$$

where the right-handed basis vectors $\{\mathbf{e}_r, \mathbf{e}_\theta, \mathbf{e}_z\}$ of a cylindrical polar coordinate system satisfy the following equations

$$\mathbf{e}_r \times \mathbf{e}_\theta \cdot \mathbf{e}_z = 1, \quad \frac{\mathrm{d}\mathbf{e}_r}{\mathrm{d}\theta} = \mathbf{e}_\theta, \quad \frac{\mathrm{d}\mathbf{e}_\theta}{\mathrm{d}\theta} = -\mathbf{e}_r. \tag{8.29}$$

Under this conditions the deformation gradient assumes the following spectral form (see Appendix A)

$$\mathbf{F} = \lambda_r(R,t)\ \mathbf{e}_r \otimes \mathbf{e}_r + \lambda(R,t)\ \mathbf{e}_\theta \otimes \mathbf{e}_\theta + \lambda_z(t)\mathbf{e}_z \otimes \mathbf{e}_z, \tag{8.30}$$

where the principal stretches corresponding to the directions r, θ, z are given by

$$\lambda_r(R,t) = \frac{\partial r(R,t)}{\partial R}, \quad \lambda_\theta(R,t) = \frac{r(R,t)}{R} = \lambda(R,t), \quad \lambda_z(t) = \frac{z(Z,t)}{Z}. \tag{8.31}$$

For the problem under consideration here, body force is neglected and tractions are applied on the top and bottom surfaces of the plate, which are consistent with axisymmetric vibrations. Specifically, axial stress $t(R,t)\mathbf{e}_z$ is applied the top of the plate and axial stress $-t(R,t)\mathbf{e}_z$ is applied to the bottom of the plate to maintain a uniform deformed thickness $h(t)$ of the plate which can depend on time. Therefore, we are assuming that the **principal stretch in the axial direction $\lambda_z(t)$ is only a function of time**. Furthermore, the first Piola-Kirchhoff stress tensor corresponding to the deformation gradient (8.30) can be shown to be also in the spectral form

$$\mathbf{S} = S_r(R,t)\ \mathbf{e}_r \otimes \mathbf{e}_r + S_\theta(R,t)\ \mathbf{e}_\theta \otimes \mathbf{e}_\theta + S_z(R,t)\mathbf{e}_z \otimes \mathbf{e}_z. \tag{8.32}$$

The principal stresses can be obtained from Eq. (8.23) and are given by

$$\begin{aligned}
S_r &= \lambda_r^{-1}\left[-K_1\frac{n_1-2}{3}\left(\lambda_r^2-\lambda_r^{-2}\right) - K_2\frac{1+n_2}{3}\left(\lambda^2-\lambda^{-2}\right) - K_3\frac{1-n_1-n_2}{3}\left(\lambda_z^2-\lambda_z^{-2}\right) - p\right],\\
S_\theta &= \lambda^{-1}\left[-K_1\frac{1+n_1}{3}\left(\lambda_r^2-\lambda_r^{-2}\right) - K_2\frac{n_2-2}{3}\left(\lambda^2-\lambda^{-2}\right) - K_3\frac{1-n_1-n_2}{3}\left(\lambda_z^2-\lambda_z^{-2}\right) - p\right],\\
S_z &= \lambda_z^{-1}\left[-K_1\frac{1+n_1}{3}\left(\lambda_r^2-\lambda_r^{-2}\right) - K_2\frac{1+n_2}{3}\left(\lambda^2-\lambda^{-2}\right) + K_3\frac{2+n_1+n_2}{3}\left(\lambda_z^2-\lambda_z^{-2}\right) - p\right],
\end{aligned} \tag{8.33}$$

where the **functions arguments have been omitted**, as in some of the following expressions, to ease the notation.

The balance of linear momentum in axial and radial directions lead to

$$\frac{\partial S_r(R,t)}{\partial R} + \frac{S_r(R,t) - S_\theta(R,t)}{R} = \rho_0 \, \ddot{r}(R,t), \tag{8.34}$$

$$\frac{\partial S_z(R,t)}{\partial Z} = \rho_0 \, \ddot{z}(Z,t). \tag{8.35}$$

Note that, for the first time in this dissertation, we consider the balance of linear momentum when approaching the problem of the cylindrical shell. In other words, we do not assume plane strain along the axial direction. Moreover, it follows from the incompressibility condition $J = \lambda_r(R,t)\lambda(R,t)\lambda_z(t) = 1$ that

$$\lambda(R,t) = \left(\frac{A^2}{R^2} \left[\lambda_a^2(t) - \lambda_z^{-1}(t) \right] + \lambda_z^{-1}(t) \right)^{1/2}, \tag{8.36}$$

where $\lambda_a(t) = \frac{a(t)}{A}$ stands for the circumferential stretch in the inner face[3]. Taking the derivatives of (8.36) with respect to R and t we obtain the following relations

$$\frac{\partial \lambda}{\partial R} = -\frac{\lambda_z \lambda^2 - 1}{R \lambda \lambda_z}, \tag{8.37}$$

$$\begin{aligned} \ddot{\lambda} =& \frac{1}{2\lambda} \left[\frac{\lambda_z \lambda^2 - 1}{\lambda_z \lambda_b^2 - 1} \left(2\dot{\lambda}_b^2 + 2\lambda_b \ddot{\lambda}_b - 2\lambda_z^{-3} \dot{\lambda}_z^2 + \lambda_z^{-2} \ddot{\lambda}_z \right) + 2\lambda_z^{-3} \dot{\lambda}_z^2 - \lambda_z^{-2} \ddot{\lambda}_z \right] \\ & - \frac{1}{4\lambda^3} \left[\frac{\lambda_z \lambda^2 - 1}{\lambda_z \lambda_b^2 - 1} \left(2\lambda_b \dot{\lambda}_b + \lambda_z^{-2} \dot{\lambda}_z \right) - \lambda_z^{-2} \dot{\lambda}_z \right]. \end{aligned} \tag{8.38}$$

Following previous chapters, let us rewrite the equation of motion along the radial direction (8.34) with $\lambda(R,t)$ as the independent space variable instead of R. With help of the expression (8.37) the result reads as

$$\frac{\partial}{\partial \lambda} \left[\frac{S_r}{\lambda} \right] = -\frac{S_\theta \lambda_z - \frac{S_r}{\lambda^2}}{\lambda_z \lambda^2 - 1} + \rho_0 B^2 \lambda_z \frac{\lambda_z \lambda_b^2 - 1}{\left(\lambda_z \lambda^2 - 1 \right)^2} \ddot{\lambda}, \tag{8.39}$$

[3]The expression (8.36) can be alternatively written as $\lambda(R,t) = \left(\frac{B^2}{R^2} \left[\lambda_b^2(t) - \lambda_z^{-1}(t) \right] + \lambda_z^{-1}(t) \right)^{1/2}$ in terms of the stretch in the outer face $\lambda_b(t) = b(t)/B$. For our purposes here, we find dealing with the form (8.36) in terms of the inner stretch $\lambda_a(t)$ more convenient.

where $\ddot{\lambda}$ is given by Eq. (8.38) and it follows from Eq. (8.33) that

$$S_\theta \lambda_z - \frac{S_r}{\lambda^2} = \frac{\lambda_z}{\lambda}\left[K_2\left(\lambda^2 - \lambda^{-2}\right) - K_1\left(\lambda_z^{-2}\lambda^{-2} - \lambda_z^2\lambda^2\right)\right]. \tag{8.40}$$

Assuming now that the inner boundary ($R = A$) is subjected to a pressure $P_a(t)$, defined **per unit of current area**. While, the outer face ($R = B$) is subjected to a pressure $P_b(t)$, the boundary conditions are given by

$$S_r(A,t) = -P_a(t)\lambda_a \quad \text{and} \quad S_r(B,t) = -P_b(t)\lambda_b, \tag{8.41}$$

where $P_a(t)$ and $P_b(t)$ are any functions of choice (suitably well behaved). Hence, Eq. (8.39) can be integrated in λ with help of (8.38), (8.40) and (8.41) to give

$$\begin{aligned}
\frac{P_a - P_b}{K_1} &= \frac{1}{8}\left(3\frac{\lambda_a^2}{\lambda_z^2}\dot{\lambda}_z^2 - 2\frac{\lambda_a^2}{\lambda_z}\ddot{\lambda}_z\right)\frac{\Lambda_B^2 - 1}{\lambda_a^2\lambda_z} \\
&+ \frac{1}{2}\left[\lambda_a^{-2}\lambda_z^{-2} - \lambda_z^{-1} + \frac{K_2}{K_1}\left(\lambda_a^{-2} - \lambda_z\right) + \dot{\lambda}_a^2 + \frac{\lambda_a}{\lambda_z}\dot{\lambda}_a\dot{\lambda}_z + \frac{1}{4}\frac{\lambda_a^2}{\lambda_z^2}\dot{\lambda}_z^2\right]\left(\frac{1 - \Lambda_B^2}{\lambda_a^2\lambda_z + \Lambda_B^2 - 1}\right) \\
&+ \frac{1}{2}\left[-\lambda_z^{-1} - \frac{K_2}{K_1}\lambda_z + \dot{\lambda}_a^2 + \lambda_a\ddot{\lambda}_a + \frac{\lambda_a}{\lambda_z}\dot{\lambda}_a\dot{\lambda}_z - \frac{1}{2}\frac{\lambda_a^2}{\lambda_z^2}\dot{\lambda}_z^2 + \frac{1}{2}\frac{\lambda_a^2}{\lambda_z}\ddot{\lambda}_z\right]\ln\left(1 + \frac{\Lambda_B^2 - 1}{\lambda_a^2\lambda_z}\right) \\
&+ \frac{1}{2}\left(\lambda_z + \frac{K_2}{K_1}\lambda_z^{-1}\right)\ln\left(\Lambda_B^2\right),
\end{aligned} \tag{8.42}$$

where the following normalized quantities have been introduced

$$\Lambda_B = \frac{B}{A}, \quad \Lambda_H = \frac{H}{A}, \quad \tau = t\sqrt{\frac{K_1}{\rho_0 A^2}}, \tag{8.43}$$

and the superposed dot denotes differentiation with respect to the dimensionless time τ.

On the other hand, the axial equation of motion (8.35) is only satisfied in the integral sense. Therefore, multiplying (8.35) by Z and integrating over Ω_0 we deduce that

$$\rho_0\frac{H^3}{12}\left(B^2 - A^2\right)\ddot{\lambda}_z(t)\lambda_z^2(t) = -2\int_A^B S_z(R,t)\lambda_z^2(t)\, R\mathrm{d}R \tag{8.44}$$

where $S_z(R,t)\,\lambda_z^2(t)$ can be written, using Eq. (8.33), as

$$S_z\,\lambda_z^2 = \frac{S_r}{\lambda} - K_1\,\lambda_z\left(\lambda_z^{-2}\lambda^{-2} - \lambda_z^2\lambda^2\right) + K_3\,\lambda_z\left(\lambda_z^2 - \lambda_z^{-2}\right), \tag{8.45}$$

Therefore, Eq. (8.44) can be integrated in R with help of (8.45) and (8.36) to obtain

$$\begin{aligned}
&\frac{1}{24}\Lambda_H^2(\Lambda_B^2-1)\ddot{\lambda}_z = \left[\frac{1}{2}\frac{P_a}{K_1}\lambda_a^2+\frac{1}{4}\lambda_z^{-2}-\frac{1}{4}\lambda_a^2\lambda_z+\frac{K_2}{4K_1}\left[1+\lambda_a^2\left(\lambda_z^{-1}-2\lambda_z\right)\right]-\frac{K_3}{2K_1}\lambda_a^2\left(\lambda_z^2-\lambda_z^{-2}\right)\right.\\
&\left.+\frac{1}{4}\lambda_a^2\left(2\dot{\lambda}_a^2+\lambda_a\ddot{\lambda}_a+2\frac{\lambda_a}{\lambda_z}\dot{\lambda}_a\dot{\lambda}_z+\frac{1}{2}\frac{\lambda_a^2}{\lambda_z^2}\dot{\lambda}_z^2\right)\right]\frac{\Lambda_B^2-1}{\lambda_a^2\lambda_z}+\frac{1}{32}\lambda_a^4\left(3\frac{\dot{\lambda}_z^2}{\lambda_z^2}-2\frac{\ddot{\lambda}_z}{\lambda_z}\right)\left[1-\left(1+\frac{\Lambda_B^2-1}{\lambda_a^2\lambda_z}\right)^2\right]\\
&+\frac{1}{4}\left[\lambda_z^{-2}-\frac{\lambda_a^2}{\lambda_z}-\frac{K_2}{K_1}\left(1-\lambda_a^2\lambda_z\right)-\lambda_a^2\left(\dot{\lambda}_a^2+\frac{\lambda_a}{\lambda_z}\dot{\lambda}_a\dot{\lambda}_z+\frac{1}{4}\frac{\lambda_a^2}{\lambda_z^2}\dot{\lambda}_z^2\right)\right]\ln\left(1+\frac{\Lambda_B^2-1}{\lambda_a^2\lambda_z}\right)\\
&+\frac{1}{4}\left[\frac{\lambda_a^2}{\lambda_z}+\frac{K_2}{K_1}\lambda_a^2\lambda_z-\lambda_a^2\left(\dot{\lambda}_a^2+\lambda_a\ddot{\lambda}_a+\frac{\lambda_a}{\lambda_z}\dot{\lambda}_a\dot{\lambda}_z-\frac{1}{2}\frac{\lambda_a^2}{\lambda_z^2}\dot{\lambda}_z^2+\frac{1}{2}\frac{\lambda_a^2}{\lambda_z}\ddot{\lambda}_z\right)\right]\left(1+\frac{\Lambda_B^2-1}{\lambda_a^2\lambda_z}\right)\ln\left(1+\frac{\Lambda_B^2-1}{\lambda_a^2\lambda_z}\right)\\
&-\left[\frac{1}{4}\lambda_a^2\left(\lambda_z+\frac{K_2}{K_1}\lambda_z^{-1}\right)\frac{\Lambda_B^2-1}{\lambda_a^2\lambda_z}-\frac{1}{2}\left(\frac{1}{2}-\lambda_a^2\lambda_z-\frac{K_2}{2K_1}\lambda_z^{-2}\right)\right]\ln\left(\Lambda_B^2\right)
\end{aligned} \tag{8.46}$$

where the same normalized quantities Λ_B, Λ_H and τ, have been used.

The equations of motion (8.42) and (8.46) form a system of two second order ordinary differential equations for the functions $\lambda_a(t)$ and $\lambda_z(t)$ that can be easily solved by a plethora of well-established implicit or explicit methods. Furthermore, it can be deduced from (8.42) and (8.46) that the parametric dependence of the problem has been reduced to the following **six non-dimensional parameters**: two material constants K_2/K_1 and K_3/K_1, two geometrical parameters Λ_B and Λ_H, and the normalized pressures P_a/K_1 and P_b/K_1. Please notice that, even when the stresses depend on n_1, n_2 and n_3 (see Eq. (8.33)), these parameters do not appear in the equations of motion due to the symmetry of the problem.

For the development of the results presented in Section 8.4 it proves necessary to introduce here the expressions for the energies involved in the deformation process. Therefore, we complete the problem formulation with the balance of mechanical power (see Section 2.3.4) that, in non-dimensional form, can be written as

$$\mathcal{P}_{\text{ext}} = \frac{\mathrm{d}\left(\mathcal{U}_{\text{int}}+\mathcal{K}\right)}{\mathrm{d}\tau}, \tag{8.47}$$

where the work exerted by the external pressures $\mathcal{P}_{\text{ext}}$, the total strain energy $\mathcal{U}_{\text{int}}$ and the kinetic energy $\mathcal{K}$ are given by

$$\mathcal{P}_{\text{ext}} = \pi\Lambda_H\lambda_z\left[\frac{P_a}{K_1}\frac{\mathrm{d}}{\mathrm{d}\tau}\left(\lambda_a^2\right) - 2\frac{P_b}{K_1}\frac{\mathrm{d}}{\mathrm{d}\tau}\left(\lambda_a^2 + \frac{\Lambda_B^2-1}{\lambda_z}\right)\right], \tag{8.48}$$

$$\begin{aligned}\mathcal{U}_{\text{int}} = {} & \frac{1}{2}\pi\Lambda_H\lambda_a^2\lambda_z\left[\left(1+\frac{K_2}{K_1}\right)\left(\lambda_z+\lambda_z^{-1}-2\right)+\frac{K_3}{K_1}\left(\lambda_z^2+\lambda_z^{-2}-2\right)\right]\left(\frac{\Lambda_B^2-1}{\lambda_a^2\lambda_z}\right)\\ & + \frac{1}{2}\pi\Lambda_H\lambda_z\left(\lambda_z^{-2}+\frac{K_2}{K_1}\right)\left(1-\lambda_a^2\lambda_z\right)\ln\left(1+\frac{\Lambda_B^2-1}{\lambda_a^2\lambda_z}\right)\\ & + \frac{1}{2}\pi\Lambda_H\left(\lambda_z^2+\frac{K_2}{K_1}\right)\left(\lambda_a^2-\lambda_z^{-1}\right)\ln\left(\Lambda_B^2\right),\end{aligned} \tag{8.49}$$

$$\begin{aligned}\mathcal{K} = {} & \frac{1}{2}\pi\Lambda_H\lambda_a^2\lambda_z\left[\frac{1}{24}\Lambda_H^2\dot{\lambda}_z^2-\frac{1}{2}\lambda_a\lambda_z^{-1}\dot{\lambda}_a\dot{\lambda}_z-\frac{1}{4}\lambda_a^2\lambda_z^{-2}\dot{\lambda}_z^2\right]\left(\frac{\Lambda_B^2-1}{\lambda_a^2\lambda_z}\right)\\ & + \frac{\pi}{16}\Lambda_H\lambda_a^4\lambda_z^{-1}\dot{\lambda}_z^2\left[\left(1+\frac{\Lambda_B^2-1}{\lambda_a^2\lambda_z}\right)^2-1\right]\\ & + \frac{1}{2}\pi\Lambda_H\lambda_a^2\lambda_z\left[\dot{\lambda}_a^2+\lambda_a\lambda_z^{-1}+\frac{1}{4}\lambda_a^2\lambda_z^{-2}\dot{\lambda}_z^2\right]\ln\left(1+\frac{\Lambda_B^2-1}{\lambda_a^2\lambda_z}\right).\end{aligned} \tag{8.50}$$

For the rest of this chapter we focus on the case of zero internal and external pressures, $P_a = P_b = 0$. Under these conditions the work of the external forces $\mathcal{P}_{\text{ext}}$ vanishes and the total energy remains constant

$$\mathcal{E}_{\text{T}} = \mathcal{U}_{\text{int}} + \mathcal{K} = \text{const.} \tag{8.51}$$

Note that the parameters associated with the orthotropic constitutive model K_3/K_1 and K_2/K_1 only appear in the total strain energy $\mathcal{U}_{\text{int}}$.

8.3 Numerical solution

In the previous section we showed that the motion of the cylindrical structure, which is defined by (8.42) and (8.46), has two degrees of freedom $\lambda_{\text{a}}(\tau)$ and $\lambda_{\text{z}}(\tau)$. The corresponding four-dimensional phase space is formed by the variables $\{\lambda_{\text{a}}, \dot{\lambda}_{\text{a}}, \lambda_{\text{z}}, \dot{\lambda}_{\text{z}}\}$. Since we limit our attention to the case for which the total energy is constant (8.51), one of the variables can be expressed as a function of the others. For the particular case developed herein we take $\dot{\lambda}_{\text{z}} = \dot{\lambda}_{\text{z}}(\lambda_{\text{a}}, \lambda_{\text{z}}, \dot{\lambda}_{\text{a}})$. Hence, for a given energy level, the phase space can be reduced from four to three dimensions without any loss of

information. In this *new* three dimensional phase space $\{\lambda_a, \lambda_z, \dot{\lambda}_a\}$, when the motion of the cylinder is periodic or quasi-periodic, the trajectory of the structure forms a torus (Lynch, 2007; Strogatz, 2014; Thompson and Stewart, 1986). As an example, let us consider $\Lambda_H = \Lambda_B = 2$, $K_2/K_1 = K_3/K_1 = 1$, $\mathcal{E}_T = 8$, $\lambda_a(0) = 1$, $\lambda_z(0) = 1$ and $\dot{\lambda}_a(0) = 1$. We insert these geometrical parameters, material constants, total energy and initial conditions in (8.51) to obtain $\dot{\lambda}_z(0) = 1.4140$. Then, we solve the system (8.42)-(8.46) to obtain the solution represented in Fig. 8.1a, which shows the torus (depicted in blue) and the trajectory corresponding to the first oscillation (represented by the red curve). To be noted that the torus is the result of plotting together the trajectories of the *infinite number* of oscillations of the structure. As occurred in Chapter 3, this type of solution naturally leads to the concept of **Poincaré Surface of Section (SOS)**. Poincaré SOS correspond to 2D representations of the motion of the structure that are constructed from the intersection between the trajectory of the cylinder in the 3D phase space and a given plane. Throughout this document we will choose the $\lambda_z = 1$ plane. In this way, the Poincaré SOS reduces a 3D trajectory in the phase space $\{\lambda_a, \lambda_z, \dot{\lambda}_a\}$ to a discrete 2D mapping in the phase space $\{\lambda_a, \dot{\lambda}_a\}$ that contains all the dynamical information of the system. As an example, Fig. 8.1b shows the Poincaré SOS corresponding to the plane $\lambda_z = 1$, for $\dot{\lambda}_z > 0$ and the initial conditions listed above.

As mentioned, Poincaré SOS shown in this chapter correspond to the intersection of the trajectories of the cylinder with the $\lambda_z = 1$ plane. This ensures that, irrespective of the energy of the system, the phase space includes all the possible trajectories described by the structure. We have checked that, in most cases, considering a plane different from $\lambda_z = 1$ does not modify the main results and trends that will be shown in Section 8.4. However, it may be the case that, for small values of the energy supplied to the system, some (or all) trajectories of the cylinder would not intersect the selected plane, which would lead to the partial (or total) loss of information on the motion of the structure. Similarly, all the Poincaré SOS of this chapter consider that $\dot{\lambda}_z > 0$, this condition being necessary to avoid overlapping between the Poincaré SOS arising from trajectories with the same energy level but different initial conditions.

The representation of the Poincaré SOS is the main technique used in the following section of the chapter to analyze the influence of the initial conditions, the total energy supplied to the system, the dimensions of the cylinder and the degree of mechanical orthotropy of the material in the dynamical response of the structure. Let us recall from Chapter 3 what are the possible outcomes of this numerical experiment:

- A single point in the Poincaré SOS corresponds to a periodic motion of the structure, which is characterized by the period T.

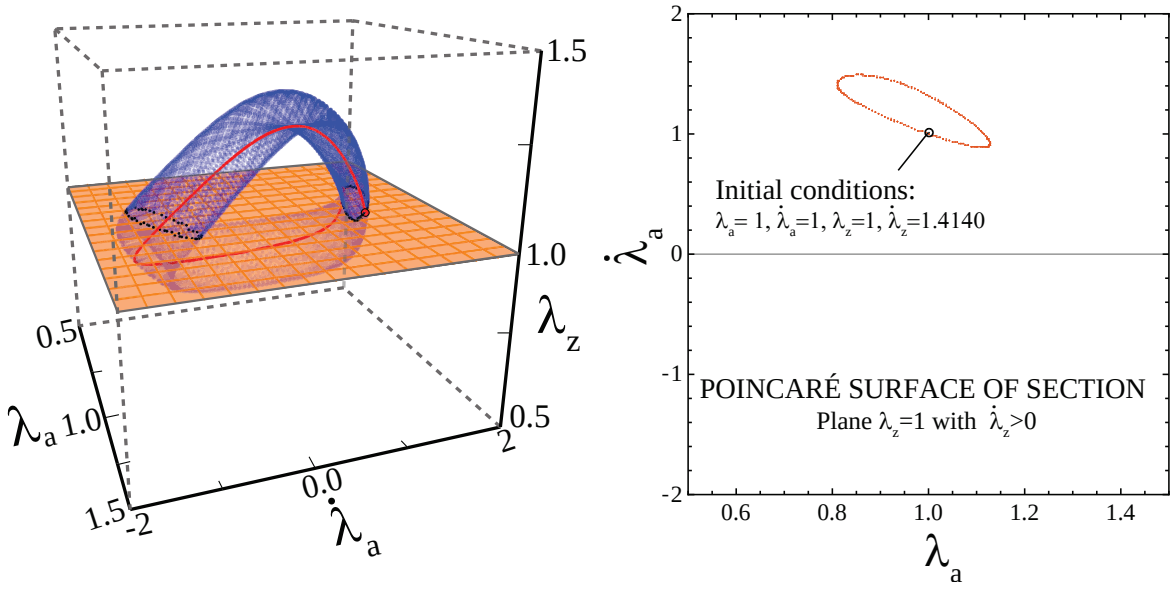

(a) *(b)*

Fig. 8.1 Geometrical parameters $\Lambda_H = \Lambda_B = 2$. *Material parameters* $\frac{K_2}{K_1} = \frac{K_3}{K_1} = 1$. *Total energy* $\mathcal{E}_T = 8$. *Initial conditions* $\lambda_a(0) = 1$, $\lambda_z(0) = 1$, $\dot{\lambda}_a(0) = 1$ *and* $\dot{\lambda}_z(0) = 1.4140$. *(a) Three-dimensional torus in the* $(\lambda_a, \lambda_z, \dot{\lambda}_a)$ *phase space corresponding to a quasi-periodic motion. The trajectory of the first oscillation is indicated in red. (b) Poincaréé SOS corresponding to the plane* $\lambda_z = 1$ *with the condition* $\dot{\lambda}_z > 0$.

- μ isolated points in the Poincaré SOS correspond to a periodic motion of the structure, which is characterized by the period μT.
- A closed curve in the Poincaré SOS (as the one presented in Fig. 8.1b) corresponds to a quasi-periodic motion of the structure.
- A filled region in the Poincaré SOS corresponds to a chaotic motion of the structure.

To obtain the Poincaré SOS, the system (8.42)-(8.46) has been solved with the fourth order Runge-Kutta method pre-implemented in Wolfram Mathematica®. To guarantee the quality of the numerical integration, we have checked that all the resultant trajectories remain in their respective energy hypersurfaces up to an error of 10^{-6}.

8.4 Sample results

In the examples presented in this section, we take as a reference the geometrical parameters, material constants and energy level used in Fig. 8.1, i.e., $\Lambda_H = \Lambda_B = 2$, $K_2/K_1 = K_3/K_1 = 1$ (isotropic material) and $\mathcal{E}_T = 8$. The influence of these parameters

on the response of the structure is explored in the following examples, where we change one parameter while keeping the other reference parameters fixed.

8.4.1 Reference case

Figure 8.2a depicts the Poincaré SOS corresponding to the reference geometrical parameters, material constants and energy level. The active 2D phase space includes all the possible combinations of $\dot{\lambda}_a$ and λ_a that fulfill the imposed energy level $\mathcal{E}_T = 8$ and the fact that $\dot{\lambda}_z$ must be greater than 0 (as anticipated in the previous section). The blue curve enclosing the active phase space has been obtained from (8.51) as the combinations of λ_a and $\dot{\lambda}_a$ that minimize $\dot{\lambda}_z$. Following the indications provided in the previous section for the interpretation of the Poincaré SOS, we observe that the phase space is divided into a chaotic domain (plotted in red), and several regions corresponding to periodic and quasi-periodic trajectories (plotted in brown, blue, purple...). It becomes apparent that the nature of the radial motion of the structure depends on the initial conditions considered. This is clearly illustrated in Fig. 8.2b, which shows the time evolution of λ_a for those two trajectories whose initial conditions are explicitly labeled in Fig. 8.2a. The solid blue curve corresponds to a periodic solution (single point in the phase space). The oscillatory motion of the structure shows a clear repetitive pattern in which the amplitude and period of the oscillations do not depend on τ. The dashed red curve, on the contrary, does not show any clear pattern; the amplitude and period of the oscillations are strongly dependent on the loading time τ. These qualitative observations can be quantified using the Lyapunov characteristic exponents (LCEs). We followed the procedure presented in Chapter 3 now extended to a four dimensional phase space. Recall that a positive LCE indicates that the response of the system is chaotic, while a zero LCE implies that the response of the system is periodic or quasi-periodic. This is exactly what we observe in Fig. 8.2c, which shows, for the two trajectories investigated in Fig. 8.2b, the evolution of their corresponding Lyapunov exponents, denoted by λ_k, where k is a coefficient that varies linearly with time (see Section 3.4.1). The LCE approaches zero for the periodic orbit as $k \to \infty$, and it tends to 0.033 ± 0.0001 for the chaotic orbit, where the error has been computed as the typical deviation of the last 200 values of κ considered.

In the next section we investigate the influence of the total energy supplied to the cylinder in the dynamic response of the system.

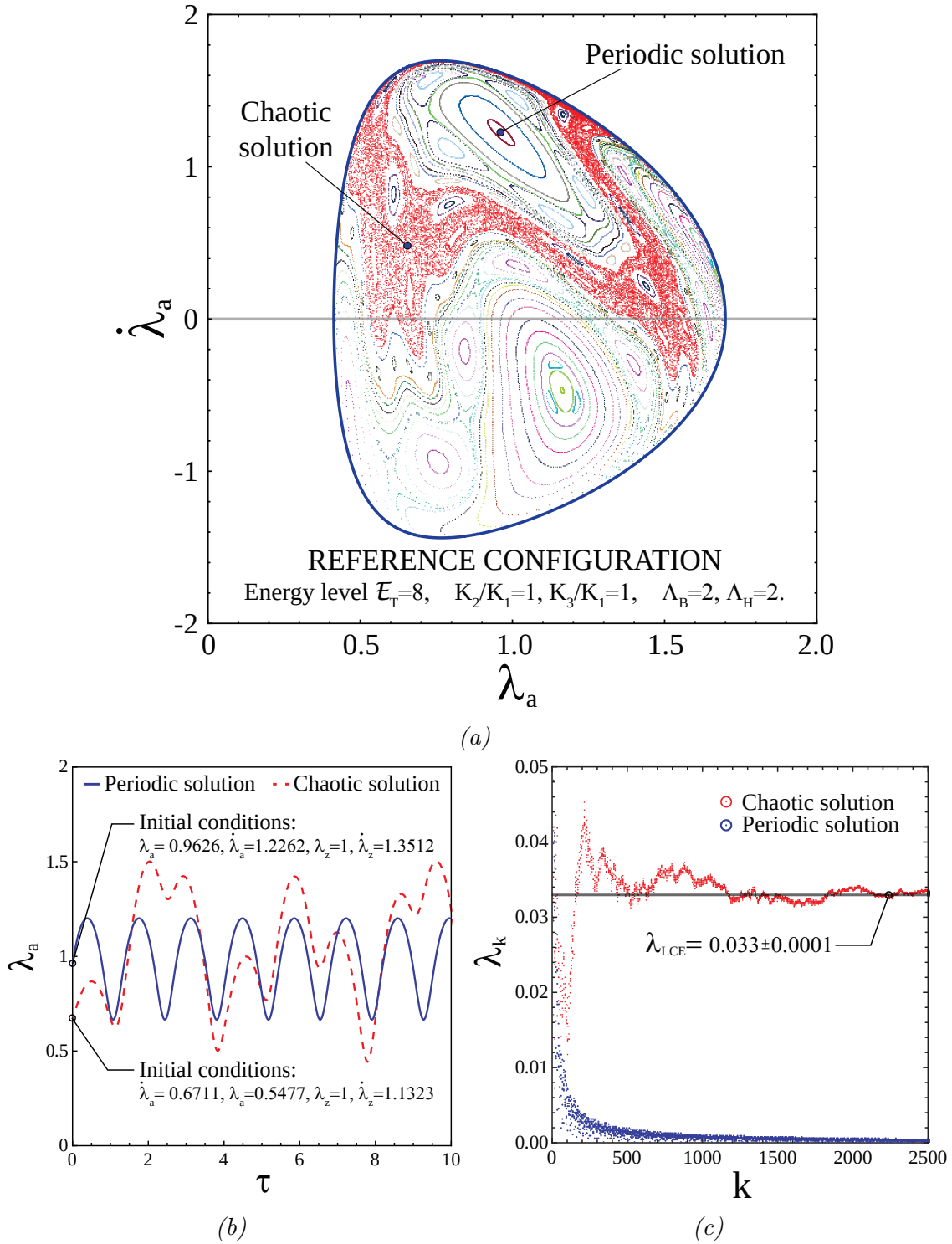

Fig. 8.2 (a) Poincaré SOS corresponding to the reference geometrical parameters, material constants and energy level: $\Lambda_H = \Lambda_B = 2$, $K_2/K_1 = K_3/K_1 = 1$ and $\mathcal{E}_T = 8$. (b) Time evolution of the stretch in the inner face of the cylinder λ_a for the periodic and chaotic trajectories indicated in subfigure (a). (c) Lyapunov exponent λ_k as a function of k for the periodic and chaotic trajectories indicated in subfigure (a). (For interpretation of the references to color in the text, the reader is referred to the web version of this dissertation).

8.4.2 Influence of the energy supplied to the system

Figure 8.3 presents the Poincaré SOS corresponding to the reference geometrical parameters $\Lambda_H = \Lambda_B = 2$, material constants $K_2/K_1 = K_3/K_1 = 1$, and two different values of the total energy supplied to the system. Namely, $\mathcal{E}_T = 6$ (lower than the reference value) is considered in Fig. 8.3a and $\mathcal{E}_T = 10$ (greater than the reference value) is considered in Fig. 8.3b. The black dashed line in Figs. 8.3a and 8.3b corresponds to the curve enclosing the active phase space of the reference configuration presented in Fig. 8.2a. Note that, from this point on, this curve will be plotted in all the Poincaré SOS presented in the chapter with the aim to compare the size of the active phase spaces. A decrease in the energy supplied to the system reduces the active area of the phase space $\{\dot{\lambda}_a, \lambda_a\}$ and favors that the system develops periodic and quasi-periodic motions rather than chaotic motion. In the case of $\mathcal{E}_T = 6$ shown in Fig. 8.3a, the cylinder does not present chaotic response for any set of initial conditions. The whole chaotic region observed in Fig. 8.2a for $\mathcal{E}_T = 8$ has been transformed in the case of $\mathcal{E}_T = 6$ in a set of closed curves and single points, which reveal the periodic and quasi-periodic nature of the radial motion of the structure. Note that the closed curves and single points, which are generated by the same trajectory, are plotted with the same color. Similarly, an increase in the energy supplied to the system enlarges the active area of the phase space $\{\dot{\lambda}_a, \lambda_a\}$ and favors the development of chaotic trajectories. In the case of $\mathcal{E}_T = 10$ shown in Fig. 8.3b, the response of the structure is chaotic for most of the initial conditions and the periodic and quasi-periodic trajectories are confined within few (relatively) small islands. We have checked that for values of $\mathcal{E}_T$ greater than 10 the chaotic region continues growing until it virtually covers the whole phase space. This is consistent with the Kolmogorov-Arnold-Moser (KAM) theory (see, e.g., Arnol'd (2013)), which predicts that, as the energy supplied to the system increases, those tori with a rational winding number [4] are destroyed. These tori (formerly closed curves in the $\{\dot{\lambda}_a, \lambda_a\}$ phase space) break up into chains of alternating elliptic and hyperbolic fixed points, as predicted by the Poincaré–Birkhoff fixed point theorem (Birkhoff, 1913). The comparison of Figs. 8.2a, 8.3a and 8.3b allows to identify these chains, and reveals that the chaos starts from the hyperbolic points of these chains.

In the next section we investigate the influence of the dimensions of the cylinder in the dynamic response of the system.

[4] When the trajectories lying on the surface of a torus are described in the angle-action variables, the winding number is defined as the ratio between the two orbiting frequencies. A system with a rational winding number is mode-locked, whereas a system with an irrational winding number is quasi-periodic. See, e.g., Arnol'd (2013) for further details.

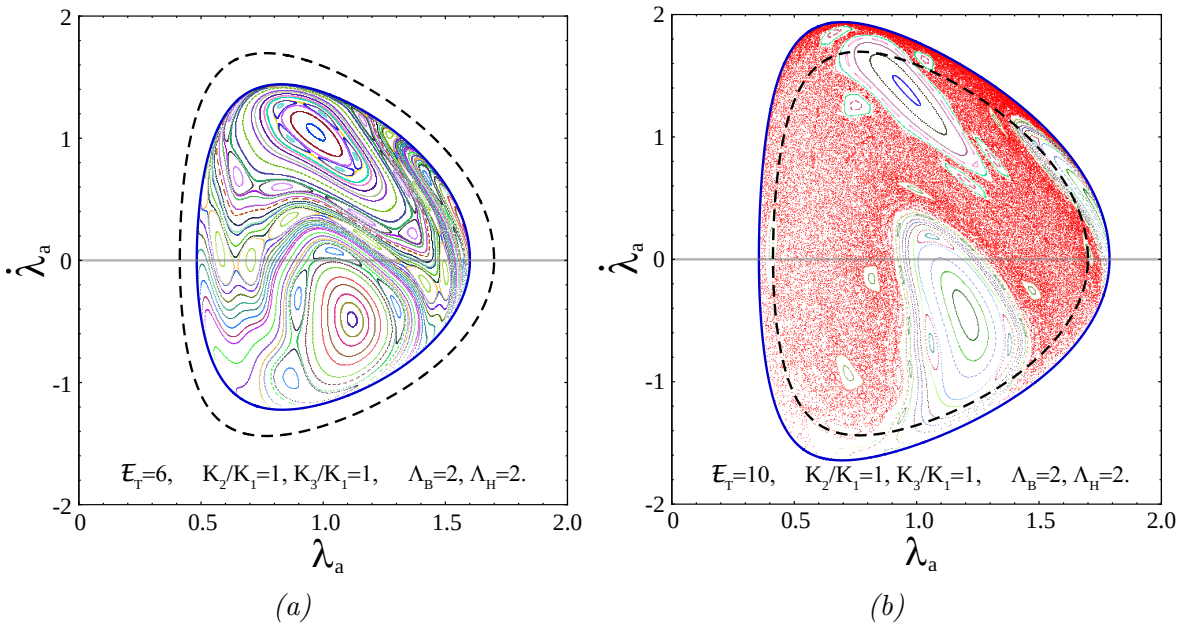

(a) *(b)*

Fig. 8.3 Poincaré SOS corresponding to the reference geometrical parameters $\Lambda_H = \Lambda_B = 2$ and material constants $K_2/K_1 = K_3/K_1 = 1$, and two different values of the total energy supplied to the system. (a) $\mathcal{E}_T = 6$ and (b) $\mathcal{E}_T = 10$. (For interpretation of the references to color in the text, the reader is referred to the web version of this dissertation).

8.4.3 Influence of the specimen dimensions

Figure 8.4 depicts the Poincaré SOS corresponding to the reference non-dimensional thickness $\Lambda_B = 2$, material constants $K_2/K_1 = K_3/K_1 = 1$, supplied energy $\mathcal{E}_T = 8$, and two different values of the non-dimensional height of the cylinder Λ_H. Namely, $\Lambda_H = 1.7$ (lower than the reference value) is considered in Fig. 8.4a and $\Lambda_H = 15$ (greater than the reference value) is considered in Fig. 8.4b. A decrease in the height of the cylinder enlarges the active surface of the phase space since a smaller structure develops radial oscillations for the same supplied energy, which are faster and have greater amplitude. Moreover, note that a decrease in Λ_H favors the development of chaotic motions. In the case of $\Lambda_H = 1.7$ shown in Fig. 8.4a, the response of the structure is chaotic for most of the initial conditions. Furthermore, we have checked that, for values of Λ_H smaller than 1.7, the chaotic region extends virtually to all the phase space. Similarly, an increase in the height of the cylinder reduces the active surface of the phase space since, as expected, a bigger structure develops radial oscillations, which are slower and have smaller amplitude. An increase in Λ_H favors the development of periodic and quasi-periodic trajectories rather than chaotic. In fact, in the case of $\Lambda_H = 15$ shown in Fig. 8.4b, the response of the system is never chaotic. In addition, we have checked that for a value of Λ_H equal or

greater than 15 (the tube becomes very long) the three dimensional tori, which describes the motion of the structure in the phase space $\{\lambda_a, \lambda_z, \dot{\lambda}_a\}$, collapse in different curves contained in the plane $\lambda_z = 1$. In other words, the response of the cylinder approaches plane strain conditions, i.e., $\lambda_z \sim 1$ and $\lambda_a >> \lambda_z$. Therefore, the curves depicted in Fig. 8.4b are no longer Poincaré SOS but *complete* phase portraits in the $\{\dot{\lambda}_a, \lambda_a\}$ phase space. Each closed curve in Fig. 8.4b corresponds to a periodic solution, i.e., we recover the 1D solution developed by Knowles (1960). It is only in the vicinity of the central point $(1, 0)$ where the plane strain conditions are not satisfied since both stretches are again of the same order of magnitude $O(\lambda_a) \sim O(\lambda_z) \sim 1$.

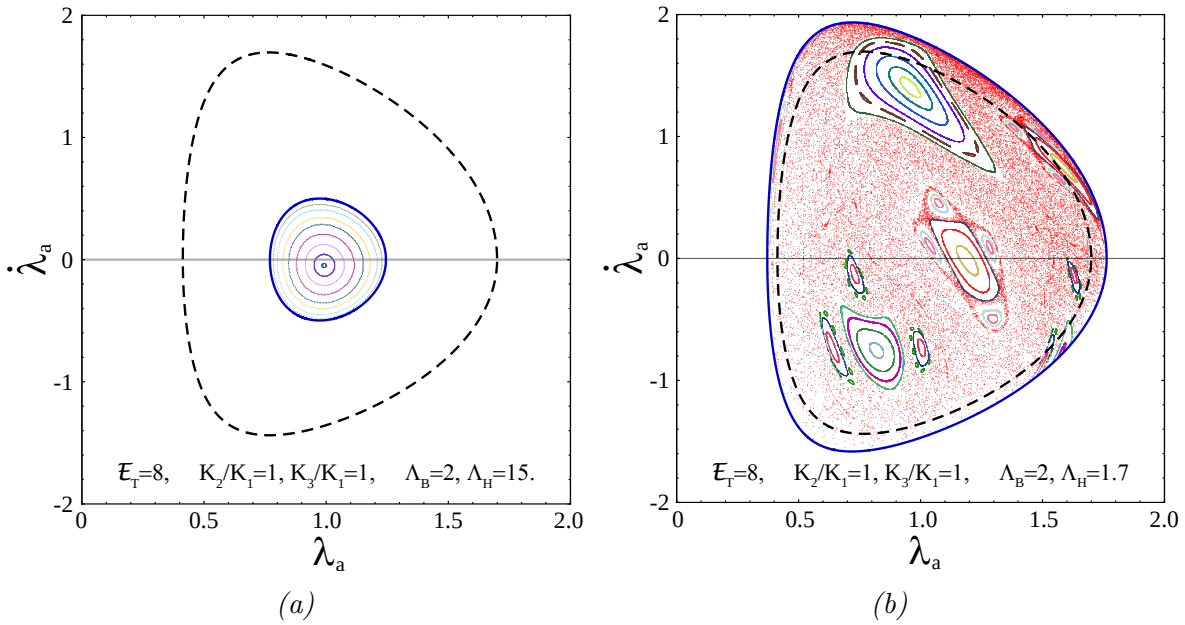

Fig. 8.4 Poincaré SOS corresponding to the reference non-dimensional thickness $\Lambda_B = 2$, material constants $K_2/K_1 = K_3/K_1 = 1$ and supplied energy $\mathcal{E}_T = 8$, and two different values of the non-dimensional height of the cylinder. (a) $\Lambda_H = 1.7$ and (b) $\Lambda_H = 15$. Note: subfigure (b) is not really a Poincaré SOS but a complete phase portrait in the $\{\dot{\lambda}_a, \lambda_a\}$ space.

In Fig. 8.5 we show the Poincaré SOS corresponding to the reference non-dimensional height $\Lambda_H = 2$, material constants $K_2/K_1 = K_3/K_1 = 1$, supplied energy $\mathcal{E}_T = 8$, and two different values of the non-dimensional thickness of the cylinder Λ_B. Namely, Fig. 8.5a depicts the solutions for the case of $\Lambda_B = 1.7$ (lower than the reference value), while Fig. 8.5b depicts $\Lambda_B = 15$ (greater than the reference value). As expected, a decrease in the thickness of the shell increases the active surface of the phase space and promotes the chaotic response of the structure. In the case of $\Lambda_B = 1.7$, shown in Fig. 8.5a, the response of the structure is chaotic for most of the initial conditions. On the other hand,

an increase of Λ_B reduces the surface of the active phase space and favors quasi-periodic and periodic responses. In fact, in the case of $\Lambda_B = 15$, depicted in Fig. 8.5b, the structure does not present chaotic motion for any initial conditions. Furthermore, we have checked that for a value of Λ_B equal or greater than 15 (the tube becomes very short; like a large plate) the three dimensional tori, which describes the motion of the structure in the phase space $\{\lambda_a, \lambda_z, \dot{\lambda}_a\}$, collapse in different curves contained in the plane $\lambda_z = 1$ (as in the case of $\Lambda_H = 15$ discussed in previous paragraph). The curves depicted in Fig. 8.5b are *complete* phase portraits in the $\{\dot{\lambda}_a, \lambda_a\}$ space and define periodic solutions. In other words, the problem becomes 1D. As in the previous case, in the vicinity of the central point $(1, 0)$ both stretches are again of the same order of magnitude $O(\lambda_a) \sim O(\lambda_z) \sim 1$.

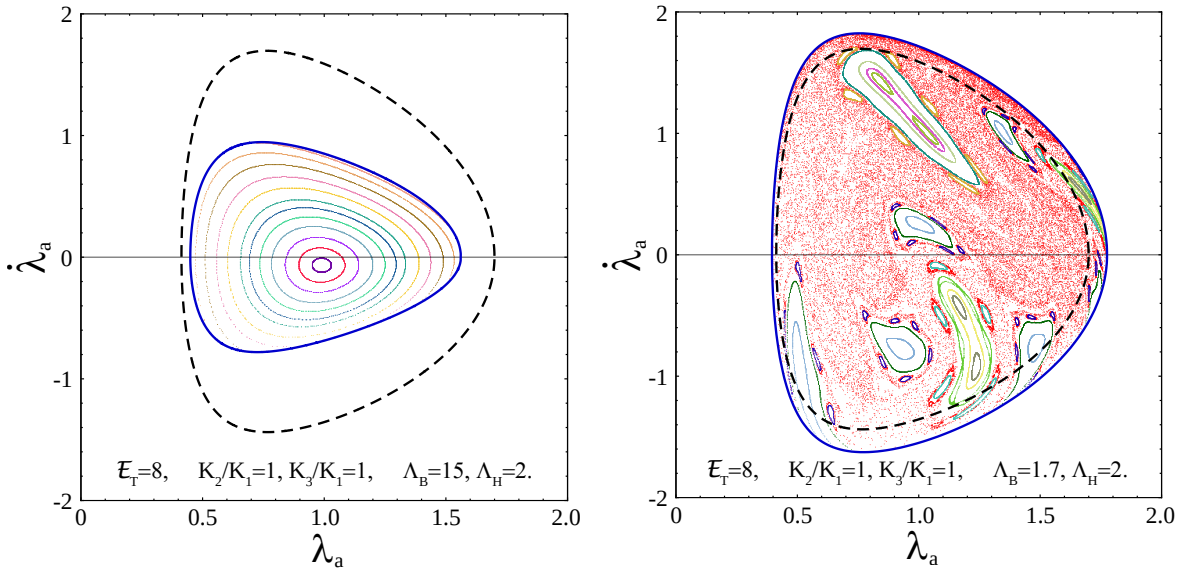

(a) *(b)*

Fig. 8.5 Poincaré SOS corresponding to the reference non-dimensional height $\Lambda_H = 2$, material constants $K_2/K_1 = K_3/K_1 = 1$ and supplied energy $\mathcal{E}_T = 8$, and two different values of the non-dimensional thickness of the cylinder. (a) $\Lambda_B = 1.7$ and (b) $\Lambda_B = 15$. Note: subfigure (b) is not really a Poincaré SOS but a complete phase portrait in the $\{\dot{\lambda}_a, \lambda_a\}$ space.

It is apparent from previous analysis that, when the volume of the structure is large enough, either because the tube is infinitely long or the plate is infinitely large, the system tends to show periodic behaviors.

In the next section we investigate the influence of the mechanical anisotropy of the material in the dynamic response of the system.

8.4.4 Influence of the material anisotropy

Figure 8.6 presents the Poincaré SOS corresponding to the reference geometrical parameters $\Lambda_H = \Lambda_B = 2$, circumferential stiffness $K_2/K_1 = 1$, supplied energy $\mathcal{E}_T = 8$, and two different values of the axial stiffness K_3/K_1. Namely, Fig. 8.6a depicts $K_3/K_1 = 0.5$ (smaller than the reference value) and Fig. 8.6b depicts $K_3/K_1 = 100$ (greater than the reference value). It has to be noticed that the area of the active phase space in the $\{\dot{\lambda}_a, \lambda_a\}$ plane remains unchanged against variations in the axial stiffness. This area may be understood as joint measure of the kinetic and strain energies associated with the radial motion, which is revealed independent of the axial stiffness. A decrease in the axial stiffness favors that the development of chaotic motion. In fact, in the case of $K_3/K_1 = 0.5$ illustrated in Fig. 8.6a, the structure presents chaotic response for most of the initial conditions. On the other hand, an increase in the axial stiffness promotes periodic and quasi-periodic trajectories. In particular, for the case of $K_3/K_1 = 100$ illustrated in Fig. 8.6b, the tori describing the 3D motion of the structure collapse in several curves contained in the plane $\lambda_z = 1$ (as in the cases of $\Lambda_H = 15$ and $\Lambda_B = 15$ presented in Section 8.4.3) and the motion of the cylinder is periodic. The curves depicted in Fig. 8.6b are *complete* phase portraits in the $\{\dot{\lambda}_a, \lambda_a\}$ space and define periodic solutions.

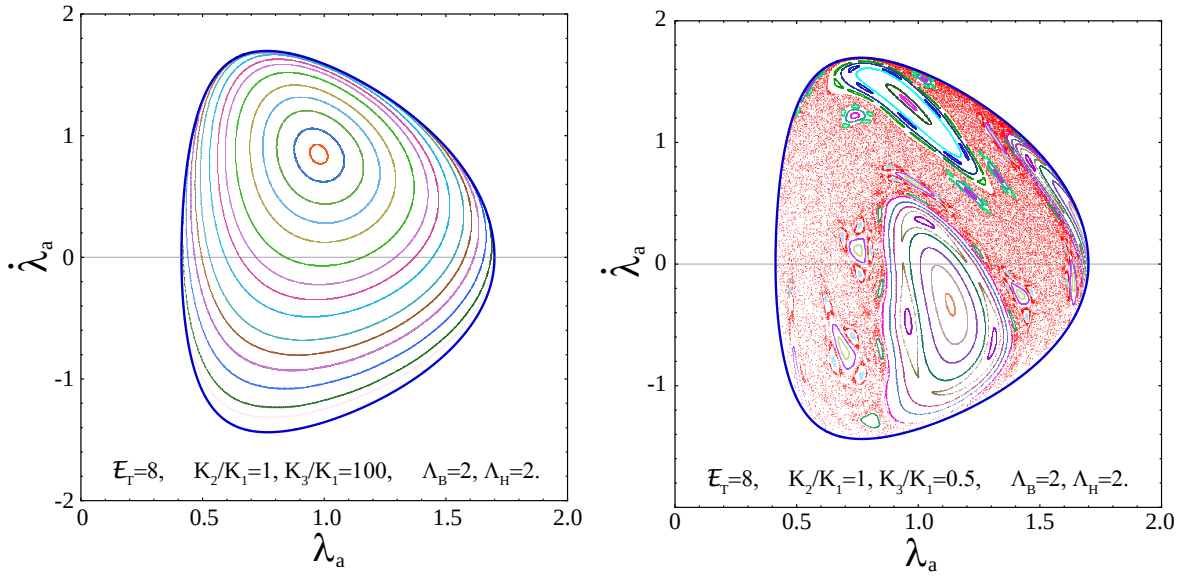

(a) *(b)*

Fig. 8.6 Poincaré SOS corresponding to the reference geometrical parameters $\Lambda_H = \Lambda_B = 2$, circumferential stiffness $K_2/K_1 = 1$ and supplied energy $\mathcal{E}_T = 8$, and two different values of the axial stiffness. (a) $K_3/K_1 = 0.5$ and (b) $K_3/K_1 = 100$. Note: subfigure (b) is not really a Poincaré SOS but a complete phase portrait in the $\{\dot{\lambda}_a, \lambda_a\}$ space.

The problem becomes 1D as the degree of freedom in the axial direction z is lost. Note that, due to the mechanical anisotropy of the material, the central point of the orbits is $(1, 0.85)$ instead of $(1, 0)$ like in the examples presented in Section 8.4.3, where the material behavior was considered isotropic.

Finally, in Fig. 8.7 we present the Poincaré SOS corresponding to the reference geometrical parameters $\Lambda_H = \Lambda_B = 2$, axial stiffness $K_3/K_1 = 1$, supplied energy $\mathcal{E}_T = 8$, and two different values of the circumferential stiffness. Namely, Fig. 8.7a depicts $K_2/K_1 = 0.4$ (smaller than the reference value), while Fig. 8.7b presents the solutions for $K_2/K_1 = 100$ (greater than the reference value). A decrease in the circumferential stiffness increases the active surface of the phase space due to the increase of the amplitude of the radial oscillations, i.e., the phase space enlarges along the λ_a axis. A decrease in K_2/K_1 also favors the development of chaotic motions. In particular, in the case of $K_2/K_1 = 0.4$, depicted in Fig. 8.7a, the chaotic region extends practically to all the phase space. On the other hand, an increase in the circumferential stiffness reduces the amplitude of the radial oscillations and, therefore, the active area of the phase space. An increase of K_2/K_1 also promotes periodic and quasi-periodic motions. Specifically, in the case of $K_2/K_1 = 100$ depicted in Fig. 8.7b, the structure does not show chaotic motion for any initial conditions. We have checked that for values of K_2/K_1 equal or greater than 100 the tori, which describe the 3D motion of the structure, collapse in different curves contained in the plane $\lambda_z = 1$ (as in the cases of $\Lambda_H = 15$, $\Lambda_B = 15$ and $K_3/K_1 = 100$ discussed in previous paragraphs) and the motion of the cylinder becomes periodic. The curves depicted in Fig. 8.7b are again *complete* phase portraits in the $\{\dot{\lambda}_a, \lambda_a\}$ space, i.e., the problem becomes 1D. Note that, due to the mechanical anisotropy of the material, the central point of the orbits is $(1, 0.35)$ instead of $(1, 0)$ like in the examples presented in Section 8.4.3.

8.5 Summary and conclusions

In this chapter we have investigated the large-amplitude axisymetric free vibrations of an incompressible nonlinear elastic cylindrical structure. The material has been described as orthotropic and hyperelastic using the constitutive model developed by Rubin and Jabareen (2007, 2010). The cylinder has been modeled using the theory of a generalized Cosserat membrane which allows for finite deformations that include displacements along the longitudinal axis of the structure. We have conducted a parametric analysis to identify the influence that the initial conditions, the energy supplied to the system, the dimensions of the specimen and the material anisotropy have on the dynamic response

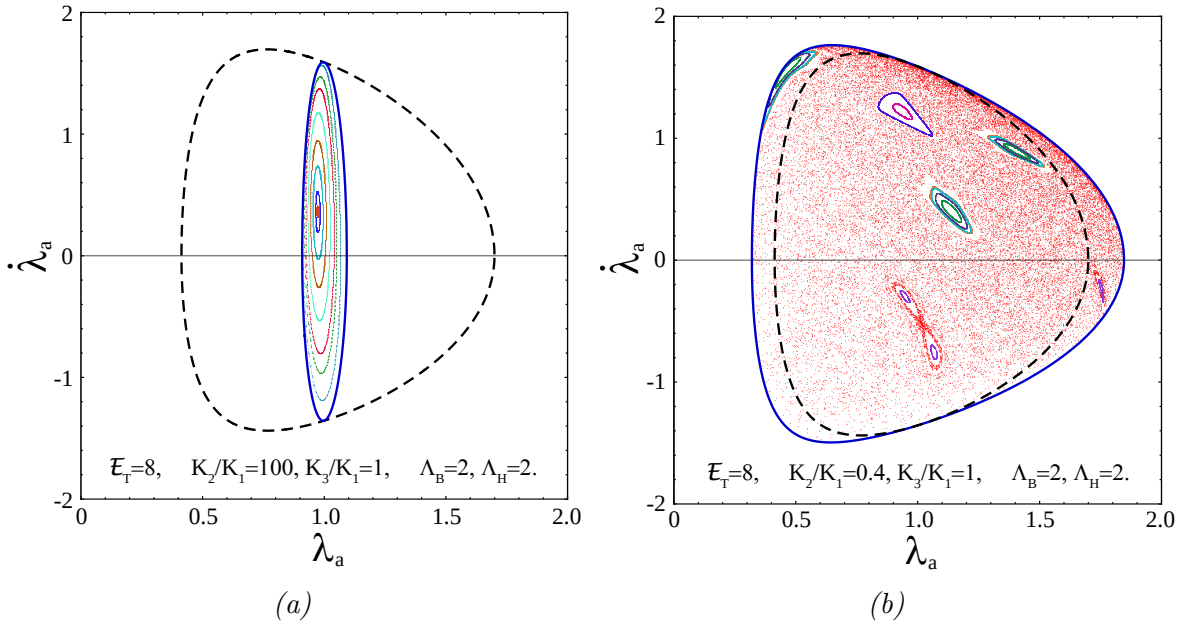

Fig. 8.7 Poincaré SOS corresponding to the reference geometrical parameters $\Lambda_H = \Lambda_B = 2$, axial stiffness $K_3/K_1 = 1$ and supplied energy $\mathcal{E}_T = 8$, and two different values of the circumferential stiffness. (a) $K_2/K_1 = 0.4$ and (b) $K_2/K_1 = 100$. Note: subfigure (b) is not really a Poincaré SOS but a complete phase portrait in the $\{\dot{\lambda}_a, \lambda_a\}$ space.

of the structure. We have used Poincaré maps and Lyapunov exponents to assess the nature of the motion of the cylinder and the following conclusions have been obtained:

- Initial conditions: the dynamic response of the system has been proved to be very sensitive to the initial conditions. For a given set of energy supplied to the system, geometrical parameters and material constants, the response of the cylinder may turn from periodic to quasi-periodic and chaotic with slight variations in the stretch and stretch rate initially imposed to the structure.

- Energy supplied to the system: as the energy supplied to the system increases, the motion of the system turns from periodic and quasi-periodic to chaotic. The tori which contain the periodic and quasi-periodic trajectories of the structure are gradually destroyed with the increase of the supplied energy, which gives rise to stochastic behavior in the dynamic response of the system. We have shown that for sufficiently small energies the response of the structure is always periodic or quasi-periodic, while for sufficiently large energies is always chaotic. These results agree with the conclusions derived in Chapter 3 and they are consistent with the KAM theory which postulates that, as the energy of the system increases, the tori which contain the regular trajectories of the structure are gradually destroyed,

which gives rise to the emergence of stochastic behavior in the dynamic response of the system.

- Specimen dimensions: as the volume of the cylinder decreases, the system is more prone to develop chaotic motion. The smaller the size of the cylinder, the smaller the amount ot energy required to destroy the tori which contain the periodic and quasi-periodic trajectories of the structure. To be highlighted that the general 2D formulation developed in this chapter allows to recover the specific cases of an infinitely long cylinder and an infinitely large plate for which the problem can be approached within a 1D framework and the response of the structure becomes periodic.

- Material anisotropy: the structure is more prone to develop chaotic motion as the stiffness along the axial and circumferential direction decreases with respect to the stiffness along the radial direction. On the other hand, if the axial stiffness or the circumferential stiffness of the material are sufficiently high, the response of the cylinder becomes periodic. This is a key result of this research that makes apparent that the degree of mechanical anisotropy of the material influences the nature of the dynamic response of the system.

Altogether, this research complements the 1D approach developed in Chapter 3 –where we studied infinitely long samples assuming plane strain conditions along their axial direction and an isotropic constitutive model– to a 2D framework which considers structures of finite axial length with anisotropic material. To take the axial displacements of the structure into account enables the system to show quasi-periodic and chaotic responses, which do not appear in the 1D approximation.

Part V

Conclusions, future works and references

9 Conclusions and future works

In this chapter we briefly summarize the main conclusions of this dissertation and propose some future work to continue the research developed in this doctoral thesis.

9.1 Conclusions

In accordance with the general objective established in Chapter 1, we have developed a thorough analysis of the free and forced nonlinear vibrations of cylindrical and spherical elastic (thick-walled) shell structures subjected to a wide variety of initial and boundary conditions using 1D and 2D theoretical frameworks. The attention has been focused on understanding the role played by the constitutive model used to describe the mechanical behavior of the material in the dynamic response of the system. The research, which started by considering isotropic, incompressible and rate independent constitutive models, was based on the systematic incorporation of compressibility, viscosity and anisotropy in the description of the mechanical response of (thick-walled) shells. While the main outcomes of this dissertation have already been described at the end of each chapter, we recall here the most relevant conclusions for the sake of completeness.

- **Part II: 1D finite vibrations of isotropic hyperelastic structures.** We focused our attention on isotropic, incompressible and compressible, hyperelastic structures subjected to constant and harmonic time dependent pressures. In the case of constant pressure, we showed that, depending on the constitutive model, there may be values of the applied pressure that impose limits to the oscillatory response of the shell. Such limiting values of pressure have been shown to be very much dependent on the compressibility of the material. In the case of harmonic time dependent pressure, we have shown that the response of the structure may be periodic, quasi-periodic or chaotic, depending on the value of the external load.

In addition, we have obtained the complete nonlinear resonance diagrams of the structure and demonstrated their strong dependence on the constitutive model.

- **Part III: 1D finite vibrations of isotropic visco-hyperelastic structures.** We focused our attention on isotropic incompressible visco-hyperelastic structures subjected to constant and harmonic time dependent pressures. In the case of constant pressure, we demonstrated that material viscosity reduces the amplitude and speed of the vibrations of the structure, up to a point that the system may reach a resting condition for sufficiently long loading times. In the case of harmonic time dependent pressure, we showed the key role played by the material rate dependence in the nonlinear resonance diagrams of the structure, which causes the emergence of scape bands for which the response of the structure is not periodic.

- **Part IV: 2D finite vibrations of anisotropic hyperelastic structures.** We focused our attention on anisotropic incompressible hyperelastic structures subjected to *ab initio* values of elastic stored and kinetic energy. The analysis revealed that the response of the structure turns from periodic, to quasi-periodic and chaotic depending on the energy supplied to the system, the size of the specimen and the degree of mechanical anisotropy of the material. Namely, the development of chaotic motion is favored by the increase of the energy supplied to the system, the decrease of the sample size and the decrease of the stiffness ratio between axial/circumferential and radial directions.

This dissertation has brought to light the relevance of accurate material constitutive descriptions in modeling the dynamic behavior of man-made and natural elastic structures. These structures are commonly found in a wide variety of applications that go from lead-rubber bearings to saccular aneurysms. The dependence of the mechanical model with respect to strain, strain rate, anisotropy or hydrostatic pressure have been proven to be of great importance for the correct modeling of the non linear dynamics of these structures. We expect that the work presented herein will contribute to encourage further research on the influence of constitutive modeling on the behavior of such nonlinear dynamical systems.

9.2 Future works

Throughout this research we have analyzed the role played by compressibility, viscosity and anisotropy in the nonlinear dynamics of thick-walled hyperelastic shells. However, as pointed out by several authors, other factors such as the temperature sensitivity also

play an important role in the dynamic deformation of nonlinear elastic structures; see e.g., Hwang and Hsu (2001); Ibrahim (2008); Wollscheid and Lion (2013). Therefore, it becomes apparent that the work developed in this dissertation should be extended considering constitutive models which include the temperature sensitivity of the material, in order to address the influence of thermo-mechanical coupling in the dynamic response of hyperelastic structures.

Moreover, the concepts, techniques and tools employed in this dissertation can be easily extended to analyze other deformation modes beyond the cylindrical and spherical cases analyzed here. For example, the shear dominated deformations presented in base isolation systems (Datta, 2010). Furthermore, there are some other interesting features about the vibrational behavior of nonlinear elastic structures, i.e., the static pre-stretch has been proved to play a major role in the nonlinear dynamics of rubber isolators (Sjöberg and Kari, 2003; Zou et al., 2010), which could be addressed as a continuation of this research. Another interesting topic of investigation could also be the vibro-acoustical coupling of rubber isolators, which is of great interest for the industry (specially for the transportation industry) in order to avoid annoying noises (Coja and Kari, 2007; Kari, 2003).

Finally, let us note that, while in recent years some experimental studies on hyperelastic cylindrical and spherical shells have been published (see e.g., Gonçalves et al. (2008); Guo et al. (2013); Lopes et al. (2006)), none of them have investigated the fundamental aspects of the nonlinear dynamics of this type of structures. Hence, the design and development of specific experiments to validate and extend the results obtained in this dissertation remains as a future work.

References

ABAQUS/Explicit (2014). *Abaqus Explicit v6.14 User's Manual*. ABAQUS Inc., Richmond, USA, version 6.14 edition.

Akkas, N. (1990). Aneurysms as a biomechanical instability problem. In *Biomechanical Transport Processes*, pages 303–311. Springer US.

Al-Anany, Y. M. and Tait, M. J. (2017). Fiber reinforced elastomeric isolators for the seismic isolation of bridges. *Composite Structures*, 160:300–311, DOI: 10.1016/j.compstruct.2016.10.008.

Alijani, F. and Amabili, M. (2014). Non-linear vibrations of shells: A literature review from 2003 to 2013. *International Journal of Non-Linear Mechanics*, 58:233–257, DOI: 10.1016/j.ijnonlinmec.2013.09.012.

Allgower, E. L. and Georg, K. (2011). *Numerical Continuation Methods*. Springer.

Amabili, M., Balasubramanian, P., Breslavsky, I. D., Ferrari, G., Garziera, R., and Riabova, K. (2016). Experimental and numerical study on vibrations and static deflection of a thin hyperelastic plate. *Journal of Sound and Vibration*, 385:81–92, DOI: 10.1016/j.jsv.2016.09.015.

Amabili, M. and Reddy, J. N. (2010). A new non-linear higher-order shear deformation theory for large-amplitude vibrations of laminated doubly curved shells. *International Journal of Non-Linear Mechanics*, 45(4):409–418, DOI: 10.1016/j.ijnonlinmec.2009.12.013.

Amin, A. F. M. S., Lion, A., Sekita, S., and Okui, Y. (2006). Nonlinear dependence of viscosity in modeling the rate-dependent response of natural and high damping rubbers in compression and shear: Experimental identification and numerical verification. *International Journal of Plasticity*, 22(9):1610–1657, DOI: doi.org/10.1016/j.ijplas.2005.09.005.

Antman, S. S. (2006). *Nonlinear Problems of Elasticity*. Springer New York, Berlin, second edition edition.

Antman, S. S. and Lacarbonara, W. (2009). Forced radial motions of nonlinearly viscoelastic shells. *Journal of Elasticity*, 96(2):155–190, DOI: 10.1007/s10659-009-9203-7.

Aranda-Iglesias, D., Vadillo, G., and Rodríguez-Martínez, J. (2015). Constitutive sensitivity of the oscillatory behaviour of hyperelastic cylindrical shells. *Journal of Sound and Vibration*, 358:199–216, DOI: 10.1016/j.jsv.2015.07.031.

References

Aranda-Iglesias, D., Vadillo, G., Rodríguez-Martínez, J., and Volokh, K. Y. (2017). Modeling deformation and failure of elastomers at high strain rates. *Mechanics of Materials*, 104:85–92, DOI: doi.org/10.1016/j.mechmat.2016.10.004.

Arnol'd, V. I. (2013). *Mathematical methods of classical mechanics*, volume 60. Springer Science & Business Media.

Austin, G. M., Schievink, W., and Williams, R. (1989). Controlled pressure-volume factors in the enlargement of intracranial aneurysms. *Neurosurgery*, 24(5):722–730, DOI: 10.1227/00006123-198905000-00011.

Balakrishnan, R. and Shahinpoor, M. (1977). Finite amplitude oscillations of a thin hyperelastic spherical shell. *Iran. J. Sci. Tech.*, 7:14–20.

Balakrishnan, R. and Shahinpoor, M. (1978). Finite amplitude oscillations of a hyperelastic spherical cavity. *International Journal of Non-Linear Mechanics*, 13(3):171–176, DOI: 10.1016/0020-7462(78)90005-7.

Ball, J. M. (1982). Discontinuous equilibrium solutions and cavitation in nonlinear elasticity. *Philosophical Transactions of the Royal Society A: Mathematical, Physical and Engineering Sciences*, 306(1496):557–661, DOI: 10.1098/rsta.1982.0095.

Bar-Cohen, Y. (2000). Electroactive polymers as artificial muscles: Capabilities, potentials and challenges. In *Robotics 2000*. American Society of Civil Engineers.

Bayraktar, E., Bessri, K., and Bathias, C. (2008). Deformation behaviour of elastomeric matrix composites under static loading conditions. *Engineering Fracture Mechanics*, 75(9):2695–2706, DOI: 10.1016/j.engfracmech.2007.03.016.

Beatty, M. F. (2007). On the radial oscillations of incompressible, isotropic, elastic and limited elastic thick-walled tubes. *International Journal of Non-Linear Mechanics*, 42(2):283–297, DOI: 10.1016/j.ijnonlinmec.2006.10.007.

Beatty, M. F. (2011a). Infinitesimal stability of the equilibrium states of an incompressible, isotropic elastic tube under pressure. *Journal of Elasticity*, 104(1-2):71–90, DOI: 10.1007/s10659-011-9321-x.

Beatty, M. F. (2011b). Small amplitude radial oscillations of an incompressible, isotropic elastic spherical shell. *Mathematics and Mechanics of Solids*, 16(5):492–512, DOI: 10.1177/1081286510387407.

Benettin, G., Galgani, L., Giorgilli, A., and Strelcyn, J.-M. (1980a). Lyapunov characteristic exponents for smooth dynamical systems and for hamiltonian systems; a method for computing all of them. part 1: Theory. *Meccanica*, 15(1):9–20, DOI: 10.1007/bf02128236.

Benettin, G., Galgani, L., Giorgilli, A., and Strelcyn, J.-M. (1980b). Lyapunov characteristic exponents for smooth dynamical systems and for hamiltonian systems; a method for computing all of them. part 2: Numerical application. *Meccanica*, 15(1):21–30, DOI: 10.1007/bf02128237.

Benettin, G., Galgani, L., and Strelcyn, J.-M. (1976). Kolmogorov entropy and numerical experiments. *Physical Review A*, 14(6):2338–2345, DOI: 10.1103/physreva.14.2338.

Benettin, G. and Strelcyn, J. M. (1978). Numerical experiments on the free motion of a point mass moving in a plane convex region: Stochastic transition and entropy. *Physical Review A*, 17(2):773–785, DOI: 10.1103/physreva.17.773.

Bergström, J. and Boyce, M. (1998a). Constitutive modeling of the large strain time-dependent behavior of elastomers. *Journal of the Mechanics and Physics of Solids*, 46(5):931–954, DOI: 10.1016/S0022-5096(97)00075-6.

Bergström, J. and Boyce, M. (1998b). Constitutive modeling of the large strain time-dependent behavior of elastomers. *Journal of the Mechanics and Physics of Solids*, 46(5):931–954, DOI: 10.1016/s0022-5096(97)00075-6.

Bergstrom, J. S. (2015). *Mechanics of solid polymers: theory and computational modeling*. Elsevier Science Publishing Co Inc.

Birkhoff, G. D. (1913). Proof of poincaré's geometric theorem. *Transactions of the American Mathematical Society*, 14(1):14–22, DOI: 10.1090/s0002-9947-1913-1500933-9.

Breslavsky, I. D., Amabili, M., and Legrand, M. (2014a). Nonlinear vibrations of thin hyperelastic plates. *Journal of Sound and Vibration*, 333(19):4668–4681, DOI: 10.1016/j.jsv.2014.04.028.

Breslavsky, I. D., Amabili, M., and Legrand, M. (2014b). Physically and geometrically non-linear vibrations of thin rectangular plates. *International Journal of Non-Linear Mechanics*, 58:30–40, DOI: 10.1016/j.ijnonlinmec.2013.08.009.

Bucchi, A. and Hearn, G. E. (2013a). Predictions of aneurysm formation in distensible tubes: Part a—theoretical background to alternative approaches. *International Journal of Mechanical Sciences*, 71:1–20, DOI: 10.1016/j.ijmecsci.2013.02.005.

Bucchi, A. and Hearn, G. E. (2013b). Predictions of aneurysm formation in distensible tubes: Part b—application and comparison of alternative approaches. *International Journal of Mechanical Sciences*, 70:155–170, DOI: 10.1016/j.ijmecsci.2013.02.008.

Buckle, C. and Rabadi, M. (2006). Bilateral pontine infarction secondary to basilar trunk saccular aneurysm. *Archives of Neurology*, 63(10):1498–1499, DOI: 10.1001/archneur.63.10.1498.

Carpi, F. and Smela, E. (2009). *Biomedical applications of electroactive polymer actuators*. John Wiley & Sons.

Carreau, P. J., De Kee, D., and Chhabra, R. P. (1997). *Rheology of polymeric systems: principles and applications*. Hanser Publishers Munich.

Chen, W., Lu, F., Frew, D., and Forrestal, M. (2002). Dynamic compressive testing of soft materials. *Journal of Applied Mechanics*, 69(3):214–223, DOI: 10.1115/1.1464871.

Chen, Y. and Ostoja-Starzewski, M. (2010). MRI-based finite element modeling of head trauma: spherically focusing shear waves. *Acta Mechanica*, 213(1-2):155–167, DOI: 10.1007/s00707-009-0274-0.

Chiba, S., Waki, M., Kornbluh, R., and Pelrine, R. (2009). Innovative wave power generation system using electroactive polymer artificial muscles. In *OCEANS 2009-EUROPE*, pages 1–3. IEEE.

Cho, K., Gent, A., and Lam, P. (1987). Internal fracture in an elastomer containing a rigid inclusion. *Journal of Materials Science*, 22(8):2899–2905, DOI: 10.1007/bf01086488.

Choksi, R. (1997). The singular limit of a hyperbolic system and the incompressible limit of solutions with shocks and singularities in nonlinear elasticity. *Quarterly of Applied Mathematics*, 55(3):485–504, DOI: 10.1090/qam/1466144.

Chou-Wang, M.-S. and Horgan, C. (1989). Cavitation in nonlinear elastodynamics for neo-hookean materials. *International Journal of Engineering Science*, 27(8):967 – 973, DOI: 10.1016/0020-7225(89)90037-2.

Chung, D. D. L. (2001). Review: Materials for vibration damping. *Journal of Materials Science*, 36(24):5733–5737, DOI: 10.1023/A:1012999616049.

Cohen, T. and Molinari, A. (2015). Dynamic cavitation and relaxation in incompressible nonlinear viscoelastic solids. *International Journal of Solids and Structures*, 69 - 70:544 – 552, DOI: 10.1016/j.ijsolstr.2015.04.029.

Coja, M. and Kari, L. (2007). Axial audio-frequency stiffness of a bush mounting—the waveguide solution. *Applied Mathematical Modelling*, 31(1):38–53, DOI: 10.1016/j.apm.2005.08.008.

Coleman, B. D. and Gurtin, M. E. (1967). Thermodynamics with internal state variables. *The Journal of Chemical Physics*, 47(2):597–613, DOI: 10.1063/1.1711937.

Coleman, B. D. and Noll, W. (1963). The thermodynamics of elastic materials with heat conduction and viscosity. *Archive for Rational Mechanics and Analysis*, 13(1):167–178, DOI: 10.1007/BF01262690.

Costalat, V., Sanchez, M., Ambard, D., Thines, L., Lonjon, N., Nicoud, F., Brunel, H., Lejeune, J., Dufour, H., Bouillot, P., Lhaldky, J., Kouri, K., Segnarbieux, F., Maurage, C., Lobotesis, K., Villa-Uriol, M., Zhang, C., Frangi, A., Mercier, G., Bonafé, A., Sarry, L., and Jourdan, F. (2011). Biomechanical wall properties of human intracranial aneurysms resected following surgical clipping (irras project). *Journal of Biomechanics*, 44(15):2685–2691, DOI: 10.1016/j.jbiomech.2011.07.026.

Cristiano, A., Marcellan, A., Long, R., Hui, C.-Y., Stolk, J., and Creton, C. (2010). An experimental investigation of fracture by cavitation of model elastomeric networks. *Journal of Polymer Science Part B: Polymer Physics*, 48(13):1409–1422, DOI: 10.1002/polb.22026.

Dario, P., Carrozza, M. C., Benvenuto, A., and Menciassi, A. (2000). Micro-systems in biomedical applications. *Journal of Micromechanics and Microengineering*, 10(2):235–244, DOI: 10.1088/0960-1317/10/2/322.

Datta, T. K. (2010). *Seismic Analysis of Structures*. John Wiley & Sons.

David, G. and Humphrey, J. (2003). Further evidence for the dynamic stability of intracranial saccular aneurysms. *Journal of Biomechanics*, 36(8):1143–1150, DOI: 10.1016/s0021-9290(03)00083-6.

Doi, M. and Edwards, S. F. (1988). *The Theory of Polymer Dynamics*, volume 73. Oxford University Press.

Fatt, M. S. H. and Ouyang, X. (2008). Three-dimensional constitutive equations for styrene butadiene rubber at high strain rates. *Mechanics of Materials*, 40(1–2):1–16, DOI: doi.org/10.1016/j.mechmat.2007.06.002.

Ferguson, G. G. (1972). Direct measurement of mean and pulsatile blood pressure at operation in human intracranial saccular aneurysms. *Journal of Neurosurgery*, 36(5):560–563, DOI: 10.3171/jns.1972.36.5.0560.

Flory, P. J. (1961). Thermodynamic relations for high elastic materials. *Transactions of the Faraday Society*, 57:829–838, DOI: 10.1039/tf9615700829.

Fung, Y.-c. (1993). *Biomechanics: mechanical properties of living tissues*. Springer Science & Business Media.

Garcia-Gonzalez, D., Jayamohan, J., Sotiropoulos, S., Yoon, S.-H., Cook, J., Siviour, C., Arias, A., and Jerusalem, A. (2017). On the mechanical behaviour of peek and ha cranial implants under impact loading. *Journal of the Mechanical Behavior of Biomedical Materials*, 69:342 – 354, DOI: http://dx.doi.org/10.1016/j.jmbbm.2017.01.012.

Gasser, T. C., Ogden, R. W., and Holzapfel, G. A. (2006). Hyperelastic modelling of arterial layers with distributed collagen fibre orientations. *Journal of The Royal Society Interface*, 3(6):15–35, DOI: 10.1098/rsif.2005.0073.

Gent, A. N. (1990). Cavitation in rubber: A cautionary tale. *Rubber Chemistry and Technology*, 63(3):49–53, DOI: 10.5254/1.3538266.

Gent, A. N. and Lindley, P. B. (1959). Internal rupture of bonded rubber cylinders in tension. *Proceedings of the Royal Society A: Mathematical, Physical and Engineering Sciences*, 249(1257):195–205, DOI: 10.1098/rspa.1959.0016.

Gent, A. N. and Park, B. (1984). Failure processes in elastomers at or near a rigid spherical inclusion. *Journal of Materials Science*, 19(6):1947–1956, DOI: 10.1007/bf00550265.

Ghobarah, A. and Ali, H. M. (1988). Seismic performance of highway bridges. *Engineering Structures*, 10(3):157–166, DOI: doi.org/10.1016/0141-0296(88)90002-8.

Giesselmann, J. and Tzavaras, A. E. (2013). Singular limiting induced from continuum solutions and the problem of dynamic cavitation. *Archive for Rational Mechanics and Analysis*, 212(1):241–281, DOI: 10.1007/s00205-013-0677-x.

Gonçalves, P., Pamplona, D., and Lopes, S. (2008). Finite deformations of an initially stressed cylindrical shell under internal pressure. *International Journal of Mechanical Sciences*, 50(1):92–103, DOI: 10.1016/j.ijmecsci.2007.05.001.

References

Gonçalves, P. B., Soares, R. M., and Pamplona, D. (2009). Nonlinear vibrations of a radially stretched circular hyperelastic membrane. *Journal of Sound and Vibration*, 327(1-2):231–248, DOI: 10.1016/j.jsv.2009.06.023.

Green, A. and Zerna, W. (1954). *Theoretical elasticity*. The Clarendon Press.

Green, A. E. and Rivlin, R. S. (1957). The mechanics of non-linear materials with memory, part i. *Archive for Rational Mechanics and Analysis*, (1):1–21.

Green, A. E. and Rivlin, R. S. (1960). The mechanics of non-linear materials with memory, part iii. *Archive for Rational Mechanics and Analysis*, (4):387–404.

Gundiah, N., Ratcliffe, M. B., and Pruitt, L. A. (2007). Determination of strain energy function for arterial elastin: Experiments using histology and mechanical tests. *Journal of Biomechanics*, 40(3):586–594, DOI: 10.1016/j.jbiomech.2006.02.004.

Guo, Z., Wang, S., Li, L., Ji, H., Wang, Z., and Cai, S. (2013). Inflation of Stressed Cylindrical Tubes: An Experimental Study. In *International Conference on Experimental Mechanics 2013 and Twelfth Asian Conference on Experimental Mechanics*, volume 9234, Bangkok, Thailand.

Haddow, J., Lorimer, S., and Tait, R. (1987a). Non-linear combined axial and torsional shear wave propagation in an incompressible hyperelastic solid. *International Journal of Non-Linear Mechanics*, 22(4):297–306, DOI: 10.1016/0020-7462(87)90022-9.

Haddow, J. B., Lorimer, S. A., and Tait, R. J. (1987b). Nonlinear axial shear wave propagation in a hyperelastic incompressible solid. *Acta Mechanica*, 66(1-4):205–216, DOI: 10.1007/bf01184294.

Haddow, J. B. and Mioduchowski, A. (1977). Dynamic expansion of a compressible hyperelastic spherical shell. *Acta Mechanica*, 26(1-4):179–187, DOI: 10.1007/bf01177145.

Hang-Sheng, H. and Abeyaratne, R. (1992). Cavitation in elastic and elastic-plastic solids. *Journal of the Mechanics and Physics of Solids*, 40(3):571–592, DOI: 10.1016/0022-5096(92)80004-a.

Harwood, J. A. C. and Schallamach, A. (1967). Dynamic behavior of natural rubber during large extensions. *Journal of Applied Polymer Science*, 11(10):1835–1845, DOI: 10.1002/app.1967.070111002.

Hashiguchi, K. and Yamakawa, Y. (2012). *Introduction to Finite Strain Theory for Continuum Elasto-Plasticity*. JOHN WILEY & SONS INC.

Haslach, H. W. and Humphrey, J. D. (2004). Dynamics of biological soft tissue and rubber: internally pressurized spherical membranes surrounded by a fluid. *International Journal of Non-Linear Mechanics*, 39(3):399–420, DOI: 10.1016/s0020-7462(02)00196-8.

Holzapfel, G. A. (2000). *Nonlinear Solid Mechanics*, volume 24. Wiley John + Sons.

Holzapfel, G. A. and Ogden, R. W. (2003). *Biomechanics of Soft Tissue in Cardiovascular Systems*, volume 441. Springer.

Hoo Fatt, M. S. and Ouyang, X. (2007). Integral-based constitutive equation for rubber at high strain rates. *International Journal of Solids and Structures*, 44(20):6491–6506, DOI: doi.org/10.1016/j.ijsolstr.2007.02.038.

Hu, M., Du, H., and Ling, S. (2002). A digital miniature pump for medical applications. *IEEE/ASME Transactions on Mechatronics*, 7(4):519–523, DOI: 10.1109/tmech.2002.805620.

Huber, N. and Tsakmakis, C. (2000). Finite deformation viscoelasticity laws. *Mechanics of materials*, 32(1):1–18, DOI: 10.1016/S0167-6636(99)00045-9.

Huilgol, R. R. (1967). Finite amplitude oscillations in curvilinearly aeolotropic elastic cylinders. *Quarterly of Applied Mathematics*, 25(3):293–298.

Humphrey, J. and Canham, P. (2000). Structure, mechanical properties, and mechanics of intracranial saccular aneurysms. *Journal of Elasticity*, 61(1/3):49–81, DOI: 10.1023/a:1010989418250.

Humphrey, J. D. and Haslach, H. W. (2003). Elastodynamics of saccular aneurysms: solid-fluid interactions and constitutive relations. *Wall/Fluid Interactions in Physiologic Flows. WIT Press, Southampton*.

Hwang, J. and Chiou, J. (1996). An equivalent linear model of lead-rubber seismic isolation bearings. *Engineering Structures*, 18(7):528 – 536, DOI: http://dx.doi.org/10.1016/0141-0296(95)00132-8.

Hwang, J. and Hsu, T. (2001). A fractional derivative model to include effect of ambient temperature on {HDR} bearings. *Engineering Structures*, 23(5):484 – 490, DOI: http://doi.org/10.1016/S0141-0296(00)00063-8.

Hwang, J. and Sheng, L. (1994). Equivalent elastic seismic analysis of base-isolated bridges with lead-rubber bearings. *Engineering Structures*, 16(3):201 – 209, DOI: http://dx.doi.org/10.1016/0141-0296(94)90078-7.

Ibrahim, R. A. (2008). Recent advances in nonlinear passive vibration isolators. *Journal of Sound and Vibration*, 314:371–452, DOI: doi.org/10.1016/j.jsv.2008.01.014.

Intanoo, P., Sirivat, A., Kunanuruksapong, R., Lerdwijitjarud, W., and Kunchornsup, W. (2012). Electroactive polymer actuator from highly doped permethylpolyazine dispersed in ethylene propylene diene elastomer. *Journal of Polymer Research*, 19(10):9981, DOI: 10.1007/s10965-012-9981-7.

IV, J. H. L. and V, J. H. L. (2008). *A Heat Transfer Textbook, 3rd edition*. Phlogiston Press.

Jaffrin, M. Y. and Shapiro, A. H. (1971). Peristaltic pumping. *Annual Review of Fluid Mechanics*, 3(1):13–37, DOI: 10.1146/annurev.fl.03.010171.000305.

Jain, J. (1963). Mechanism of rupture in intracranial saccular aneurysms. *Surgery*, 54:347–350.

References

Janele, P., Haddow, J. B., and Mioduchowski, A. (1989a). *Continuum Mechanics and its Applications*, chapter Finite dynamic expansion of a hyperelastic circular cylinderical tube, pages 81–91. . Hemisphere Publishing Corporation.

Janele, P., Haddow, J. B., and Mioduchowski, A. (1989b). Finite amplitude spherically symmetric wave propagation in a compressible hyperelastic solid. *Acta Mechanica*, 79(1-2):25–41, DOI: 10.1007/bf01181478.

Janele, P., Mioduchowski, A., and Haddow, J. (1991). A note on finite dynamic deformation of concentric cylinders. *International Journal of Engineering Science*, 29(12):1585–1592, DOI: 10.1016/0020-7225(91)90128-p.

Jansen, E. L. (2007). The effect of geometric imperfections on the vibrations of anisotropic cylindrical shells. *Thin-Walled Structures*, 45(3):274–282, DOI: 10.1016/j.tws.2007.02.014.

Jansen, E. L. (2008). A perturbation method for nonlinear vibrations of imperfect structures: Application to cylindrical shell vibrations. *International Journal of Solids and Structures*, 45(3-4):1124–1145, DOI: 10.1016/j.ijsolstr.2007.07.007.

Kaal, W. and Herold, S. (2011). Electroactive polymer actuators in dynamic applications. *IEEE/ASME Transactions on Mechatronics*, 16(1):24–32, DOI: 10.1109/tmech.2010.2089529.

Kabaria, H., Lew, A. J., and Cockburn, B. (2015). A hybridizable discontinuous galerkin formulation for non-linear elasticity. *Computer Methods in Applied Mechanics and Engineering*, 283:303–329, DOI: 10.1016/j.cma.2014.08.012.

Kari, L. (2003). On the dynamic stiffness of preloaded vibration isolators in the audible frequency range: Modeling and experiments. *The Journal of the Acoustical Society of America*, 113(4):1909–1921, DOI: 10.1121/1.1557214.

Karlsson, F. and Persson, A. (2003). Modelling non-linear dynamics of rubber bushings-parameter identification and validation. *Lund University*.

Keplinger, C., Kaltenbrunner, M., Arnold, N., and Bauer, S. (2010). Rontgens electrode-free elastomer actuators without electromechanical pull-in instability. *Proceedings of the National Academy of Sciences*, 107(10):4505–4510, DOI: 10.1073/pnas.0913461107.

Khan, A. and Farrokh, B. (2006). Thermo-mechanical response of nylon 101 under uniaxial and multi-axial loadings: Part i, experimental results over wide ranges of temperature and strain rates. *International Journal of Plasticity*, 22(8):1506–1529, DOI: 10.1016/j.ijplas.2005.10.001.

Knowles, J. K. (1960). Large amplitude oscillations of a tube of incompressible elastic material. *Quarterly of Applied Mathematics*, 18(1):71–77, DOI: 10.1090/qam/112336.

Knowles, J. K. (1962). On a class of oscillations in the finite-deformation theory of elasticity. *Journal of Applied Mechanics*, 29(2):283–286, DOI: 10.1115/1.3640542.

Knowles, J. K. and Jakub, M. T. (1965). Finite dynamic deformations of an incompressible elastic medium containing a spherical cavity. *Archive for Rational Mechanics and Analysis*, 18(5):367–378, DOI: 10.1007/bf00281326.

Kumar, A., Aranda-Iglesias, D., and Lopez-Pamies, O. (2016). Some remarks on the effects of inertia and viscous dissipation in the onset of cavitation in rubber. *Journal of Elasticity*, 126(2):201–213, DOI: 10.1007/s10659-016-9589-y.

Kumar, A. and Lopez-Pamies, O. (2016). On the two-potential constitutive modeling of rubber viscoelastic materials. *Comptes Rendus Mécanique*, 344(2):102–112, DOI: 10.1016/j.crme.2015.11.004.

Kwak, G. H., Inoue, K., Tominaga, Y., Asai, S., and Sumita, M. (2001). Characterization of the vibrational damping loss factor and viscoelastic properties of ethylene-propylene rubbers reinforced with micro-scale fillers. *Journal of Applied Polymer Science*, 82(12):3058–3066, DOI: 10.1002/app.2161.

Lacarbonara, W. and Antman, S. S. (2012). Parametric instabilities of the radial motions of non-linearly viscoelastic shells under pulsating pressures. *International Journal of Non-Linear Mechanics*, 47(5):461–472, DOI: 10.1016/j.ijnonlinmec.2011.09.017.

Lacarbonara, W., Arena, A., and Antman, S. S. (2014). Flexural vibrations of nonlinearly elastic circular rings. *Meccanica*, 50(3):689–705, DOI: 10.1007/s11012-014-0038-3.

Lawson, J. D. (1966). An order five runge-kutta process with extended region of stability. *SIAM Journal on Numerical Analysis*, 3(4):593–597, DOI: 10.1137/0703051.

Lax, P. D. (1973). *Hyperbolic Systems of Conservation Laws and the Mathematical Theory of Shock Waves*. Society for Industrial and Applied Mathematics.

Le Tallec, P., Rahier, C., and Kaiss, A. (1993). Three-dimensional incompressible viscoelasticity in large strains: Formulation and numerical approximation. *Computer Methods in Applied Mechanics and Engineering*, 109(3-4):233–258, DOI: 10.1016/0045-7825(93)90080-h.

Lefèvre, V. and Lopez-Pamies, O. (2017). Nonlinear electroelastic deformations of dielectric elastomer composites: I - ideal elastic dielectrics. *Journal of the Mechanics and Physics of Solids*, 99:409–437, DOI: 10.1016/j.jmps.2016.07.004.

Lefèvre, V. and Lopez-Pamies, O. (2017). Nonlinear electroelastic deformations of dielectric elastomer composites: Ii - non-gaussian elastic dielectrics. *Journal of the Mechanics and Physics of Solids*, 99:438–470, DOI: 10.1016/j.jmps.2016.07.005.

Lefevre, V., Ravi-Chandar, K., and Lopez-Pamies, O. (2014). Cavitation in rubber: an elastic instability or a fracture phenomenon? *International Journal of Fracture*, 192(1):1 – 23, DOI: 10.1007/s10704-014-9982-0.

Li, S. and Qian, D. (2013). *Multiscale Simulations and Mechanics of Biological Materials*. JOHN WILEY & SONS INC.

Lian, Y. and Li, Z. (2012). Position and size effects on voids growth in nonlinear elasticity. *International Journal of Fracture*, 173(2):147–161, DOI: 10.1007/s10704-011-9674-y.

References

Lion, A. (1996). A constitutive model for carbon black filled rubber: experimental investigations and mathematical representation. *Continuum Mechanics and Thermodynamics*, 8(3):153–169, DOI: 10.1007/BF01181853.

Lockett, F. J. (1972). *Nonlinear viscoelastic solids*. Academic Press.

Lopes, S., Gonçalves, P., and Pamplona, D. (2006). Influence of initial geometric imperfections on the stability of thick cylindrical shells under internal pressure. *Communications in Numerical Methods in Engineering*, DOI: 10.1002/cnm.916.

Lopez-Pamies, O. (2008). Onset of cavitation in compressible, isotropic, hyperelastic solids. *Journal of Elasticity*, 94(2):115–145, DOI: 10.1007/s10659-008-9187-8.

Lopez-Pamies, O. (2010). A new i_1-based hyperelastic model for rubber elastic materials. *Comptes Rendus Mécanique*, 338(1):3 – 11, DOI: 10.1016/j.crme.2009.12.007.

Lopez-Pamies, O., Idiart, M. I., and Nakamura, T. (2011a). Cavitation in elastomeric solids: I—a defect-growth theory. *Journal of the Mechanics and Physics of Solids*, 59(8):1464 – 1487, DOI: 10.1016/j.jmps.2011.04.015.

Lopez-Pamies, O., Nakamura, T., and Idiart, M. I. (2011b). Cavitation in elastomeric solids: II—onset-of-cavitation surfaces for neo-hookean materials. *Journal of the Mechanics and Physics of Solids*, 59(8):1488 – 1505, DOI: 10.1016/j.jmps.2011.04.016.

Lubliner, J. (1985). A model of rubber viscoelasticity. *Mechanics Research Communications*, 12(2):93–99, DOI: doi.org/10.1016/0093-6413(85)90075-8.

Lynch, S. (2007). *Dynamical Systems with Applications using Mathematica®*. Birkhäuser Boston.

MacCormack, R. W. (1969). The effect of viscosity in hypervelocity impact cratering. *Journal of Spacecraft and Rockets*, 40(5):757–763, DOI: 10.2514/2.6901.

MacDonald, D. J., Finlay, H. M., and Canham, P. B. (2000). Directional wall strength in saccular brain aneurysms from polarized light microscopy. *Annals of Biomedical Engineering*, 28(5):533–542, DOI: 10.1114/1.292.

Mason, D. P. and Maluleke, G. H. (2007). Non-linear radial oscillations of a transversely isotropic hyperelastic incompressible tube. *Journal of Mathematical Analysis and Applications*, 333(1):365–380, DOI: 10.1016/j.jmaa.2006.12.031.

Matsagar, V. A. and Jangid, R. S. (2003). Seismic response of base-isolated structures during impact with adjacent structures. *Engineering Structures*, 25(10):1311–1323, DOI: 10.1016/S0141-0296(03)00081-6.

Mendez-Nuñez, L. R. and Carroll, J. J. (1993). Comparison of leapfrog, smolarkiewicz, and MacCormack schemes applied to nonlinear equations. *Monthly Weather Review*, 121(2):565–578, DOI: 10.1175/1520-0493(1993)121<0565:colsam>2.0.co;2.

Miehe, C. and Keck, J. (2000). Superimposed finite elastic–viscoelastic–plastoelastic stress response with damage in filled rubbery polymers. experiments, modelling and algorithmic implementation. *Journal of the Mechanics and Physics of Solids*, 48(2):323–365, DOI: 0.1016/S0022-5096(99)00017-4.

Miroshnikov, A. and Tzavaras, A. (2015). On the construction and properties of weak solutions describing dynamic cavitation. *Journal of Elasticity*, 118(2):141–185, DOI: 10.1007/s10659-014-9488-z.

Mockensturm, E. M. and Goulbourne, N. (2006). Dynamic response of dielectric elastomers. *International Journal of Non-Linear Mechanics*, 41(3):388–395, DOI: 10.1016/j.ijnonlinmec.2005.08.007.

Mohan, A. and Krishnankutty, S. V. (2017). Bridge bearings - a review. *International Research Journal of Engineering and Technology*, 4(01).

Mollica, F., Preziosi, L., and Rajagopal, K. R. (2007). *Modeling of Biological Materials*. Birkhäuser Boston.

Nakamura, T. and Lopez-Pamies, O. (2012). A finite element approach to study cavitation instabilities in non-linear elastic solids under general loading conditions. *International Journal of Non-Linear Mechanics*, 47(2):331–340, DOI: 10.1016/j.ijnonlinmec.2011.07.007.

nan Hung, E. J. and Botwin, M. R. (1975). Mechanics of rupture of cerebral saccular aneurysms. *Journal of Biomechanics*, 8(6):385–392, DOI: 10.1016/0021-9290(75)90074-3.

Nowinski, J. and Wang, S. (1966). Galerkin's solution to a severely non-linear problem of finite elastodynamics. *International Journal of Non-Linear Mechanics*, 1(4):239–246, DOI: 10.1016/0020-7462(66)90007-2.

Oberth, A. E. and Bruenner, R. S. (1965). Tear phenomena around solid inclusions in castable elastomers. *Transactions of the Society of Rheology*, 9(2):165–185, DOI: 10.1122/1.548997.

Ogden, R. W. (1972). Large deformation isotropic elasticity - on the correlation of theory and experiment for incompressible rubberlike solids. *Proceedings of the Royal Society A: Mathematical, Physical and Engineering Sciences*, 326(1567):565–584, DOI: 10.1098/rspa.1972.0026.

Ogden, R. W. (1997). *Non-Linear Elastic Deformations*. Dover Pubn Inc.

Papaspiridis, F. G. and Antoniadis, I. (2008). Dielectric elastomer actuators as elements of active vibration control systems. *Advances in Science and Technology*, 61:103–111, DOI: 10.4028/www.scientific.net/ast.61.103.

Payan, Y. (2012). *Soft Tissue Biomechanical Modeling for Computer Assisted Surgery*, volume 11. Springer Berlin Heidelberg.

Peeters, M., Viguié, R., Sérandour, G., Kerschen, G., and Golinval, J.-C. (2009). Nonlinear normal modes, part II: Toward a practical computation using numerical continuation techniques. *Mechanical Systems and Signal Processing*, 23(1):195 – 216, DOI: 10.1016/j.ymssp.2008.04.003.

References

Peng, W., Zhengtao, S., Liangqing, L., Honggang, J., and Jinghe, W. (2015). Engine isolate mount elastomers. *Advances in Engineering Research: International Conference on Structural, Mechanical and Materials Engineering ((ICSMME 2015))*, pages 5–9, DOI: 10.2991/icsmme-15.2015.2.

Pericak-Spector, K. and Spector, S. (1988). Nonuniqueness for a hyperbolic system: Cavitation in nonlinear elastodynamics. *Archive for Rational Mechanics and Analysis*, 101(4):293–317, DOI: 10.1007/BF00251490.

Pericak-Spector, K. A. and Spector, S. J. (1997). Dynamic cavitation with shocks in nonlinear elasticity. *Proceedings of the Royal Society of Edinburgh: Section A Mathematics*, 127(04):837 – 857, DOI: 10.1017/s0308210500023866.

Poulain, X., Lefèvre, V., Lopez-Pamies, O., and Ravi-Chandar, K. (2017). Damage in elastomers: nucleation and growth of cavities, micro-cracks, and macro-cracks. *International Journal of Fracture*, 205(1):1–21, DOI: 10.1007/s10704-016-0176-9.

Preumont, A. (2011). *Vibration Control of Active Structures*. Springer Netherlands.

Rao, S., Shim, V. P. W., and Quah, S. E. (1997). Dynamic mechanical properties of polyurethane elastomers using a nonmetallic hopkinson bar. *Journal of Applied Polymer Science*, 66(4):619–631, DOI: 10.1002/(SICI)1097-4628(19971024).

Reese, S. and Govindjee, S. (1998a). A theory of finite viscoelasticity and numerical aspects. *International Journal of Solids and Structures*, 35(26):3455–3482, DOI: 10.1016/S0020-7683(97)00217-5.

Reese, S. and Govindjee, S. (1998b). A theory of finite viscoelasticity and numerical aspects. *International Journal of Solids and Structures*, 35(26-27):3455–3482, DOI: 10.1016/s0020-7683(97)00217-5.

Robinson, W. H. (1982). Lead-rubber hysteretic bearings suitable for protecting structures during earthquakes. *Earthquake Engineering & Structural Dynamics*, 10(4):593–604, DOI: 10.1002/eqe.4290100408.

Rodríguez-Martínez, J. A., Fernández-Sáez, J., and Zaera, R. (2015). The role of constitutive relation in the stability of hyper-elastic spherical membranes subjected to dynamic inflation. *International Journal of Engineering Science*, 93:31–45, DOI: 10.1016/j.ijengsci.2015.04.004.

Rubin, M. B. and Jabareen, M. (2007). Physically based invariants for nonlinear elastic orthotropic solids. *Journal of Elasticity*, 90(1):1–18, DOI: 10.1007/s10659-007-9119-z.

Rubin, M. B. and Jabareen, M. (2010). Further developments of physically based invariants for nonlinear elastic orthotropic solids. *Journal of Elasticity*, 103(2):289–294, DOI: 10.1007/s10659-010-9276-3.

Ryan, J. M. and Humphrey, J. D. (1999). Finite element based predictions of preferred material symmetries in saccular aneurysms. *Annals of Biomedical Engineering*, 27(5):641–647, DOI: 10.1114/1.208.

Sahoo, D., Deck, C., and Willinger, R. (2016). Brain injury tolerance limit based on computation of axonal strain. *Accident Analysis & Prevention*, 92:53–70, DOI: 10.1016/j.aap.2016.03.013.

Sarban, R., Jones, R., Mace, B., and Rustighi, E. (2011). A tubular dielectric elastomer actuator: Fabrication, characterization and active vibration isolation. *Mechanical Systems and Signal Processing*, 25(8):2879–2891, DOI: 10.1016/j.ymssp.2011.06.004.

Sarban, R. and Jones, R. W. (2010). Active vibration control using deap actuators. In Bar-Cohen, Y., editor, *Electroactive Polymer Actuators and Devices (EAPAD) 2010*, volume 7642. SPIE.

Sarban, R., Jones, R. W., Mace, B., and Rustighi, E. (2010). Active vibration control of periodic disturbances using a deap damper. In Bar-Cohen, Y., editor, *Electroactive Polymer Actuators and Devices (EAPAD) 2010*, pages 76422Q–76422Q. International Society for Optics and Photonics, SPIE.

Schallamach, A., Sellen, D., and Greensmith, H. (1966). Dynamic behavior of rubber during moderate extensions. *Rubber Chemistry and Technology*, 39(2):328–339, DOI: 10.5254/1.3544845.

Sekhar, L. N. and Heros, R. C. (1981). Origin, growth, and rupture of saccular aneurysms. *Neurosurgery*, 8(2):248–260, DOI: 10.1227/00006123-198102000-00020.

Sekhar, L. N., Sclabassi, R. J., Sun, M., Blue, H. B., and Wasserman, J. F. (1988). Intra-aneurysmal pressure measurements in experimental saccular aneurysms in dogs. *Stroke*, 19(3):352–356, DOI: 10.1161/01.str.19.3.352.

Selvadurai, A. (2006). Deflections of a rubber membrane. *Journal of the Mechanics and Physics of Solids*, 54(6):1093–1119, DOI: 10.1016/j.jmps.2006.01.001.

Seydel, R. U. (2009). *Practical Bifurcation and Stability Analysis*. Springer New York.

Shah, A. and Humphrey, J. (1999). Finite strain elastodynamics of intracranial saccular aneurysms. *Journal of Biomechanics*, 32(6):593–599, DOI: 10.1016/s0021-9290(99)00030-5.

Shahinpoor, M. (1972a). Exact solution to finite amplitude oscillation of an anisotropic thin rubber tube. *The Journal of the Acoustical Society of America*, 56(2):477–480, DOI: 10.1121/1.1903281.

Shahinpoor, M. (1972b). Large amplitude oscillations of a hollow spherical dielectric. *International Journal of Non-Linear Mechanics*, 7(5):527–537, DOI: 10.1016/0020-7462(72)90042-x.

Shahinpoor, M. (2002). Electrically-controllable multi-fingered resilient heart compression devices. US Patent 6,464,655.

Shahinpoor, M. and Balakrishnan, R. (1978). Large amplitude oscillations of thick hyperelastic cylindrical shells. *International Journal of Non-Linear Mechanics*, 13(5):295–301, DOI: 10.1016/0020-7462(78)90035-5.

Shahinpoor, M. and Nowinski, J. (1971). Exact solution to the problem of forced large amplitude radial oscillations of a thin hyperelastic tube. *International Journal of Non-Linear Mechanics*, 6(2):193–207, DOI: 10.1016/0020-7462(71)90055-2.

Simkins, T. and Stehbens, W. (1973). Vibrational behavior of arterial aneurysms. *Letters in Applied and Engineering Sciences*, 1(85):100.

Sjöberg, M. (2002). *On dynamic properties of rubber isolators*. PhD thesis, Institutionen för farkostteknik.

Sjöberg, M. and Kari, L. (2003). Nonlinear isolator dynamics at finite deformations: An effective hyperelastic, fractional derivative, generalized friction model. *Nonlinear Dynamics*, 33(3):323–336, DOI: 10.1023/A:1026037703124.

Soares, R. M. and Gonçalves, P. B. (2012). Nonlinear vibrations and instabilities of a stretched hyperelastic annular membrane. *International Journal of Solids and Structures*, 49(3):514–526, DOI: 10.1016/j.ijsolstr.2011.10.019.

Soares, R. M. and Gonçalves, P. B. (2014). Large-amplitude nonlinear vibrations of a mooney–rivlin rectangular membrane. *Journal of Sound and Vibration*, 333(13):2920–2935, DOI: 10.1016/j.jsv.2014.02.007.

Sracic, M. W. and Allen, M. S. (2011). Numerical continuation of periodic orbits for harmonically forced nonlinear systems. In Proulx, T., editor, *Civil Engineering Topics, Volume 4*, pages 51–69. Springer New York, New York, NY.

Stringfellow, R. and Abeyaratne, R. (1989). Cavitation in an elastomer: Comparison of theory with experiment. *Materials Science and Engineering: A*, 112:127–131, DOI: 10.1016/0921-5093(89)90351-1.

Strogatz, S. H. (2014). *Nonlinear dynamics and chaos: with applications to physics, biology, chemistry, and engineering*. Westview press.

Suzuki, J. and Ohara, H. (1978). Clinicopathological study of cerebral aneurysms. *Journal of Neurosurgery*, 48(4):505–514, DOI: 10.3171/jns.1978.48.4.0505.

Thompson, J. M. T. and Stewart, H. B. (1986). *Nonlinear Dynamics and Chaos: Geometrical Methods for Engineers and Scientists*. Wiley.

Toorani, M. H. (2003). Dynamics of the geometrically non-linear analysis of anisotropic laminated cylindrical shells. *International Journal of Non-Linear Mechanics*, 38(9):1315–1335, DOI: 10.1016/S0020-7462(02)00073-2.

Tóth, B. K., Raffai, G., and Bojtár, I. (2005). Analysis of the mechanical parameters of human brain aneurysm. *Acta of Bioengineering & Biomechanics*, 7(1):3 – 22.

Treloar, L. R. G. (1944). Stress-strain data for vulcanised rubber under various types of deformation. *Transactions of the Faraday Society*, 40:59–70, DOI: 10.1039/tf9444000059.

Tsopelas, P., Constantinou, M., Kim, Y., and Okamota, S. (1996). Experimental study of fps system in bridge seismic isolation. *Earthquake Engineering & Structural Dynamics*, 25:65–78, DOI: 10.1002/(SICI)1096-9845(199601)25:1.

Vahdati, N. and Saunders, L. K. L. (2002). High frequency testing of rubber mounts. *ISA transctions*, 41:145–154, DOI: 10.2991/icsmme-15.2015.2.

Verron, E., Khayat, R. E., Derdouri, A., and Peseux, B. (1999). Dynamic inflation of hyperelastic spherical membranes. *Journal of Rheology*, 43(5):1083–1097, DOI: 10.1122/1.551017.

Verron, E., Marckmann, G., and Peseux, B. (2001). Dynamic inflation of non-linear elastic and viscoelastic rubber-like membranes. *International Journal for Numerical Methods in Engineering*, 50(5):1233–1251, DOI: 10.1002/1097-0207(20010220)50:5<1233::aid-nme77>3.3.co;2-n.

Wang, C.-C. (1965). On the radial oscillations of a spherical thin shell in the finite elasticity theory. *Quarterly of Applied Mathematics*, 23(3):270–274, DOI: 10.1090/qam/187477.

Wang, T., Farajollahi, M., Choi, Y. S., Lin, I.-T., Marshall, J. E., Thompson, N. M., Kar-Narayan, S., Madden, J. D. W., and Smoukov, S. K. (2016). Electroactive polymers for sensing. *Interface Focus*, 6(4), DOI: 10.1098/rsfs.2016.0026.

Wang, Z., Wang, C., and Tomizuka, M. (2015). Vibration cancellation of semiconductor manufacturing robots. *Manufacturing Letters*, 4:6–9, DOI: 10.1016/j.mfglet.2015.01.004.

Wesolowsky, M. and Wilson, J. (2003). Seismic isolation of cable-stayed bridges for near-field ground motions. *Earthquake Engineering & Structural Dynamics*, 32(3):2107–2126, DOI: 10.1002/eqe.318.

Wineman, A. (2009). Nonlinear viscoelastic solids-a review. *Mathematics and Mechanics of Solids*, 14(3):300–366, DOI: doi.org/10.1016/j.ijsolstr.2007.02.038.

Wollscheid, D. and Lion, A. (2013). Predeformation- and frequency-dependent material behaviour of filler-reinforced rubber: Experiments, constitutive modelling and parameter identification. *International Journal of Solids and Structures*, 50(9):1217–1225, DOI: 10.1016/j.ijsolstr.2012.12.015.

Wright, R. M., Post, A., Hoshizaki, B., and Ramesh, K. T. (2013). A multiscale computational approach to estimating axonal damage under inertial loading of the head. *Journal of Neurotrauma*, 30(2):102–118, DOI: 10.1089/neu.2012.2418.

Xu, X. and Henao, D. (2011). An efficient numerical method for cavitation in nonlinear elasticity. *Mathematical Models and Methods in Applied Sciences*, 21(08):1733–1760, DOI: 10.1142/s0218202511005556.

Yamabe, J., Matsumoto, T., and Nishimura, S. (2011). Application of acoustic emission method to detection of internal fracture of sealing rubber material by high-pressure hydrogen decompression. *Polymer Testing*, 30(1):76–85, DOI: 10.1016/j.polymertesting.2010.11.002.

Yun, Z. and Zhuping, H. (2003). Void growth and cavitation in nonlinear viscoelastic solids. *Acta Mechanica Sinica*, 19(4):380 – 384, DOI: 10.1007/bf02487816.

Zhao, Z., Shuai, C., Gao, Y., Rustighi, E., and Xuan, Y. (2016). An application review of dielectric electroactive polymer actuators in acoustics and vibration control. *Journal of Physics: Conference Series*, 744(1):012162.

Zhong-Heng, G. and Solecki, R. (1963). Free and forced finite amplitude oscillations of an elastic thick-walled hollow sphere made of incompressible material. *Arch Mech Stos*, 15(3):427–433.

Zou, L. H., Huang, K., Zhang, W., Rao, Y., and Wang, L. Y. (2010). Prestress rubber isolator and its mechanical properties. *Advanced Materials Research*, 163-167:4405–4414, DOI: 10.4028/www.scientific.net/AMR.163-167.4405.

Zukas, J. and Scheffler, D. (2000). Practical aspects of numerical simulations of dynamic events: effects of meshing. *International Journal of Impact Engineering*, 24(9):925–945, DOI: 10.1016/s0734-743x(00)00012-9.

A Mathematical preliminaries

With the aim to make this document self-contained, the main mathematical operations employed throughout this dissertation are detailed in this appendix. Attention is restricted to those basic operations needed to follow this thesis. For a more elaborative and inclusive discussion the reader is referred to the work of Hashiguchi and Yamakawa (2012) or Holzapfel (2000), for example, from where this appendix has been adapted.

Throughout this dissertation and unless otherwise is specified, lowercase bold-face Latin letters are used for *vectors*, uppercase bold-faced Latin letters for *second-order tensors*, uppercase bold-faced calligraphic letters for *third-order tensors* and uppercase blackboard Latin letters for *fourth-order* tensors. Any other not bold-face Latin or Greek letter refers to a *scalar value*.

$$\begin{gathered} a, b, c, \alpha, \beta, \gamma, ...(\text{scalars}), \quad \mathbf{a}, \mathbf{b}, \mathbf{c}, ...(\text{vectors}), \\ \mathbf{A}, \mathbf{B}, \mathbf{C}, ...(2^{nd} \text{ order tensors}), \quad \mathcal{A}, \mathcal{B}, \mathcal{C}, ...(3^{rd} \text{ order tensors}), \\ \mathbb{A}, \mathbb{B}, \mathbb{C}, ...(4^{th} \text{ order tensors}). \end{gathered} \tag{A.1}$$

A.1 Algebra of vectors

In this section the basic definitions to operate with vectors are presented.

Scalar product The *inner product* or *scalar product* or *dot product* of the vectors $\mathbf{a}$ and $\mathbf{b}$ is defined by

$$\mathbf{a} \cdot \mathbf{b} = |\mathbf{a}| \ |\mathbf{b}| \cos(\theta), \tag{A.2}$$

where θ is the angle between the vectors $\mathbf{a}$ and $\mathbf{b}$, and $|\ |$ defines the magnitude such that

$$|\mathbf{v}| = \sqrt{\mathbf{v} \cdot \mathbf{v}} \geq 0. \tag{A.3}$$

The scalar product presents the following mathematical properties

$$\begin{aligned} \mathbf{a}\cdot\mathbf{b} &= \mathbf{b}\cdot\mathbf{a}, \\ \mathbf{a}\cdot(\mathbf{b}+\mathbf{c}) &= \mathbf{a}\cdot\mathbf{b}+\mathbf{a}\cdot\mathbf{c}, \\ s(\mathbf{a}\cdot\mathbf{b}) = (s\mathbf{a}\cdot\mathbf{b}) &= \mathbf{a}\cdot(s\mathbf{b}) = (\mathbf{a}\cdot\mathbf{b})s, \\ (a\mathbf{a}+b\mathbf{b})\cdot\mathbf{c} &= a\mathbf{a}\cdot\mathbf{c}+b\mathbf{b}\cdot\mathbf{c}. \end{aligned} \tag{A.4}$$

Vector product The *vector* or *cross product* produces a new vector and it is not commutative. It is defined as

$$\mathbf{a}\times\mathbf{b} = |\mathbf{a}|\,|\mathbf{b}|\sin(\theta)\,\mathbf{n}, \tag{A.5}$$

where $\mathbf{n}$ is the unit vector which forms a right-handed basis $(\mathbf{a},\mathbf{b},\mathbf{n})$ in this order.

Some of the main properties of the vector product are

$$\begin{aligned} \mathbf{a}\times\mathbf{a} &= 0, \\ \mathbf{a}\times\mathbf{b} &= -\mathbf{b}\times\mathbf{a}, \\ \mathbf{a}\times(\mathbf{b}+\mathbf{c}) &= \mathbf{a}\times\mathbf{b}+\mathbf{a}\times\mathbf{c}, \\ |\mathbf{a}\times\mathbf{b}|^2+(\mathbf{a}\cdot\mathbf{b})^2 &= (|\mathbf{a}|\,|\mathbf{b}|)^2. \end{aligned} \tag{A.6}$$

Index notation The algebra of this dissertation is mainly presented in *symbolic* (or *direct* or *absolute*) notation, which makes use exclusively of bold-faced letters. However, to gain more insight in some quantities and to carry out mathematical operations with three and four order tensors (see Chapter 6) it proves convenient to refer vector and tensor components to a basis. The vector $\mathbf{v}$ is represented in terms of its components and the basis vectors as follows

$$\mathbf{v} = v_1\mathbf{e}_1+v_2\mathbf{e}_2+v_3\mathbf{e}_3 = v_i\cdot\mathbf{e}_i, \tag{A.7}$$

where the *Einstein* or *summation convention* has been used. In this convention whenever an index is repeated in the same term, then, a summation over the range of this index is implied (unless otherwise is indicated as in some expressions of Chapter 8). Furthermore, the Cartesian basis vectors $\{\mathbf{e}_1,\mathbf{e}_2,\mathbf{e}_3\}$ satisfy the following properties

$$\mathbf{e}_i\cdot\mathbf{e}_j = \delta_{ij} \equiv \begin{cases} 1, & \text{if } i=j, \\ 0, & \text{if } i\neq j, \end{cases} \qquad i,j=1,2,3, \tag{A.8}$$

which defines the *Kronecker delta* δ_{ij} with properties $\delta_{ii} = 3$, $\delta_{ij}u_i = u_j$, $\delta_{ij}\delta_{jk} = \delta_{ik}$. Note that δ_{ij} serves as a replacement operator; i.e., the index on u_i becomes an j when the components u_i are multiplied by δ_{ij}.

There are several common notations for the Cartesian basis vectors, including $\{\mathbf{e}_1, \mathbf{e}_2, \mathbf{e}_3\}$, $\{\mathbf{i}, \mathbf{j}, \mathbf{k}\}$ or $\{\mathbf{e}_x, \mathbf{e}_y, \mathbf{e}_z\}$. The cylindrical $\{\mathbf{e}_r, \mathbf{e}_\theta, \mathbf{e}_z\}$ and spherical $\{\mathbf{e}_r, \mathbf{e}_\theta, \mathbf{e}_\phi\}$ vector basis are also widely used throughout this document. This basis satisfy the following conditions, respectively.

$$\mathbf{e}_r \times \mathbf{e}_\theta \cdot \mathbf{e}_z = 1, \quad \frac{\mathrm{d}\mathbf{e}_r}{\mathrm{d}\theta} = \mathbf{e}_\theta, \quad \frac{\mathrm{d}\mathbf{e}_\theta}{\mathrm{d}\theta} = -\mathbf{e}_r, \tag{A.9}$$

$$\mathbf{e}_r \times \mathbf{e}_\theta \cdot \mathbf{e}_\phi = -1, \quad \frac{\mathrm{d}\mathbf{e}_r}{\mathrm{d}\phi} = \mathbf{e}_\phi, \quad \frac{\mathrm{d}\mathbf{e}_\phi}{\mathrm{d}\phi} = -\mathbf{e}_r. \tag{A.10}$$

Please notice that with previous convention θ is the azimuth $0 \leq \theta \leq 2\pi$ angle and ϕ is the inclination $0 \leq \phi \leq \pi$ angle. [1]

The scalar and vector products introduced in A.2 and A.5, respectively, can be expressed in index notation as

$$\mathbf{a} \cdot \mathbf{b} = a_i b_i, \qquad \mathbf{a} \times \mathbf{b} = \epsilon_{i,j,k} a_i b_j \mathbf{e}_k, \tag{A.11}$$

where the *permutation* (or *alternating* or *Levi-Civita*) $\varepsilon_{i,j,k}$ is defined as

$$\varepsilon_{i,j,k} = \begin{cases} 1, & \text{for even permutations of } i,j,k \text{ i.e. } 123, 231, 312, \\ -1, & \text{for odd permutations of } i,j,k \text{ i.e. } 132, 213, 321, \\ 0, & \text{if there is a repeated index,} \end{cases} \tag{A.12}$$

Triple scalar product The *triple scalar* (or *box*) product represents the volume V of the paralelepiped created from the right-handed triad $\mathbf{a}$, $\mathbf{b}$ and $\mathbf{c}$. It is defined as

$$V = (\mathbf{a} \times \mathbf{b}) \cdot \mathbf{c} = (\mathbf{b} \times \mathbf{c}) \cdot \mathbf{a} = (\mathbf{c} \times \mathbf{a}) \cdot \mathbf{b} = \varepsilon_{i,j,k} a_i b_j c_k. \tag{A.13}$$

The triple scalar product can be also written using the determinant form as follows

$$(\mathbf{a} \times \mathbf{b}) \cdot \mathbf{c} = \begin{vmatrix} a_1 & b_1 & c_1 \\ a_2 & b_2 & c_2 \\ a_3 & b_3 & c_3 \end{vmatrix}. \tag{A.14}$$

[1] Although the spherical coordinates are usually ordered as $\{r, \theta, \phi\}$, this arrangement gives a left-handed basis as it can be seen from Eq. A.10$_1$. Expressions in this appendix are for a right-handed basis, which can be obtained by rearranging the basis as $\{\mathbf{e}_r, \mathbf{e}_\phi, \mathbf{e}_\theta\}$.

If the triple scalar product is zero, then the vectors $\mathbf{a}$, $\mathbf{b}$ and $\mathbf{c}$ are linearly dependent, that is, the parallelepiped has no volume.

Triple vector product The product $\mathbf{a} \times (\mathbf{b} \times \mathbf{c})$ is called the triple vector product. The formula of the vector product in terms of the scalar product introduced above is given by (the demonstration is omitted)

$$\mathbf{a} \times (\mathbf{b} \times \mathbf{c}) = (\mathbf{a} \cdot \mathbf{c})\, \mathbf{b} - (\mathbf{b} \cdot \mathbf{c})\, \mathbf{a}, \tag{A.15}$$

or in a similar way

$$(\mathbf{a} \times \mathbf{b}) \times \mathbf{c} = (\mathbf{a} \cdot \mathbf{c})\, \mathbf{b} - (\mathbf{b} \cdot \mathbf{c})\, \mathbf{a}. \tag{A.16}$$

Note that, in general, this operation is not associative, i.e. $(\mathbf{a} \times \mathbf{b}) \times \mathbf{c} \neq \mathbf{a} \times (\mathbf{b} \times \mathbf{c})$. The expressions in (A.15) and (A.16) are called *back-cab* rule from vector algebra.

A.2 Algebra of tensors

A second-order tensor $\mathbf{A}$ can be defined as a linear operator that acts on a vector $\mathbf{u}$ generating a vector $\mathbf{v}$ following the next linear transformation

$$\mathbf{v} = \mathbf{A}\mathbf{u}. \tag{A.17}$$

Tensor product The *tensor* (or *dyadic* or *matrix* or *direct*) product of two vectors $\mathbf{a}$ and $\mathbf{b}$ leads to a second-order tensor defined as $\mathbf{a} \otimes \mathbf{b}$. This second order tensor linearly transforms a vector $\mathbf{c}$ into a vector with the direction of $\mathbf{a}$ according to the rule

$$(\mathbf{a} \otimes \mathbf{b})\mathbf{c} = \mathbf{a}(\mathbf{b} \cdot \mathbf{c}) = (\mathbf{b} \cdot \mathbf{c})\mathbf{a}. \tag{A.18}$$

Some interesting properties of this operator are

$$\begin{aligned} \mathbf{a} \otimes \mathbf{b}\mathbf{c} &= \mathbf{a}\,(\mathbf{b} \cdot \mathbf{c})\,, \\ (\mathbf{a} \otimes \mathbf{b})^{\mathrm{T}} &= \mathbf{b} \otimes \mathbf{a}, \\ \mathbf{a} \otimes (\mathbf{b} + \mathbf{c}) &= \mathbf{a} \otimes \mathbf{b} + \mathbf{a} \otimes \mathbf{c}, \\ (\mathbf{b} \otimes \mathbf{c} - \mathbf{c} \otimes \mathbf{b})\, \mathbf{a} &= \mathbf{a} \otimes (\mathbf{b} \otimes \mathbf{c}) = (\mathbf{a} \cdot \mathbf{c})\, \mathbf{b} - (\mathbf{a} \cdot \mathbf{b})\, \mathbf{c}. \end{aligned} \tag{A.19}$$

Normally, the dyadic product is *not commutative*; i.e., $\mathbf{a} \otimes \mathbf{b} \neq \mathbf{b} \otimes \mathbf{a}$. Any second-order tensor may be expressed as a dyadic, using the tensor product. For instance, if we consider the second-order tensor $\mathbf{A}$, it can be represented as a linear combination of

dyads formed by the Cartesian basis $\{\mathbf{e}_i\}$

$$\mathbf{A} = A_{ij}\mathbf{e}_i \otimes \mathbf{e}_j \tag{A.20}$$

and tensor $\mathbf{A}$ can be also represented in the so-called *matrix notation* by its components A_{ij} with respect to $\{\mathbf{e}_i\}$; i.e.,

$$[\mathbf{A}] = \begin{pmatrix} A_{11} & A_{12} & A_{13} \\ A_{21} & A_{22} & A_{23} \\ A_{31} & A_{32} & A_{33} \end{pmatrix}. \tag{A.21}$$

Hence, the Cartesian components of the unit tensor $\mathbf{I}$ are given by

$$\mathbf{I} = \delta_{ij}\mathbf{e}_i \otimes \mathbf{e}_j = \mathbf{e}_j \otimes \mathbf{e}_j. \tag{A.22}$$

Scalar product The *scalar* (or *dot*) product $\mathbf{AB}$ of two second-order tensors $\mathbf{A}$ and $\mathbf{B}$ is a second-order tensor whose components along an orthonormal basis $\mathbf{e}_i$ are

$$(\mathbf{AB})_{ij} = A_{ik}B_{kj} \tag{A.23}$$

The dot product of second-order tensors is, in general, *not commutative*, that is, $\mathbf{AB} \neq \mathbf{BA}$.

Transpose of a tensor The transpose $\mathbf{A}^{\mathrm{T}}$ of a tensor $\mathbf{A}$ is defined such that

$$\mathbf{a} \cdot \mathbf{Ab} = \mathbf{b} \cdot \mathbf{A}^{\mathrm{T}}\mathbf{a} = \mathbf{Ab} \cdot \mathbf{a} \tag{A.24}$$

for all generic vectors $\mathbf{a}$ and $\mathbf{b}$. Some properties of the tensor transpose are

$$\begin{aligned} \left(\mathbf{A}^{\mathrm{T}}\right)^{\mathrm{T}} &= \mathbf{A}, \\ (\mathbf{AB})^{\mathrm{T}} &= \mathbf{B}^{\mathrm{T}}\mathbf{A}^{\mathrm{T}}, \\ (\alpha\mathbf{A} + \beta\mathbf{B})^{\mathrm{T}} &= \alpha\mathbf{A}^{\mathrm{T}} + \beta\mathbf{B}^{\mathrm{T}}, \\ (\mathbf{a} \otimes \mathbf{b})^{\mathrm{T}} &= \mathbf{a} \otimes \mathbf{b}. \end{aligned} \tag{A.25}$$

In the rectangular Cartesian coordinate system, selecting $\mathbf{a} = \mathbf{e}_i$ and $\mathbf{b} = \mathbf{e}_j$ in equation (A.24) leads to

$$A_{ij}^{\mathrm{T}} = A_{ij} \tag{A.26}$$

or, equivalently

$$\mathbf{A}^{\mathrm{T}} = (A_{ij}\mathbf{e}_i \otimes \mathbf{e}_j)^{\mathrm{T}} = A_{ij}\mathbf{e}_j \otimes \mathbf{e}_i \tag{A.27}$$

Trace and contraction The trace of a tensor $\mathbf{A}$ is a scalar denoted by tr$\mathbf{A}$ that is obtained summing the terms of its diagonal. For example, in the case of the dyad $\mathbf{a} \otimes \mathbf{b}$, the trace is given by the dot product $\mathbf{a} \cdot \mathbf{b} = a_i b_i$. The trace of a generic tensor $\mathbf{A}$ with respect to the orthonormal basis $\{\mathbf{e}_i\}$ is given by

$$\begin{aligned} \text{tr}\mathbf{A} &= \text{tr}\left(A_{ij}\mathbf{e}_i \otimes \mathbf{e}_j\right) = A_{ij}\text{tr}\left(\mathbf{e}_i \otimes \mathbf{e}_j\right) \\ &= A_{ij}\left(\mathbf{e}_i \cdot \mathbf{e}_j\right) = A_{ij}\delta_{ji} \\ &= A_{ii} = A_{11} + A_{22} + A_{33}. \end{aligned} \tag{A.28}$$

The following properties hold for the trace of a tensor

$$\begin{aligned} \text{tr}\mathbf{A}^{\mathrm{T}} &= \text{tr}\mathbf{A}, \\ \text{tr}\left(\mathbf{AB}\right) &= \text{tr}\left(\mathbf{BA}\right), \\ \text{tr}\left(\mathbf{A} + \mathbf{B}\right) &= \text{tr}\mathbf{A} + \text{tr}\mathbf{B}, \\ \text{tr}\left(\alpha\mathbf{A}\right) &= \alpha\text{tr}\mathbf{A}. \end{aligned} \tag{A.29}$$

The *double dot product* or *contraction* $\mathbf{A} : \mathbf{B}$ of two tensors $\mathbf{A}$ and $\mathbf{B}$ is an operation that produces a scalar result. In index notation, a contraction means to identify two indices and sum over them as dummy indices. Using the tensor components with respect to the orthonormal basis $\{\mathbf{e}_i\}$, the double contraction is defined by

$$\mathbf{A} : \mathbf{B} = A_{ij}B_{ij} \tag{A.30}$$

Since the i and j subscripts appear in both factors, they are both summed to give

$$\begin{aligned} &\mathbf{A} : \mathbf{B} = A_{ij}B_{ij} = A_{11} \cdot B_{11} + A_{12} \cdot B_{12} + A_{13} \cdot B_{13} + \\ &A_{21} \cdot B_{21} + A_{22} \cdot B_{22} + A_{23} \cdot B_{23} + A_{31} \cdot B_{31} + A_{32} \cdot B_{32} + A_{33} \cdot B_{33} \end{aligned} \tag{A.31}$$

considering that $\mathbf{A}$ and $\mathbf{B}$ are second order tensors. The double contraction of two tensors $\mathbf{A}$ and $\mathbf{B}$ can be also defined in terms of the trace as

$$\begin{aligned} \mathbf{A} : \mathbf{B} &= \text{tr}\left(\mathbf{A}^{\mathrm{T}}\mathbf{B}\right) = \text{tr}\left(\mathbf{B}^{\mathrm{T}}\mathbf{A}\right) \\ &= \text{tr}\left(\mathbf{AB}^{\mathrm{T}}\right) = \text{tr}\left(\mathbf{BA}^{\mathrm{T}}\right) = \mathbf{B} : \mathbf{A} \end{aligned} \tag{A.32}$$

Some of the properties of double contraction are now listed

$$\begin{gathered}\mathbf{I} : \mathbf{A} = \mathrm{tr}\mathbf{A} = \mathbf{A} : \mathbf{I}, \\ \mathbf{A} : (\mathbf{BC}) = \left(\mathbf{B}^{\mathrm{T}}\mathbf{A}\right) = \left(\mathbf{B}^{\mathrm{T}}\mathbf{A}\right) : \mathbf{C} = \left(\mathbf{AC}^{\mathrm{T}}\right) : \mathbf{B}, \\ \mathbf{A} : (\mathbf{a} \otimes \mathbf{b}) = \mathbf{a} \cdot \mathbf{Ab} = (\mathbf{a} \otimes \mathbf{b}) : \mathbf{A}, \\ (\mathbf{a} \otimes \mathbf{b}) : (\mathbf{c} \otimes \mathbf{d}) = (\mathbf{a} \cdot \mathbf{c})\,(\mathbf{b} \cdot \mathbf{d})\,, \\ (\mathbf{e}_i \otimes \mathbf{e}_j) : (\mathbf{e}_k \otimes \mathbf{e}_l) = (\mathbf{e}_i \cdot \mathbf{e}_k)\,(\mathbf{e}_j \cdot \mathbf{e}_l)\,.\end{gathered} \tag{A.33}$$

Orthogonal tensor An orthogonal tensor $\mathbf{Q}$ is a linear transformation which fulfills the condition

$$\mathbf{Qa} \cdot \mathbf{Qb} = \mathbf{a} \cdot \mathbf{b}, \tag{A.34}$$

for all vectors $\mathbf{a}$ and $\mathbf{b}$. The set of orthogonal tensors is denoted as *Orth* throughout this dissertation (see Chapter 6). As can be seen in Eq. (A.34), the orthogonal transformation does not affect to the dot product $\mathbf{a} \cdot \mathbf{b}$. This means that both the magnitude of the vectors $|\mathbf{a}|$ and $|\mathbf{b}|$ and the angle θ formed by the vectors are unchanged (see Fig. A.1).

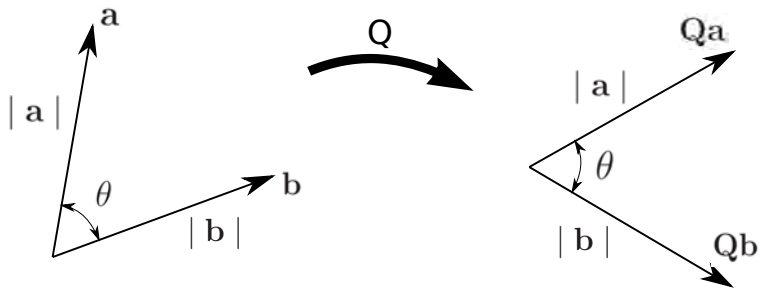

Fig. A.1 Orthogonal tensor. Adapted from Holzapfel (2000).

Combining the left-hand side in (A.34) with the transpose property given by Eq. (A.24), the equation becomes

$$\mathbf{Qa} \cdot \mathbf{Qb} = \mathbf{a} \cdot \left(\mathbf{Q}^{\mathrm{T}}\mathbf{Qb}\right). \tag{A.35}$$

From equations (A.34) and (A.35) it can be deduced that an orthogonal tensor must satisfy

$$\mathbf{QQ}^{\mathrm{T}} = \mathbf{Q}^{\mathrm{T}}\mathbf{Q} = \mathbf{I}, \tag{A.36}$$

which implies that

$$\mathbf{Q}^{-1} = \mathbf{Q}^{\mathrm{T}}. \tag{A.37}$$

Based on previous equation, the following property holds

$$\det\left(\mathbf{Q}^{\mathrm{T}}\mathbf{Q}\right) = (\det\mathbf{Q})^2 = 1, \tag{A.38}$$

where $\det\mathbf{Q} = \pm 1$. If $\det\mathbf{Q} = +1$ (-1), then $\mathbf{Q}$ is said to be proper (improper) orthogonal corresponding to a rotation (reflection), respectively. To be noticed that, the orthogonal transformation also leaves the trace of two tensors unchanged

$$\mathrm{tr}\left\{\left(\mathbf{Q}\mathbf{A}\mathbf{Q}^{\mathrm{T}}\right)\left(\mathbf{Q}\mathbf{B}\mathbf{Q}^{\mathrm{T}}\right)\right\} = \mathrm{tr}\left(\mathbf{A}\mathbf{B}\right). \tag{A.39}$$

In addition, the magnitude of a tensor is unchanged under this transformation

$$\left|\mathbf{Q}\mathbf{T}\mathbf{Q}^{\mathrm{T}}\right| = \left|\mathbf{T}\right|. \tag{A.40}$$

Symmetric and skew tensors Any tensor $\mathbf{A}$ can always be uniquely decomposed into a *symmetric tensor* $\mathbf{S}$ and a *skew* or *antisymmetric* tensor $\mathbf{W}$ as follows

$$\mathbf{A} = \mathbf{S} + \mathbf{W} \tag{A.41}$$

where

$$\mathbf{S} = \frac{1}{2}\left(\mathbf{A} + \mathbf{A}^{\mathrm{T}}\right), \quad \mathbf{W} = \frac{1}{2}\left(\mathbf{A} - \mathbf{A}^{\mathrm{T}}\right). \tag{A.42}$$

In matrix notation, $\mathbf{S}$ and $\mathbf{W}$ are given by

$$[\mathbf{S}] = \begin{bmatrix} S_{11} & S_{12} & S_{13} \\ S_{12} & S_{22} & S_{23} \\ S_{13} & S_{23} & S_{33} \end{bmatrix}, \qquad [\mathbf{W}] = \begin{bmatrix} 0 & W_{12} & W_{13} \\ -W_{12} & 0 & W_{23} \\ -W_{13} & -W_{23} & 0 \end{bmatrix}. \tag{A.43}$$

Tensors $\mathbf{S}$ and $\mathbf{W}$ satisfy the following properties

$$\begin{gathered} \mathbf{S} = \mathbf{S}^{\mathrm{T}}, \quad \mathbf{W} = -\mathbf{W}^{\mathrm{T}}, \\ \mathbf{a}\cdot\mathbf{S}\mathbf{b} = \mathbf{b}\cdot\mathbf{S}\mathbf{a}, \\ \mathbf{a}\cdot(\mathbf{W}\mathbf{b}) = -\mathbf{b}\cdot(\mathbf{W}\mathbf{a}), \\ \mathbf{S}\mathbf{S}^{\mathrm{T}} = \mathbf{S}^2, \\ \mathrm{tr}\left(\mathbf{S}\mathbf{W}\right) = \mathrm{tr}\left(\mathbf{S}\mathbf{W}^{\mathrm{T}}\right) = 0. \end{gathered} \tag{A.44}$$

Using the double dot contraction presented in Eq. (A.30), the following properties are derived

$$\begin{aligned} \mathbf{S}:\mathbf{B} &= \mathbf{S}:\mathbf{B}^{\mathrm{T}} = \mathbf{S}:\frac{1}{2}\left(\mathbf{B}+\mathbf{B}^{\mathrm{T}}\right), \\ \mathbf{W}:\mathbf{B} &= -\mathbf{W}:\mathbf{B}^{\mathrm{T}} = \mathbf{W}:\frac{1}{2}\left(\mathbf{B}-\mathbf{B}^{\mathrm{T}}\right), \\ \mathbf{S}:\mathbf{W} &= 0, \end{aligned} \tag{A.45}$$

where $\mathbf{B}$ is any second-order tensor.

Spherical and deviatoric tensors Any generic tensor $\mathbf{A}$ can be decomposed into a *spherical part* and a *deviatoric part*

$$\mathbf{A} = \alpha\mathbf{I} + \mathrm{dev}\mathbf{A}, \quad \alpha = \frac{1}{3}\mathrm{tr}\mathbf{A} = \frac{1}{3}\left(\mathbf{I}:\mathbf{A}\right). \tag{A.46}$$

The first term in (A.46), in which α is a scalar, is known as a spherical tensor, while the second term in (A.46) is the deviatoric part of tensor $\mathbf{A}$. The deviatoric part of the tensor $\mathbf{A}$ must satisfy

$$\mathrm{tr}\left(\mathrm{dev}\mathbf{A}\right) = 0. \tag{A.47}$$

A.3 Higher-order tensors

Any tensor of order n may be expressed in the form

$$A_{i_1 i_2 \ldots i_n}\mathbf{e}_{i_1} \otimes \mathbf{e}_{i_2} \otimes \ldots \otimes \mathbf{e}_{i_n}, \tag{A.48}$$

where a tensor of order n has 3^n components $A_{i_1 i_2 \ldots i_n}$ provided with n indices $i_1, i_2, \ldots, i_n$; i.e., 27 components for third-order tensors or 81 components for fourth-order tensors.

Third-order tensors Let $\boldsymbol{\mathcal{A}}$ denote a third-order tensor, according to previous expression $\boldsymbol{\mathcal{A}}$ can be expressed as

$$\boldsymbol{\mathcal{A}} = \mathcal{A}_{ijk}\mathbf{e}_i \otimes \mathbf{e}_j \otimes \mathbf{e}_k, \tag{A.49}$$

where the components $\mathcal{A}_{ijk}$ of $\boldsymbol{\mathcal{A}}$ are given by

$$\mathcal{A}_{ijk} = \left(\mathbf{e}_i \otimes \mathbf{e}_j\right) : \boldsymbol{\mathcal{A}}\,\mathbf{e}_k. \tag{A.50}$$

The double contraction of a third-order tensor $\boldsymbol{\mathcal{A}}$ with a second-order tensor $\mathbf{B}$ produces a vector such that

$$\boldsymbol{\mathcal{A}} : \mathbf{B} = \mathcal{A}_{ijk}\mathbf{B}_{jk}\mathbf{e}_i. \tag{A.51}$$

Fourth-order tensors Any tensor of order four $\mathbb{A}$ may be expressed in terms of its components $\mathcal{A}_{ijkl}$ and the Cartesian basis $\{\mathbf{e}_i, \mathbf{e}_j, \mathbf{e}_k, \mathbf{e}_l\}$ as

$$\mathbb{A} = \mathcal{A}_{ijkl}\mathbf{e}_i \otimes \mathbf{e}_j \otimes \mathbf{e}_k \otimes \mathbf{e}_l, \tag{A.52}$$

where the components $\mathcal{A}_{ijkl}$ of $\mathbb{A}$ are given by

$$\mathcal{A}_{ijk} = (\mathbf{e}_i \otimes \mathbf{e}_j) : \mathbb{A} : (\mathbf{e}_k \otimes \mathbf{e}_l). \tag{A.53}$$

Hence, the double contraction of a fourth-order tensor $\mathbb{A}$ with a second-order tensor $\mathbf{B}$ produces a second-order tensor such that

$$\mathbb{A} : \mathbf{B} = \mathcal{A}_{ijkl}\mathbf{B}_{kl}\mathbf{e}_i \otimes \mathbf{e}_j. \tag{A.54}$$

A.4 Gradients and related operators

A *tensor function* is a function whose input arguments are one or more tensor variables and whose output values are scalars, vectors or tensors. The functions $\Phi(\mathbf{B})$, $\mathbf{u}(\mathbf{B})$ and $\mathbf{A}(\mathbf{B})$ are examples of so-called *scalar-valued*, *vector-valued* and *tensor-valued* tensor functions of one tensor variable $\mathbf{B}$, respectively. In a similar way, $\Phi(\mathbf{u})$, $\mathbf{v}(\mathbf{u})$ and $\mathbf{A}(\mathbf{u})$ are vector functions of one vector variable $\mathbf{u}$ with the output value of a scalar, vector and tensor, respectively. Moreover, we can consider *scalar functions* of one scalar variable; for example, time t such that $\Phi = \Phi(t)$, $\mathbf{u} = \mathbf{u}(t) = u_i(t)\mathbf{e}_i$ and $\mathbf{A} = \mathbf{A}(t) = A_{ij}(t)\mathbf{e}_i \otimes \mathbf{e}_j$ are scalar-valued, vector-valued and tensor-valued scalar functions.

From the point of view of Continuum Mechanics the most interesting functions are those with vector inputs, the so-called fields. In this section the fundamental differential operators for scalar, vector and tensor fields are presented.

Gradient of a scalar field If we consider a smooth scalar field $\Phi(\mathbf{x})$ continuously differentiable, then the gradient of Φ is given by the following vector field

$$\text{grad}\Phi = \nabla\Phi = \frac{\partial\Phi}{\partial x_i}\mathbf{e}_i = \frac{\partial\Phi}{\partial x_1}\mathbf{e}_1 + \frac{\partial\Phi}{\partial x_2}\mathbf{e}_2 + \frac{\partial\Phi}{\partial x_3}\mathbf{e}_3, \tag{A.55}$$

where the **Nabla** or **vector operator** ∇ is defined as

$$\nabla(\bullet) \equiv \frac{\partial}{\partial x_i} \equiv \left(\frac{\partial}{\partial x_1}, \frac{\partial}{\partial x_2}, \frac{\partial}{\partial x_3}\right) \tag{A.56}$$

The dot, cross and tensor products of the vector operator ∇ with a smooth vector or tensor field $(\bullet)$ are given by

$$\nabla \cdot (\bullet) = \frac{\partial(\bullet)}{\partial x_i} \cdot \mathbf{e_i}, \qquad \nabla \times (\bullet) = \mathbf{e_i} \times \frac{\partial(\bullet)}{\partial x_i}, \qquad \nabla \otimes (\bullet) = \frac{\partial(\bullet)}{\partial x_i} \otimes \mathbf{e_i} \tag{A.57}$$

Laplacian and Hessian of a scalar field The Laplacian operator ∇^2 or Δ is defined as follows

$$\nabla^2(\bullet) = \nabla \cdot \nabla(\bullet) = \nabla \cdot \frac{\partial(\bullet)}{\partial x_i}\mathbf{e}_i = \frac{\partial^2(\bullet)}{\partial x_i \partial x_j}\mathbf{e}_i \cdot \mathbf{e}_j = \frac{\partial^2(\bullet)}{\partial x_i \partial x_j}\delta_{ij} = \frac{\partial^2(\bullet)}{\partial x_i^2} \tag{A.58}$$

The Laplacian ∇^2 of a scalar field Φ results in another scalar field given by

$$\nabla^2(\Phi) = \frac{\partial^2 \Phi}{\partial x_1^2} + \frac{\partial^2 \Phi}{\partial x_2^2} + \frac{\partial^2 \Phi}{\partial x_3^2} \tag{A.59}$$

The Hessian operator $\nabla\nabla$ (or more explicitly $\nabla \otimes \nabla$) applied on an scalar field results in a second-order tensor field given by

$$\nabla\nabla\Phi = \nabla \otimes \nabla\Phi = \nabla \otimes \frac{\partial \Phi}{\partial x_i}\mathbf{e}_i = \frac{\partial^2 \Phi}{\partial x_i \partial x_j}\mathbf{e}_i \otimes \mathbf{e}_j \tag{A.60}$$

Gradient of a vector field The gradient of a smooth vector field $\mathbf{u}(\mathbf{x})$ returns a *second-order tensor field* and is given by

$$\text{grad}\mathbf{u} = \nabla \otimes \mathbf{u} = \frac{\partial u_i}{\partial x_j}\mathbf{e}_i \otimes \mathbf{e}_j \tag{A.61}$$

or, in matrix notation

$$[\text{grad}\mathbf{u}] = \begin{bmatrix} \frac{\partial u_1}{\partial x_1} & \frac{\partial u_1}{\partial x_2} & \frac{\partial u_1}{\partial x_3} \\ \frac{\partial u_2}{\partial x_1} & \frac{\partial u_2}{\partial x_2} & \frac{\partial u_2}{\partial x_3} \\ \frac{\partial u_3}{\partial x_1} & \frac{\partial u_3}{\partial x_2} & \frac{\partial u_3}{\partial x_3} \end{bmatrix} \tag{A.62}$$

Divergence of a vector field The divergence of a smooth vector field $\mathbf{u}(\mathbf{x})$ is a *scalar field* given by

$$\text{div } \mathbf{u} = \nabla \cdot \mathbf{u} = \frac{\partial u_i}{\partial x_i} = \frac{\partial u_1}{\partial x_1} + \frac{\partial u_2}{\partial x_2} + \frac{\partial u_3}{\partial x_3} \tag{A.63}$$

If div $\mathbf{u} = 0$ the vector field $\mathbf{u}$ is said to be solenoidal.

Curl of a vector field The cross product of the vector operator ∇ with a smooth vector field $\mathbf{u}(\mathbf{x})$ is called the curl of $\mathbf{u}$ and is given by

$$\text{curl } \mathbf{u} = \nabla \times \mathbf{u} = \frac{\partial u_i}{\partial x_i}\mathbf{e}_i \times \mathbf{e}_j = \varepsilon_{i,j,k}\frac{\partial u_j}{\partial x_i}\mathbf{e}_k \tag{A.64}$$

If curl $\mathbf{u} = 0$ the vector field $\mathbf{u}$ is said to be irrotational or conservative.

Gradient of a second-order tensor field The gradient of a smooth second-order tensor field $\mathbf{A}(\mathbf{x})$ leads to a *third-order tensor field* and is given by

$$\text{A} = \nabla \otimes \mathbf{A} = \frac{\partial A_{ij}}{\partial x_k}\mathbf{e}_i \otimes \mathbf{e}_j \otimes \mathbf{e}_k \tag{A.65}$$

Divergence of a second-order tensor field The divergence of a smooth second-order tensor field $\mathbf{A}(\mathbf{x})$ is the following *vector field*

$$\text{div}\mathbf{A} = \nabla \cdot \mathbf{A} = \frac{\partial A_{ij}}{\partial x_j}\mathbf{e}_i \tag{A.66}$$

A.5 Integral theorems

Divergence theorem The divergence theorem, also known as *Gauss's* or *Ortrogradsky's* theorem, states that the volume integrals of the smooth vector field $\mathbf{u}(\mathbf{x})$ or the smooth tensor field $\mathbf{A}(\mathbf{x})$ can be converted to surface integrals according to

$$\begin{aligned} \int_s \mathbf{u} \cdot \mathbf{n} ds &= \int_v \text{div}\mathbf{u} dv \\ \int_s \mathbf{A} \cdot \mathbf{n} ds &= \int_v \text{div}\mathbf{A} dv \end{aligned} \tag{A.67}$$

where $\mathbf{n}$ is the outward unit normal field acting along the surface s and $\text{d}v$ is the infinitesimal volume elements at $\mathbf{x}$.

Reynolds' transport theorem Reynolds' transport theorem or Leibniz-Reynolds' transport theorem allows

Stokes Curl Theorem A surface integral on an open surface s can be converted into a contour integral around the bounding closed curve c using the following theorem (proof is omitted)

$$\int_s \text{curl } \mathbf{u} \cdot \mathbf{n} \text{d}s = \oint_c \mathbf{u} \text{d}\mathbf{x} \tag{A.68}$$